Università degli Studi di Padova
Dipartimento di Fisica e Astronomia "Galileo Galilei"

SCUOLA DI DOTTORATO DI RICERCA IN FISICA
CICLO XXVIII

Confined event samples using Compton coincidence measurements for signal and background studies in the GERDA experiment

Doctoral Dissertation of
Katharina Cäcilie von Sturm zu Vehlingen

Head of doctoral school
Prof. Andrea Vitturi

Supervisor
Prof. Alberto Garfagnini

for my family

Summary

In rare event searches, such as the search for Neutrinoless Double-Beta Decay ($0\nu\beta\beta$), the experimental sensitivity critically depends on the remaining background after all data cuts in the region of interest, where signal events are expected. Background reduction is essential to obtain the necessary experimental sensitivity. The Germanium Detector Array (Gerda) experiment is searching for $0\nu\beta\beta$ decay in ^{76}Ge. Recently, 30 newly produced germanium detectors of Broad Energy Germanium (BEGe) type have been implemented in Gerda. Analyzing the shape of detector pulses, background can be distinguished from signal events and discarded. The major advantage of the new BEGe detectors are their excellent properties for this kind of analysis.

The main focus of this thesis is the preparation of pure $0\nu\beta\beta$-like event samples from confined interaction regions in a BEGe in order to study the response of the detector with respect to the interaction position. This is useful to validate and improve pulse shape simulations of germanium detectors and can help creating new algorithms which effectively reduce the background in Gerda. An experimental setup was assembled and used to collect events due to single Compton interactions of photons with a BEGe detector. Because of their localized energy deposition single Compton events can be used as prototypes for $0\nu\beta\beta$ event pulse shapes. The assembly is capable of a full three-dimensional scan of the BEGe detector. An extensive characterization of all detectors used was realized to assure stable conditions of the experimental setup. Furthermore, detailed fine grain surface scans were performed which can give valuable input for simulation. A comprehensive Monte Carlo (MC) description of the assembly was implemented in a Geant4 based framework. The simulations provided means to conduct detailed studies of the spatial and energy distribution of single and multiple Compton events. Based on these studies the selection of pure samples of single Compton events from localized regions in the BEGe was optimized. In a data taking campaign event samples were collected for different experimental configurations. Differences in the pulse shape are observed when changing the scanned detector location or the High Voltage (HV) on the BEGe. In particular it was found that the first part of the average pulse is most sensitive.

Another aspect of rare event searches is the detailed analysis and decomposition of background events. A major background component in Gerda Phase I is introduced by the isotope ^{42}Ar. In this work, the specific activity of ^{42}Ar in the Gerda liquid Argon (LAr) was analyzed using a Bayesian approach. The detection efficiencies were calculated by means of MC simulations of part of the Gerda experimental setup. This permitted to study systematic effects introduced by inhomogeneities of the distribution of the studied background component in the LAr. The final value of the specific activity was obtained with a binned maximum likelihood fit of two fit models. Correcting the result for the time the LAr was kept under ground the specific activity can be compared to other experimental results, and furthermore, to theoretical calculations regarding production mechanisms of ^{42}Ar in the atmosphere. A corrected specific activity of $A_0(^{42}\mathrm{Ar}) = 101.0^{+2.5}_{-3.0}(\mathrm{stat}) \pm 7.4(\mathrm{syst})\ \mu\mathrm{Bq/kg}$ was found in this analysis; it is compatible with a theoretical calculation based on a major production mechanisms of ^{42}Ar in the atmosphere. However, it results incompatible with the upper limit, 43 Bq/kg at 90 % CL, reported in a previous measurement.

Riassunto

Nelle ricerche di eventi rari, come, per esempio, il decadimento doppio beta senza neutrini ($0\nu\beta\beta$), la sensibilità sperimentale dipende dal numero di eventi di fondo che rimangono nella regione di interesse dopo tutti i tagli di analisi. Per raggiungere una elevata sensibilità sperimentale è pertanto essenziale ridurre gli eventi di fondo. L'esperimento GERDA sta cercando il decadimento $0\nu\beta\beta$ mediante l'impiego dell'isotopo ^{76}Ge. Recentemente l'esperimento si è dotato di 30 nuovi rivelatori al germanio del tipo BEGe. Il maggiore vantaggio di tali rivelatori è di permettere una efficace separazione degli eventi di segnale da quelli di fondo mediante lo studio della forma del segnale elettrico.

Lo scopo primario di questa tesi è la ricerca di un metodo di raccolta di eventi che possano simulare quelli del decadimento $0\nu\beta\beta$. Si vuole inoltre che tali eventi siano distribuiti su tutto il volume del rivelatore. Questo risulta molto utile per creare algoritmi che permettano di ridurre gli eventi di fondo in GERDA. Inoltre, lo studio della risposta del rivelatore a seconda del punto di interazione del fotone incidente permette di controllare e migliorare la descrizione della forma d'impulso ottenuta dalle simulazioni. È stato allestito un apparato sperimentale che permette di selezionare eventi caratterizzati da una singola interazione Compton provenienti da regioni ben definite del rivelatore sotto esame (nel nostro caso un rivelatore di tipo BEGe). Gli eventi provenienti da una singola interazione Compton giacché rilasciano l'energia in una regione ben circoscritta del rivelatore simulano gli eventi doppio beta. L'apparato ha la capacità di analizzare l'intero volume del BEGe nelle sue tre dimensioni. Come passo propedeutico è stato eseguito uno studio delle caratteristiche fondamentali dei rivelatori usati. Questo è servito per assicurare un funzionamento stabile e affidabile all'apparato sperimentale. Lo studio ha comportato anche l'esecuzione di dettagliate scansioni superficiali dei rivelatori utili queste come informazioni in ingresso ai programmi di simulazione. Le simulazioni hanno permesso un'analisi della distribuzione spaziale ed energetica degli eventi caratterizzati da una singola interazione Compton come di quelli da molteplici interazioni Compton. Basandosi su tale studio e' stata ottimizzata la selezione degli eventi provenienti da un solo scattering Compton e da una posizione nota del rivelatore. Durante la campagna di raccolta dati sono stati acquisiti dei campioni di dati sotto diverse configurazioni dell'apparato sperimentale. Sono stati osservati delle differenze nella forma degli impulsi cambiando sia la posizione da cui proviene l'interazione che il valore di alta tensione applicata sul BEGe. In particolare, si è notato che la regione più sensibile è la parte iniziale dell'impulso.

Per poter rigettare gli eventi di fondo è importante anche conoscerli e classificarli. L'analisi dei dati di Gerda nella sua prima fase sperimentale ha mostrato che una delle componenti principali degli eventi di fondo è dovuta all'isotopo ^{42}Ar presente nel LAr. L'attività dell'^{42}Ar è stata studiata con un approccio bayesiano usando dati di Gerda fase I. Il risultato finale è stato ottenuto tramite un ottimizzazione di una binned likelihood. Una cura particolare è stata rivolta all'analisi di possibili effetti sistematici dovuti ad una possibile distribuzione spaziale non omogenea dell'^{42}Ar nel criostato di Gerda. Il risultato finale dell'attività specifica dell'^{42}Ar è $A_0(^{42}\mathrm{Ar}) = 101.0^{+2.5}_{-3.0}(\mathrm{stat}) \pm 7.4(\mathrm{syst})\,\mu\mathrm{Bq/kg}$. Tale valore risulta compatibile con una stima derivata da un particolare modello di produzione di tale isotopo raro nell'atmosfera. Risulta invece incompatibile con il limite superiore, 43 Bq/kg al 90 % CL, riportato in una precedente misura sperimentale.

Contents

Introduction

I have done a terrible thing, I have postulated a particle that cannot be detected.

— W. Pauli

Pauli could not have been more wrong with this statement after postulating the existence of the neutrino in 1930, which ever since has been challenging the physics world. It has been 60 years since its first experimental confirmation. Although a lot has been learned about neutrinos, the picture unrevealed still has obvious and profound flaws: the absolute neutrino masses are unmeasured and their smallness is unexplained, it is unknown which of the three generations of neutrinos is the lightest and experimental data is not sufficient to decide whether the neutrino is of Dirac or Majorana nature.

To complete the picture, neutrinos are and will be a main focus of fundamental research for many years to come. They offer an exciting field of study as Neutrinos are very different from other constituents of the Standard Model of Particle Physics (SM) [1], and findings in the neutrino sector have far reaching implications also in other fields, for instance in cosmology [2]. Neutrinos have opened a window to new physics beyond the SM when solar neutrino oscillation experiments found compelling evidence for a nonzero neutrino mass [3–5]. Moreover, neutrino mixing could be a source of Charge Parity (CP) violation in the leptonic sector of the SM [6,7]. The utmost importance is given to determining whether the neutrino is of Dirac or Majorana nature [8]. It is fundamental for the understanding of the origin of neutrino masses, mixing and symmetries in the leptonic sector.

The only realistic probe of the existence of a Majorana neutrino mass term in the next $20-30$ years is the search for Neutrinoless Double-Beta Decay ($0\nu\beta\beta$) [9]. This decay would be Lepton number violating by two units and require physics beyond the SM. A very brief introduction to $0\nu\beta\beta$ decay will be given in Chapter 1; a fully comprehensive review is beyond the scope of this work and excellent, recent reviews about neutrinos in general and $0\nu\beta\beta$ decay in particular can be found in [9–11].

Several experiments are looking for $0\nu\beta\beta$ decay in different isotopes and with very different detection techniques [12–17]. They have one thing in common: they are looking for a very rare — if existing — decay, which makes them *low background* *experiments*. Reduction of background which can mimic signal events and understanding of the background components present is vital for all of them, and becomes more important with higher active mass. This is explained in a little more detail in Chapter 2.

Background can be reduced in three ways: 1) *passively*, by building experiments deeper underground, selecting radiopure construction materials and shielding with lead, water or similar; 2) *actively vetoing background* which enters from the outside leaving traces inside a veto system; 3) *discriminating background from signal events* by studying the shape of pulses from the detector(s). This work focuses on the latter.

This thesis has been conducted in the framework of the GERDA experiment, which is searching for $0\nu\beta\beta$ decay in ^{76}Ge [14]. In GERDA, High Purity Germanium (HPGe) detectors enriched in ^{76}Ge are used as source and detector simultaneously. An introduction to germanium detectors and interaction of photons with the detector material can be found in Chapter 3. A comprehensive characterization of the detectors used in this work is described in the following Chapter 4.

The properties of signal-like events are studied in order to improve background rejection by Pulse Shape Discrimination (PSD) in germanium detectors for application in $0\nu\beta\beta$ experiments. An existing experimental setup for the purpose of collecting single site event (SSE) (interactions with localized energy deposition) samples of confined regions inside a Broad Energy Germanium (BEGe) detector [18] has been rebuilt and significantly improved. It is based on measurement of energy deposited inside a BEGe detector by photon interacting via Compton scattering and coincident tagging of the scattered photons. The setup has the potential of a full three-dimensional scan of any HPGe detector. The collected event samples can be used to improve background rejection, for Pulse Shape Analysis (PSA) and for comparison with pulse shape simulations. Chapter 5ff contain a description of the experimental purpose and functionality, a full Monte Carlo (MC) description of the setup, and finally, results of *Compton coincidence measurements* taken with the apparatus.

Another aspect of low background experiments is the study of different background components present in the experimental setup, which can mimic signal events. The unique setup of the GERDA experiment, operating bare HPGe detectors in liquid Argon (LAr), gives the possibility to study the content of ^{42}Ar in LAr which is a major background source for GERDA. The last Chapter 8 contains a study of the specific activity of ^{42}Ar in the GERDA LAr with a Bayesian approach using Phase I data .

Chapter 1

Neutrinoless Double-Beta Decay

Double-Beta Decay ($\beta\beta$) is a second order weak decay transforming two neutrons bound in a nucleus simultaneously into two protons via virtual levels. In addition to the ordinary decay mode ($2\nu\beta\beta$) with two neutrinos in the final state, a second mode ($0\nu\beta\beta$) without neutrinos is theoretically possible:

$$2\nu\beta\beta: \quad A(Z,N) \rightarrow A(Z+2,N-2) + 2\,e^- + 2\,\bar{\nu}_e \tag{1.1}$$

$$0\nu\beta\beta: \quad A(Z,N) \rightarrow A(Z+2,N-2) + 2\,e^- \tag{1.2}$$

Two Neutrino Double-Beta Decay ($2\nu\beta\beta$) can be observed in even-even nuclei for which ordinary beta decay is energetically forbidden but an energetically preferable energy level exists. It has been measured in a handful of isotopes with lifetimes of $(10^{18} - 10^{24})$ yr [19,20]. The latest value for ^{76}Ge is $T_{1/2}^{2\nu} = \left(1.84^{+0.14}_{-0.10}\right) \cdot 10^{21}$ yr [21].

Neutrinoless Double-Beta Decay ($0\nu\beta\beta$) is a by two units Lepton Number Violating (LNV) decay; thus forbidden in the Standard Model of Particle Physics (SM). Lepton number conservation however is just an accidental symmetry in the SM as no operator can be found which violates Lepton number. LNV is introduced taking higher dimension operators into account giving rise to physics beyond the SM.

The possible Majorana nature of neutral spin-1/2 particles was pointed out already in 1937 by Ettore Majorana [8]. Being the only neutral fermion, the neutrino is the sole candidates for a Majorana particle in the SM. Moreover, compelling evidence for a nonzero neutrino mass was found by neutrino oscillation experiments [3–5]. The standard interpretation of $0\nu\beta\beta$ decay is the *mediation by light massive neutrinos which fulfill the Majorana condition* $\nu = \bar{\nu}$ *as dominant process.* $0\nu\beta\beta$ decay — mediated by light Majorana neutrinos — is visualized in contrast to the known decay mode, $2\nu\beta\beta$, in Figure 1.1, by the corresponding Feynman diagrams.

The expected signature of such a decay — in the standard interpretation — would be a peak at the end-point of the continuous $2\nu\beta\beta$ spectrum (see Figure 1.2).

It shall be noted that quite some non-standard interpretations of $0\nu\beta\beta$ decay exist but are not considered in the following. See e.g. [9] for a compilation of non-standard interpretations and further reference. They become interesting if experiments looking for $0\nu\beta\beta$ decay see a signal, while experiments which are sensitive to other combinations of neutrino masses e.g. measurements of the endpoint of the tritium decay [22, 23] or cosmological observations of Baryon Acoustic Oscillations (BAO) and the Cosmic Microwave Background (CMB) [24] do not confirm the measurements; i.e. a signal is found outside the allowed parameter space of $0\nu\beta\beta$ being mediated by light massive neutrinos. That parameter space will be discussed in a moment.

Neutrinos of Majorana nature are interesting also in other theoretical aspects. An elegant solution for the smallness of neutrino masses is provided via the see-saw type I mechanism [25] adding only three right-handed components of the neutrino fields to the SM. This mechanism is possible if neutrinos are of Majorana nature.

The only practical way to prove that neutrinos are Majorana particles [26] for the next 20 − 30 years is to search for $0\nu\beta\beta$ decay [9].

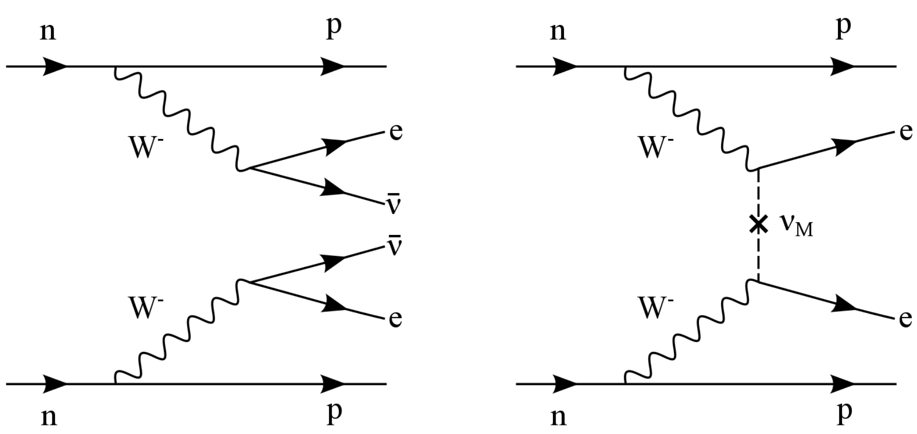

Figure 1.1: Feynman diagrams of $2\nu\beta\beta$ (left) and the standard interpretation of $0\nu\beta\beta$ (right).

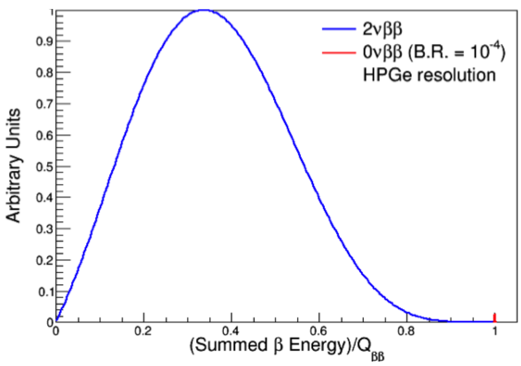

Figure 1.2: Expected spectral signature of $0\nu\beta\beta$ decay.

The inverse half-life of $0\nu\beta\beta$ is given by

$$\Gamma^{0\nu} = \frac{1}{T^{0\nu}_{1/2}} = G^{0\nu}(Q,Z)\, g_{\mathrm{A}}^4 \,\frac{\langle m_{\beta\beta}\rangle^2}{m_{\mathrm{e}}^2}\,|\mathcal{M}^{0\nu}|^2 \tag{1.3}$$

The phase space factor $G^{0\nu}$ scales with the end-point energy of $2\nu\beta\beta$ decay to the fifth power $Q^5_{\beta\beta}$ and is calculated numerically. For recent calculations of $G^{0\nu}$ see [27] and [28]. The so called Q-value or end-point energy, $Q_{\beta\beta} = M_{\mathrm{i}} - M_{\mathrm{f}} - 2\,m_{\mathrm{e}}$, is given by the difference of initial, M_{i}, and final mass, M_{f}, of the decaying nucleus and the mass of the two electrons, $2\,m_{\mathrm{e}}$. It defines the maximal kinetic energy of the two electrons in the final state of $2\nu\beta\beta$. The $0\nu\beta\beta$ signal is expected at this energy. In general, values of $Q_{\beta\beta}$ are measured experimentally. In Table 1.1 numerical values of $G^{0\nu}$, the Q-value and the natural abundance of selected isotopes can be found.

The axial vector coupling constant g_{A} and the Nuclear Matrix Element (NME) $\mathcal{M}^{0\nu}$ are problematic parameters which will be discussed shortly at the end of this chapter and $m_{\beta\beta}$ is called the *effective Majorana mass.*

As $m_{\beta\beta}$ is a combination of neutrino mass Eigenstates m_i

$$m_{\beta\beta} = \left|\, e^{i\alpha_1}|U^2_{\mathrm{e}1}|m_1 + e^{i\alpha_2}|U^2_{\mathrm{e}2}|m_2 + |U^2_{\mathrm{e}3}|m_3 \,\right| \tag{1.4}$$

$0\nu\beta\beta$ gives a handle on the neutrino mass scale and is sensitive to the two Majorana phases α_1 and α_2 which only show in LNV decays as is $0\nu\beta\beta$ decay. The unitary Pontecorvo-Maki-Nakagawa-Sakata (PMNS) [31–33] matrix U describes neutrino mixing. In the standard parametrization, PMNS is given by

$$U = \begin{pmatrix} 1 & 0 & 0 \\ 0 & c_{23} & s_{23} \\ 0 & -s_{23} & c_{23} \end{pmatrix} \times \begin{pmatrix} c_{13} & 0 & s_{13}e^{-i\delta} \\ 0 & 1 & 0 \\ -s_{13}e^{i\delta} & 0 & c_{13} \end{pmatrix} \times \begin{pmatrix} c_{12} & s_{12} & 0 \\ -s_{12} & c_{12} & 0 \\ 0 & 0 & 1 \end{pmatrix} \tag{1.5}$$

with $s_{ab} \equiv \sin\vartheta_{ab}$ and $c_{ab} \equiv \cos\vartheta_{ab}$ and the mixing angles ϑ_{ab}. The Dirac phase δ could be responsible for *Charge Parity (CP) violation in the leptonic sector of the SM.*

The effective Majorana mass $m_{\beta\beta}$ can be constrained from parameters obtained in neutrino oscillation experiments, as $m_{\beta\beta} = f(\vartheta_{12},\, \vartheta_{13},\, \alpha_1,\, \alpha_2,\, m_1,\, m_2,\, m_3)$. The parameters and their uncertainties are listed in Table 1.2. Three general parameter spaces for $m_{\beta\beta}$ are obtained. They are

- normal hierarchy (NH): $m_1 < m_2 < m_3$; $\Delta m^2_{\odot} \ll \Delta m^2_{\mathrm{a}} \equiv \Delta m^2_{23}$
- inverted hierarchy (IH): $m_3 < m_1 < m_2$; $\Delta m^2_{\odot} \ll \Delta m^2_{\mathrm{a}} \equiv |\Delta m^2_{13}|$
- quasi-degeneracy (QD): $m_1 \simeq m_2 \simeq m_3$; $0 \gg \Delta m^2_{\mathrm{a}} \gg \Delta m^2_{\odot}$

With the *solar* and *atmospheric* squared mass differences $\Delta m^2_{\odot} \equiv \Delta m^2_{12} = m^2_2 - m^2_1$ and $\Delta m^2_{\mathrm{a}} \equiv \Delta m^2_{23} = m^2_3 - m^2_2$ ($|\Delta m^2_{13}| = m^2_3 - m^2_1$) for the NH (IH).

Table 1.1: Phase space factor $G^{0\nu}$, Q-value and natural abundance for $0\nu\beta\beta$ candidate isotopes with $Q_{\beta\beta} \geq 2\,\mathrm{MeV}$. Using $r_0 = 1.2\,\mathrm{fm}$ for the nuclear size corrections. Isotopic abundance from Table 1 in [9] all other values taken from Table III in [27].

Isotope	$G^{0\nu}$ $[10^{-15}\,\mathrm{y}^{-1}]$	$Q_{\beta\beta}$ [keV]	nat. Abundance
^{48}Ca	24.81	4272.26(404)	0.187
^{76}Ge	2.363	2039.04(16)†	7.8
^{82}Se	10.16	2995.12(201)	9.2
^{96}Zr	20.58	3350.37(289)	2.8
^{100}Mo	15.92	3034.40(17)	9.6
^{110}Pd	4.815	2017.85(64)	11.8
^{116}Cd	16.70	2813.50(13)	7.6
^{124}Sn	9.040	2286.97(153)	5.6
^{130}Te	14.22	2526.97(23)	34.5
^{136}Xe	14.58	2457.83(37)	8.9
^{150}Nd	63.03	3371.38(20)	5.6

† A more precise Q-value $Q_{\beta\beta}(^{76}\mathrm{Ge}) = 2039.061(7)\,\mathrm{keV}$ can be found in [29].

Table 1.2: Parameters from a global analysis of oscillation experiments which constrain $m_{\beta\beta}$; values are taken from [30]. $\Delta m^2_{12} = m^2_2 - m^2_1$ and $\Delta m^2_{31} = m^2_3 - (m^2_1 + m^2_2)/2$ where $\Delta m^2_{31} > 0\,(< 0)$ for the NH (IH).

hierarchy	parameter	value	1σ	3σ
NH or IH	Δm^2_{12} $[10^{-5}\mathrm{eV}^2]$	7.54	7.32 – 7.80	6.99 – 8.18
	$\sin(2\vartheta_{12})$ $[10^{-1}]$	3.08	2.91 – 3.25	2.59 – 3.59
NH	Δm^2_{31} $[10^{-3}\mathrm{eV}^2]$	2.43	2.37 – 2.49	2.23 – 2.61
	$\sin(2\vartheta_{13})$ $[10^{-2}]$	2.34	2.15 – 2.54	1.76 – 2.95
	$\sin(2\vartheta_{23})$ $[10^{-1}]$	4.37	4.14 – 4.70	3.74 – 6.26
	δ/π	1.39	1.12 – 1.77	0 – 2
IH	Δm^2_{31} $[10^{-3}\mathrm{eV}^2]$	2.38	2.32 – 2.44	2.19 – 2.56
	$\sin(2\vartheta_{13})$ $[10^{-2}]$	2.40	2.18 – 2.59	1.78 – 2.98
	$\sin(2\vartheta_{23})$ $[10^{-1}]$	4.55	4.24 – 5.94	3.80 – 6.41
	δ/π	1.31	0.98 – 1.60	0 – 2

The allowed parameter space for $m_{\beta\beta}$ using Table 1.2 can be represented depending on $m_\beta = \sqrt{\sum_i |U_{ei}|^2 m_i^2}$ (from tritium decay end-point) or $\Sigma = \sum_i m_i$ (from cosmology). Both representations can be seen in Figure 1.3 for the NH as well as the IH.

A large uncertainty on $T_{1/2}^{0\nu}$ is introduced by $\mathcal{M}^{0\nu}$, and lately also g_A quenching is discussed [34, 35]. In Figure 1.4 a compilation of NME values obtained in various models can be found. The models predict NME values with up to one order of magnitude difference, which has to be taken into account when making predictions about experimental sensitivities and when comparing $0\nu\beta\beta$ searches with different isotopes.

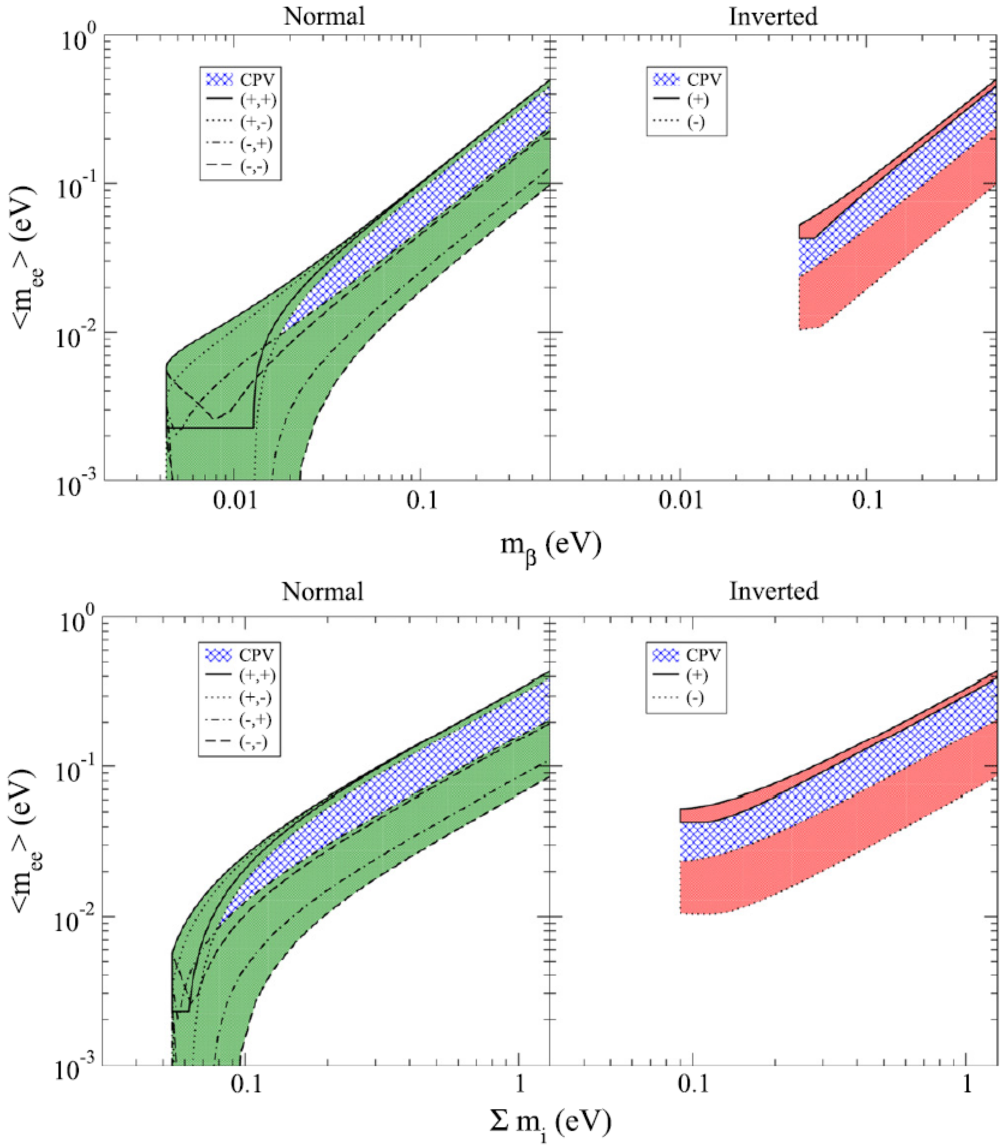

Figure 1.3: Dependence of allowed parameter space of $m_{\beta\beta}$ on m_β (top) and Σ (bottom) from [36] obtained using values from [37]. The values for relative signs of the mass Eigenvalues m_i, and the areas which can only be realized for non-trivial CP phases δ, are indicated.

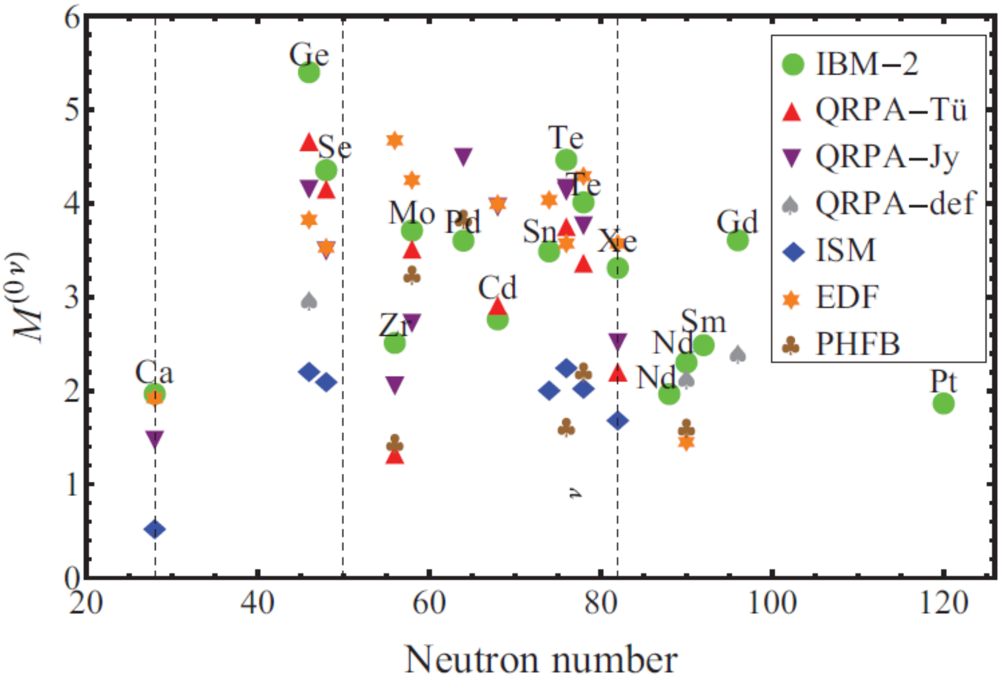

Figure 1.4: Predictions of NME values calculated in various models taken from [34]. Note that the maximal value of $\mathcal{M}^{0\nu}$ for ^{76}Ge is more than 2.5 times larger than the minimally predicted one. This introduces a large uncertainty to $T_1/2^{0\nu}$ and has to be taken into account when making predictions about experimental sensitivities and when comparing $0\nu\beta\beta$ searches with different isotopes.

Chapter 2

Experimental view on Neutrinoless Double-Beta Decay

Background reduction is one of the main issues low background experiments have to face. In this chapter we derive an expression for the sensitivity of $0\nu\beta\beta$ experiments [38] which shows how important it is to keep the background as low as possible. Finally, the GERDA experiment is introduced.

2.1 Experimental sensitivity

The sensitivity of a $0\nu\beta\beta$ experiment depends strongly on the experimental conditions. Every experiment conducted with presently known techniques will have background. If assumed flat, the number of background events can be written as

$$N_\mathrm{B} = B_\mathrm{i}\, M\, \Delta t\, \Delta E \tag{2.1}$$

with the source mass M[1] and the measurement time Δt in the energy window ΔE which depends on the energy resolution. The background index (BI) B_i is usually given in counts kg^{-1} keV^{-1} yr^{-1}.

A criterion for the discovery potential of a $0\nu\beta\beta$ decay experiment can be expressed as $N_{\beta\beta} = C_1\sqrt{N_{\beta\beta} + N_\mathrm{B}}$ with the confidence level C_1 in units of the σ of a Poisson distribution and the number of signal counts from $0\nu\beta\beta$ decay $N_{\beta\beta}$. If we require a certain signal to background ratio $N_{\beta\beta}/N_B \equiv r_\mathrm{SB}$ the number of signal events is given as

$$N_{\beta\beta} = C_1\sqrt{(1 + r_\mathrm{SB})\, N_\mathrm{B}} = C_1\gamma\sqrt{N_\mathrm{B}} \tag{2.2}$$

We can further express the number of signal events using the decay rate $\lambda_{\beta\beta}$

$$N_{\beta\beta} = \lambda_{\beta\beta}\,\frac{N_\mathrm{A}}{W}\, a\,\epsilon\, M\,\Delta t \tag{2.3}$$

where Avogadro's number N_A and the atomic weight W are physical constants and the isotopic abundance $0 < a \leq 1$ is defined by the natural abundance or the enrichment fraction.

[1] In the GERDA experiment, as detector and source are equivalent, M is the total detector mass.

Combining equations 2.1-2.3 and writing the decay rate in terms of the half-life $T_{1/2}^{0\nu} = \ln(2)/\lambda_{\beta\beta}$ we get an expression for the sensitivity

$$T_{1/2}^{0\nu} = \alpha_1 \, a \, \epsilon \sqrt{\frac{M \Delta t}{B_\mathrm{i} \, \Delta E}} \tag{2.4}$$

where

$$\alpha_1 = \frac{\ln(2) N_A}{W} \left(C_1 \sqrt{1 + r_\mathrm{SB}} \right)^{-1} \tag{2.5}$$

When comparing different experiments r_SB is chosen and is then fixed.

If we assume that the isotopic abundance, the detection efficiency and the energy resolution are naturally given, a higher sensitivity can be reached increasing the source mass M, the measurement time Δt and reducing the background B_i as much as possible. In general, the source material is expensive and sometimes hard to get, and each experimental setup has a limit on how much material can be hosted. Also, the measurement time has to stay in reasonable boundaries, let's say $< 10\,\mathrm{yr}$. In conclusion, the only real handle to get a better sensitivity is to reduce the background.

For a certain time no background counts are expected in the Region of Interest (ROI)[2]. Optimal experimental conditions are reached if this *limit of zero-background* is maintained for the major part of the experimental runtime. Without background the sensitivity takes the form

$$T_{1/2}^{0\nu} = \alpha_2 \, a \, \epsilon \, M \, \Delta t \tag{2.6}$$

with $\alpha_2 = \alpha_1 \sqrt{1 + r_\mathrm{SB}}$.

Note that the dependence on source mass and measurement time in Equation 2.6 is linear, in contrast to Equation 2.4 where $T_{1/2}^{0\nu} \propto \sqrt{M \Delta t}$. Thus, in the limit of zero-background the experimental resources of source mass and time are used in the most efficient way. In general, the design goal for the background index of every low background experiment is based on the objective to reach this limit. From Equation 2.1 it is evident that the higher the source mass and measurement time the lower B_i has to be, in order to stay in the limit of zero-background.

2.2 Germanium as a $0\nu\beta\beta$ candidate

Experiments in $0\nu\beta\beta$ decay searches make use of very different $0\nu\beta\beta$ candidate isotopes. In some sense germanium is not a preferable $0\nu\beta\beta$ candidate isotope: the decay rate (Equation 1.3) depends upon the phase space factor (see Table 1.1), hence, the expected half-life is lower for many other $0\nu\beta\beta$ candidates as can be seen in Figure 2.1.

[2]The region around $Q_{\beta\beta}$

In the case of nonzero-background the sensitivity of a $0\nu\beta\beta$ experiment depends upon the energy resolution (see Equation 2.4). Hence, the relatively long expected half-life is partly compensated by the exceptional energy resolution achievable with germanium detectors (see Section 3.3). Moreover, $2\nu\beta\beta$ decay is an irreducible background source for $0\nu\beta\beta$ decay searches. Thus, for longer half-lives a good energy resolution is necessary to distinguish the peak expected from $0\nu\beta\beta$ decay from the tail of the distribution of $2\nu\beta\beta$ decay.

2.3 The Gerda experiment

The Germanium Detector Array (Gerda) experiment is located at Laboratori Nazionali del Gran Sasso (LNGS) of Istituto Nazionale di Fisica Nucleare (INFN) in Italy with an overburden of about 3600 m.w.e.. Gerda is operating High Purity Germanium (HPGe) detectors bare in liquid Argon (LAr) [14], which are enriched in the $0\nu\beta\beta$ candidate isotope ^{76}Ge. The setup, which is shown in Figure 2.3, incorporates a copper lined stainless steel cryostat, 4 m in diameter, containing 63 m^3 of LAr. It is surrounded by a 3-m-thick active Muon Cerenkov Water Veto, which serves also as a passive γ and neutron shield. The Muon Veto is instrumented with 66 photomultipliers in order to identify muon induced events. The detectors are submerged into the cryostat through a lock-system from a glove box in the clean room above the neck of the cryostat. An additional muon veto made of plastic scintillator panels is installed on the roof of the clean room. It is meant to cover the weak spot of the water veto: the neck of the cryostat. Special care was devoted to the selection of radiopure materials for construction, and to a sparse design of all components near the detectors (holders, electronics, cables, etc.) to reduce thereby introduced background.

2.3.1 The Gerda detectors

The Gerda detectors are p-type HPGe detectors (for details see the next Chapter 3) enriched in the isotope ^{76}Ge. In the experimental Phase I mainly semi-coaxial (Coax) detectors were used while new detectors were produced for the second experimental stage. The Phase II detectors are of Broad Energy Germanium (BEGe) type. In Figure 2.2 the Coax and BEGe detector geometry can be seen alongside the P-type Point Contact (PPC) detector geometry which is similar to the BEGe but has an even smaller read-out contact.

2.3.2 Phase I result

Gerda has concluded the first experimental phase publishing a lower limit on the half-life of $0\nu\beta\beta$ of $T^{0\nu}_{1/2} > 2.1 \cdot 10^{25}$ yr (90% C.L.), with a median sensitivity of $T^{0\nu}_{1/2} > 2.4 \cdot 10^{25}$ yr [39]. The achieved background index of 10^{-2} cts/(keV^{-1}kg^{-1}yr^{-1}) at $Q_{\beta\beta}$ was unpreceded. By combining results with prior $0\nu\beta\beta$ searches by the Heidelberg-Moscow experiment (HDM) [40] and the International Germanium Experiment (IGEX) [41] the limit was strengthened to $T^{0\nu}_{1/2} > 3.0 \cdot 10^{25}$ yr (90% C.L.).

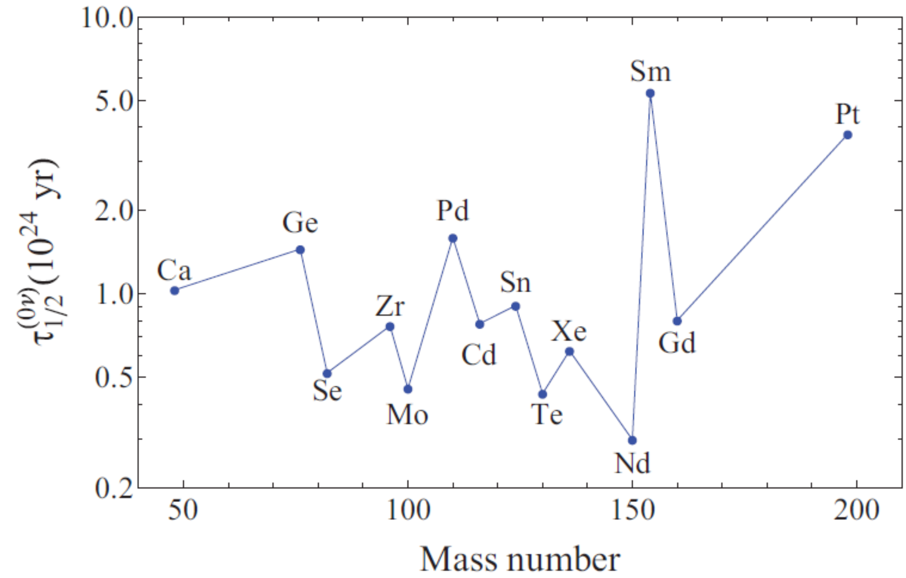

Figure 2.1: Expected $0\nu\beta\beta$ half-lives for different candidate isotopes. $m_{\beta\beta} = 1\,\text{eV}$ and $g_A = 1.269$. Figure adapted from [34].

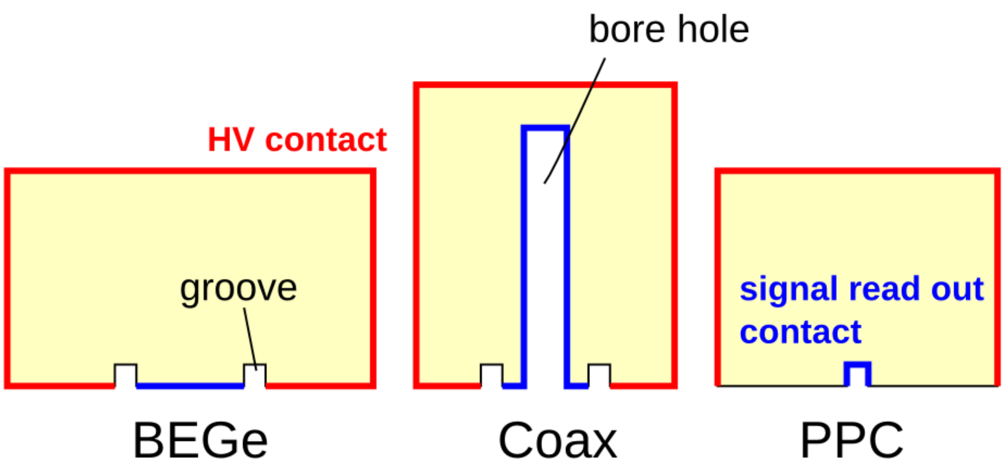

Figure 2.2: HPGe detector geometries. For p-type detectors the HV electrode is the n^+ contact which is lithium diffused and the signal readout contact is the boron implanted p^+ contact. This is inverted for n-type material.

This strongly disfavors a claim that was pending since a subgroup of the HDM experiment in 2004 reported the observation of $0\nu\beta\beta$ decay in ^{76}Ge [42]. A comparison of the found limits by Gerda with the half-life reported in 2004 and limits published by $0\nu\beta\beta$ searches in ^{136}Xe can be seen in Figure 2.4.

2.3.3 Phase II upgrade

The transition to the second experimental phase is almost complete [43]. A new lock-system has been installed, and a new detector assembly incorporating seven detector strings has been custom produced and is currently being tested. The LAr has been instrumented with a hybrid of 8" photomultipliers tubes (PMTs) and silicon photomultipliers (SiPMs) coupled to wavelength shifting fibers which uses the scintillation light of the LAr to identify background from components close to the detectors. Additional 30 HPGe detectors of BEGe type were produced and tested; they add 20 kg of enriched material to the total detector mass. A new holder design replaces the Phase I spring-loaded contacts to the detectors by wire bonds. The challenging goal for Phase II is to achieve a new BI of 10^{-3} cts/(keV kg yr) and to reach a sensitivity in the range of 10^{26} yr.

Figure 2.3: The Gerda experimental setup. Through a lock system HPGe detectors are lowered into the copper-lined stainless steel cryostat which is filled with LAr. The cryostat is surrounded by a Muon Cerenkov Water Veto.

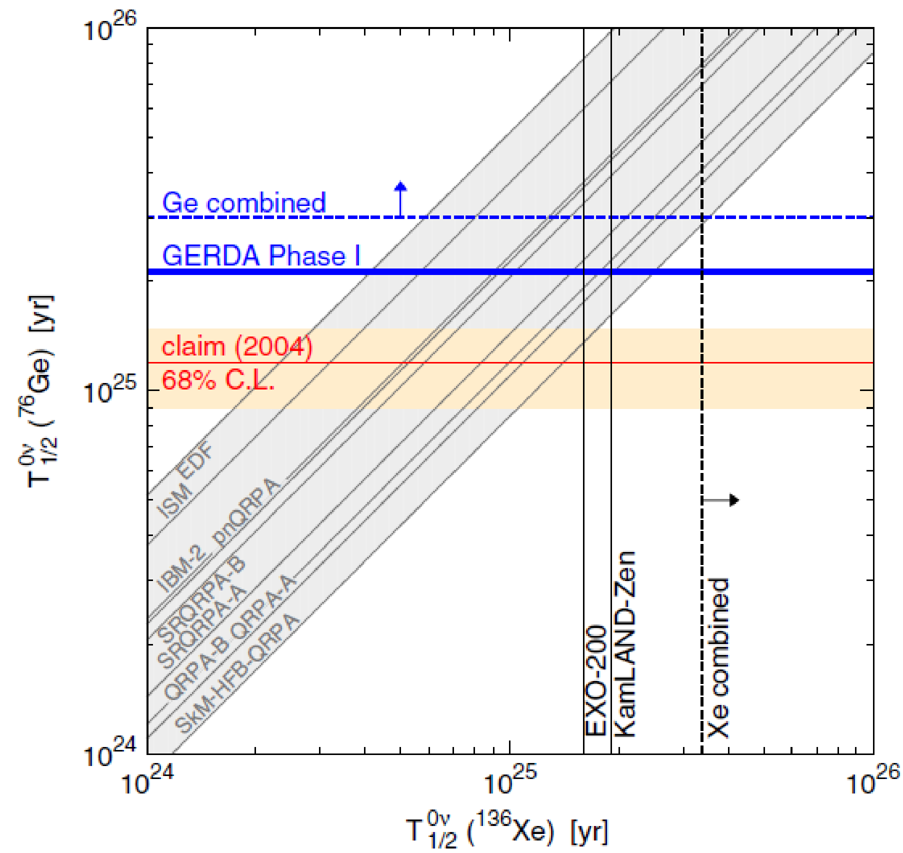

Figure 2.4: Comparison of half-life limits of $0\nu\beta\beta$ in ^{76}Ge and ^{136}Xe with the signal claim reported in 2004. The lines in the shaded gray band are predictions for the correlation of the half-lives in ^{136}Xe and in ^{76}Ge according to different NME calculations. Figure adapted from [39].

Chapter 3

High Purity Germanium detectors

In the next section a short overview of interactions of photons with matter is given. Hereafter, germanium is introduced as a semiconductor material and the properties of semiconductor diode detector are discussed. The following information can easily be found in every text book about radiation and detection measurements and semiconductor devices. Still one of the best and easiest to understand introductions is given in [44].

3.1 Interaction of photons with matter

Photons are neutral and massless, thus being able to travel deeper in material than charged particles. In their interactions with matter the incident photon can be absorbed and disappear, or be scattered and change energy and/or direction. When detecting γ radiation, i.e. high-energetic photon radiation originating from nuclear decays, only inelastic processes play a role where energy is absorbed in the detector material or transferred to it. Nevertheless, a very brief description of elastic processes is given.

3.1.1 Elastic scattering

An interactions in which the photon energy in the initial and final state of the reaction is conserved is called elastic scattering.

Thomson scattering is the low energy limit (visible part of the electromagnetic spectrum) of Compton scattering, where a photon gets elastically scattered on free unpolarizable charged particles e.g. free electrons. The electromagnetic component of the photon field accelerates a free electron which in turn radiates at the same frequency. Depending on the observation angle the observed radiation is more or less polarized.

Rayleigh scattering is the elastic scattering of photons on harmonically bound electrons e.g. shell electrons in an atom. The differential cross section of Rayleigh scattering depends on the wavelength of the photon to the fourth power, in contrast to Thomson scattering, which does not depend on the photon wavelength.

3.1.2 Photoelectric effect

The absorption of a photon by a shell electron of an atom is called *Photoelectric effect*. The photon has to have at least the binding energy of the electron E_b in the respective shell. After the reaction, the electron is free and can be detected. Electrons emitted in this way are called *photoelectrons* and their kinetic energy is given by

$$E_\mathrm{kin} = h\nu - E_\mathrm{b} \tag{3.1}$$

where h is the Planck constant and ν is the frequency of the photon field. $h\nu$ is the initial energy of the photon.

A free place in the electronic shell can be filled by an electron from an energetically higher shell emitting characteristic photon radiation with an energy equal to the difference of the two energy levels $E_\gamma = \Delta E_\mathrm{b}$. A sketch of these processes can be found in Figure 3.1.

3.1.3 Compton scattering

Compton scattering describes the scattering of a photon on a loosely bound (virtually free) electron with energy transfer. An electron which is gaining energy in this manner is called *recoil electron*. The kinetics are completely characterized by energy and momentum conservation if the scattering angle θ is given (see Figure 3.2). The energy of the scattered photon E'_γ and electron E_e can be written as

$$E'_\gamma = E_\gamma \cdot \left(1 + \frac{E_\gamma}{m_\mathrm{e}c^2} \cdot (1 - \cos\theta)\right)^{-1} = E_\gamma \cdot P(E_\gamma, \theta) \tag{3.2}$$

$$E_\mathrm{e} = E_\gamma - E'_\gamma \tag{3.3}$$

where E_γ is the incident photon energy, m_e is the rest mass of the electron and c is the speed of light.

Figure 3.3 shows the energy dependence of the scattered photon and electron on the scattering angle θ, with an incident photon energy of 662 keV.

The differential cross section $\mathrm{d}\sigma/\mathrm{d}\Omega$ of photons on free electrons for Thomson as well as for Compton scattering is given by the Klein-Nishina formula

$$\frac{\mathrm{d}\sigma}{\mathrm{d}\Omega} = \frac{\alpha^2\lambda_\mathrm{c}^2}{2} P(E_\gamma,\theta)^2 \left[P(E_\gamma,\theta) + P(E_\gamma,\theta)^{-1} - 1 + \cos^2\theta\right], \tag{3.4}$$

with the fine-structure constant α, the Compton wavelength $\lambda_\mathrm{c} = \hbar/m_\mathrm{e}c$ and $P(E_\gamma, \theta)$ as defined in Equation 3.2. In Figure 3.4 the differential cross section is plotted for various photon energies.

3.1.4 Pair production

For photons with at least twice the rest mass energy of the electron $E_\gamma \geq 1022\,\mathrm{keV}$ *pair production* becomes energetically possible. In the Coulomb field of a nucleus

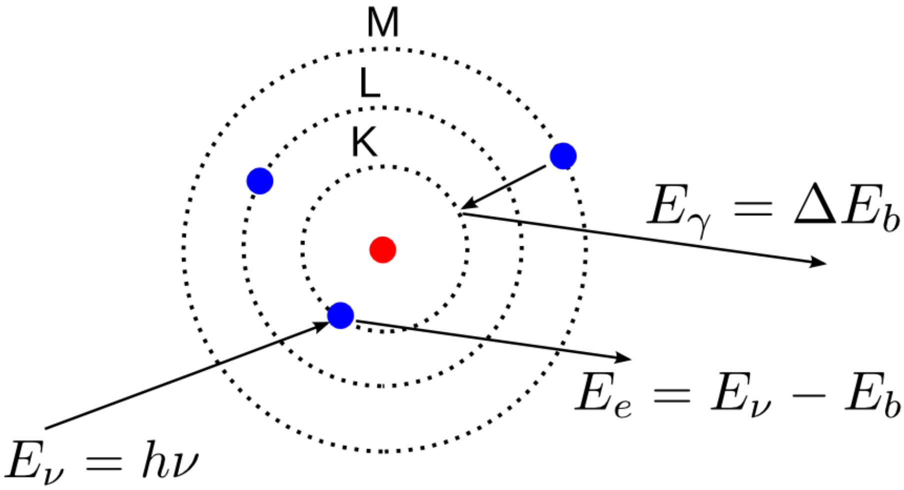

Figure 3.1: Photoelectric effect. A photon with incident energy $E_\nu = h\nu$ is absorbed by a shell electron which gets emitted carrying the kinetic energy $E_e = E_\nu - E_b$. Subsequently an electron from a higher shell can fall to the free place left vacant by the photo electron emitting characteristic photon radiation with an energy equal to the difference of the two shell levels.

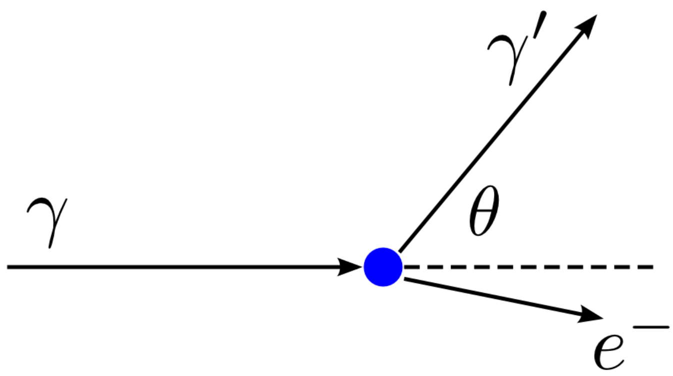

Figure 3.2: Compton scattering. A photon is scattered on a free electron, dynamics are defined by the incident photon energy and the scattering angle θ.

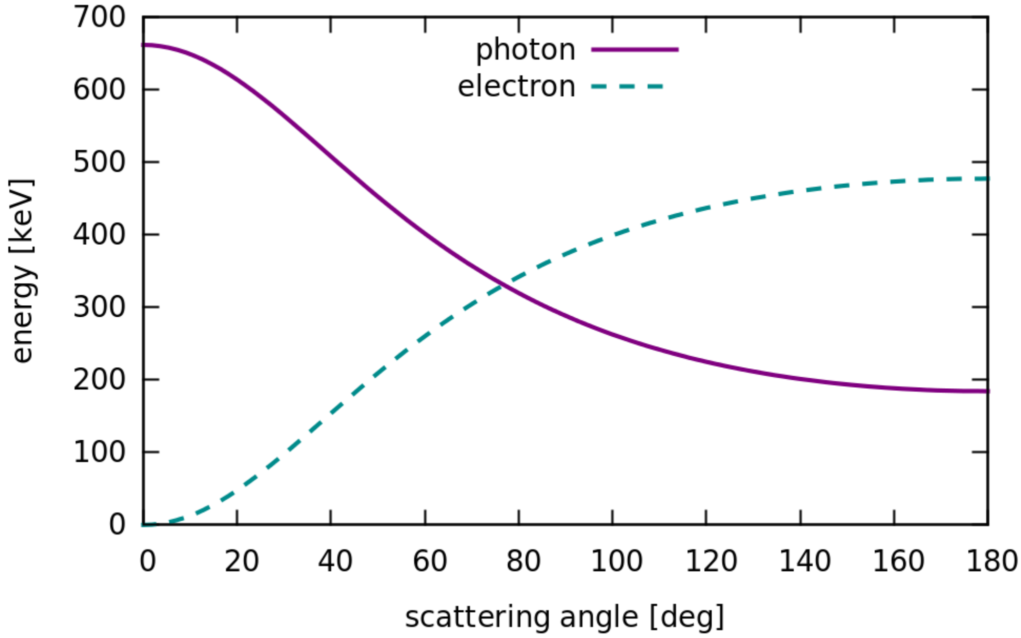

Figure 3.3: Energy of photon and electron after a Compton scattering for an incident photon energy of 662 keV.

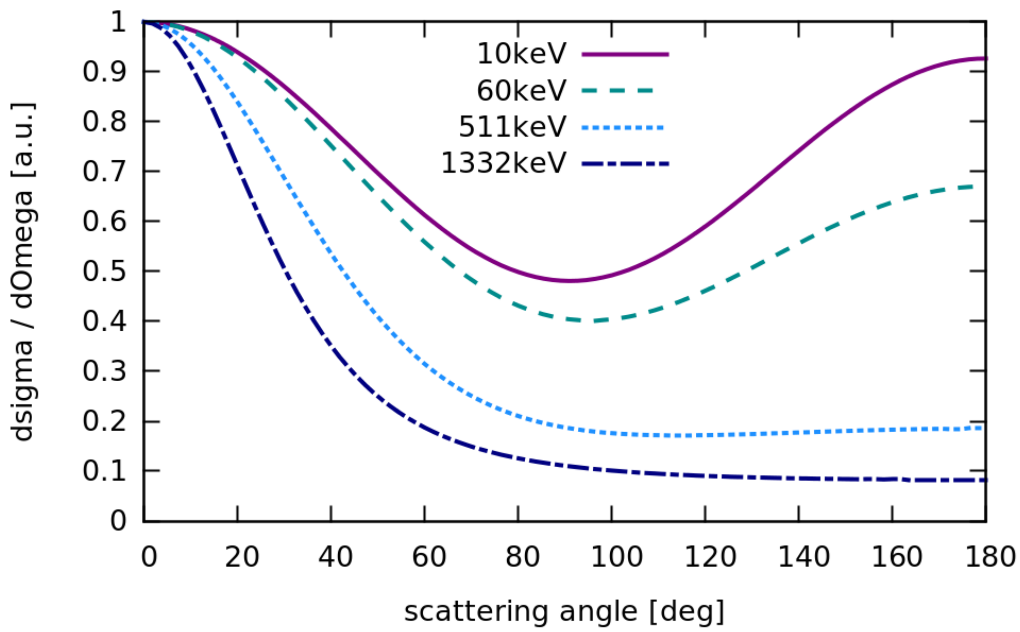

Figure 3.4: Differential cross section in Thomson and Compton scattering normalized to $d\sigma/d\Omega$ at 0° scattering angle.

the photon can be transformed into an electron-positron pair, as can be seen in Figure 3.5. All energy which exceeds $2\,m_e$ gets converted into kinetic energy which is shared between the electron and the positron. The positron subsequently thermalizes and finally annihilates with an e^- creating two back-to-back photons with an energy of 511 keV each.

3.1.5 Gamma ray attenuation

When passing through a medium, photons experience all processes described in Section 3.1. The surviving fraction of photons at incident energy in dependence of the material thickness d is given by an exponential law

$$\frac{N(d)}{N_0} = \exp(-\mu\rho \cdot d) \tag{3.5}$$

Where N_0 is the incident number of photons, ρ is the material density and μ is the total mass attenuation coefficient. μ depends on the material and on the photon energy and is composed of the coefficients for the respective inelastic processes

$$\mu = \mu_{\text{photo}} + \mu_{\text{Compton}} + \mu_{\text{pair}} \tag{3.6}$$

For photons with an energy of 662 keV $\mu_{\text{pair}} = 0$, as the energy is below the threshold for pair production.

3.2 Semiconductors

Every material can be characterized with respect to its electrical properties. The allowed and forbidden energy states of electrons inside a material are described by band theory. They are derived by studying the wave functions of electrons in a periodic lattice of condensed matter. A simplified model of the band structure of insulators, semiconductors and conductors is given in Figure 3.6. The lower band represents the *valence band* in which outer shell electrons are contained that are part of covalent bonds between atoms. The next higher band is called the *conduction band*. The structure of valence and conduction band define the conductive/resistive properties of a material.

In *insulators* a large gap, typically > 5 eV, separates the two bands, whereas *conductors* have either overlapping or only partially filled valence and conduction bands. In conductors electrons can easily be excited and migrate freely through the crystal. *Semiconductors* have a band gap which is small compared to insulators, of about 1 eV. Electrons in a semiconductor can only be excited into the conduction band if they are provided with enough energy to pass the band gap.

At absolute zero temperature the energy states in the valence band of insulators and semiconductors would be completely filled and the conduction band would be completely empty. In a semiconductor at non zero temperature a valence electron

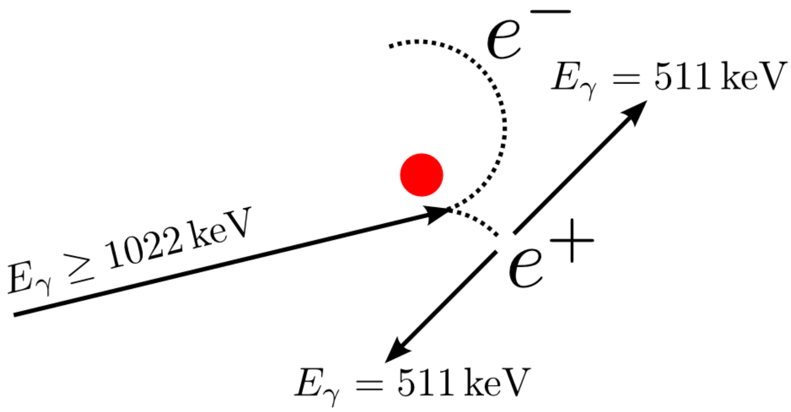

Figure 3.5: Pair production. In the Coulomb field of a nucleus a photon can be converted to an electron-positron pair if its energy is $E_\gamma \geq 1022\,\mathrm{keV}$. The positron slows down and annihilates with an electron emitting two photons back-to-back with the characteristic energy of 511 keV each.

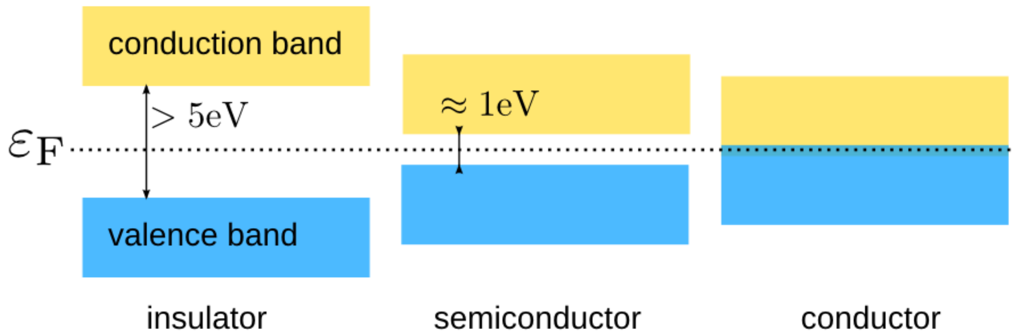

Figure 3.6: Simplified band structure model of isolators, semiconductors and conductors.

can gain enough thermal energy to be excited into the conduction band. It leaves a vacancy behind forming an electron-hole pair. The probability for an electron to gain enough energy to form an electron-hole pair by thermal excitation is temperature dependent

$$p(T) = C\,T^{3/2}\,\exp\left(-\frac{E_{\mathrm{g}}}{2k_{\mathrm{B}}T}\right) \tag{3.7}$$

Where T denotes the absolute temperature, C is a material constant, E_{g} is the gap energy which an electron has to gain in order to pass the band gap and k_{B} is the Boltzmann constant.

The probability of thermal excitation is critically dependent on the gap energy E_{g} and decreases fast if the material is cooled.

In reality, band structures are much more complex and depend on the material temperature and on the crystal axis. Figure 3.7 shows a realistic model of the band structure of germanium. Germanium is an indirect semiconductor as the minimal state in the conduction band and the maximal state in the valence band are not at the same k-vector. When going from the valence band to the conduction band the electron has to change its momentum. Some useful properties of germanium are given in Table 3.1.

3.2.1 Doping of semiconductors

The electric properties of semiconductors can be altered by doping. Impurities are introduced in a pure semiconductor material which donate or accept electrons and alter thus the conductivity. It is possible to create an excess or a deficiency of electrons and hence obtain n or p doped material.

There are different methods of doping a semiconductor. Depending on the donor/ acceptor atoms, they can either replace an atom and become part of the crystal, or stay in the intermediate spaces of the lattice. Germanium for example is usually doped with boron as acceptor and lithium as donor atoms. The boron atoms replace a germanium atom in the crystal lattice; as germanium has four outer shell electrons and boron has only three a vacancy is created, which can be easily filled by other electrons. Lithium on the other hand has only one outer shell electron it can share with other atoms. Lithium is very small and can thus stay in between the crystal lattice acting as a donor impurity.

3.2.2 P-n junctions as diode detectors

A p - n junction is formed, by bringing n and p doped material in contact. The excess of electrons in the n doped region diffuses to the p doped side and the holes from the p doped region vice versa. Diffusion of charge carriers will, however, upset the local electric neutrality inside the crystal. A small portion of charge carriers diffuses, resulting in a *built-in electric field* directed from n to p. P - n junctions reveal an

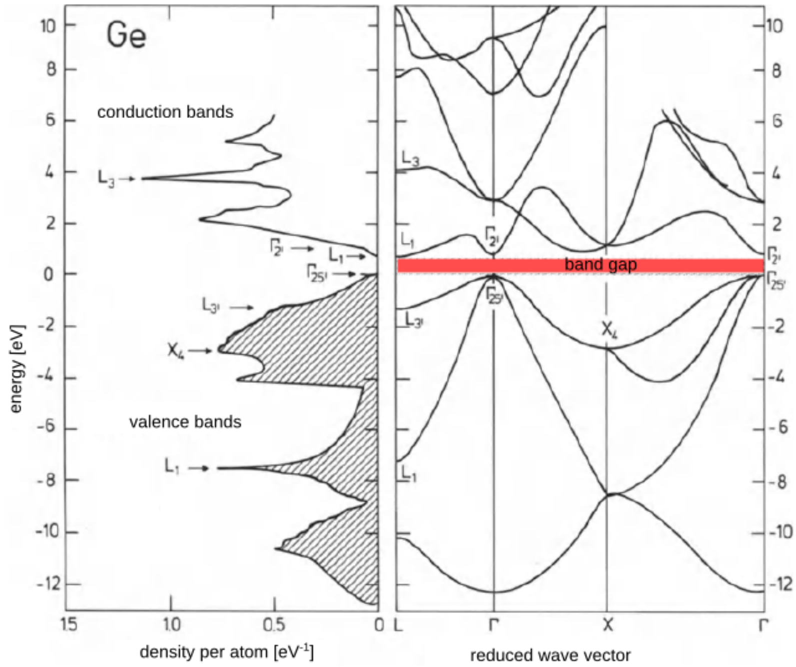

Figure 3.7: Realistic band structure model of germanium. Adapted from [45].

Table 3.1: Properties of germanium adapted from Table 11.1 in [44].

atomic number	32
density	$5.323\,\mathrm{g/cm^3}$
dielectric constant	16
energy gap	0.665
energy gap†	0.746
intrinsic carrier density†	$2.4 \cdot 10^{13}\,\mathrm{cm^{-3}}$
electron mobility†	$3.6 \cdot 10^{4}\,\mathrm{cm^2/V{\cdot}s}$
hole mobility†	$4.2 \cdot 10^{4}\,\mathrm{cm^2/V{\cdot}s}$
energy per e-h pair†	$2.96\,\mathrm{eV}$
Fano Factor†	0.057 - 0.130

† values at 77 K all other values given at at 300 K asymmetric conductance transmitting current only in one direction; they are diodes.

The contact zone in a p - n junction is depleted of free charge carriers. We call this the *depletion region*. It can be enlarged applying an inverse bias voltage. If energy is deposited inside the depletion region, e.g. by ionizing radiation, electron-hole pairs are created. They drift along the internal electric field lines and can be collected and read. Thus, semiconductor diodes can be used as detectors for ionizing radiation.

3.3 High Purity Germanium detectors

To further enlarge the depletion zone, diode detectors are built as p - I - n junctions instead of simple p - n junctions. I stands for *intrinsic* semiconductor material as it is undoped and has intrinsic impurities only. The outer surface is doped to form an n^{+}[1] and a p^{+} contact and the interior region can be fully depleted.

Germanium detectors are produced with depletion layers of several centimeters in height and areas of many square centimeters. They are operated at a reverse bias of a few thousand volts. To achieve such thick depletion layers and collect all the charges generated in the depletion region it is essential that the net-impurity concentration does not exceed $2.5 \cdot 10^{-13}$ impurities / Ge-atom [46]. Because of the ultra-purity of the detector material these detectors are called High Purity Germanium (HPGe) detectors.

All properties of HPGe detectors are defined by the intrinsic impurity concentration: a surplus of negative (positive) intrinsic charges will create an n-type (p-type) germanium detector. In the production process the intrinsic impurities can be influenced within certain limits and the type of detector can be chosen.

3.3.1 Signal formation

If energy is deposited in a diode detector a charge cloud is formed. The charges drift along the field lines of the interior electric field. An induced charge Q on the read out electrode is formed by their movement along the trajectory[2] $r_{\mathrm{q}}(t)$. As demonstrated independently by Shockley and Ramo [47] the charge signal on the electrode is given by

$$Q(t) = -q\,\phi_{\mathrm{w}}(r_{\mathrm{q}}(t)) \tag{3.8}$$

The current signal, which is given by the time derivative of $Q(t)$, is then

$$I(t) = \frac{\mathrm{d}Q}{\mathrm{d}t} = q\,v_{\mathrm{d}}(r_{\mathrm{q}}(t)) \cdot E_{\mathrm{w}}(r_{\mathrm{q}}(t)) \tag{3.9}$$

with the total charge q, the *weighting potential* $\phi_{\mathrm{w}}(r_{\mathrm{q}}(t))$ and the *weighting field* $E_{\mathrm{w}}(r_{\mathrm{q}}(t)) = -\nabla\phi_{\mathrm{w}}(r_{\mathrm{q}}(t))$; and the charge carrier drift velocity $v_{\mathrm{d}}(r_{\mathrm{q}}(t)) = \mathrm{d}r_{\mathrm{q}}(t)/\mathrm{d}t$.

[1] Here: $^{+}$ stands for highly doped material

[2] position r_{q} at time t

The weighting potential is defined as the potential that can be calculated solving the Laplace equation $\nabla^2\phi_{\mathrm{w}} = 0$ for the boundary conditions $\phi_{\mathrm{w}}(b^*) = 1$ on the read out electrode b^* and $\phi_{\mathrm{w}}(\overline{b^*}) = 0$ on all other boundaries when removing all internal charges.

3.3.2 Charge carrier mobilities

The determination of the charge carrier mobilities and thereby the drift velocities v_{d} inside the detector crystal is a rather non-trivial problem: e.g. it depends on the field orientation with respect to the crystal lattice. Therefore, we will not discuss this in detail. It shall be noted that both for electrons and for holes the mobility is strongly anisotropic. Large differences for the longitudinal and tangential velocity anisotropy of electrons and holes are observed [48]. They cause specific rise times and pulse shapes as a function of the location of energy deposition inside the crystal [49]. Along the three crystallographic axis $\langle 100\rangle$, $\langle 110\rangle$ and $\langle 111\rangle$ direct information on the longitudinal anisotropy can be obtained experimentally; when simulating pulse shapes of germanium detectors the anisotropy of the charge carrier mobilities has to be taken into account.

3.3.3 Energy resolution and the Fano factor

Semiconductor detectors have a very good energy resolution. It is better than what is expected for a purely Poissonian process, as the production of charge carriers is not independent but restricted by the atomic shell structure of the semiconductor material.

To quantify this effect, the Fano factor F is introduced. It is defined as the fraction of the observed energy variance σ_{E}^2 and the quantum efficiency

$$F = \frac{\sigma_{\mathrm{E}}^2}{N_{\mathrm{Q}}} \tag{3.10}$$

The quantum efficiency N_{Q} is given by the total deposited energy divided by the energy necessary to create an electron-hole pair; simply the number of charge carriers produced. The energy necessary to create an electron-hole pair in germanium is $w \approx 2.96\,\mathrm{eV}$ (see Table 3.1).

Without electronic noise and charge collection inefficiency, the theoretical resolution limit at some energy E is given by [50]

$$\mathrm{FWHM} = \sqrt{8\ln(2)FwE} \tag{3.11}$$

with the Full Width at Half Maximum (FWHM). For a Gaussian distribution $\mathrm{FWHM} = \sqrt{8\ln(2)}\,\sigma$, where σ is the standard deviation of the Gaussian.

Assuming that the electron-hole pair creation w is independent of the total energy deposition, the Fano factor is < 0.06 [51] for germanium and the theoretically achievable energy resolution at $Q_{\beta\beta}(^{76}\mathrm{Ge})$ is better than 1‰.

3.3.4 Spatial resolution limit

The limitation on spatial resolution inside a semiconductor detector is given by the random electron drift along their path to the read out electrode. The distribution will have a spatial variance of

$$\sigma_{\mathrm{S}}^2 = \frac{2\,k_{\mathrm{B}}\,T\,x}{e\,E_{\mathrm{p}}} \tag{3.12}$$

Where x is the drift length of the charges from their creation point to the read out electrode and E_{p} is the electric potential. For $E_{\mathrm{p}} = 1\,\mathrm{kV/cm}$ and $x < 7\,\mathrm{cm}$ resulting in a maximal dispersion of $\sigma_{\mathrm{S}} = 100\,\mu\mathrm{m}$. This limits the precision to which position measurements of energy deposition inside the crystal can be made.

3.3.5 Operational voltage and temperature

HPGe detectors are generally mounted inside a vacuum cryostat connected to a liquid Nitrogen (LN_2) dewar vessel, through a heat conducting cold finger. In order to keep thermal excitation of electrons to the conduction band at a minimum germanium detectors have to be cooled to cryogenic temperatures. The operational High Voltage (HV) varies from detector to detector; the HV is increased until the interior region is fully depleted. This happens typically at around 4 kV depending on the detector geometry.

As the donor lithium atoms are not fixed in the lattice of the crystal they can move due to thermal excitation of the lattice itself. Especially p-type germanium detectors should be kept at cryogenic temperatures as much as possible also if no HV is applied to prevent further lithium diffusion inside the crystal. In the lithium diffused region electron-hole pairs partly recombine and consequently do not contribute to the signal on the read out electrode. Therefore, a growth of the lithium diffused outer layer results in a deterioration of detection efficiency, and also, the detection threshold for external low energetic radiation becomes higher with a thicker lithium diffused outer layer.

Chapter 4

Detector characterization

In order to perform the measurement campaign described in the following chapters in a reliable manner, it was necessary to conduct an extensive characterization of the various detectors used. This is the argument of the following chapter. First of all, the data acquisition system (DAQ) including signal amplification is described; next, the energy reconstruction and calibration are explained and the determination of the operational voltage with an HV scan is illustrated. Finally, an automatized system is presented which serves to perform fine grain surface scans of HPGe detectors. Surface scans of two detectors taken with this system are compared.

4.1 Detectors and voltage supply

The HPGe detectors at hand are three Coax n-type detectors, one BEGe detector and one detector of PPC geometry. The last two are made of p-type material. All of them, except for the BEGe, contain a *natural* mixture of germanium isotopes. A sketch of the detector geometries can be found in Figure 2.2 and a summary of their basic properties is listed in Table 4.1.

The germanium of the GERDA detectors is *enriched* in the $0\nu\beta\beta$ candidate isotope ^{76}Ge. The residual material remaining after the enrichment process is commonly referred to as *depleted* material. It behaves chemically identical to natural and en-

Table 4.1: Available detectors. The BEGe and the PPC detector are of p-type material with holes as dominant charge carriers, the Coax detectors are n-type detectors with electrons as main charge carrier type.

detector	material	operational voltage [kV]	dewar volume [l]	height [mm]	diameter [mm]
BEGe	depleted	+4.0	7	40.7	74.1
PPC	natural	+4.4	7	50.5	66.7
Coax1-3	natural	−4.0	3	74.0	72.0

riched germanium.

For the second experimental Phase of the Gerda experiment 30 enriched BEGe detectors were produced. The remaining depleted germanium was processed, in order to test the detector production chain [52], and the BEGe used here is one of the detectors that were produced. It cannot used be for $0\nu\beta\beta$ search but serves as an optimal test detector.

The three Coax detectors are cylindrical with a borehole on the lower surface which measures 10.0 mm in diameter and 30.0 mm in depth. The read-out electrode is placed on the inner surface of the borehole and the HV contact is located on the outer surface. The BEGe detector has a boron implanted read-out contact on the lower surface, 15.0 mm in diameter, which serves as read out electrode. The HV and the read-out electrode are separated by a groove which is 3.0 mm in width and 2.0 mm in depth. The PPC detector is similar to the BEGe but has an even smaller read-out contact inside a small ditch on the lower surface 3.1 mm in diameter and 1.3 mm in depth. For the BEGe as well as the PPC detector the HV contact is formed by the lithium diffused outer surface.

All detector preamplifiers (PreAmp) are supplied with Low Voltage (LV) which is implemented in the Spectroscopy Amplifiers (SpecAmp)[1 2]. The HV is supplied by two programmable HV modules[3] which can deliver positive as well as negative HV.

4.2 Data acquisition

Two data acquisition systems are used depending on the information needed:

- **MCA** Energy spectra can be recorded using a Multichannel Analyzer (MCA)[4]. They provide information about energy resolution and operational voltage. The usage is limited, since only the energy information is available. On the other hand, the storage needed on disk is minimal and is independent of the measurement time and number of signals analyzed.

- **FADC** A Flash Analog to Digital Converter (FADC)[5] is available, which continuously records the detector electrical signal (trace). In case a trigger is generated the event is recorded on disk. The information that can be extracted from the full event traces is rich and serves for Pulse Shape Analysis (PSA) and to obtain timing information. However, the disk space needed is quite high in comparison to the MCA system. It scales with the trace length and number of events recorded.

[1] Coax: Silena Model 7611/L spectroscopy amplifier
[2] BEGe/PPC: ORTEC Model 672 spectroscopy amplifier.
[3] CAEN: Model N1471H 4 channel programmable HV.
[4] ORTEC: Model 926 ADCAM Multichannel Buffer.
[5] CAEN: Model DT5724 Desktop Digitizer 4 channels, 14-bit, 100 MHz.

4.2.1 Signal amplification

Each system is implemented with its proper amplification method.

The MCA system is used in combination with a SpecAmp[12] which amplifies the signal and applies a semi-Gaussian shaping to the pulses. The SpecAmps feature pole-zero adjustment, and the shaping constant and amplification gain can be chosen manually. The gain is set such as to utilize the full range of the MCA if possible.

When taking data with the FADC, a signal amplification without shaping is preferable to prevent loss of information. Some detectors can be used without amplification because the pre-amplification is already high enough to utilize the FADC dynamic range. For signal amplification without shaping a Genius Shaper, developed at the Max-Planck-Institute for Nuclear Physics (MPIK) Heidelberg and used in GERDA, was chosen.

Sketches of both the MCA and the FADC DAQ systems including signal amplification can be seen in Figure 4.1.

4.2.2 Genius Shaper

The Genius Shaper, used for linear amplification without signal shaping, has 4 channels with two outputs each (see Figure 4.2). The gain is adjustable between roughly 2 x and 8 x for each channel and is common to both outputs, while an offset can be adjusted for each of the two outputs separately.

A comparison of uncalibrated ^{60}Co spectra taken with a Coax detector at maximal amplification for each channel can be found in Figure 4.3. As the position of spectral lines in uncalibrated spectra depends on the gain it is evident that the maximal amplification of the Genius Shaper channels is comparable. All parameters and settings are listed in Table 4.2.

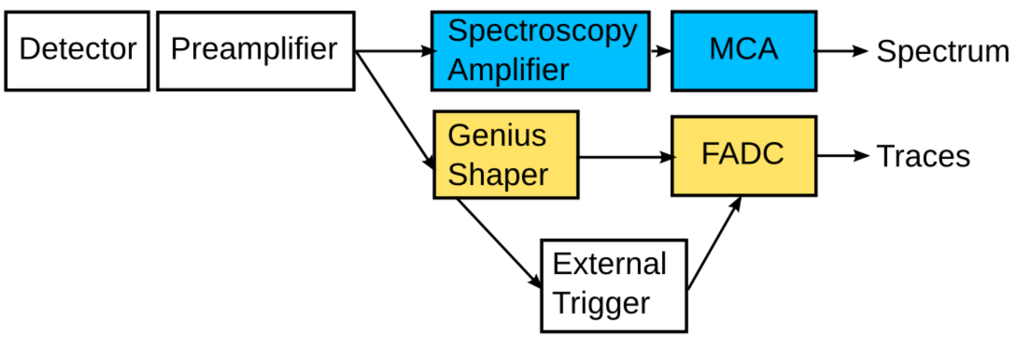

Figure 4.1: Sketch of MCA and FADC DAQ systems. The external trigger logic for the FADC is optional and is used further on.

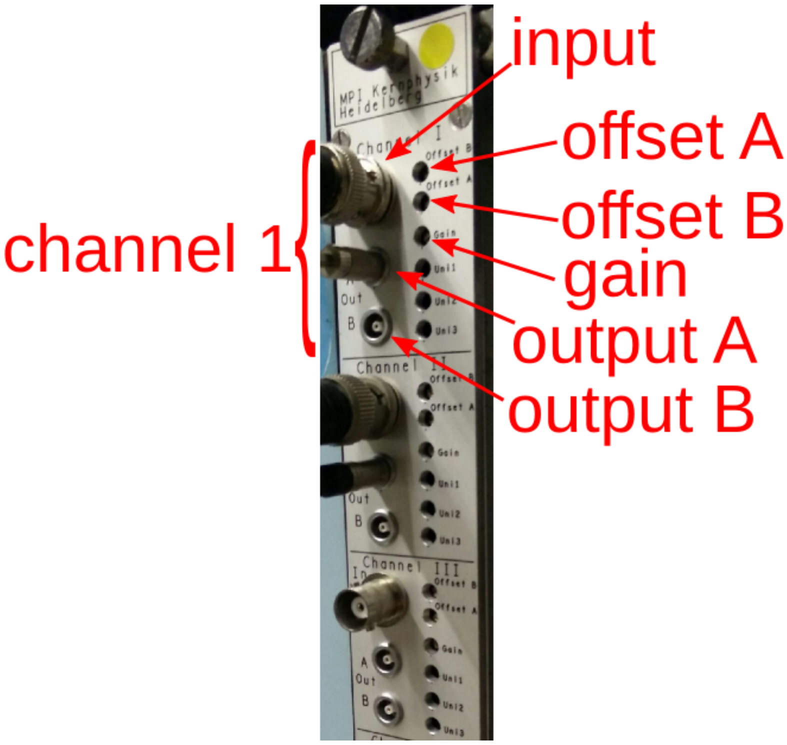

Figure 4.2: Genius Shaper module for amplification without shaping with four input channels. Each input channel has adjustable gain and two output channels. For each output channel an offset can be set separately.

Table 4.2: Genius Shaper parameters and settings.

ch	out	offset [V]	gain max	gain min	note
1	A	0	8x	2x	
	B	0	8x	2x	
2	A	0	7.6x	1.8x	broken
	B	0	8x	1.9x	
3	A	0	7.8x	2x	
	B	0	7.8x	2x	
4	A	0	7.9x	2x	
	B	0	7.9x	2x	noisy

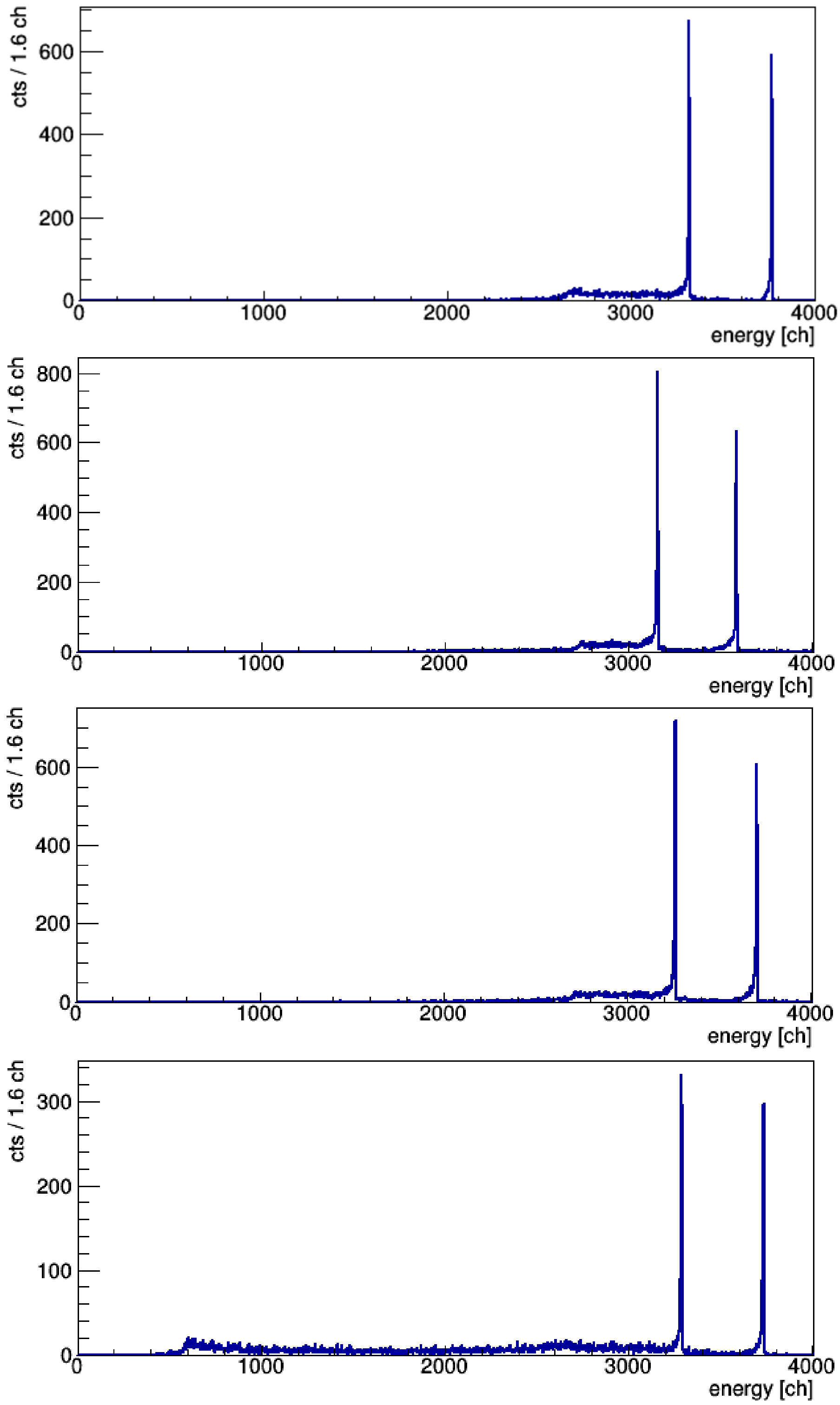

Figure 4.3: Coax3 uncalibrated ^{60}Co spectra recorded with Genius Shaper maximal amplification. Top to bottom channels 1 to 4. In the measurement using channel 4 a lower energy threshold was set of ca. 600 ch.

4.3 Data processing

Pulses recorded with the FADC system can be fully analyzed off-line and contain all information that can be extracted from the traces.

The data is processed as is usually done with Gerda data, using a multi-tier approach. The raw data is transformed into a format based on Cern ROOT classes [53] which is compressed by a factor of about two. We call the raw data format *tier0* and the rootified format *tier1*. Both formats contain the same information but the tier1 format can be read by the Gerda analysis software [54, 55]. A new decoder for this conversion was written and integrated into the Gerda software. It reads the tier0 data recorded with the FADC DAQ (see Section 4.2) and transforms it into the tier1 format. For details about the multi-tier structure and the implemented decoder see Appendix A.

4.4 Energy reconstruction and optimization

To extract the energy of an FADC trace we use a pseudo-Gaussian filter which corresponds to a high-pass filter followed by n low-pass filters. First step is a deconvolution of the original trace $x_0[t]$ by the transform

$$\begin{aligned} x'[t] &= x_0[t] - x_0[t-\delta] \\ x_1[t] &= x'[t] + f \cdot \sum_{t'=0}^{t-1} x'[t'], \end{aligned} \tag{4.1}$$

where δ is called delay and $f = 1 - \exp(-1/\tau)$. The decay parameter $\tau \sim 50\,\mu\text{s}$ is supposed to compensate the exponential decay of the trace which by design is caused by a feedback circuit in the PreAmp [56]. As can be seen in the first step of Figure 4.4, this parameter is chosen such that the tail of the traces becomes flat after applying Equation 4.1.

Thereafter, n moving window averages (MWA) are applied:

$$x_{i+1}[t] = \frac{1}{\delta} \sum_{t'=t-\delta}^{t} x_i[t'] \qquad i = 2, ..., n \tag{4.2}$$

The signal is transformed into a pseudo-Gaussian and its height is proportional to the energy deposition in the detector. After each MWA, its maximum moves further to the right side of the trace (see Figure 4.4) which has a limited size. The maximum of the pseudo-Gaussian has to stay inside the trace: this is the limiting factor for n, the number of MWAs applicable.

The standard energy reconstruction in Gerda is done with $f = 0$, $\delta = 5\,\mu\text{s}$ and $n = 25$ [56] and a trace length of $160\,\mu\text{s}$. Here, shorter FADC traces were chosen in order to save disk space, and therefore the combination of δ and n was optimized to minimize the energy resolution σ (see Section 4.5). As can be seen in Figure 4.5 for the PPC detector a better energy resolution is achieved with larger n and δ. With $\delta = 10\,\mu s$ a slightly better energy resolution is achieved with $n = 0$ than with $\delta = 6\,\mu s$ and $n = 15$. For the PPC detector we chose $\delta = 10\,\mu s$ and $n = 7$ or lower if the trace length is too short for seven iterations. In general, the higher δ and n, the better the energy resolution. Also if the resolution worsens after some iterations the effect is small with respect to the gain in resolution achieved beforehand. If an optimization is too time consuming the parameters δ and n can be chosen in a quick manner shifting the pseudo-Gaussian to the end of the trace.

Also the MCA shaping time τ_s, which can be set on the SpecAmp, has to be optimized in order to minimize the energy resolution (see Section 4.5). In Figure 4.6 the resolution of the BEGe detector at ^{60}Co energies is plotted as a function of the MCA shaping time. The best resolution is achieved for a shaping time of $\tau_s = 6\,\mu s$.

The chosen shaping parameters for all detectors and for FADC as well as MCA systems is summarized in Table 4.3.

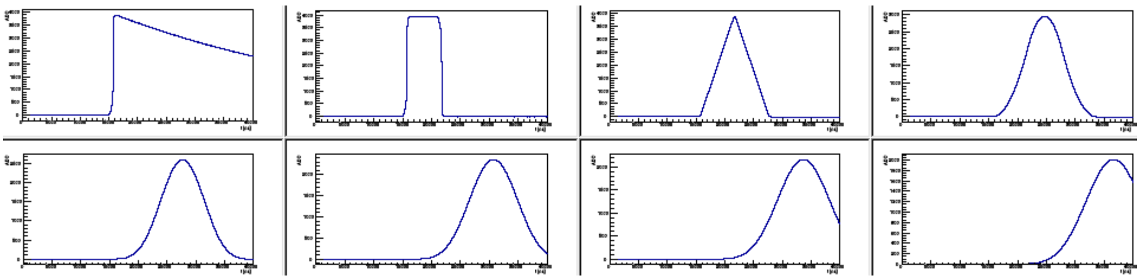

Figure 4.4: Visualization of the pseudo-Gaussian energy reconstruction algorithm. Sequence of applied steps from left to right top row then bottom row. The sequence starts with the raw trace, first step is the application of Equation 4.1 and subsequently six MWAs are applied Equation 4.2.

Table 4.3: Shaping parameters for energy reconstruction from FADC (off-line signal processing) and MCA (on-line using a SpecAmp) data.

	FADC			MCA
detector	τ [μs]	δ [μs]	n	τ_s [μs]
BEGe	45.5	6	10	6
PPC	54.0	10	7	10
Coax1	39.0	4	8	-
Coax2	47.0	6	10	-
Coax3	44.0	5	7	-

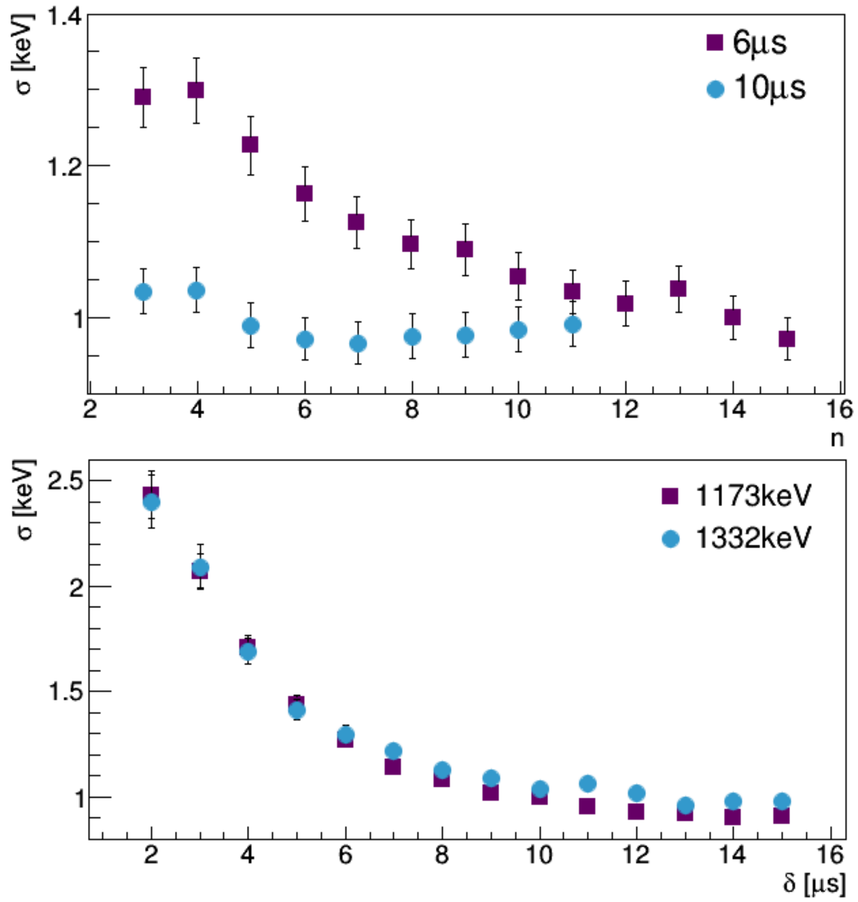

Figure 4.5: Energy reconstruction parameter optimization of the PPC detector using ^{60}Co FADC data. Top: energy resolution at 1332 keV for $\delta = 6\,\mu s$ and $10\,\mu s$ in function of the MWA number n. Bottom: energy resolution for $n = 3$ in function of the delay or the MWA width δ.

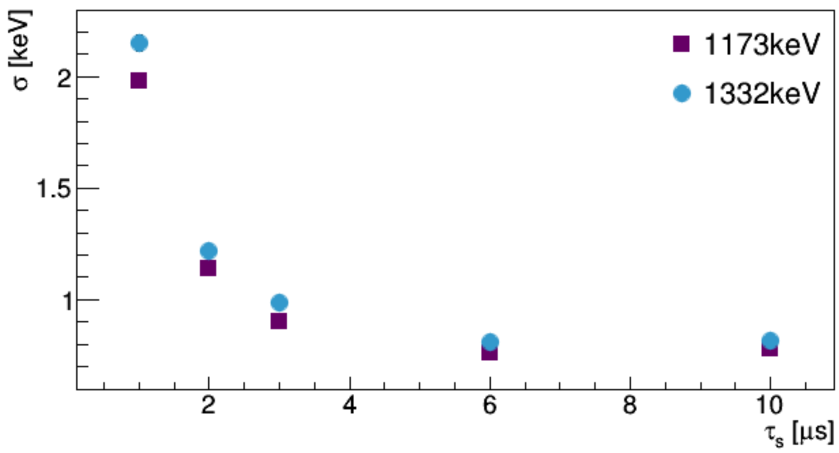

Figure 4.6: Shaping time optimization of the BEGe detector using ^{60}Co MCA data. The energy resolution reaches a minimum for a shaping time of $\tau_s = 6\,\mu s$.

4.5 Energy calibration and resolution

Various γ sources were used for energy calibrations and dedicated measurements, precisely:

- ^{22}Na: energy calibration, external trigger gate calibration (Section 5.4.2)
- ^{60}Co: energy calibration
- ^{137}Cs: coincidence measurement (Chapter 5-7)
- ^{228}Th: energy calibration, PSA calibration (Section 7.8)
- ^{241}Am: fine grain surface scan (Section 4.8)

The decay schemes of these sources with their individual γ energies and branching ratios can be found in Appendix B.

Energy calibration and resolution measurements are performed regularly using mostly ^{60}Co with γ-lines at 1173 keV and 1332 keV. To calibrate the recorded spectra the ROOT [53] *TSpectrum* class is used to find the γ-lines, and the spectrum is calibrated assuming a linear calibration function. The calibration curves obtained can be used to calibrate other data; e.g. ^{137}Cs spectra in which usually only one γ-line is observed.

Finally all γ-lines are fitted using two different fit functions in order to determine the energy resolution and Gaussianity of the lines.

The first fit is done using a Gaussian peak on a background modeled with an inverse error function (erfc)

$$f(x) = b_\mathrm{l} + \frac{b_\mathrm{l} - b_\mathrm{r}}{2} \cdot \mathrm{erfc}\left(\frac{\mu - x}{\sqrt{2}\,\sigma}\right) + \frac{a}{\sqrt{2\pi}\,\sigma} \cdot \exp\left(-\frac{(x-\mu)^2}{2\,\sigma^2}\right) \tag{4.3}$$

With the background on the left b_l and on the right b_r side of the peak, the centroid μ and the standard deviation σ. The amplitude a is also the integral of the Gaussian itself.

The second fit models the background with the same inverse error function but the peak is allowed to have a low energy tail

$$\begin{aligned} g(x) = {} & b_\mathrm{l} + \frac{b_\mathrm{l} - b_\mathrm{r}}{2} \cdot \mathrm{erfc}\left(\frac{\mu - x}{\sqrt{2}\,\sigma}\right) \\ & + \frac{a}{\sqrt{2\pi}\,\sigma} \cdot \begin{cases} \exp\left(-\frac{(x-\mu)^2}{2\,\sigma^2}\right), & \text{if } x < (\mu - C) \\ \exp\left(\frac{C\,(2\,(x-\mu)+C)}{2\,\sigma^2}\right), & \text{if } x \geq (\mu - C) \end{cases} \end{aligned} \tag{4.4}$$

At the joining point C, to the left of the centroid μ, the fit function starts to deviate from the Gaussian form and fits a low energy tail. An example of a γ-line fit of the ^{60}Co 1332 keV line recorded with Coax3 can be found in Figure 4.7; showing all components of the two fit functions 4.3 and 4.4.

The FWHM, Full Width at one Tenth Maximum (FWTM) and Full Width at one Fiftieth Maximum (FWFM) of the peak maximum provide a measure of the energy resolution and Gaussianity of the γ-lines. Purely Gaussian values can be calculated analytically using

- $\text{FWHM} = 2\sqrt{2 \cdot \ln(2)}\,\sigma$
- $\text{FWTM}/\text{FWHM} = \sqrt{\ln(10)/\ln(2)} \approx 1.82$
- $\text{FWFM}/\text{FWHM} = \sqrt{\ln(50)/\ln(2)} \approx 2.38$

The FWHM and the Gaussianity parameters, FWTM/FWHM and FWFM/FWHM, of all detectors are listed in Table 4.4. Considering that the measurements were taken with some time difference, and the detector grounding was optimized after the MCA measurements were recorded, the resolution obtained with the MCA is comparable to the FADC measurement.

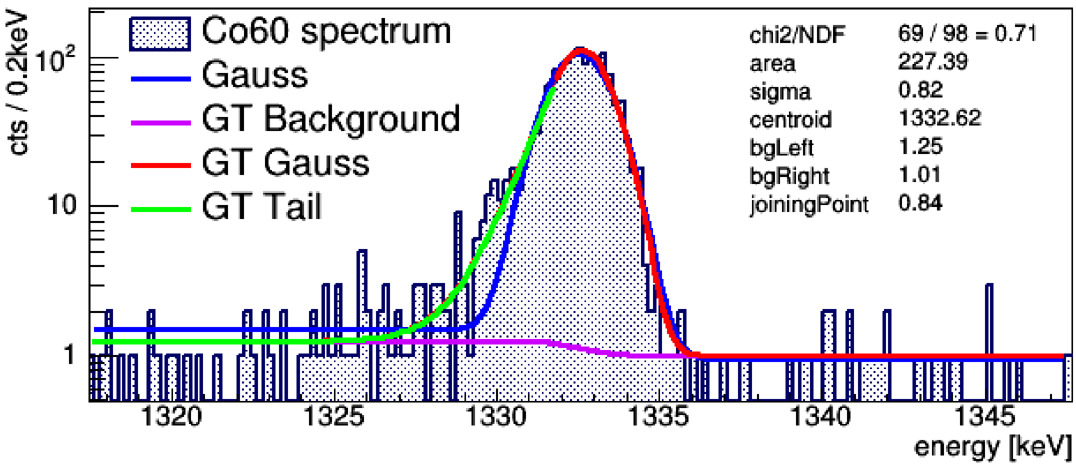

Figure 4.7: Peak fit of the ^{60}Co 1332 keV γ-line recorded with Coax3. The fit with a Gaussian plus erfc from Equation 4.3 is shown in blue and the fit function from Equation 4.4 is shown in three parts: Gaussian (red), Tail (green) and erfc (magenta).

Table 4.4: Resolution and Gaussianity parameters of for all detectors; obtained by fitting the ^{60}Co 1332 keV γ-line.

	HV	FWHM		FADC	
detector	[kV]	MCA	FADC	FWTM/FWHM	FWFM/FWHM
BEGe	4.0	2.05 ± 0.02	2.16 ± 0.06	1.85	2.55
BEGe	4.5	-	2.06 ± 0.04	1.84	2.52
PPC	4.4	-	2.07 ± 0.04	1.85	2.58
Coax1	4.0	2.96 ± 0.03	2.39 ± 0.07	1.87	2.83
Coax2	4.0	2.24 ± 0.02	2.14 ± 0.05	1.85	2.64
Coax3	4.0	2.17 ± 0.03	1.99 ± 0.07	2.09	3.37

4.6 High voltage scan

In order to determine the depletion and operational voltage of germanium detectors, MCA measurements with ^{60}Co (or a different γ source) are taken: the detector HV is varied while the acquisition time is fixed. We call this a *High Voltage Scan*. When the peak position and area of the γ-lines reach a plateau the detector is fully depleted (depletion voltage). To obtain the operational voltage, the HV is increased until the standard deviation σ of the Gaussian fit function is minimized.

In Figure 4.8 peak area, position and σ are plotted for both γ-lines of a ^{60}Co HV scan of the BEGe detector. The voltage was varied between 2000 V and 4350 V. The depletion voltage is reached at 3700 V and the operational voltage was determined to be 4000 V.

This BEGe detector shows an atypical behavior for such a kind of measurement. This is clearly visible in the resolution σ versus HV plot in Figure 4.8. Usually σ improves with increasing HV; in this case however, before reaching full depletion, σ worsens drastically reaching a maximum at 3650 V.

This effect is due to the geometry of the BEGe detector. The BEGe was produced larger than usual and for certain values of the bias voltage the configuration of the internal electric field is such that charges are accumulated in the detector center and only slowly released. Consequently, for many events the energy is reconstructed wrong and resolution deteriorates strongly as can be seen in Figure 4.9.

A high voltage scan for the PPC respectively is shown in Figure 4.10. The PPC does not show atypical behavior like the BEGe, although it is even one centimeter larger in height. This seems to be due to the smaller read out contact which creates a more favorable field configuration for charge collection. The depletion and operational voltage are slightly higher than for the BEGe with 4.0 kV and 4.4 kV − 4.5 kV respectively.

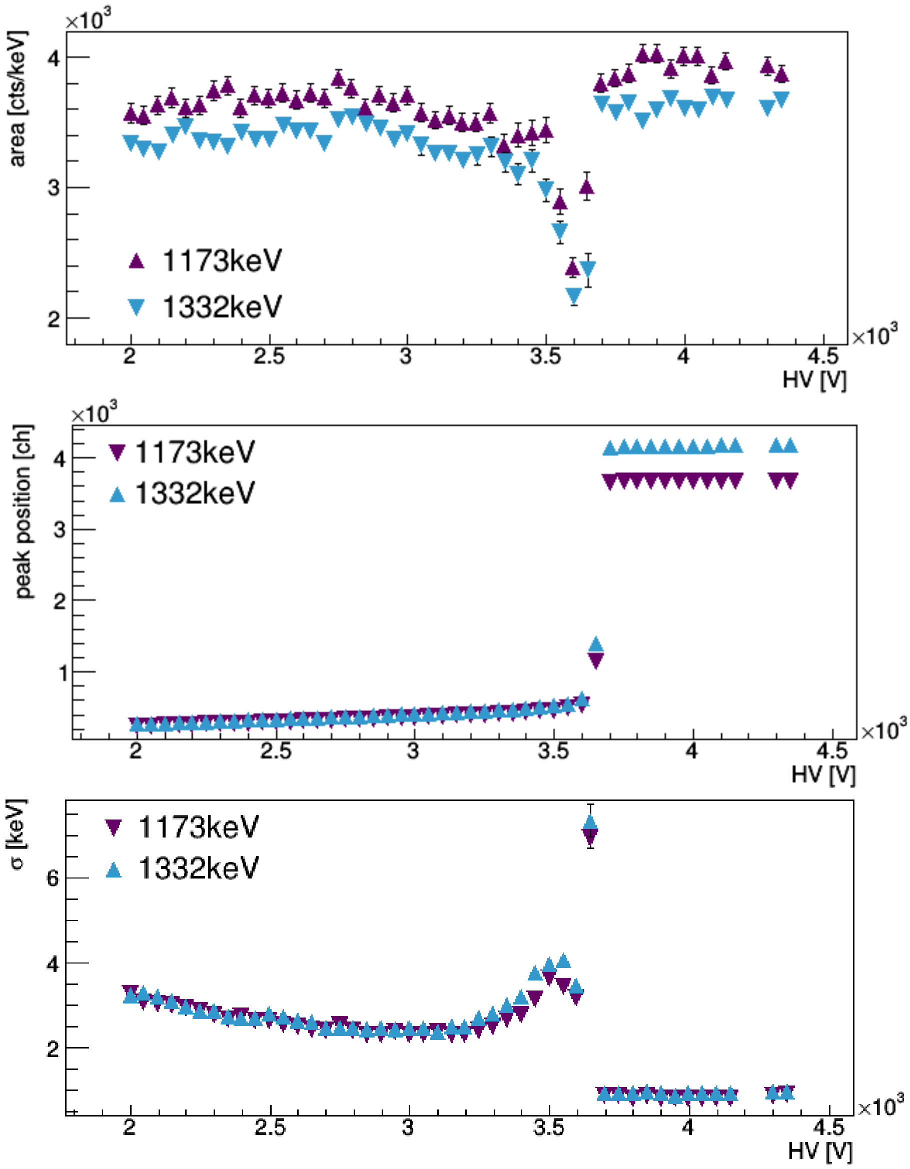

Figure 4.8: BEGe ^{60}Co HV scan. Top to bottom: area, peak position and σ as function of the HV.

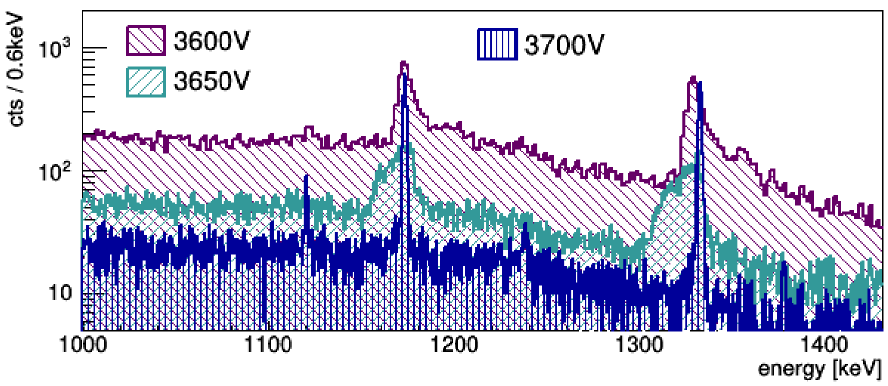

Figure 4.9: BEGe ^{60}Co spectrum at 3600 V, 3650 V and 3700 V. Electric field configuration traps charges in the detector center and the resolution deteriorates strongly below the depletion voltage of 3700 V.

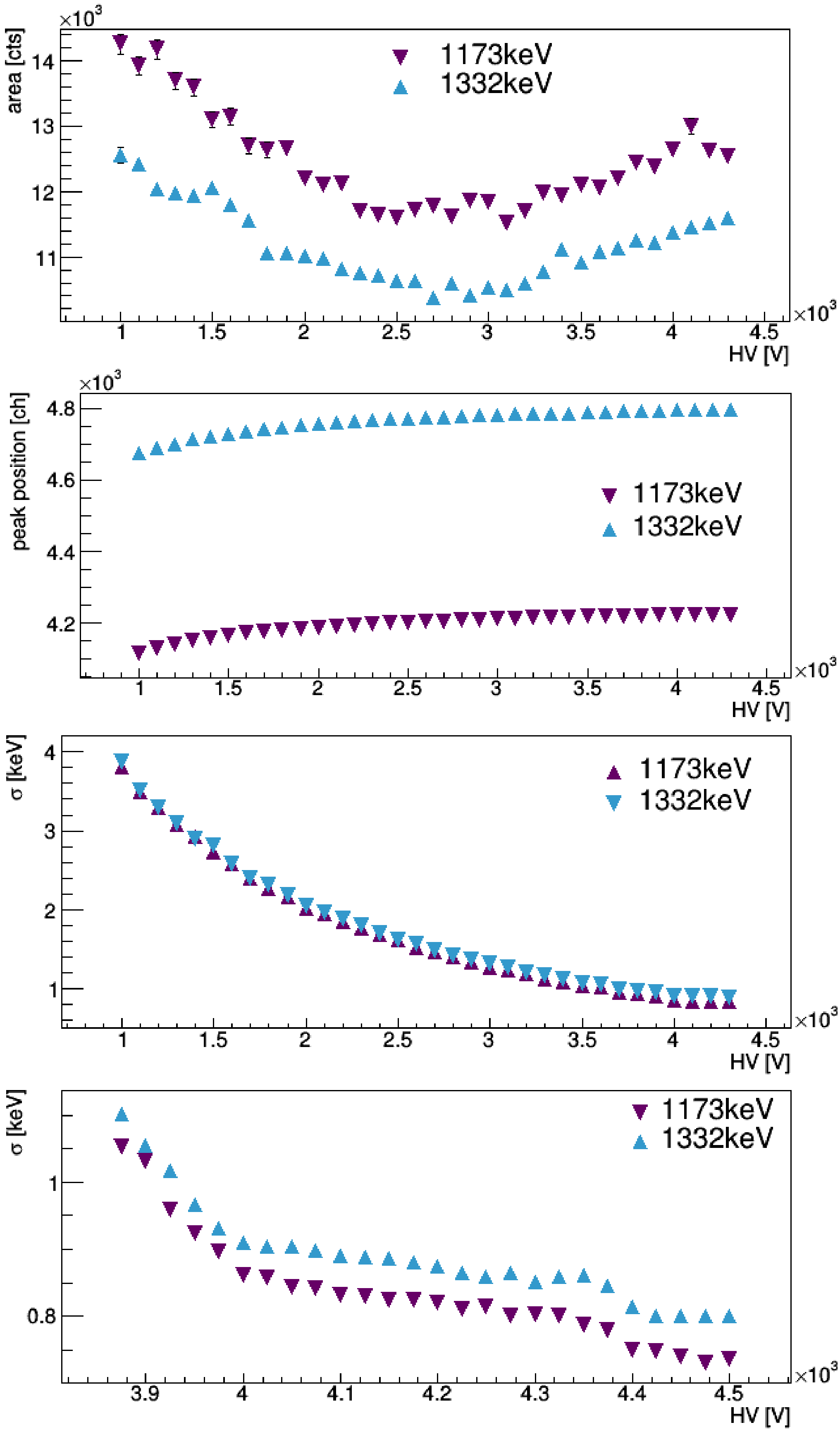

Figure 4.10: PPC ^{60}Co HV scan. Top to bottom: area, peak position, σ and a zoom of σ, showing the last part of the HV scan, from 3850 V up to 4500 V as function of the HV.

4.7 Baseline stability

For FADC measurements a fixed trigger threshold was used. Thus, baseline drifts influence the trigger level. The stability of the baseline is analyzed for a measurement with a lifetime of 130 h. All detectors reveal a smooth rise in baseline level. This can be seen in Figure 4.11 for the BEGe and Coax1 detector. Over a period of 130 h the baseline of the BEGe increased slightly by about 20 channels. Through determination of the baseline level and adjustment of the trigger threshold before each measurement we ensured stable conditions for measurements not exceeding a time period of a week. The periodic spikes, present in the plots, coincide with the filling of the dewars with LN_2.

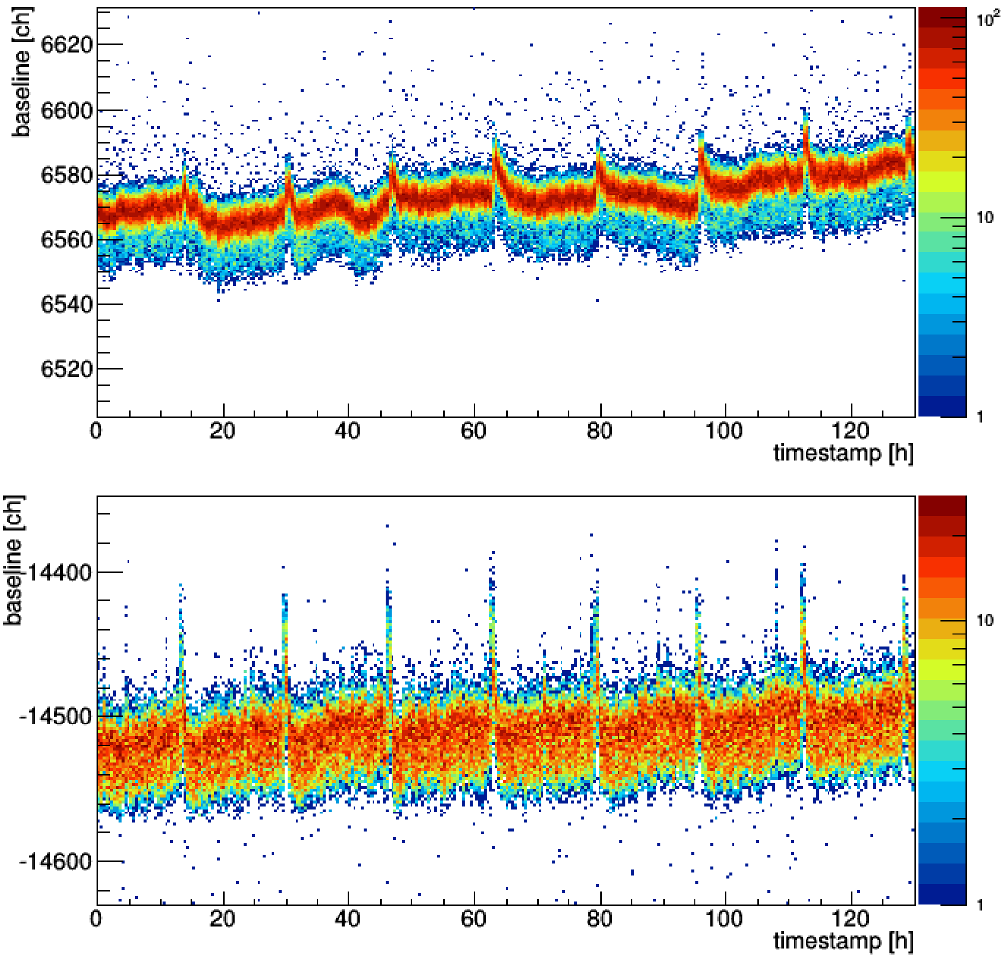

Figure 4.11: Baseline of BEGe (top) and Coax1 (bottom) over a time period of 130 h. The periodic spikes in the baseline coincide with the filling of the dewars with LN_2.

4.8 Fine grain surface scans

Positioning of detectors inside their vacuum cryostats as well as the homogeneity of their outer contacts can only be measured from the outside. A dedicated setup is used which is able to perform automatized, fine grain, full surface scans [52].

4.8.1 Scanning table setup

The setup incorporates a collimated ^{241}Am γ source with an activity of 5 MBq. ^{241}Am has a prominent γ-line at 60 keV. These photons penetrate only the outer layer of the detector interacting almost exclusively through photoelectric effect and are sensitive to changes of the outer contact of the order of a few tens of µm. All numbers derived in the following are valid for 60 keV photons.

The source is hosted in a copper encapsulation with a collimation diameter of 1 mm. The collimator is attached to a movable arm whose motion is controlled by precision motors. The arm position can be changed between vertical and horizontal orientation and the collimator can be moved along the arm. The vertical orientation serves to scan lateral detector surfaces, the horizontal orientation is used for top surface scans. Moreover, in vertical as well as horizontal position the arm can be rotated. In this manner complete and fully automatized, fine grain scans of the detector top and lateral surfaces can be performed. Thanks to the precision motors and a standard positioning calibration the reproducible precision is better than 1 mm [52]. The setup and possible movements along three axes can be seen in Figure 4.12.

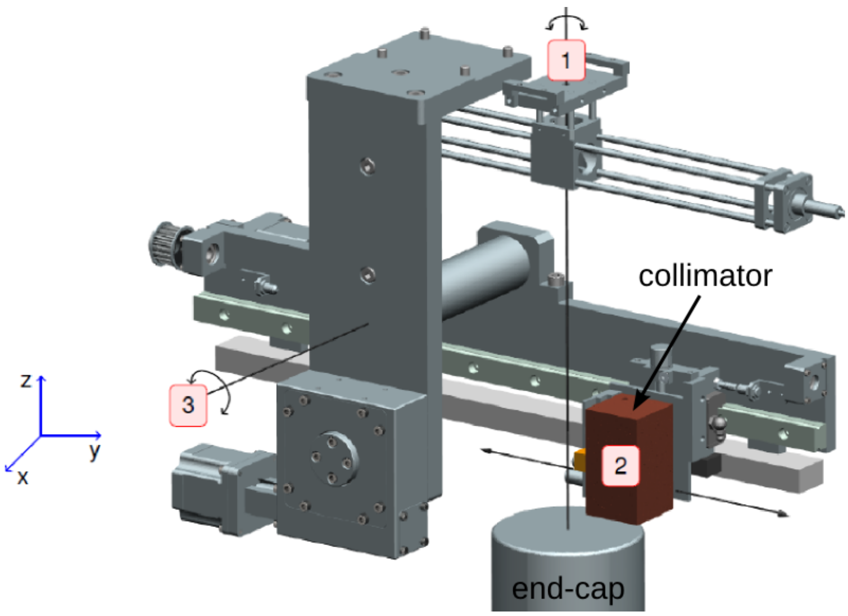

Figure 4.12: Fine grain surface scanning table setup and motion axes. The detector vacuum cryostat endcap is placed upright below the scanning arm and its center is aligned with the rotation axis 1. Rotation around axis 3 permits to change between horizontal and vertical arm orientation, the collimator can be moved along axis 2, and the whole arm can be rotated around axis 1. Figure taken from [52].

4.8.2 Analysis of surface scans

For each position an ^{241}Am spectrum is taken and the count rate C of the 60 keV γ-line is calculated by subtracting the background at the left B_{left} and the right B_{right} from the peak region P

$$\begin{aligned} C &= P - B_{\text{left}} - B_{\text{right}} \\ &= \sum_{i=E-w}^{E+w} b_i - \sum_{j=E-2\,w}^{E-w} b_j - \sum_{k=E+w}^{E+2\,w} b_k \end{aligned} \tag{4.5}$$

Where E is the centroid of the γ-line and b denotes the respective bin content. The window size w is large enough to contain all the peak and small enough so that the background is flat on the left and on the right side of the γ-line.

4.8.3 Alignment

The detector has to be carefully aligned with the robotic arm; laser optics help to center the detector and adjust inclination.

Slight inclination of the detector with respect to the scanning arm is almost unavoidable. When scanning the lateral detector surface structures which should be on a fixed height are seen at different heights depending on the inclination. This is visualized in Figure 4.13; a sketch of a sharp edge scan is shown for small and large inclination. The count rate pattern observed depends on the inclination value.

4.8.4 Collimation

The initial source collimation is 1 mm but the further the collimator is placed from the scanned surface the more the photon beam diverges. The divergence of the source beam can be measured by the change of rate on sharp edges. The sketch shown in Figure 4.14 shows the movement of the source beam over the edge.

A count rate simulation of a sharp edge scan with a step size of 1 mm can be seen in Figure 4.15. Ten different start positions were simulated at random. The most

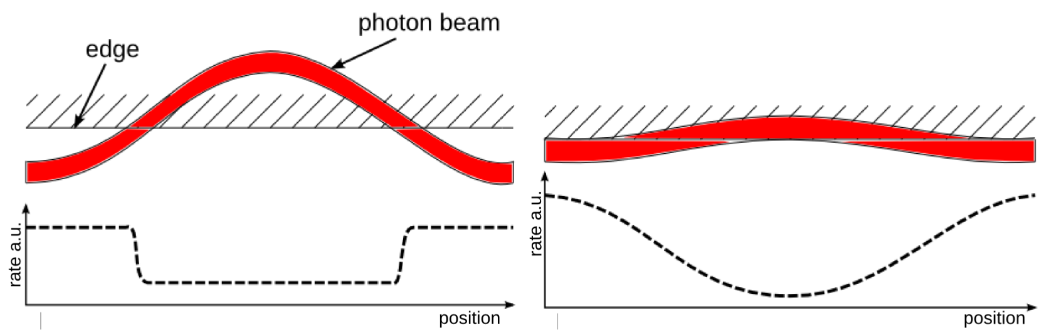

Figure 4.13: Sketch of the count rate pattern observed in a sharp edge scan for a large (left) and for a small inclination value (right).

probable number of intermediate points where the photon beam is partly on the left and partly on the right side of the edge is given by $p = w_b/\Delta x$; dividing the photon beam divergence w_b by the step size Δx. This is used in the following to estimate the photon beam divergence w_b.

4.8.5 Linear surface scans

As linear surface scan we intend changing only the source position along motion axis 2 in Figure 4.12. Linear scans on the detector top (lateral) surface can be done with a horizontal (vertical) arm position. A fixed position for the rotation axis 1 is chosen and the collimator is only moved along the scanning arm (motion axis 2).

Results of linear top and lateral scanning measurements of the PPC and BEGe detector are presented in the following. The position of the detector inside the end-cap and the detector holder geometry can be measured.

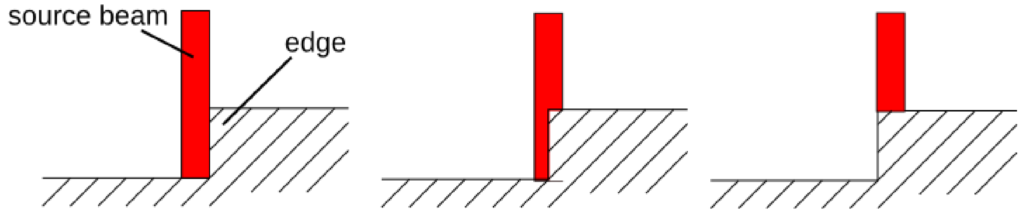

Figure 4.14: Sketch of the movement of a source beam over a sharp edge.

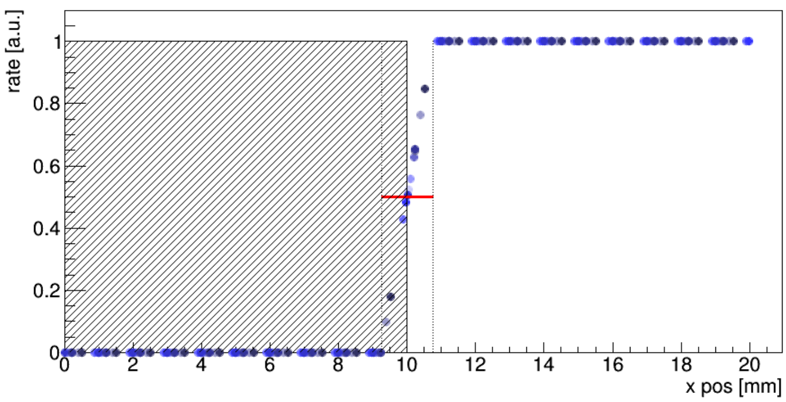

Figure 4.15: Simulation of a sharp edge scan with a step size of $\Delta x = 1\,\mathrm{mm}$ for 10 different start positions and a photon beam divergence of $w_b = 1.5\,\mathrm{mm}$. The edge is drawn hatched while the collimation width is indicated with a red horizontal line.

4.8.6 PPC detector top and lateral linear surface scan

The PPC detector top and lateral surface were scanned with a step size of $\Delta x = 1\,\mathrm{mm}$; each point with a measurement lifetime[6] of $T_\mathrm{L} = 120\,\mathrm{s}$. The source position along the scanning arm will be denoted by x in the following. In Figure 4.16 the count rate of the 60 keV ^{241}Am γ-line is plotted versus the scanning position for both measurements.

In the lateral scan we see that from $x = 266\,\mathrm{mm}$ to $x = 271\,\mathrm{mm}$ the count rate drops significantly; we infer that in this region the holder material is substantially thicker than the rest of the holder cup and exhibits a sort of ring structure; this is common for germanium detector holders.

With the difference in count rate and the knowledge that the holder cup is made of copper we can estimate the thickness of the ring structure rearranging Equation 3.5. Fitting the flat parts of the graph with a constant we can extract the different count rates

$$\begin{aligned} d_\mathrm{ring} &= \ln\left(\frac{N_1}{N_2}\right) \cdot \frac{1}{\mu_\mathrm{Cu}\rho_\mathrm{Cu}} = \ln\left(\frac{819 \pm 7}{284 \pm 9}\right) \cdot \frac{1}{1.485\,\mathrm{cm}^2/\mathrm{g} \cdot 8.9\,\mathrm{g/cm}^3} \\ &= (0.80 \pm 0.03)\,\mathrm{mm} \end{aligned}$$

The ring structure has a sharp edge hence we can analyze the divergence of the source beam w_b. It is at least 1 mm from collimation and maximal 2 mm considering that at $x = 264\,\mathrm{mm}$ the source beam is on the left side of the edge and at $x = 266\,\mathrm{mm}$ it has already passed it; therefore we make the conservative estimate of $w_\mathrm{b} = (1.5 \pm 0.5)\,\mathrm{mm}$.

The height of the ring is estimated making use of the photon beam divergence w_b as

$$h_\mathrm{ring} = 271\,\mathrm{mm} - 266\,\mathrm{mm} + w_\mathrm{b} = (6.5 \pm 1.5)\,\mathrm{mm}$$

considering a position uncertainty of $\Delta x = \pm 1\,\mathrm{mm}$.

The edges of the PPC are rounded as can be seen in both the top and the lateral scan possibly to ensure a good charge collection as the internal electric field is weak in corners.

We estimate the active length of the PPC from the lateral scan as $L_\mathrm{a} = 48.5 \pm 1.5\,\mathrm{mm}$ and the active diameter from the top scan as $D_\mathrm{a} = 62.5 \pm 1.5\,\mathrm{mm}$.

[6] The lifetime of a measurement is given by the real measurement time minus the dead time.

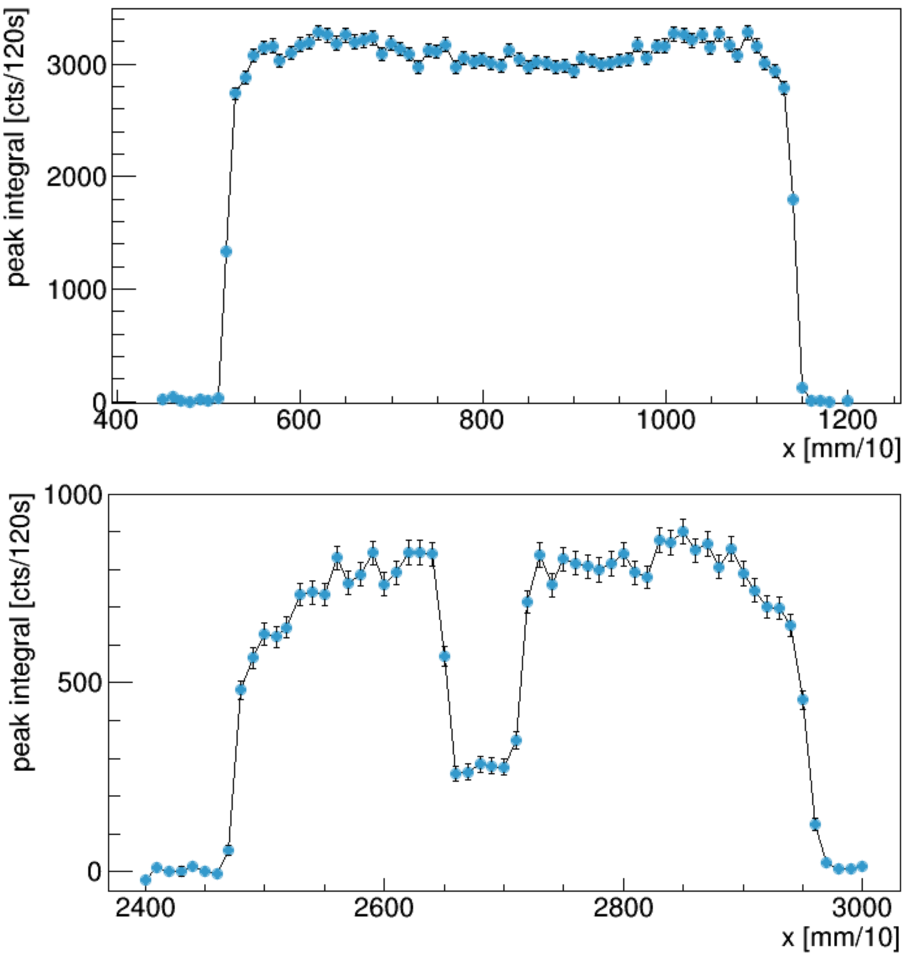

Figure 4.16: PPC top (top) and lateral (bottom) linear surface scans with a step size of $\Delta x = 1\,\mathrm{mm}$ and a lifetime of $120\,\mathrm{s}$ for each position.

4.8.7 BEGe detector top and lateral surface scan

Also for the BEGe detector a top and lateral linear surface scan were performed. For the top scan $T_\mathrm{L} = 60\,\mathrm{s}$ was chosen for each point and for the lateral scan $T_\mathrm{L} = 120\,\mathrm{s}$ respectively. The step size is $\Delta x = 1\,\mathrm{mm}$ like before.

The count rate as function of the source position can be seen in Figure 4.17.

In the lateral surface scan which is shown on bottom of Figure 4.17 at $x = 300\,\mathrm{mm}$ we see a part of the detector which is uncovered by the cup with a count rate of about 4000/120 s. Augmenting the source position, the count rate drops and, in compatibility with a technical drawing, shows the detector holder with a two ring structure.

We analyze the thickness of the copper holder and rings, comparing the count rate of the uncovered part with the count rate at the ring position, and the thinner part of the detector holder

$$d_\mathrm{ring} = \ln\left(\frac{4076 \pm 64}{64 \pm 7}\right) \cdot \frac{1}{1.485\,\mathrm{cm}^2/\mathrm{g} \cdot 8.9\,\mathrm{g/cm}^3} = (3.14 \pm 0.08)\,\mathrm{mm}$$
$$d_\mathrm{cup} = \ln\left(\frac{4076 \pm 64}{566 \pm 8}\right) \cdot \frac{1}{1.485\,\mathrm{cm}^2/\mathrm{g} \cdot 8.9\,\mathrm{g/cm}^3} = (1.49 \pm 0.02)\,\mathrm{mm}$$

d_cup denotes the thickness of the holder cup and d_ring the thickness of the ring structure. Both are in accordance with a technical drawing where the holder thickness is given with 1.5 mm and the ring thickness with 3.0 mm.

The BEGe is slightly cone shaped; this is seen in a picture taken of the BEGe crystal before being contacted. Hence, the active diameter is not a meaningful figure; for its active length we find $L_\mathrm{a} = 39.5 \pm 1.5\,\mathrm{mm}$.

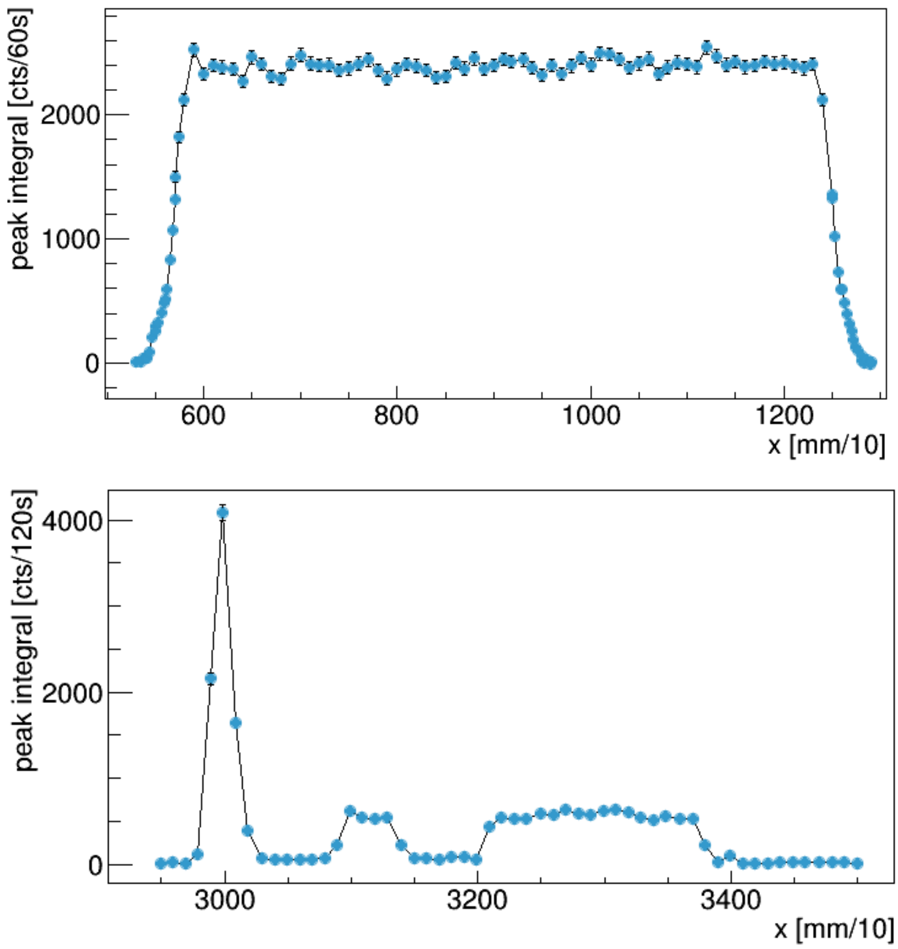

Figure 4.17: BEGe top (top) and lateral (bottom) linear surface scan with a step size of $\Delta x = 1\,\mathrm{mm}$ and a lifetime of $60\,\mathrm{s}$ (top surface) and $120\,\mathrm{s}$ (lateral surface) for each position.

4.8.8 Circular surface scans

For a so called top (lateral) circular scan the scanning arm is placed horizontally (vertically), as was done for the top (lateral) linear scan. To change the scanning position the source is moved along axis 2 and the arm is rotated around axis 1 (see Figure 4.12).

In the following, for all top surface scans the scanning points will be denoted in polar coordinates $[r, \theta]$ where r is the source position along motion axis 2 in mm/10 and θ is the rotation angle around axis 1 in degrees. Note that all coordinates are given in the system of reference of the scanning table, not to be confused with the coordinate system of the detector. The largest radius scanned in the coordinate system of the detector is the scan with the smallest r value.

For lateral surface scans the scanning points are denoted in cylindrical coordinates $[h, \theta]$ with the scanning height h along motion axis 2 in mm/10 and the rotation angle θ around axis 1 in degrees.

4.8.9 PPC detector top circular surface scan

The positions and the count rates of a top circular surface scan of the PPC detector are shown in Figure 4.18. The step sizes are $\Delta r = 5\,\mathrm{mm}$ and $\Delta\theta = 10\,°$, and the measurement lifetime for each point $T_\mathrm{L} = 120\,\mathrm{s}$. The detector is not perfectly centered with rotation axis 1 and in the PPC center the count rate is systematically lower than on the outer parts. Count rates for all scanned points are shown in Figure 4.19.

In positions $[r = 480,\, \theta = 310°]$ and $[r = 530, \theta = 240°]$ the count rate drops drastically. The spectra in these two points reveal a double peak structure and are therefore ignored in the following. Apart from these two points the detector is rotationally symmetric.

The outermost ring which was scanned at $r = 480$ shows a change in count rate in function of the rotation angle θ. This is due to a slight misalignment of the detector center with the arm rotation axis 1: the source beam only partly hits the detector and is moving with respect to the detector edge. This was explained in Section 4.8.3f.

The top contact thickness the PPC detector is not homogeneous. The largest difference in count rate is observed for $r = 630$ and $r = 680$. Averaging over all rotation angles θ at these positions and using Equation 3.5 we find

$$\Delta = \ln\left(\frac{3317 \pm 10}{3060 \pm 10}\right) \cdot \frac{1}{1.9\,\mathrm{cm}^2 \cdot 5.323\,\mathrm{g/cm}^3} = (80 \pm 4)\,\mu\mathrm{m} \tag{4.6}$$

This is about 11% of the design contact thickness which is about 0.7 mm as given in the detector data sheet.

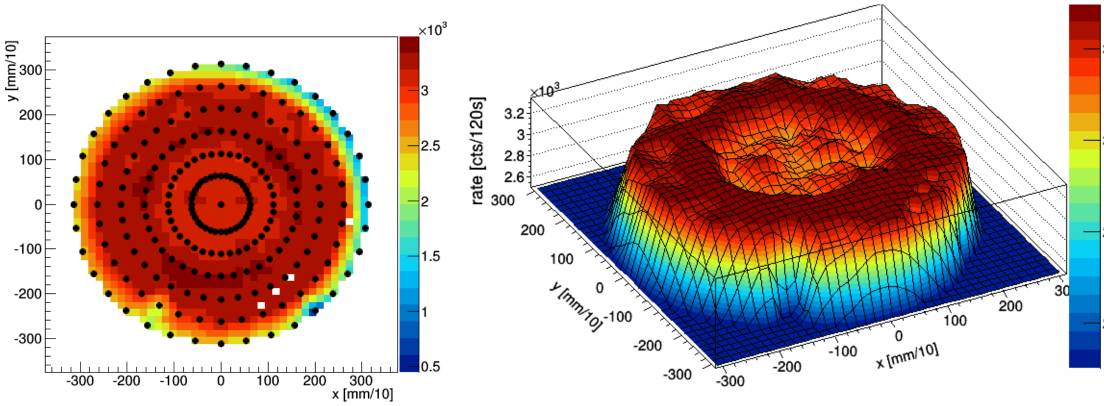

Figure 4.18: PPC circular top surface scan: scanned points (left) and three dimensional surface (right). The count rate is indicated with a color scale. In the left figure a couple of points are white because there are no data; they can be neglected.

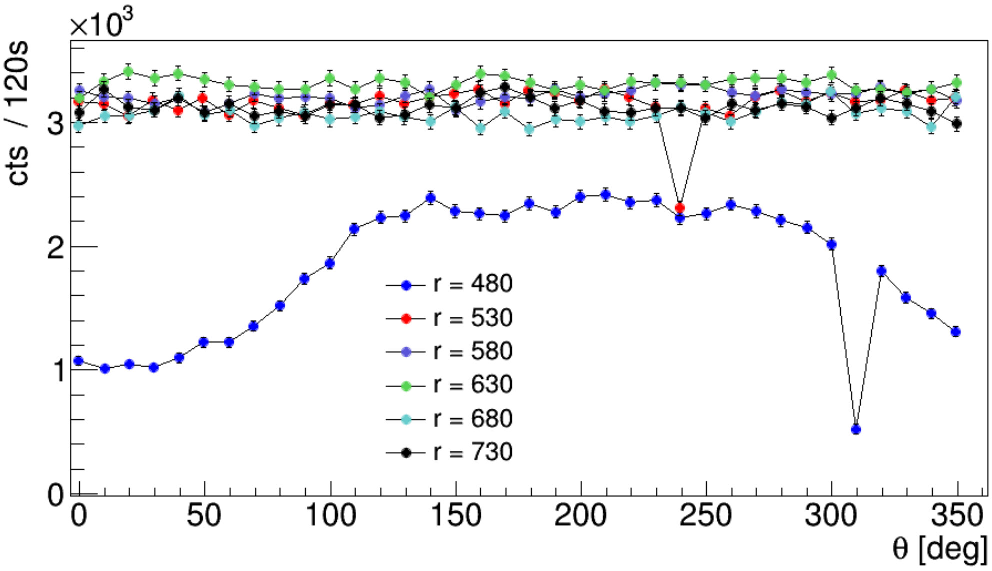

Figure 4.19: Count rate as function of the polar rotation angle θ measured with the PPC in a circular top surface scan.

4.8.10 PPC detector lateral circular surface scan

Also the PPC's lateral surface has been analyzed for several scanning heights h, with a rotation step size of $\Delta\theta = 10°$ and $T_{\mathrm{L}} = 120\,\mathrm{s}$ in each point. See Figure 4.20 for the scan points. Count rates as a function of the rotation angle θ are found in Figure 4.21.

As in the top surface scan we observe one point $[h = 2990, \theta = 120°]$ where the count rate drops and which exhibits a double peak structure. This is peculiar as the top and the lateral scan are about 180° rotated with respect to each other. This means that the peculiarity occurs in almost the same region of the detector surface as before. To further investigate this peculiar behavior, the effect would have to be checked for reproducibility and the respective region would have to be scanned with a higher resolution.

Fitting a constant function to all count rates at scanning heights $h = 3170$ and $h = 3080$ in Figure 4.21 we can calculate again the thickness of the ring structure and find $d_{\mathrm{ring}} = (0.88 \pm 0.01)\,\mathrm{mm}$. This value is higher than the one found with the linear scan. The reasons can be various. As we have seen in the top scan the contact thickness is not homogeneous. Also, the production precision of the holder cup can vary. This has to be taken into account as a systematic effect e.g. when making predictions with simulations. The ring structure thickness averaged over the value found in the linear and the circular scan is $\langle d_{\mathrm{ring}} \rangle = (0.84 \pm 0.02)\,\mathrm{mm}$.

4.8.11 BEGe detector top and lateral surface scan

The scan points and count rates are plotted for a circular top surface scan of the BEGe detector in Figure 4.22 and Figure 4.23. The scan was performed with step sizes of $\Delta r = 4\,\mathrm{mm}$ and $\Delta\theta = 10°$ and a measurement lifetime of $T_{\mathrm{L}} = 60\,\mathrm{s}$.

At $r = 540$ the source beam is outside the detector radius and the count rate observed in 0. Again, the outermost scanned detector radius at $r = 580$ shows a change in count rate due to misalignment of the detector center and the rotation axis 1.

The top contact of the BEGe seems more homogeneous than the PPC one. However, the largest difference found for radii $r = 780$ and $r = 860$ translates to $40 \pm 5\,\mu\mathrm{m}$ which is 10% of the contact thickness $(0.40 \pm 0.05)\,\mathrm{mm}$. Hence, the same order of inhomogeneity as for the PPC outer contact is found for the BEGe. The smaller contact thickness of the BEGe explains the higher count rate observed in top scans with respect to the PPC detector.

Scan points and a three dimensional plot of the lateral circular scan of the BEGe are shown in Figure 4.24. Measurement step sizes are $\Delta h = 5\,\mathrm{mm}$ and $\Delta\theta = 10°$ and the measurement lifetime per point is $T_{\mathrm{L}} = 120\,\mathrm{s}$. Some points have not been scanned, the points are missing in Figure 4.24 on the left. The positions were scanned but the automatized system failed to save the data.

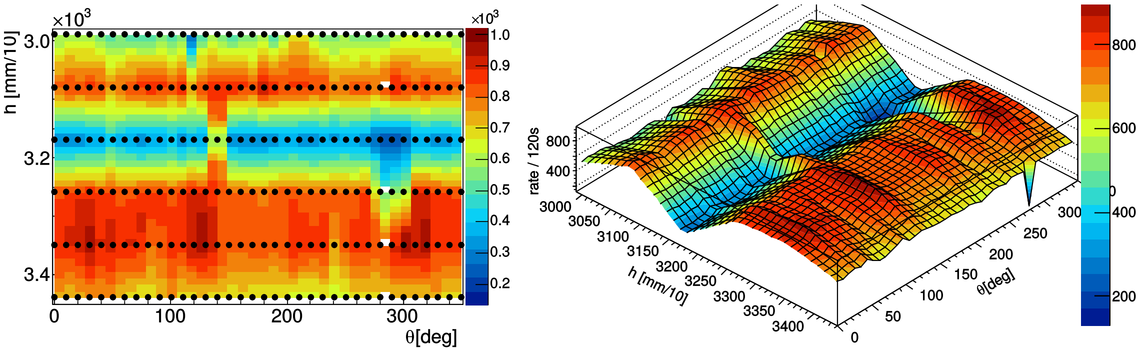

Figure 4.20: PPC circular lateral surface scan: scanned points (left) and three dimensional surface (right). The count rate is indicated with a color scale. In the left figure a couple of points are white because there are no data; they can be neglected.

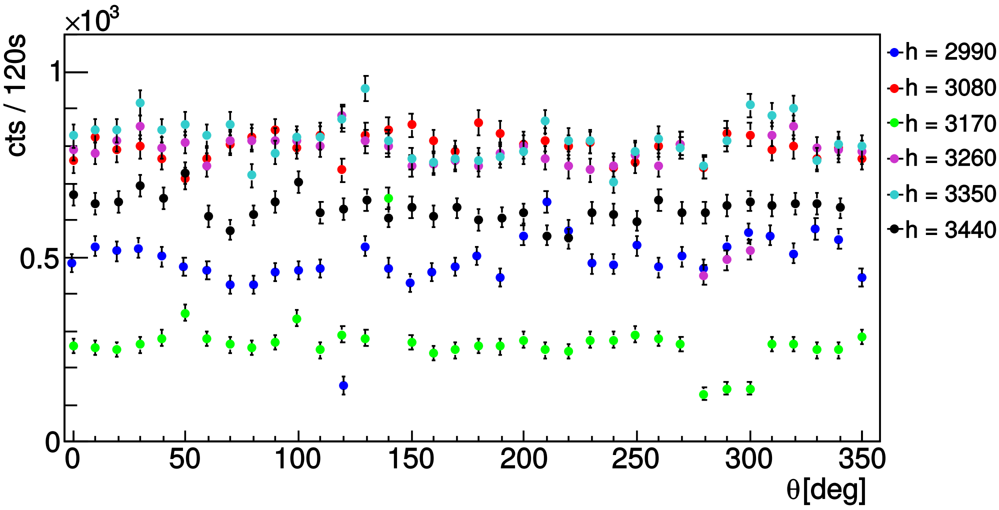

Figure 4.21: Count rate as function of the polar rotation angle θ measured with the PPC in a circular lateral surface scan.

As can be seen in Figure 4.25 at three scanning heights $h = 2920$, $h = 3020$ and $h = 3070$ a sinusoidal change in count rate is observed, which is expected for a slight tilt of the scanning arm with respect to the lateral detector surface (see Figure 4.13). If we assume that the change in scanning height for a 180° rotation is not more than the photon beam divergence w_b this translates to an inclination of less than 1°.

At the uppermost scanning height the count rate is higher as the source beam hits the part of the BEGe which is uncovered by the copper holder.

The three lower most scan positions $h = 3220$, $h = 3270$ and $h = 3300$ show a structure from $\theta = 250°$ to $\theta = 280°$ which measures at least 8 mm in height and 30° in circumference. This can be a screw in the holder structure or similar. These small details are necessary to know and can be implemented in Monte Carlo (MC) simulations. In case very precise simulations have to be performed, measurements with a higher resolution or clarification by the manufacturer are necessary.

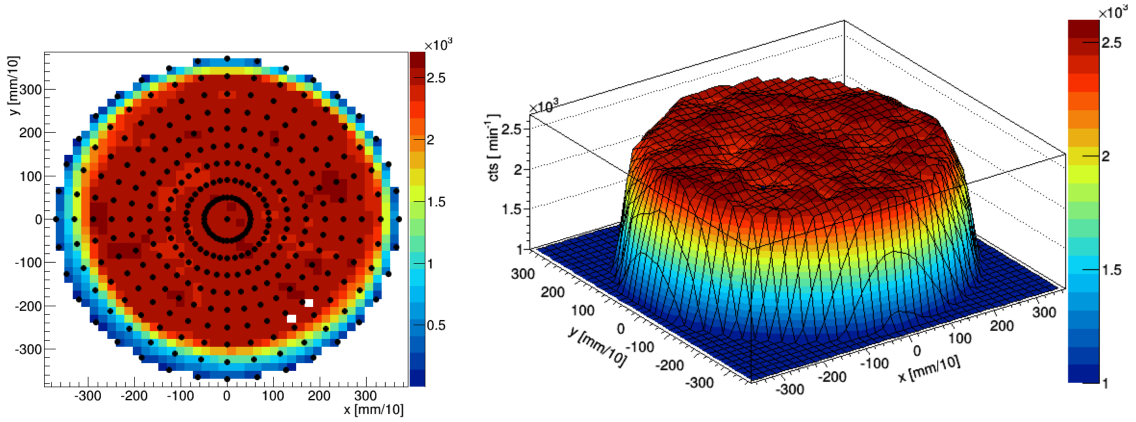

Figure 4.22: BEGe circular top surface scan: scanned points (left) and three dimensional surface (right). The count rate is indicated with a color scale. In the left figure a couple of points are white because there are no data; they can be neglected.

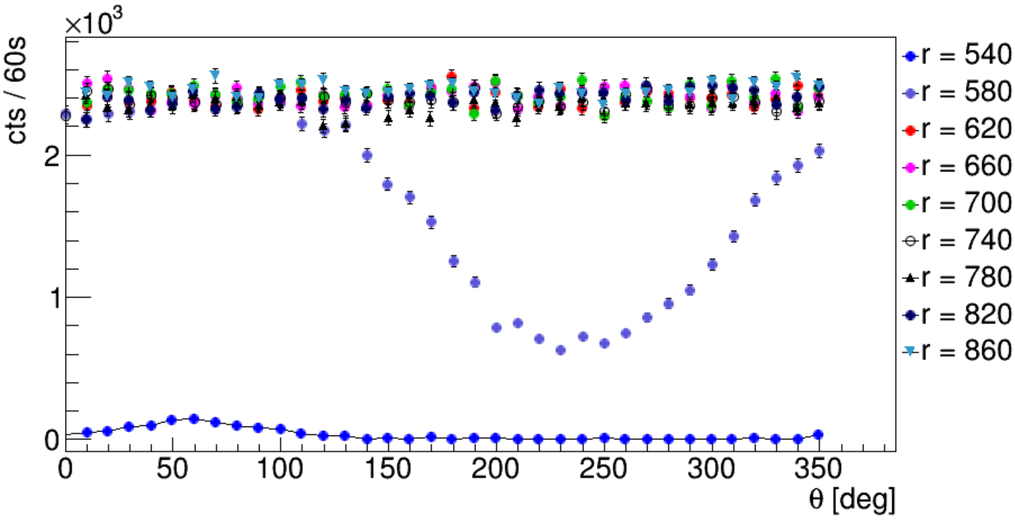

Figure 4.23: Count rate as function of the polar rotation angle θ measured with the BEGe in a circular top surface scan.

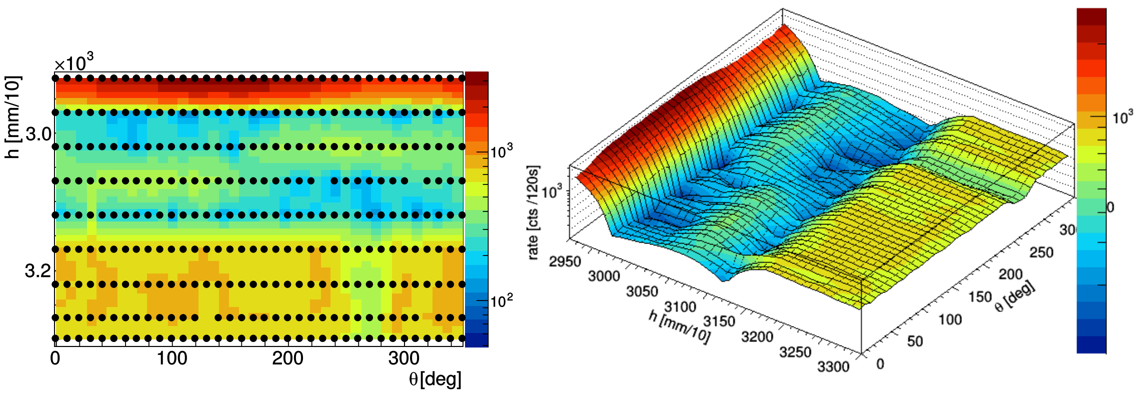

Figure 4.24: BEGe circular lateral surface scan: scanned points (left) and three dimensional surface (right). The count rate is indicated with a color scale.

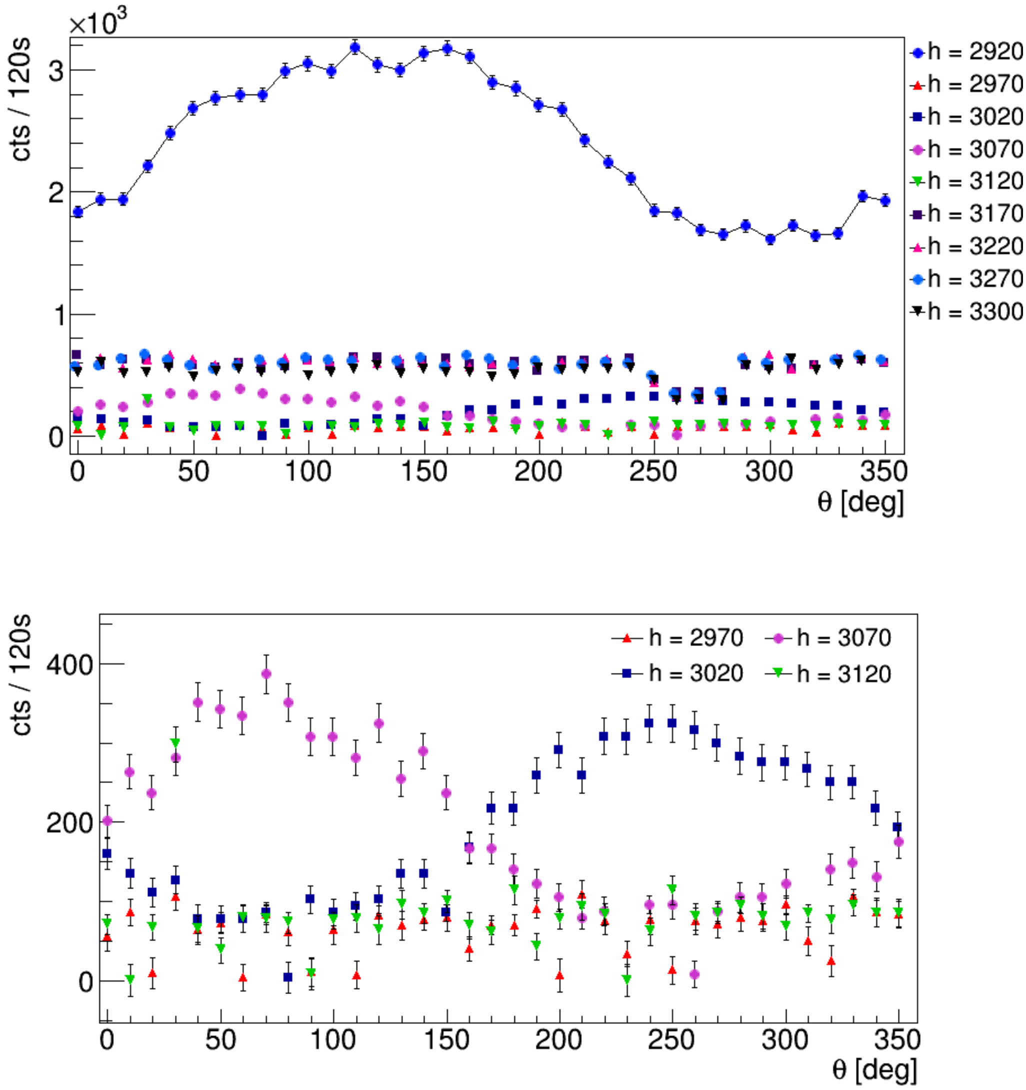

Figure 4.25: Count rate as function of the polar rotation angle θ measured with the BEGe in a circular lateral surface scan: all scanned positions (top), zoom to scans with lower count rate (bottom).

Chapter 5

Compton coincidences: Setup

In order to develop new algorithms for background rejection in GERDA Phase II, detailed knowledge of signal-like event structure in BEGe detectors is of great importance.

In this chapter an experimental setup is described which has been designed and constructed with the purpose of performing three-dimensional scans of BEGe detectors in order to study signal-like pulse shapes in confined detector regions. We base the selection of such events on single Compton interactions in coincidence measurements.

The method has been used with non-segmented and segmented HPGe detectors [57, 58] and for detector characterization in the GRETA and AGATA experiment [59–61]. It is adapted in this work for a BEGe detector in the context of the GERDA experiment. The Compton coincidence measurements described in the following have never been successfully performed before with a BEGe detector.

After an introduction in which we explain the principle of operation, the experimental setup is described in detail. Finally, the measurement campaign is displayed.

5.1 Motivation for single site event studies

In Figure 5.1 measured charge and respective current pulses for three different event classes are plotted. The current pulse $x'[t]$ was calculated based on the charge pulse $x[t]$ by a moving window differentiation with a width of $w_d = 80\,\mathrm{ns}$

$$x'[t] = x[t] - x[t - w_d] \tag{5.1}$$

The three event types shown are a single site event (SSE) depositing energy in one small region, a multiple site event (MSE) depositing energy in two well separated regions and a slow pulse event which deposits energy in the outer n^+ contact of the detector. The latter type is called slow pulse because charge carriers have to diffuse from the outer contact layer into the active volume of the detector, before drifting along the electric field lines and being collected on the read-out electrode. The diffusion process is rather slow, resulting in a distinct pulse shape. MSE events reveal a multiple peak structure in their current pulse while SSE events show a single peak.

In $0\nu\beta\beta$ decay energy is released in form of two electrons (see Section 1). An upper limit of the extension of the subsequent energy deposition $d_\varepsilon^{\mathrm{UL}}$ is given by the range of the two electrons at $\sim 1\,\mathrm{MeV}$ in germanium in the continuous-slowing-down approximation (CSDA) [62] divided by the density of germanium ρ_{Ge}

$$d_\varepsilon^{\mathrm{UL}} < 2 \cdot \frac{r_{\mathrm{CSDA}}}{\rho_{\mathrm{Ge}}} = 2 \cdot \frac{6.56 \cdot 10^{-1}\,\mathrm{g\,cm^{-2}}}{5.323\,\mathrm{g\,cm^{-3}}} \approx 2.5\,\mathrm{mm} \tag{5.2}$$

An energy deposition in a volume smaller than the spatial resolution of the detector is commonly referred to as SSE. In unsegmented HPGe detectors the $0\nu\beta\beta$ events belong to the SSE event class. In order to gain knowledge about signal-like events which deposit energy similar to $0\nu\beta\beta$ the properties of SSE events are studied.

Being able to discriminate MSE from SSE events helps identifying and reducing background in the GERDA experiment and is a key feature of background reduction in GERDA Phase II. One handle for such a discrimination using PSA is the *A over E parameter* (A/E) [63]; the amplitude of the current pulse divided by the energy of the event. On the left side of Figure 5.1 energy and current amplitude are indicated for an SSE event. An MSE event is composed of multiple, spatially well separated interactions. The energy, which is an integrated parameter, contains all interactions whereas the maximum amplitude of the current pulse contains only the interaction which deposits most energy. Therefore, the A/E parameter of an MSE is smaller than for an SSE of the same energy.

To study the spatial homogeneity of the A/E parameter of signal-like events we need samples of SSE events of well defined interaction regions. Furthermore, the comparison of measured and simulated SSE pulse shapes, due to interactions in confined detector regions, can be used to improve and verify pulse shape simulations. And last but not least, confined SSE event samples can help in creating new strategies and algorithms to reduce background in GERDA Phase II.

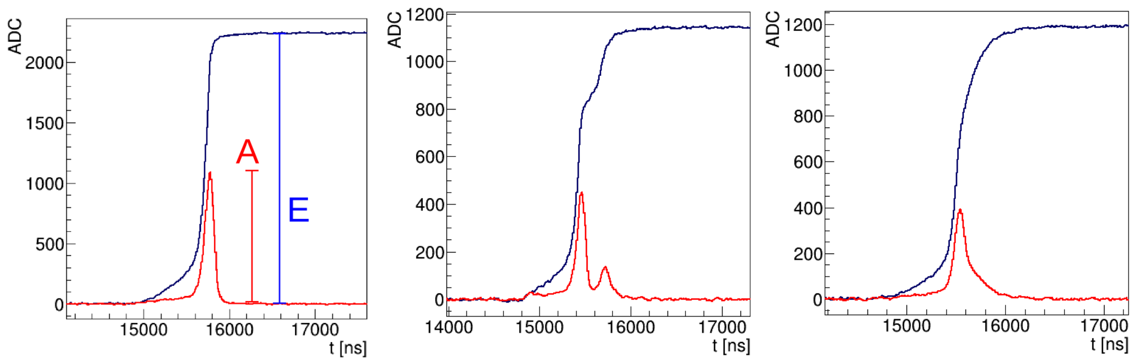

Figure 5.1: SSE (left), MSE (middle) and a slow pulse event (right) in a BEGe detector. The charge pulse as recorded by the FADC is shown in blue and the calculated current pulse (Equation 5.1) in red. The *energy E* and the *amplitude of the current pulse A* are indicated.

In the next section the physical prerequisites of Compton coincidence measurements are describe, which make it possible to select SSE event samples from confined regions in a HPGe detector. The experiment presented in the following is based on single Compton interactions of ^{137}Cs photons with a scattering angle of 90°.

5.2 Single Compton events

^{137}Cs has only one prominent γ-line, with an energy of 661.657 keV ($\approx$ 662 keV in the following) and a branching ratio of $R_B = (84.99 \pm 0.20)\,\%$ (see Figure B.3). The interaction cross section of photons in germanium, as a function of energy and depending on the interaction mechanism, is shown in Figure 5.2. The ^{137}Cs γ energy is indicated with a black vertical line. At this energy, Compton scattering is the dominant interaction process of photons with germanium.

5.2.1 Topology

In Compton scattering energy is transfered from a γ-photon to a shell electron of an atom (see Section 3.1.3). The energy of the scattered photon and the energy transferred to the electron, for an incident photon energy of 662 keV, are listed in Table 5.1. Different scattering angles are tabulated. For a scattering angle of 90° an energy of 373 keV is transfered to the shell electron.

The stopping power of germanium for electrons at 373 keV is about 31 MeV cm^2/g [62]. Thus, the scattered electron has a maximal range of about

$$r_{\mathrm{CSDA}}/\rho_{\mathrm{Ge}} = 0.2\,\mathrm{g\,cm^{-2}}/5.323\,\mathrm{g\,cm^{-3}} \approx 0.4\,\mathrm{mm} \tag{5.3}$$

This limit is smaller region than was derived for $0\nu\beta\beta$ events (see Equation 5.2). Thus, a single Compton event has SSE event topology and can be studied as a prototype for $0\nu\beta\beta$ events.

Table 5.1: Energies of single Compton scattered photon E'_γ and transferred energies to electron E_e for different scattering angles and an incident photon energy of 662 keV.

scattering angle [deg]	E'_γ [keV]	E_e [keV]
90	288	373
60	402	260
45	480	182

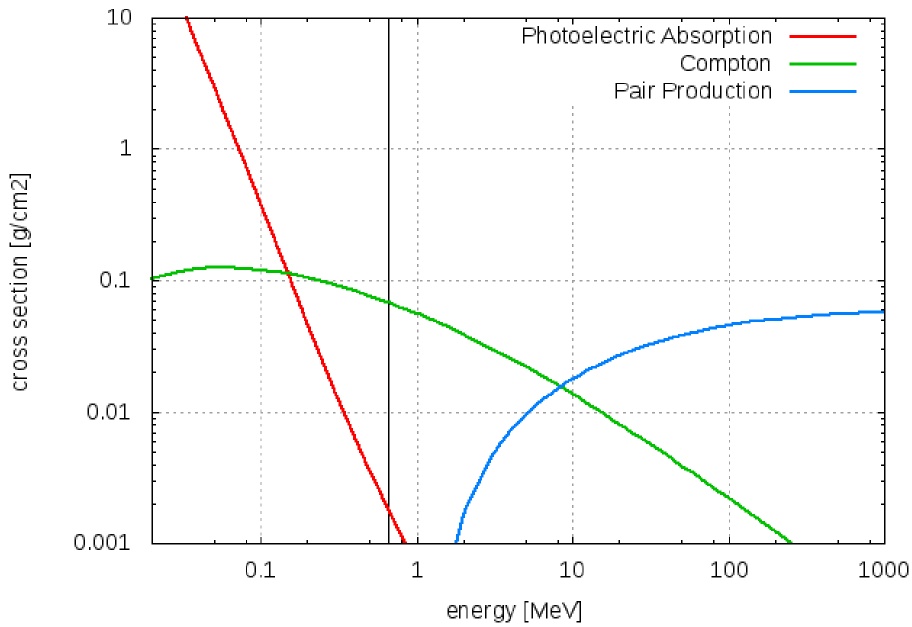

Figure 5.2: Interaction cross section of photons in Germanium depending on energy and interaction mechanism. The black vertical line indicates the 662 keV ^{137}Cs γ-line [64].

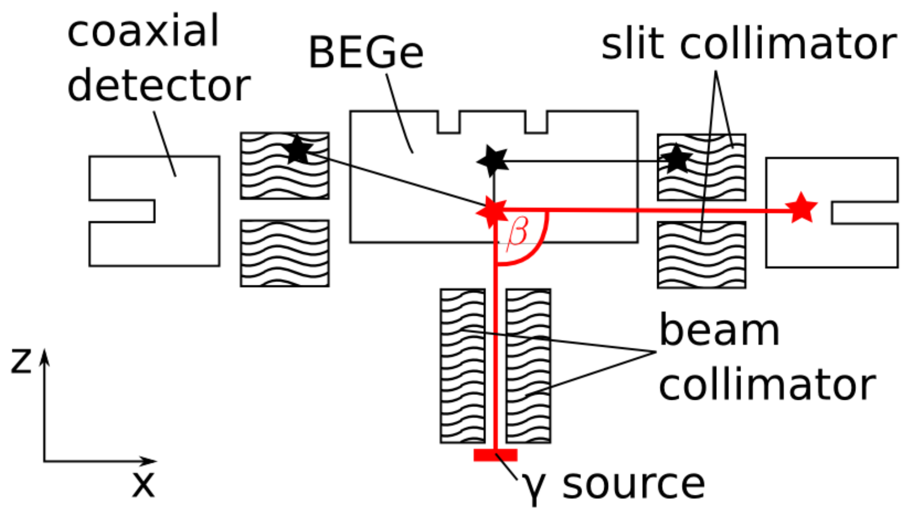

Figure 5.3: The selection of a confined interaction region of single Compton interactions inside a BEGe through tagging of the scattered photon and collimation is shown.

5.2.2 Selection

Photons can interact in various ways and multiple times inside a detector (see Chapter 3.1). From all those possible interactions and combinations of interactions we want to filter only single Compton events; and only from specifically selected interaction regions.

To select Compton events it is important to tag the scattered photons and measure their energy using additional detectors; triggering only on coincidences eliminates the major part of background events. The dynamics of the Compton effect provides a simple tool to ensure that only one interaction took place: The energies for a given scattering angle are fixed (see Section 3.1.3). Therefore, by choosing the right energies for the respective scattering angle (see Table 5.1), we select *single Compton events*.

The selection of scattered photons originating from a *distinct interaction region* is ensured by collimation. The experimentally most practical scattering angle of 90° is chosen which has the advantage that the additional detectors are easy to mount, and the scanned region is the same for all of them.

A simplified schematic of the experimental setup can be seen in Figure 5.3. A beam collimated ^{137}Cs source is installed below a BEGe detector. Slit collimated Coax detectors are installed at a Compton scattering angle of $\beta = 90°$ with respect to the incident photon beam to detect the scattered photons.

5.3 Experimental setup

A detailed sketch of the experimental setup is shown in Figure 5.4. A top view on the left and a side view on the right show a BEGe detector, mounted top-down in the middle of the setup. Four Coax detectors are facing the BEGe under an angle of 90°. Lead collimators are placed between the BEGe and the Coax detectors; their aperture is variable and selects photons scattered under 90° with respect to the incident photon beam. A collimator is mounted below the BEGe which holds the ^{137}Cs source.

A close up of the setup can be found on the left side of Figure 5.5. The BEGe is mounted top-down in the middle of the setup and three Coax detectors (out of four possible) are mounted on a table platform tagging the scattered photons. The source is held by a standard source collimator which is shown on the right side of the same figure.

The whole experimental setup is shown in Figure 5.6. The various parts are explained in the following.

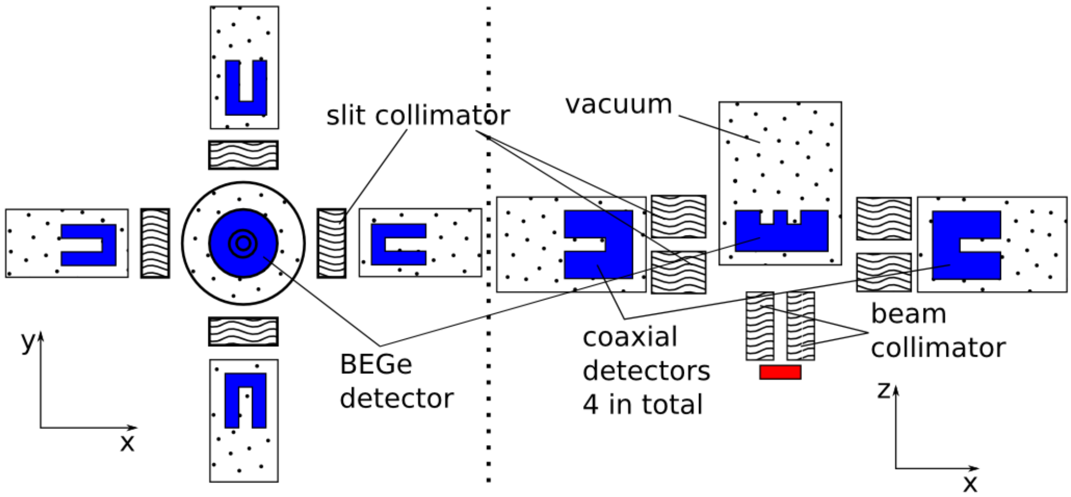

Figure 5.4: Sketch of top view (left) and side view (right) of the Compton coincidence experimental setup. Germanium detectors are shown in blue, vacuum cryostats as dotted volumes, lead collimators as wavy blocks and the ^{137}Cs source is drawn in red.

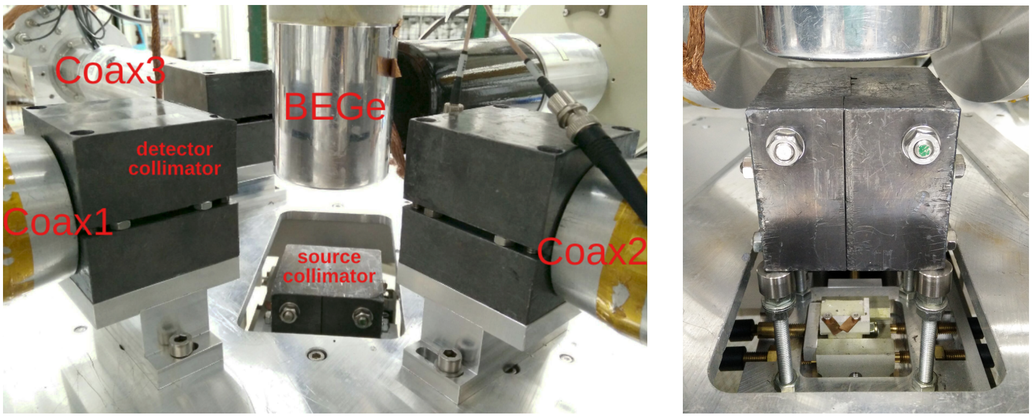

Figure 5.5: Close up of the coincidence measurement setup (left) with the BEGe detector in the middle and three Coax detectors measuring the scattered photons and the standard source collimator (right).

Figure 5.6: Picture of the full experimental setup for Compton coincidence measurements with LN_2 dewar on the left, table with detectors in the middle and DAQ system in a crate on the right side.

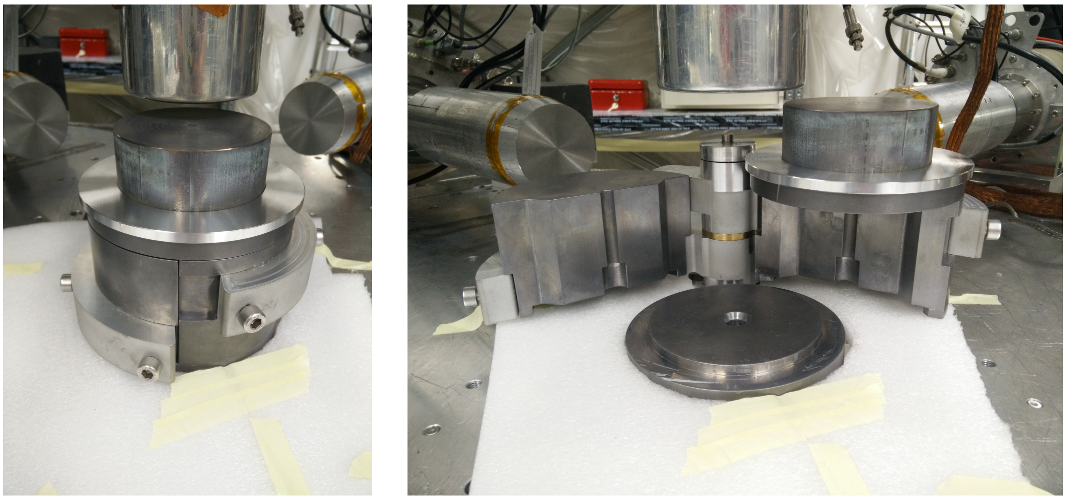

Figure 5.7: Closed (left) and open (right) source collimator designed to shield a 780 MBq ^{137}Cs source. The hole in the table has been covered for source installation to prevent it from falling down.

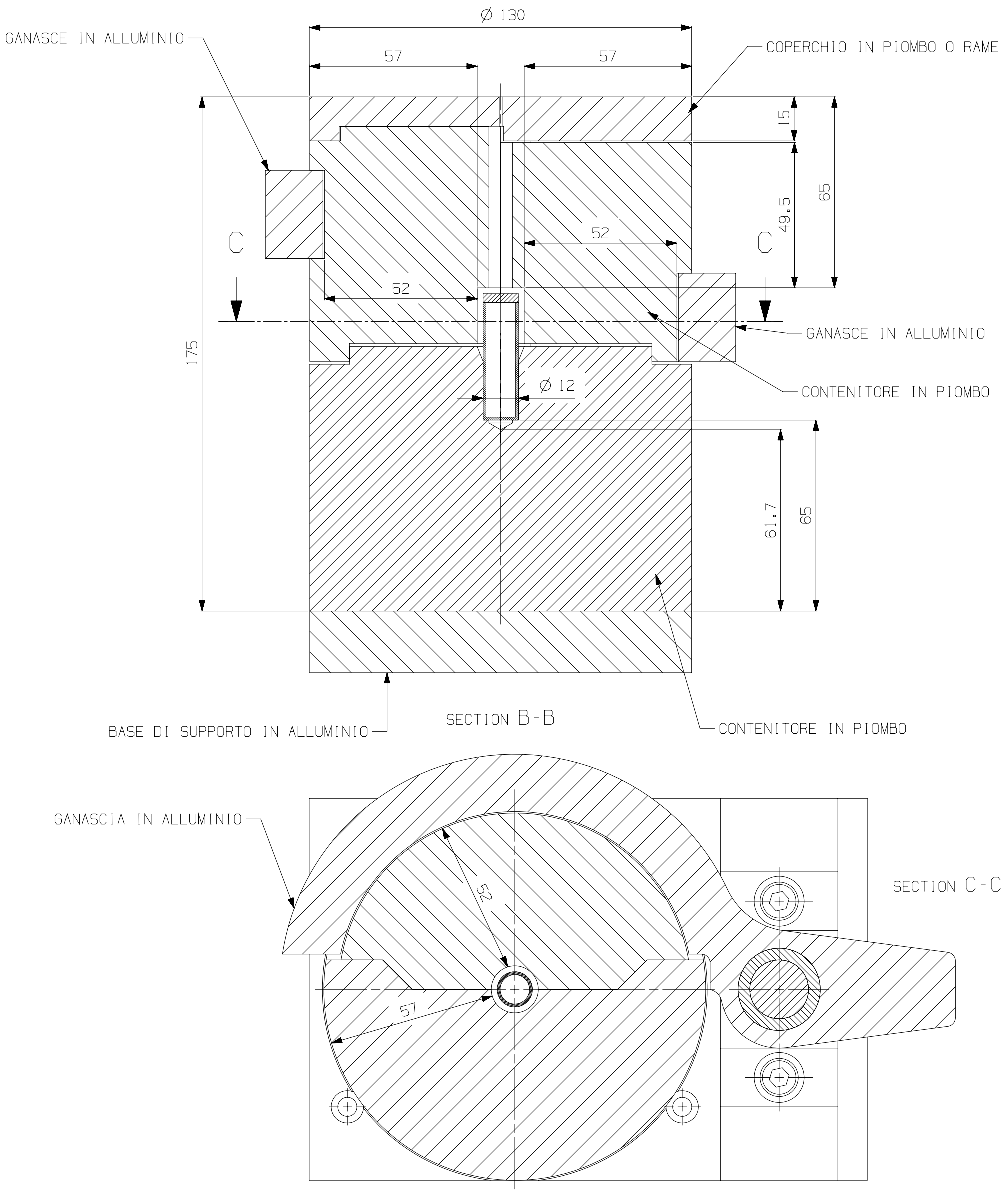

Figure 5.8: Technical drawing of the new source collimator. It can host a strong ^{137}Cs source with an activity of about 780 MBq. Provided by Matteo Turcato.

5.3.1 Source collimation

Two different collimators were designed for different types of sources:

- **Standard collimator**
  A simple collimator (see Figure 5.5) can hold a standard ^{137}Cs source with a point-like activity of about 350 kBq. The activity is sealed inside a small plastic tile of dimensions $20 \times 10 \times 1.9\,\text{mm}^3$. The collimator has a length of 8 cm which can be extended to 16 cm and a square collimation of 1.5 mm or 3 mm. The collimator can be lifted in order to prevent divergence of the photon beam. It is mounted on a movable slide controlled by precision motors with a positioning reproducibility better than 1 mm.

- **Collimator for a strong ^{137}Cs source**
  The source is collimated and the angular acceptance of the Coax detectors is reduced with collimators, hence, the expected event rate is very low. We use a strong ^{137}Cs source which has an activity of about 780 MBq, augmenting the rate, in order to be able to measure within an acceptable time frame. To shield the strong ^{137}Cs source the standard source collimator is not thick enough and too difficult to handle. The absorption and scattering of photons in lead was studied in order to choose an adequate thickness for a collimator (see Table 5.2). A dedicated collimator with a side thickness of 57 mm was produced and installed. Pictures of the collimator can be found in Figure 5.7, while Figure 5.8 shows a detailed technical drawing. It can be opened and closed from a distance in order to minimize personal risk due to exposure to radiation. An extension with a smaller diameter has been added on top of the collimator which adds 35 mm to a total length of 100 mm. The incident collimation measures 1 mm in diameter.

Using Equation 3.5 with $\rho_{\text{Pb}} = 11.35\,\text{g/cm}^3$, $\mu_{\text{photo}}(\text{Pb}, 662\,\text{keV}) = 6.017 \cdot 10^{-2}\,\text{cm}^2/\text{g}$ and $\mu_{\text{Compton}}(\text{Pb}, 662\,\text{keV}) = 4.347 \cdot 10^{-2}\,\text{cm}^2/\text{g}$ [64] the survival fraction of 662 keV photons for different lead thicknesses can be calculated. Some values are listed in Table 5.2.

Table 5.2: Photon survival fractions of photoelectric absorption (photo), Compton scattering (Compton) and the total attenuation (total) of 662 keV photons in lead. d denotes the lead thickness and A_s the equivalent surviving activity for an incident activity of 780 MBq.

d [cm]	photo [%]	Compton [%]	total [%]	A_s [MBq]
3	12.9	22.8	2.9	22.9
4	6.5	13.9	0.9	7.0
5	3.3	8.5	0.3	2.2
6	1.7	5.2	0.1	0.7

5.3.2 Automatic filling system

Germanium detectors have to be operated at cryogenic temperatures. All detectors are mounted in vacuum cryostats connected to dewar vessels, which contain LN_2, by a cold finger. The Coax detectors, mounted on the table platform, have very small dewars with a volume of 3 l only. They have to be filled within a time interval of ~ 16 h, which makes manual filling unfeasible.

Therefore, all dewar vessels have been connected to an automatic filling system controlled by a Keysight[1] Data Acquisition Unit[2]. The unit has been programmed to read the values of temperature sensors inside the vacuum cryostats of each detector. Moreover, it reads the temperature of all valves in the automatic filling system and manages an opening and closing sequence in order to fill all dewars in a predefined time interval.

Originally, the filling interval was set to 14 h; after a couple of months of stable operation the interval was changed to 16 h. The system can also be managed remotely via a Graphical User Interface (GUI) and detectors can be manually excluded from refilling via the GUI.

The LN_2 is provided by a storage tank with a total volume of about 180 l. This vessel has to be filled manually in a five day interval if all detectors are connected.

5.3.3 Low and high voltage supply and safety shutdown

The PreAmps of all detectors are powered by SpecAmps[3][4], with a LV of 6 V.

The Coax detectors use negative HV and the BEGe positive HV (see Table 4.1). This is provided by two programmable HV modules[5].

Each detector has an HV inhibit signal output which changes its voltage level if the crystal becomes too warm; this happens typically above 110 K. All HV inhibit signals are collected in a dedicated unit which further connects to the HV modules. If one detector is sending the HV inhibit signal the unit sends a shut down signal to the HV modules in order to ramp down all detector HVs; it is assumed that none of the detectors has been refilled.

The Keysight unit can provide a shutdown trigger with a programmable temperature trigger level. In this manner the shutdown can be triggered at a lower temperature than with the HV inhibit signals.

[1]Former Agilent
[2]34970A Data Acquisition / Data Logger Switch Unit
[3]Coax: Silena 7611/L Spectroscopy Amplifier
[4]BEGe: Ortec 762 Spectroscopy Amplifier
[5]CAEN N1471H: NIM HV Power Supply High Accuracy Module

Moreover, the HV is also shut down in case of power failure or malfunction of the Keysight unit, or if the power on the HV handling unit fails.

If a detector has to be warmed up the HV shutdown trigger can be suppressed for the respective channel, by means of a physical switch on the HV handling unit.

5.3.4 Three dimensional accessibility

The Compton table has three degrees of freedom

- $\boldsymbol{y}$ The source with its collimator can be moved along the y-axis to select a position along the diameter of the BEGe detector.
- $\boldsymbol{\theta}$ The BEGe can be rotated along the z-axis.

By changing the $\boldsymbol{y}$ and $\boldsymbol{\theta}$ parameter the full top surface of the BEGe can be scanned. Last

- $\boldsymbol{z}$ The height of the table platform on which the detector collimators and Coax detectors are mounted can be raised and lowered.

By changing the height of the table a scanning height inside the BEGe detector is chosen. A full three-dimensional scan can be performed using all three degrees of freedom.

The $\boldsymbol{z}$-movement has to be performed manually, all other movements can also be controlled remotely. The precision of the table height is about ± 0.5 mm and is read from a measure which is installed on the side of the table (see Figure 5.9). The precision motors controlling the $\boldsymbol{y}$- and $\boldsymbol{\theta}$-movements have a reproducibility better than 1 mm and 1°.

5.3.5 Position calibration of source and table

Position calibrations were performed in order to align the source position and the table height to the desired scanning region in the BEGe.

A ^{137}Cs source was installed in the source collimator, and the rate of the 662 keV photons was measured with the BEGe in dependence of the $\boldsymbol{y}$-position of the source collimator. The result of this top scan can be found in Figure 5.10. The center of the BEGe along the $\boldsymbol{y}$-movement of the source collimator was determined to be (53 ± 1) mm.

For the table height calibration a ^{22}Na source was placed inside one of the detector collimators as can be seen in Figure 5.11. As ^{22}Na decays via β^+ it emits a prominent 511 keV γ-line due to annihilation photons. The rate of the 511 keV γs from the ^{22}Na source was measured with the BEGe in dependence of the table height $\boldsymbol{z}$. In Figure 5.12 the result of this lateral scan can be seen. The table cannot be lifted higher than 120 mm, hence, this is the last point scanned. The middle of the

Figure 5.9: Measure installed on the side of the scanning table platform to read its height.

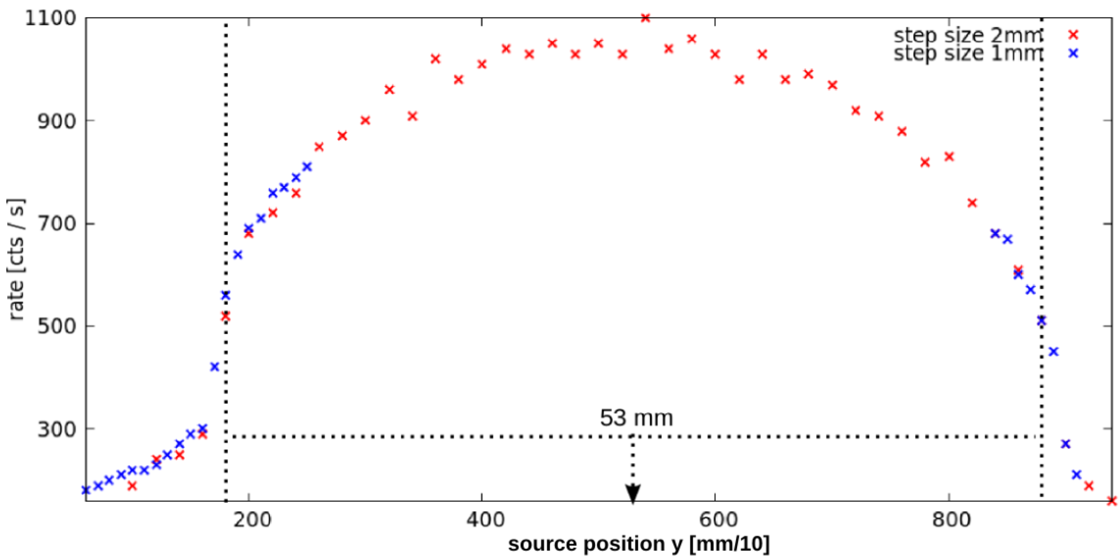

Figure 5.10: Top scan of the BEGe detector inside the Compton coincidence setup using a ^{137}Cs source. Plotted is the rate of 662 keV γs versus the source position given by the precision motor which moves the collimator. The BEGe center is indicated.

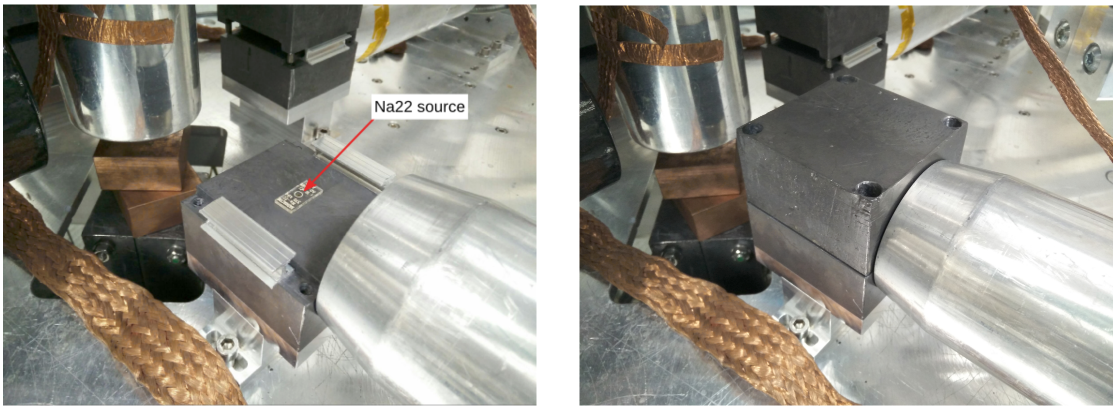

Figure 5.11: ^{22}Na source inside a detector collimator; with the collimator open (left) and closed (right). This setup is used for detector position calibration (Section 5.3.5) and external trigger gate calibration (Section 5.4.2). The collimator aperture is equal to the thickness of the ^{22}Na source which measures $\sim 1.9\,\mathrm{mm}$.

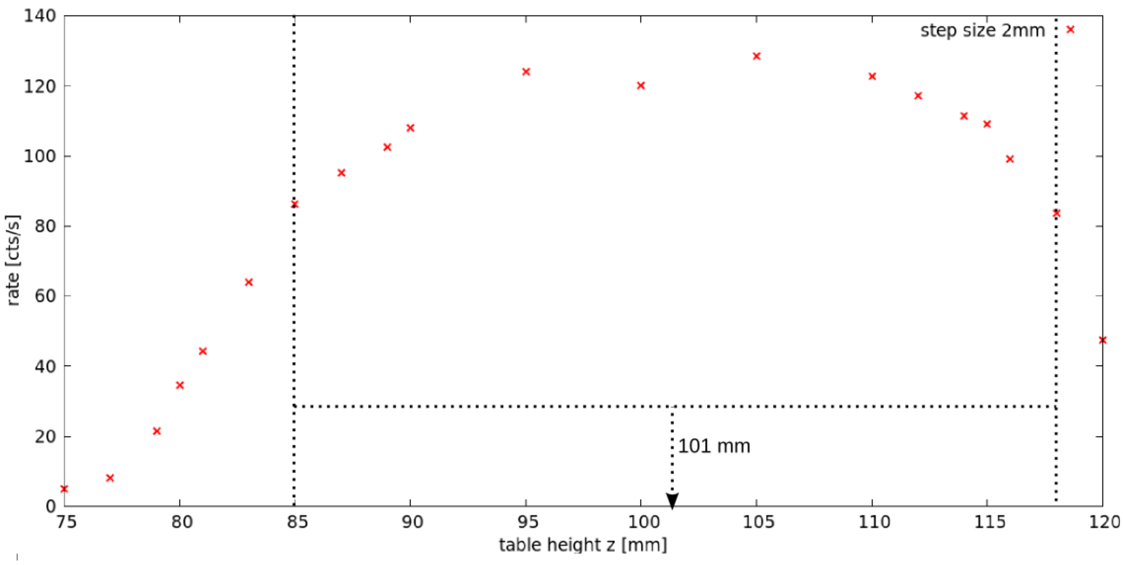

Figure 5.12: Lateral scan of BEGe detector inside the Compton coincidence setup using a ^{22}Na source. Plotted is the rate of 511 keV γs versus the table height given by the measure at the side of the table.

detector with respect to table height z was determined to be (101 ± 1) mm. Thus, subtracting half of the BEGe height $40.7/2\,\text{mm} \approx 20\,\text{mm}$ from this value we find its lower surface at a z-value of $101\,\text{mm} - 20\,\text{mm}) = 81\,\text{mm}$.

5.4 DAQ and trigger

We us an FADC, with four channels and a sampling frequency of 100 MHz, to digitize the detector signals. For a trigger generation we demand coincidence of the BEGe and at least one of the Coax detectors BEGe $\wedge$ (Coax1 $\vee$ Coax2 $\vee \ldots$. To reduce the number of random coincidences an external trigger logic was designed and implemented.

5.4.1 External trigger logic

The FADC can generate a trigger gate on its own. A fixed trigger threshold is set, the gate is opened when the signal rises above threshold and closes when it falls back below threshold. Consequently, the length of the internal trigger gate depends on the trigger threshold and the signal height.

The first approach to trigger on coincidences was to set the internal trigger logic to a multiplicity of two channels. However, in this manner a lot of random coincidences are recorded. The real coincidences from single Compton events are expected at a fixed and short trigger time delay between the BEGe and one Coax detector.

The solution is the installation of a dual timer unit (DTU) which generates a leading edge trigger with adjustable gate size, using the trigger gate generated by the FADC as input signal. The calibration of the DTU gate size is described in the following Section 5.4.2. Ultimately, the external trigger gate is set to a length of 2 µs.

A sketch of the full external trigger logic can be found in Figure 5.13. The FADC we are using has only one internal trigger output. To trigger on coincidences we need a trigger gate for the BEGe as well as for the Coax detectors. Hence, two FADCs are used: The first one only generates a trigger gate for the BEGe detector; in Figure 5.13 it is called DIGI0. The second FADC (DIGI1) creates a trigger gate if one of the Coax detector triggers. Both gates are shortened by the DTU and finally we demand a coincidence by combining both with an AND logic. This external trigger is lead back to DIGI1 which subsequently writes all traces on disk.

An example of a random coincidence which would be recorded using the internal trigger logic only, but is excluded by the external DTU trigger logic, is shown in Figure 5.14.

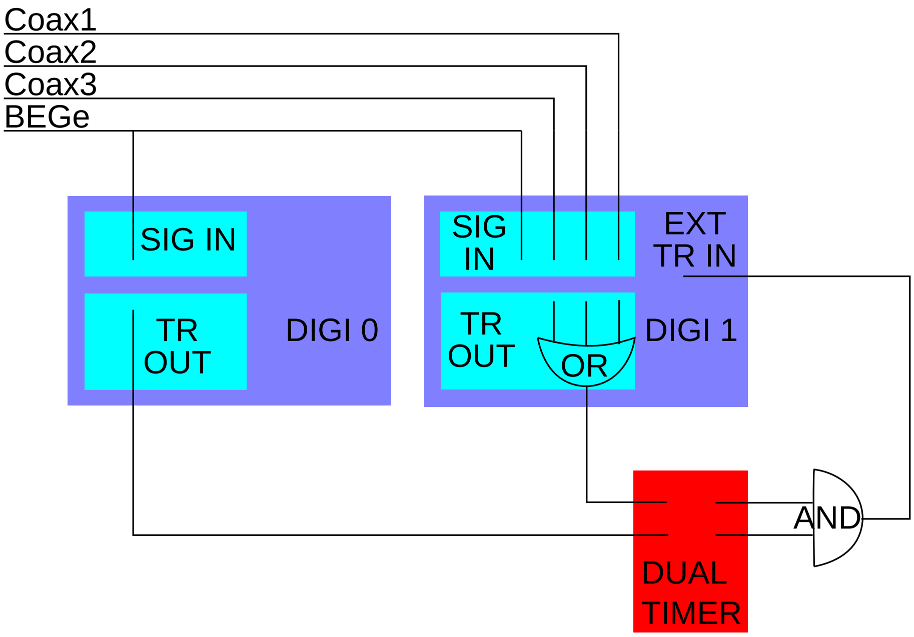

Figure 5.13: External trigger logic. Digi0 creates trigger gate for BEGe, Digi1 creates trigger gate for the coaxial detectors if either of them is above threshold. The DTU adjusts the gate length to a chosen value using a leading edge trigger. The DTU gates are combined in a logic AND to get only coincident events. Coincidence logic: BEGe$\wedge$(Coax1$\vee$Coax2$\vee$Coax3).

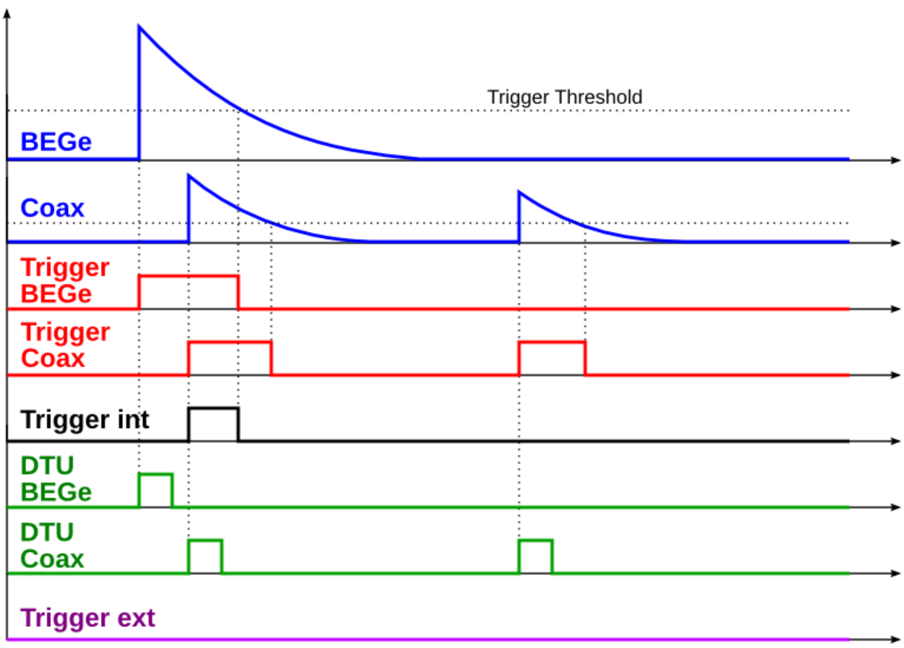

Figure 5.14: Example of a random coincidence which would be recorded using the internal trigger logic (Trigger int) but excluded by the external Trigger logic (Trigger ext).

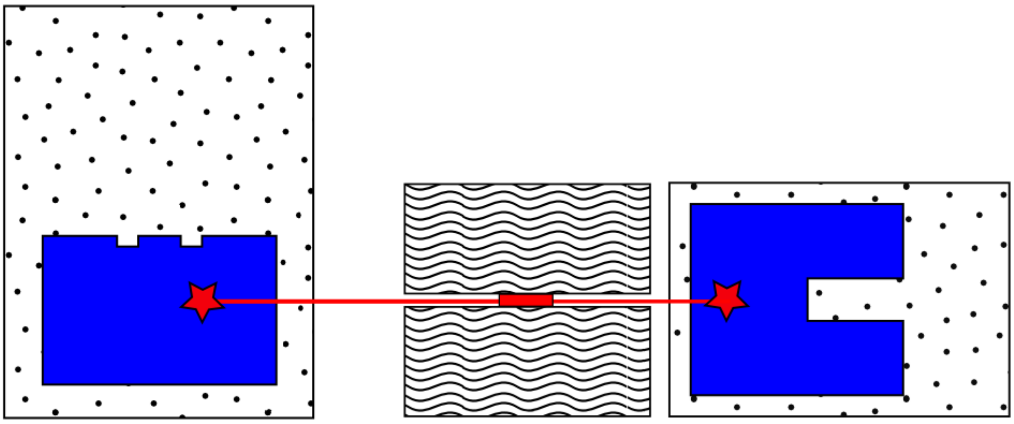

Figure 5.15: Sketch of ^{22}Na DTU gate calibration measurement setup. Not up to scale. A ^{22}Na source is installed inside a detector collimator. ^{22}Na decays via β^+ and the subsequently emitted annihilation γs can be measured in coincidence.

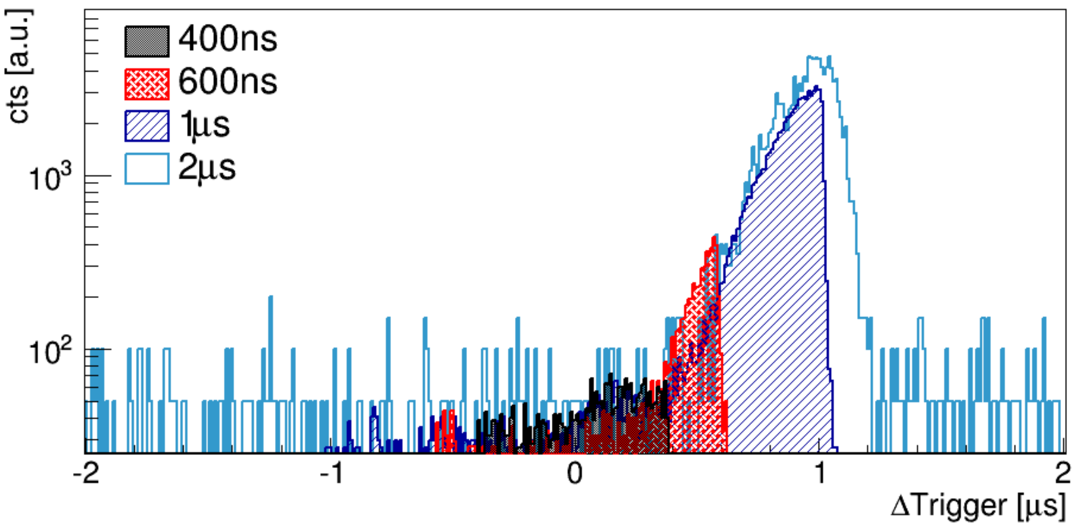

Figure 5.16: Trigger time difference for different DTU gate sizes divided by measurement real-time. A Peak containing true coincidences on top of flat background of random coincidences is observed. Any DTU gate size shorter than $\sim 1.3\,\mu s$ cuts a part of true coincidences.

5.4.2 Trigger gate calibration

To calibrate the trigger gate size on the DTU we use a Na^{22} source. Na^{22} is decaying via β^+ and the emitted positron annihilates with an electron. Two annihilation photons of 511 keV each are emitted back-to-back. They can be measured in coincidence using the external trigger logic described before. We measure coincidences of one Coax detector and the BEGe with the source installed in a detector collimator (Figure 5.11), as was done for the lateral position calibration. A sketch of the setup can be seen in Figure 5.15.

The measurement is repeated for DTU gate sizes of 0.4 µs, 0.6 µs, 1 µs and 2 µs. Histograms of the trigger time difference $\Delta\text{Trigger} = \text{Trigger}_{\text{BEGe}} - \text{Trigger}_{\text{Coax}}$ are plotted in Figure 5.16. All bin contents are divided by the real-time of the respective measurement for normalization.

An asymmetric peak with a mode of roughly 1 µs on a flat background can be seen. The background contains random uncorrelated coincidences while the peak contains truly correlated events. The peak of true coincidences is asymmetric as ΔTrigger depends mostly on the relation between the trigger threshold and the shapes of the traces which are asymmetric by themselves and contain single as well as multiple Compton events. If the DTU gate size is too short, $<$ 1.2 µs, real coincidences are cut from the distribution.

The DTU gate size calibration is performed for all coincident detectors. They behave all very similar and a DTU gate size of 2 µs was determined to be sufficiently large for all of them, leaving some freedom for baseline drifts, different trigger thresholds and different measurement positions. Individual plots can be found in Appendix D.

5.5 Data taking campaign

^{137}Cs coincidence measurements were taken with the standard collimator and a standard ^{137}Cs source. However, the measurement time for one scanning position in order to see coincidences was about one week. After installation of the 780 MBq ^{137}Cs source and its collimator, measurement time went down to about one day per position. Various locations were scanned with different detector collimation and different BEGe HV.

A list of measurements taken with the 780 MBq ^{137}Cs source can be found in Table 5.3 and the positions scanned are visualized in Figure 5.17. Run14 will be shown in the following for illustration purpose.

Table 5.3: List of ^{137}Cs coincidence measurements taken with a 780 MBq source. For all measurements the rotation angle was fixed at $\theta = 0°$. The measurements presented were performed in the second half of 2015.

Run	start date	real time [h]	detector coll. [mm]	table height z [mm]	source pos. y [mm]	BEGe HV [kV]	Coax
1^a	0715	18.0	5	90	53	4.0	1
1^b	0716	26.9	5	90	53	4.0	1
2^a	0717	33.4	5	100	85	4.0	1
2^b	0721	7.0	5	100	85	4.0	1
2^c	0722	49.4	5	100	85	4.0	1
3	0724	3.6	5	115	53	4.0	1
4	0923	13.1	3	100	53	4.5	1,2,4
5	0924	13.9	3	100	53	5.0	1,2,4
6	0925	13.5	3	105	85	5.0	1,2,4
7	0928	10.4	3	115	85	5.0	1,2,4
8	1022	12.3	1	120	53	4.5	1,2,4
9	1026	12.3	1	118	53	4.5	1,2,4
10	1027	12.3	1	115	53	4.5	1,2,4
11	1028	12.4	1	102	53	4.5	1,2,4
12	1029	20.9	1	89	53	4.5	1,2,4
13	1031	21.0	1	86	53	4.5	1,2,4
14	1102	20.5	3	86	53	4.5	1,2,4
15	1103	21.4	3	117	53	4.5	1,2,4
16	1104	26.4	3	100	86	4.5	1,2,4
17	1107	25.4	3	82	85	4.5	1,2,4
18	1109	23.7	3	85	83	4.5	1,2,4

5.6 Data processing and selection

All data, taken with the FADC DAQ system, are processed in the same manner as described in Section 4.2, using a multi-tier approach (see Appendix A).

A number of quality cuts are applied in order to get rid of *unphysical* and *pile-up* events, events with *very noisy baseline (BL)* and *random coincidences*. Only events which satisfy the following requirements have been kept

- Over/Underflow-cut: The dynamic range of the FADC has not to be exceeded.
- IsGood: No error occurred during processing.
- σ_{BL}-cut: The distribution of standard deviation of the restored BL σ_{BL} is fit for each run using a Gaussian fit function. All events with $\sigma_{\mathrm{BL}} > \mu_{\mathrm{Gauss}} + 3\,\sigma_{\mathrm{Gauss}}$[6] are discarded.
- TriggerNumber-BEGe: The number of triggers found in the BEGe trace has to be one, using a fixed trigger threshold.
- TriggerNumber-Coax: The number of triggers found in any Coax trace has to be either smaller than two, or the second trigger has to have at least a distance of 6 µs from the first one.
- ΔTrigger-cut: $0\,\mu < \Delta\mathrm{Trigger} = \mathrm{Trigger}_{\mathrm{BEGe}} - \mathrm{Trigger}_{\mathrm{Coax}} < 1.2\,\mu\mathrm{s}$.

The most stringent cut is the σ_{BL}-cut. This cut excludes noisy events and events with a poorly restored BL which can be due to pile-up.

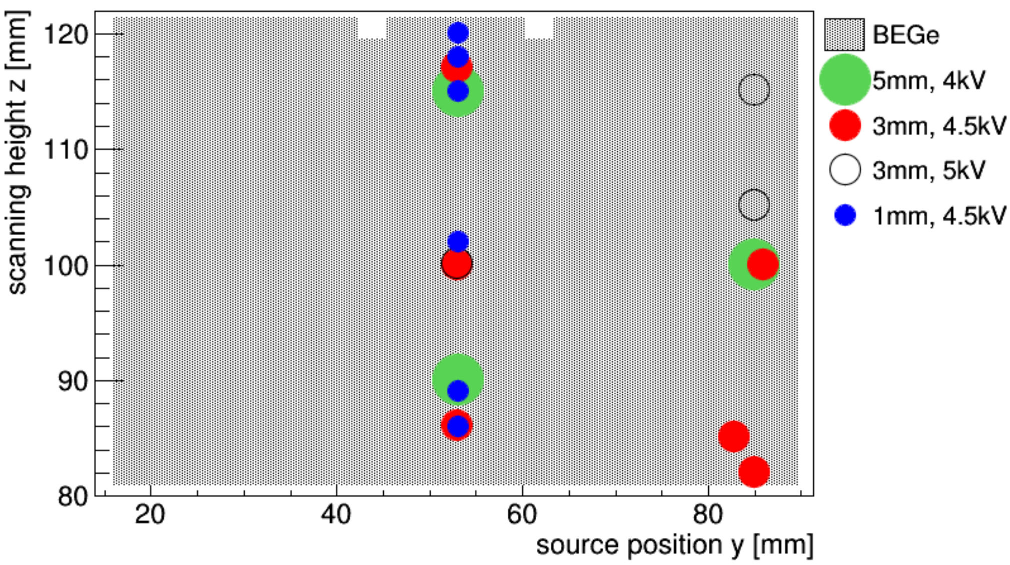

Figure 5.17: Scanned points using the 780 MBq ^{137}Cs source with different detector collimation and BEGe HV.

[6] μ_{Gauss} and σ_{Gauss} are the centroid and standard deviation of the Gaussian fit function.

The effects of the quality cuts on uncalibrated energy spectra is exemplary shown in Figure 5.18, for the BEGe and Coax1 data of Run14. The dark blue spectra contain all events with no quality cuts applied, the light blue spectra include all cuts except for the σ_{BL}-cut and in the spectra shown in magenta also the σ_{BL}-cuts is applied.

Note that the σ_{BL}-cut restores the resolution of γ-lines in the BEGe spectrum and has little to no effect in the spectrum of Coax1. The reason is most probably the high activity of the ^{137}Cs source and, therefore, high amount of pile-up events in the BEGe detector. The energy reconstruction for pile-up events is mostly poor and worsens the energy resolution. The Coax detectors show much less pile-up as they are not directly in the γ beam of the ^{137}Cs source.

Finally, the energy is calibrated for each detector by means of calibration curves, calculated using dedicated ^{60}Co calibration spectra. This was explained in Section 4.5.

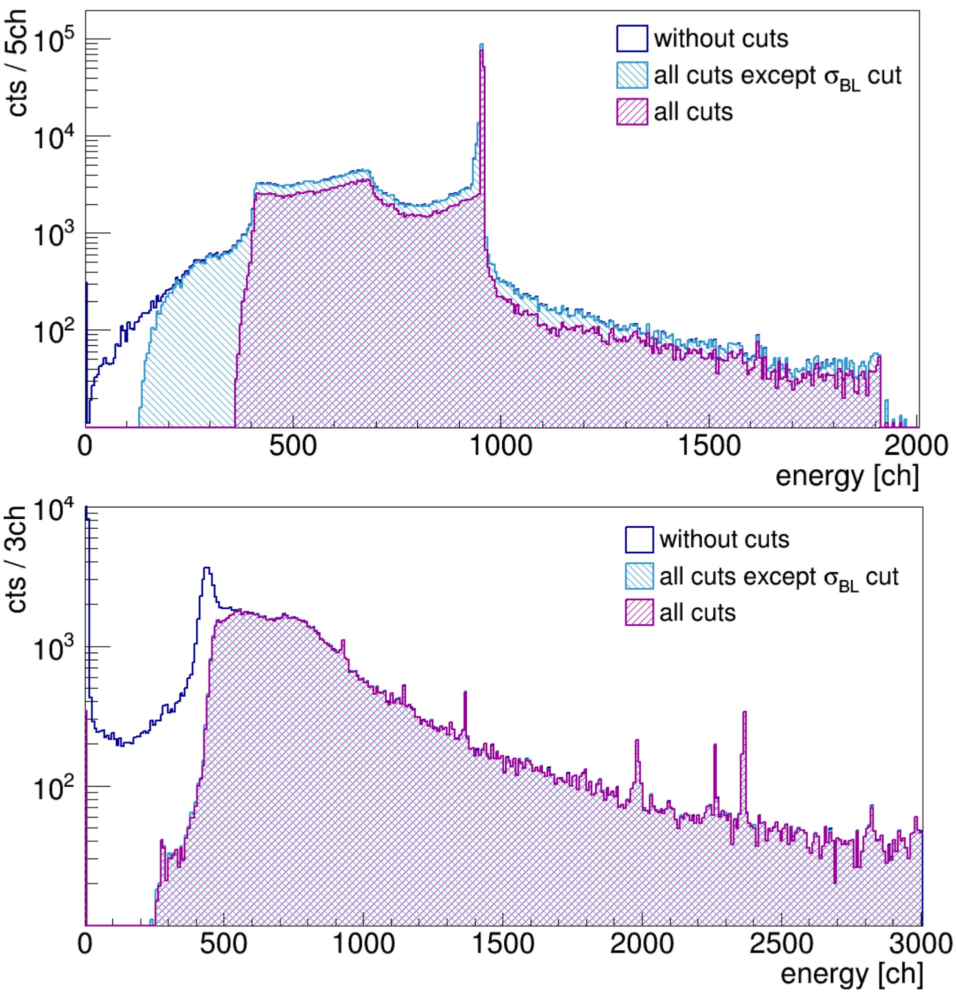

Figure 5.18: Run14 uncalibrated energy spectra of BEGe (top) and Coax1 (bottom). The σ_{BL}-cut restores the resolution of γ-lines in the BEGe spectrum and has little to no effect in the spectrum of Coax1.

5.7 Compton coincidences

In the top Figure 5.19 the calibrated energy of Coax1 E_{Coax1} is plotted versus the calibrated energy of the BEGe E_{BEGe}. The ^{137}Cs γ-line is visible as a vertical line for $E_{\mathrm{BEGe}} \approx 662\,\mathrm{keV}$. The Compton coincidences appear as a diagonal line at $E_{\mathrm{BEGe}} + E_{\mathrm{Coax1}} \approx 662\,\mathrm{keV}$. The two lines mark the sum spectrum which is plotted in the bottom Figure 5.19. To check the goodness of the energy calibration the sum spectrum is fit using a Gaussian fit function for the Compton coincidences and an erfc function to describe the background (see Equation 4.3). The centroid is found at $(662.1 \pm 0.1)\,\mathrm{keV}$ which means the energy calibration is accurate within $\approx 0.5\,\mathrm{keV}$.

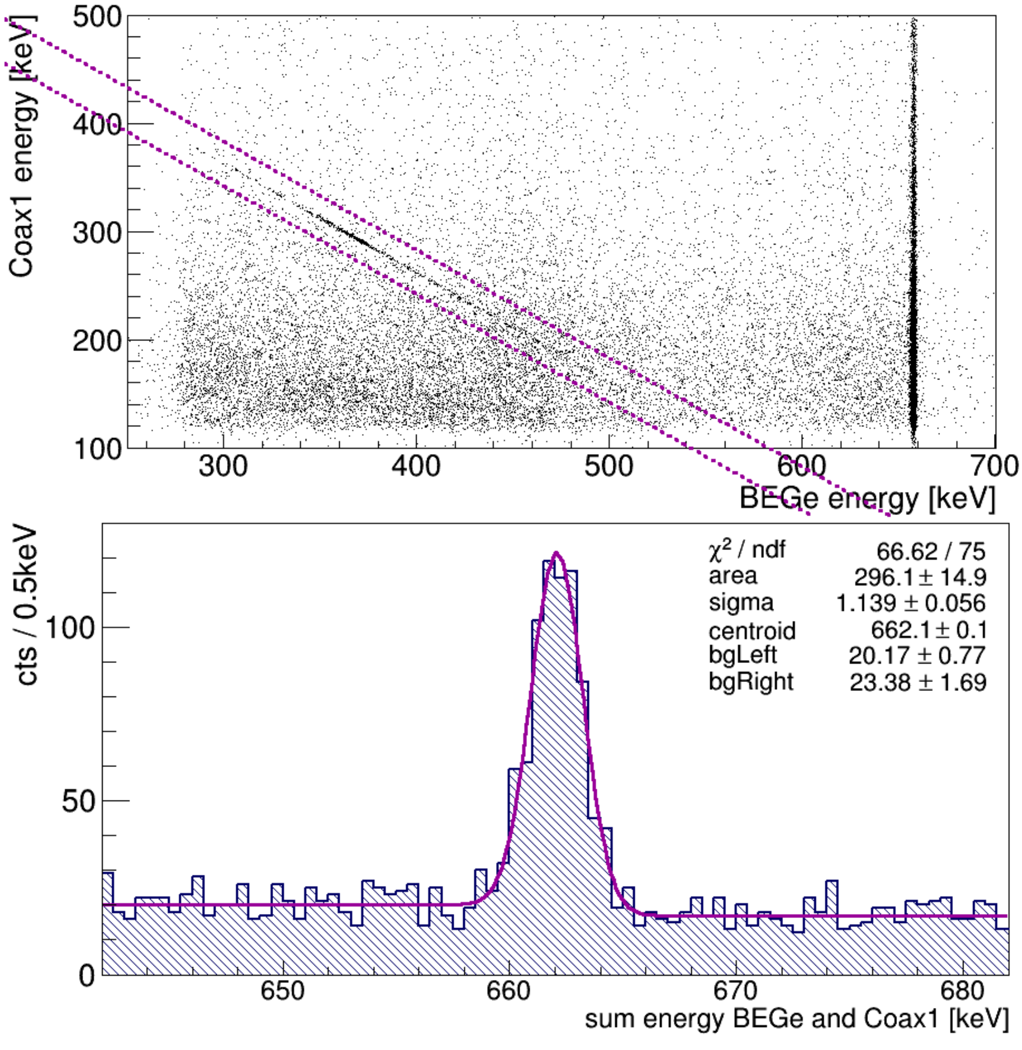

Figure 5.19: Scatter plot (top) and sum energy histogram (bottom) of calibrated BEGe and Coax1 energies, for ^{137}Cs coincidence measurement Run14. All quality cuts are applied. The sum energy of $E_{\mathrm{BEGe}} + E_{\mathrm{Coax1}} \approx 662\,\mathrm{keV}$ is indicated, in the top figure, by two diagonal lines. In the bottom figure, the result of a fit with a Gaussian on an erfc background is shown. The centroid of the Gaussian is shifted by $\approx 0.5\,\mathrm{keV}$ with respect to the expected value of 661.657 keV.

Chapter 6

Compton coincidences: Simulation

A full simulation of the experimental setup has been developed and implemented in the Geant4 [65] based MC simulation framework MaGe [66]. It contains a detailed description of the detector and source geometries, materials and shielding and has been used to optimize the setup and evaluate the expected event rates. Moreover, the energy and spatial distributions of Single Compton Events (singleCE) events with respect to background events have been studied to optimize the analysis cuts.

6.1 Setup implementation

The geometry implemented in MaGe contains all important parts of the setup (schematics in Figure 6.1): the detectors with their encapsulations, the detector and source collimators, the table platform on which the Coax detectors are mounted, the BEGe holder and the source geometry.

As the Coax detectors face the BEGe at a scattering angle of 90° their holders have not been implemented in the setup. Detector contact layer effects have not been taken into consideration, e.g. loss of charge carriers due to recombination in the lithium diffused surface.

Some geometry details can be varied at run time. A short description of the MC options can be found in Appendix E.

6.1.1 ^{137}Cs source implementation

The geometry of the strong ^{137}Cs source used for the coincidence measurements is not point-like. A realistic implementation of the source geometry in MaGe is shown in Figure 6.2. The source itself is embedded in a cylindrical ceramic which measures about 3 mm in height and diameter. It is encapsulated in a stainless-steel container, which is held by a nylon vessel for better handling.

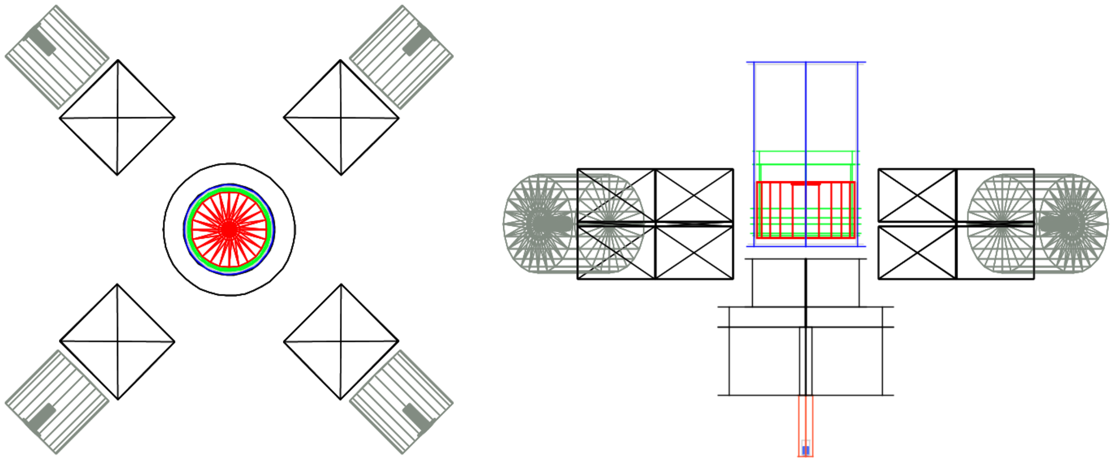

Figure 6.1: MC geometry top view (left) and side view (right). For better visibility, the vacuum cryostats of the Coax detectors and the table platform are not shown. The BEGe aluminum cryostat is displayed in blue, the BEGe detector is drawn in red and its holder in green. The black structures are the lead source and detector collimators and the Coax detectors are shown in gray. Below the source collimator the orange nylon vessel that holds the source is shown. For details of the source implementation see Figure 6.2.

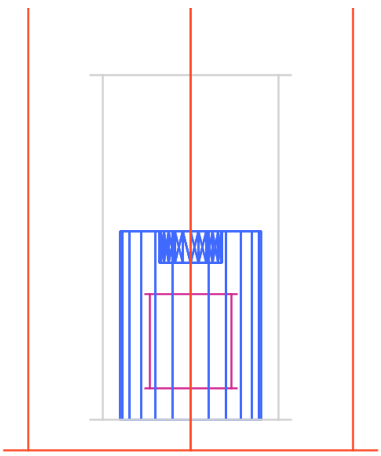

Figure 6.2: Realistic implementation of the strong ^{137}Cs source geometry. From inside out: in magenta the activity 3 mm in height and diameter, a stainless steel sealing in blue and the outer nylon vessel in orange.

6.1.2 Setup optimization

In order to see if important details of the setup are missing in the MaGe representation an uncollimated ^{137}Cs spectrum, taken with a standard point-like source with an activity of about 380 kBq, was compared to simulation.

The spectra can be seen in Figure 6.3; two MC spectra are shown which are normalized to the measurement by adjusting the height of the Compton edge at ≈ 478 keV to the measurement. The MC spectrum shown in red takes the copper holder of the BEGe detector in consideration, the spectrum shown in green does not.

As can be seen, the inclusion of the BEGe copper holder in the simulation changes the shape of the spectrum between 100 keV and 250 keV. The shape of the simulated spectrum including the holder is in much better agreement with the measurement. In the energy region below 70 keV both MC spectra are still not in a very good agreement with the measurement. This energy region is, however, not important in the following: all FADC trigger thresholds are set to ≈ 150 keV.

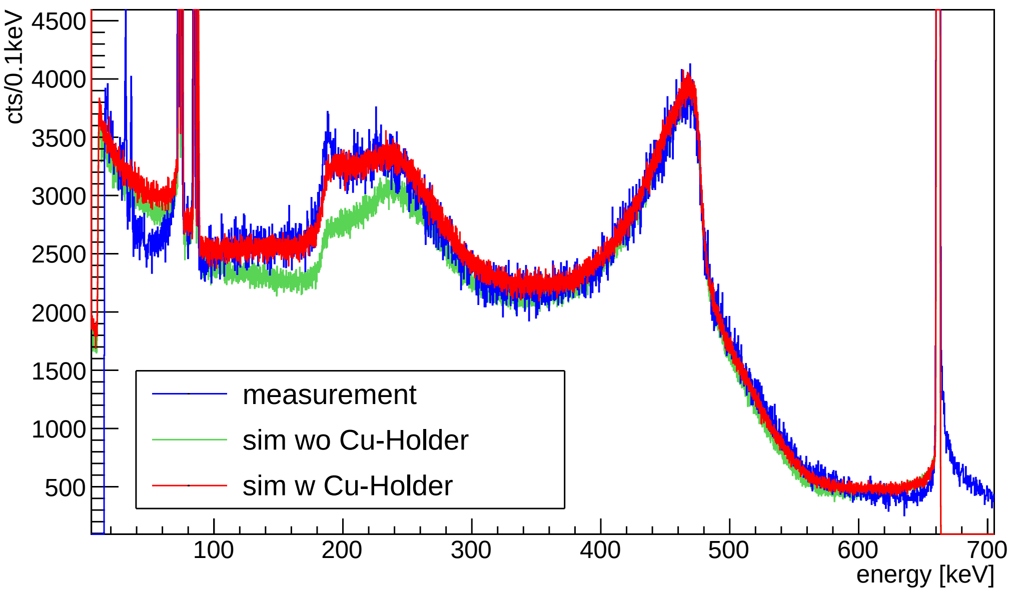

Figure 6.3: BEGe uncollimated ^{137}Cs spectrum. Measurement in blue, MC simulation without the BEGe copper holder in green and with the holder shown in red.

6.2 Energy distribution of single Compton events

The simulation provides a tool to study the energy distribution of singleCE events, considered as *signal events*, and multiple Compton events, which will be labeled *background* in the following. What we define here as signal events, namely singleCE events, is only a part of signal-like events. In reality all events which deposit energy in a volume smaller than the spatial resolution of the BEGe detector are to be considered signal-like, also if energy is deposited through multiple Compton scatterings. This implies that the signal to background ratio in the data will differ from what is estimated here with MC simulations. The signal to background ratio has to be ultimately evaluated for real data.

In this section we will look at a simulation for a detector collimation of 10 mm, restricting the angular acceptance of the Coax detectors, a source collimation of 1.5 mm and a scanning height of 1 cm. The scanning height is measured from the lower edge of the BEGe detector. The collimators are placed as close as possible to the BEGe vacuum cryostat and the observation angle is 90°. Only events releasing energy in the BEGe and at least one of the Coax detectors are saved on disc, equivalent to the external trigger logic.

In Figure 6.4 a scatter plot of the energy released in the BEGe and in one of the Coax detectors is shown. The distribution is split in singleCE events, drawn in red, and background shown in blue. A diagonal line is clearly visible at a sum of energies of 662 keV which corresponds to events in which the full γ energy is released in the two detectors. A band of singleCE events at BEGe energy (373 ± 30) keV can be noticed; it corresponds to events with a scattering angle of $\sim 90°$ with respect to the incident photon beam, where the energy of the scattered photon is not fully contained in the Coax detector.

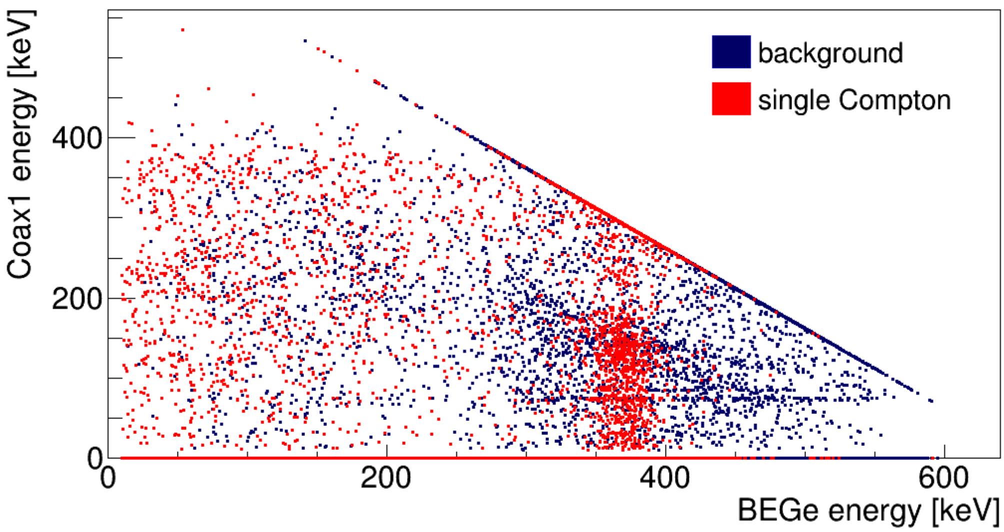

Figure 6.4: BEGe energy versus Coax1 energy from MC simulation. Single Compton (signal) events are shown in red and background events in blue.

The BEGe energy spectrum of all events, regardless of the Coax detector in coincidence, is plotted in Figure 6.5. Both the distribution of singleCE and background are shown; they differ from each other in their shape. In the singleCE spectrum a peak is clearly seen at an energy of 373 keV as expected for a singleCE scattering at an angle of $\sim 90°$. The distribution of background events is much broader.

Calculating the signal to background ratio from the two distributions (see Figure 6.6) an energy cut for the BEGe detector can be defined as

$$352\,\mathrm{keV} < E_{\mathrm{BEGe}} < 388\,\mathrm{keV} \tag{6.1}$$

corresponding to a signal to background ratio above one.

The respective signal and background energy spectra for one Coax detector, without any energy cut applied, can be found in Figure 6.7. As for the BEGe detector the spectral distribution of signal events displays a peak of Gaussian form whereas the distribution of background events is broader. Events with zero energy are events which deposit energy in a different Coax detector.

In the Coax background spectrum at ~ 74 keV a line is observed which coincides with lead x-Ray fluorescence energies. As all collimators are made of lead this is a plausible explanation for its appearance in the spectrum. Also in the BEGe spectrum lead fluorescence lines are observed but their relative strength is much lower.

The same Coax energy spectra but with the BEGe energy cut (Equation 6.1) applied can be seen in Figure 6.8.

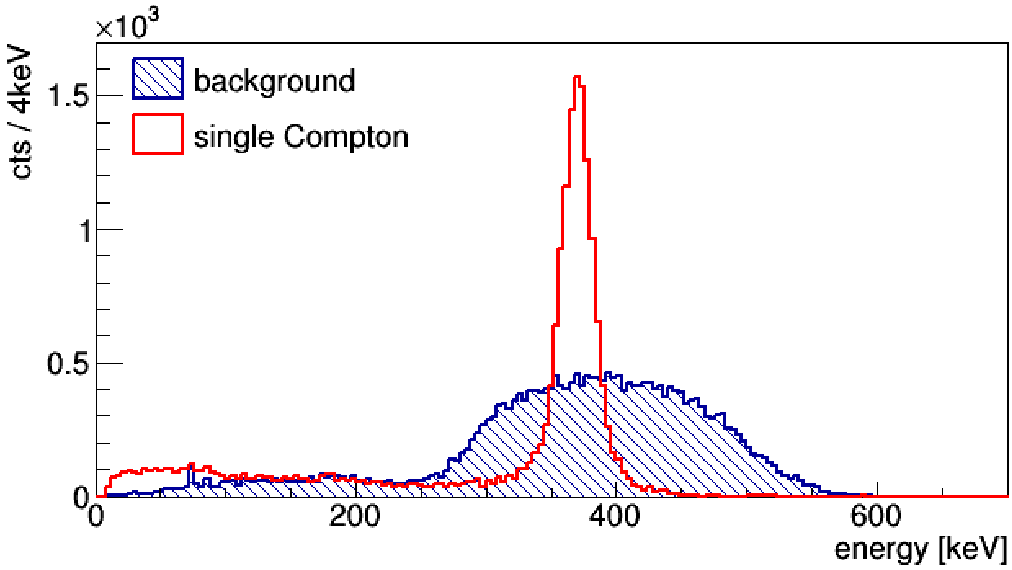

Figure 6.5: BEGe energy spectrum of singleCE events and background; no energy cut is applied.

In the signal distribution we find a peak on a flat background and define an energy cut for the Coax detectors

$$E_{\text{Coax}} > 272\,\text{keV} \tag{6.2}$$

as indicated in Figure 6.8 by a vertical line. We require that *at least one of the Coax detectors* satisfies this condition. This energy cut will be called *Coax energy cut* in the following.

The impact of the Coax energy cut on the BEGe signal to background ratio is presented in Figure 6.9. The ratio improves at all energies selected with the BEGe energy cut.

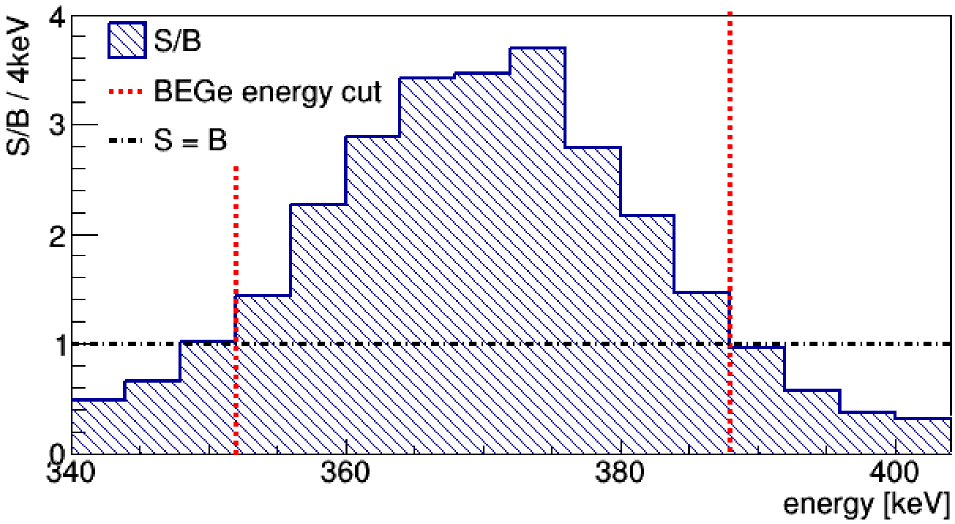

Figure 6.6: BEGe signal to background ratio as a function of energy. The signal and background equality where S/B = 1 is marked with a black horizontal line. This defines the BEGe energy cut, indicated by two red vertical lines.

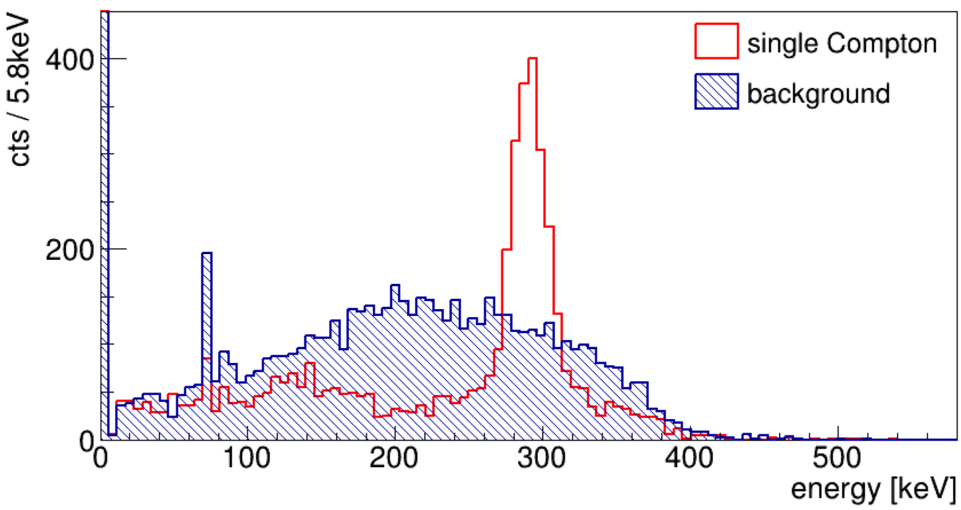

Figure 6.7: Coax energy spectrum for singleCE events and background; no energy cut is applied.

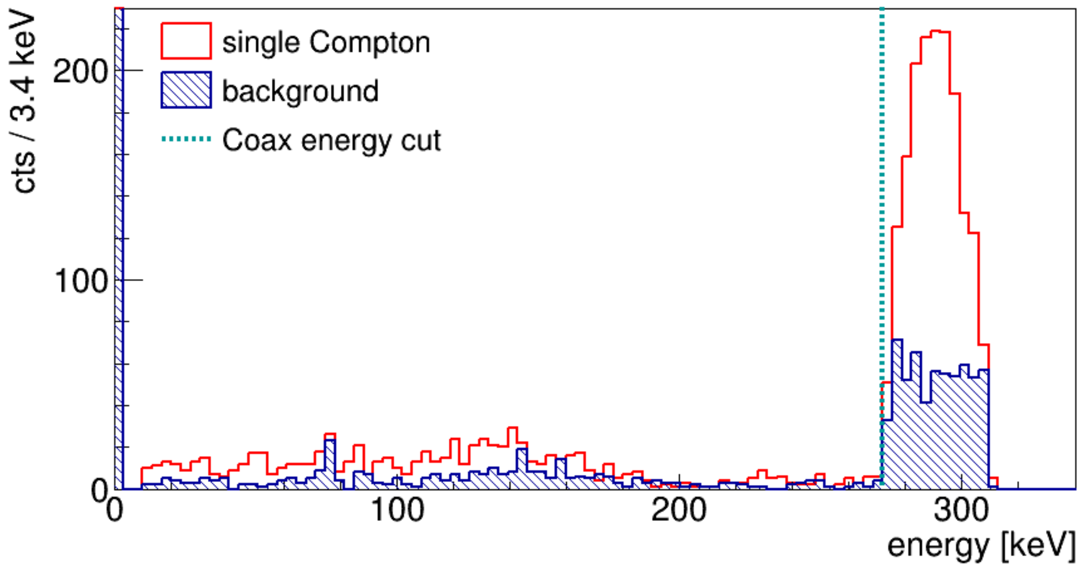

Figure 6.8: Coax energy spectrum for singleCE events and background. The BEGe energy cut is applied. A lower energy cut chosen for the Coax detectors is indicated by a vertical line.

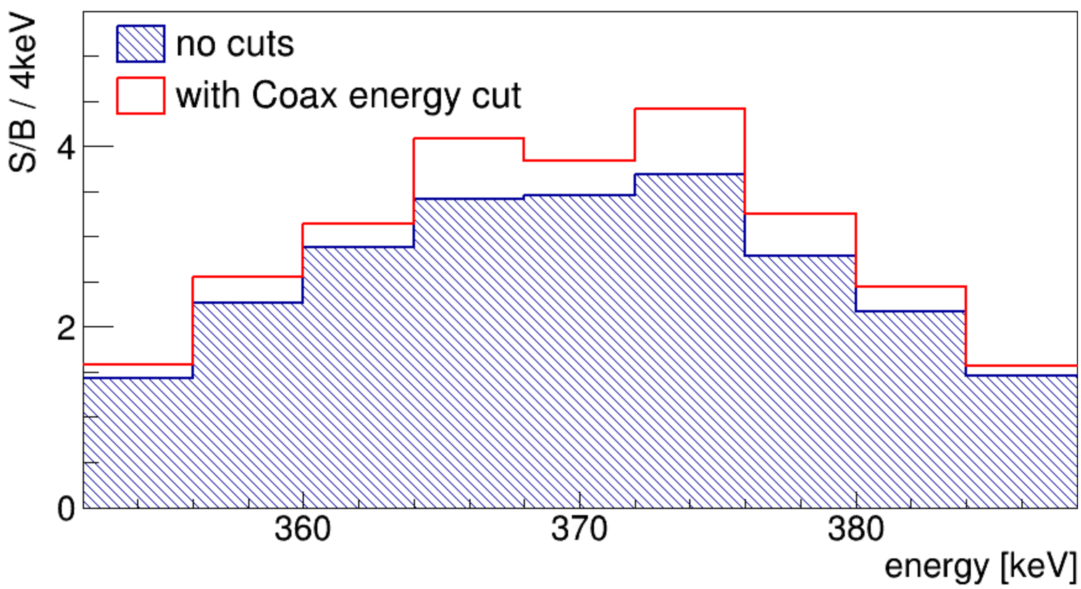

Figure 6.9: BEGe signal to background ratio comparison; in blue without energy cuts and in red with the Coax energy cut applied.

6.3 Interaction region and confinement

In this section we take a close look at the interaction region of signal and background events we have selected with the energy cuts introduced in Section 6.2. In Figure 6.10 the hit distribution of all events, only signal and only background events can be seen respectively; no energy cuts were applied. The position of the BEGe and two Coax detectors is indicated in the uppermost figure. In the following figures the position of the detectors is the same as illustrated here. We observe that only by collimation the signal events are not well confined.

As already outlined the, BEGe energy cut is chosen according to the signal to background ratio as a function of energy. As the first interaction happens in the BEGe detector this is the first energy cut implemented. In Figure 6.11 the hit distributions are shown as before, but with the BEGe energy cut applied. As can be seen, the confinement of all events is much better than before.

We add the Coax energy cut for the coincidence detectors in Figure 6.12. The cut further improves the confinement of all events.

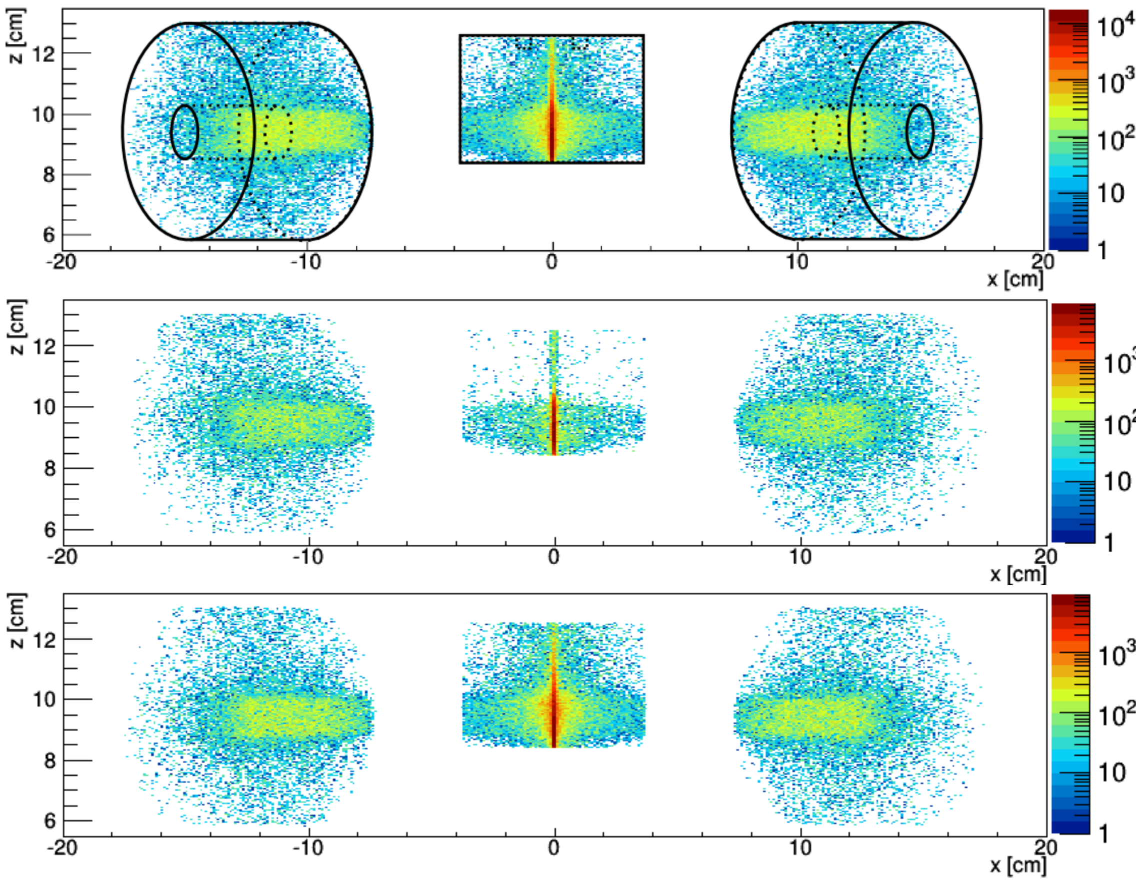

Figure 6.10: Hit distribution side view for *all events* (top), *signal events* (middle) and *background events* (bottom); no energy cuts were applied.

The hit distribution of signal and background in the BEGe detector after all energy cuts can be seen in Figure 6.13, projected on the z-axis, and in Figure 6.14, projected on the x-axis. Each hit has been assigned a weight equal to its energy deposition. The detector and source collimation windows are indicated in red.

In the z-projection, 69% of signal energies are deposited within the 10 mm wide detector collimation window, whereas almost 100% can be found within 20 mm corresponding to twice the collimation window. In x, the energy distribution is a bit more compact. 83% of signal energy is deposited within $x = \pm 0.75$mm which corresponds to the source collimation; 97% can be found within $x = \pm 1.5$mm which corresponds to twice the source collimation diameter. In x-projection as well as in z-projection, the spatial distribution of the background is found to be very similar to the signal distribution.

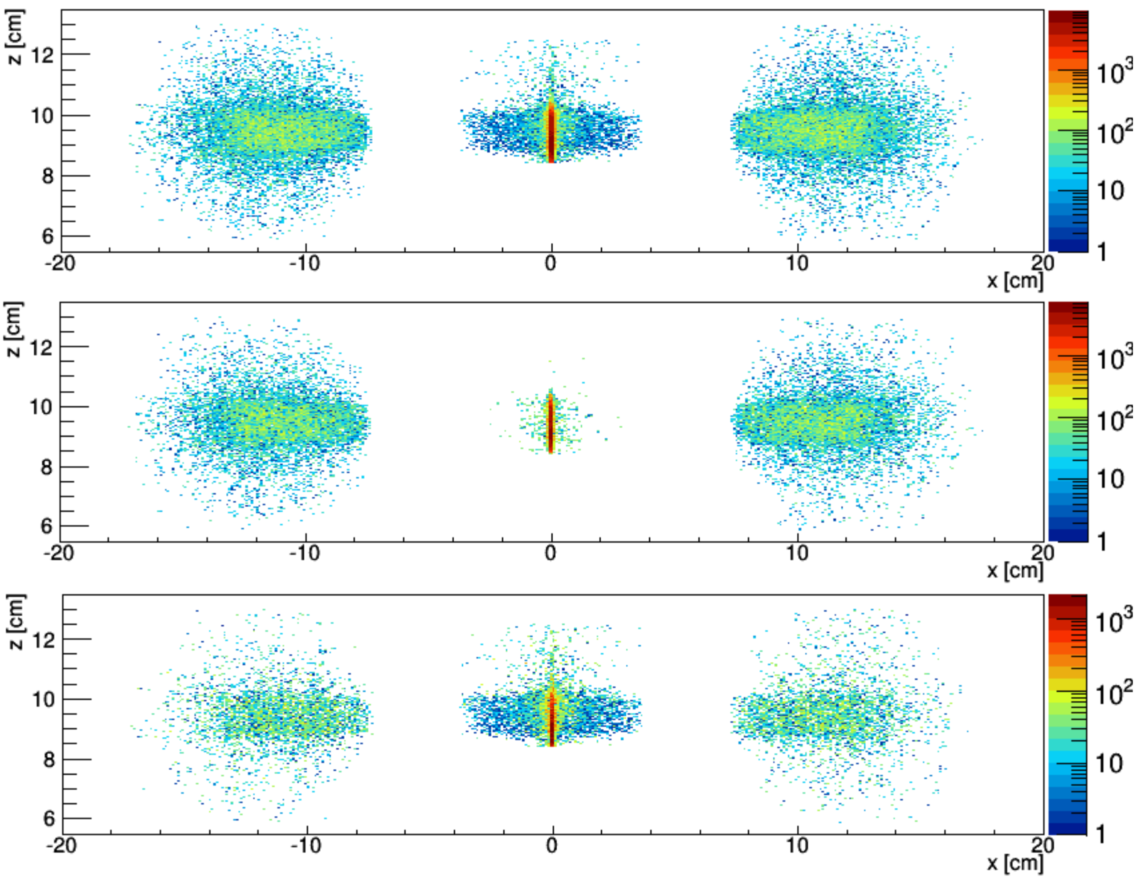

Figure 6.11: Hit distribution side view for *all events* (top), *signal events* (middle) and *background events* (bottom). The BEGe energy cut is applied (see Equation 6.1).

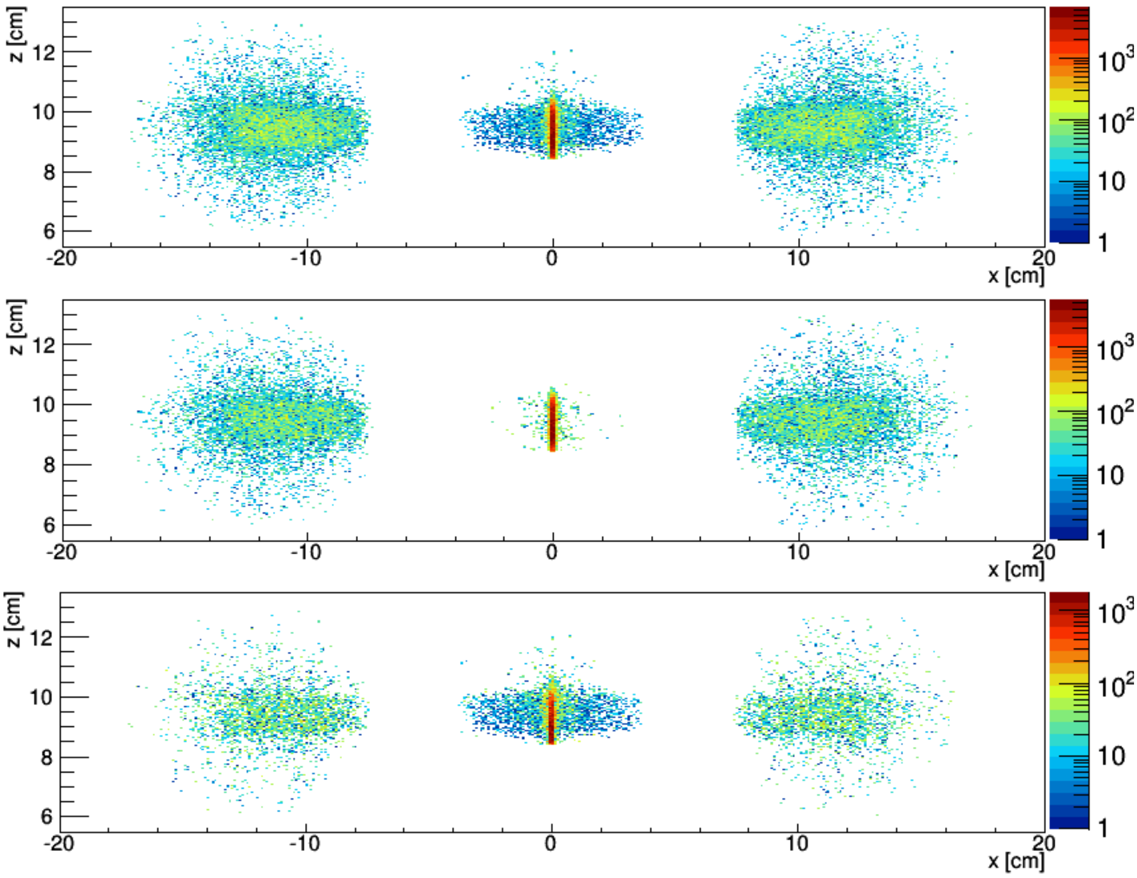

Figure 6.12: Hit distribution side view for *all events* (top), *signal events* (middle) and *background events* (bottom). The BEGe energy cut (Equation 6.1) and the Coax energy cut (Equation 6.2) are applied.

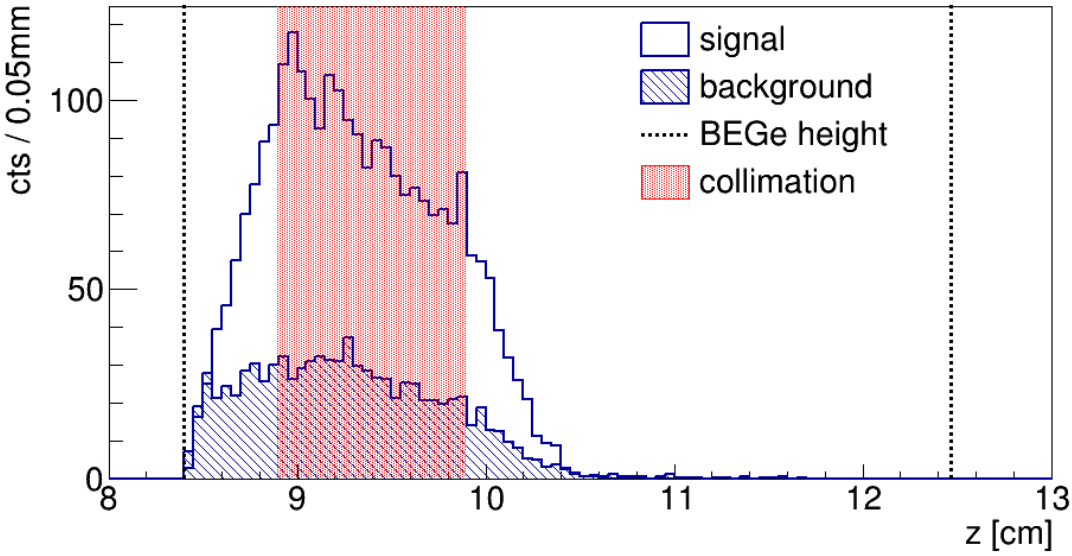

Figure 6.13: Z-projection of signal and background spatial distribution in the BEGe. Each hit has been assigned a weight equal to its energy deposition. The detector collimation window is indicated by a red band and the BEGe z dimension (height) by two vertical lines.

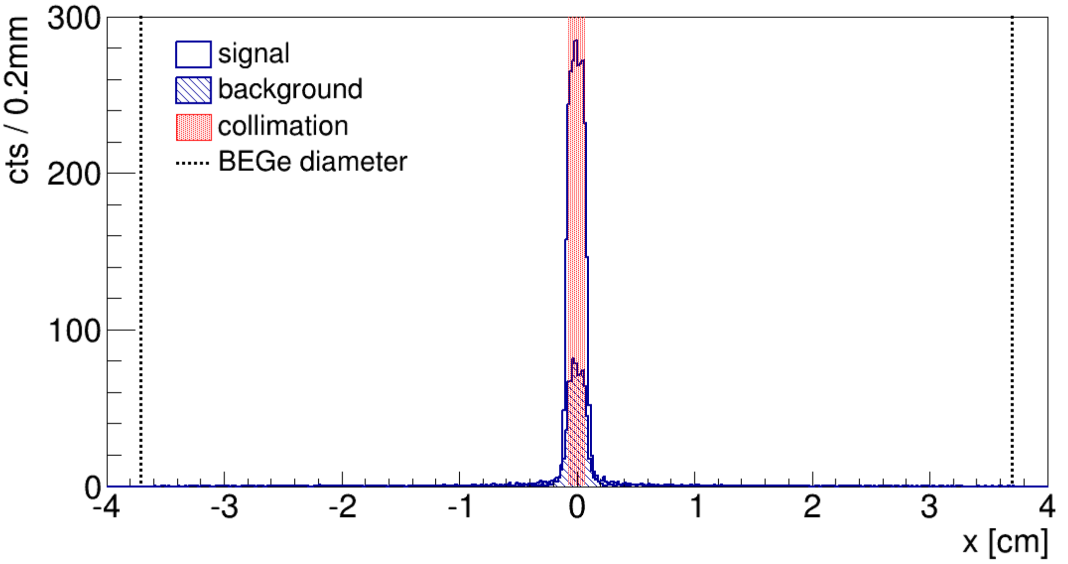

Figure 6.14: X-projection of signal and background spatial distribution in the BEGe. Each hit has been assigned a weight equal to its energy deposition. The source collimation diameter is indicated by a red band and the BEGe x dimension (diameter) by two vertical lines.

6.4 Energy cuts

Summarizing Section 6.2 and Section 6.3, we have defined energy cuts for the BEGe detector and the Coax detectors in order to select signal events from a confined interaction region.

In the MC simulation pile-up events and random coincidences are not considered. Thus, above the sum energy of 662 keV no events are found in the MC spectra. As was shown before (see Figure 5.19), this is different for real data. Therefore, we introduce an additional cut on the BEGe and Coax sum energy for data analysis. The sum energy spectra are fit with a Gaussian fit function modeling the background by an erfc and the cut is defined as

$$662\,\mathrm{keV} - 3\sigma < E_{\mathrm{BEGe}} + E_{\mathrm{Coax}} \equiv E_{\mathrm{Sum}} < 662\,\mathrm{keV} + 3\sigma \tag{6.3}$$

where σ is the standard deviation of the Gaussian. An example of the fit was already shown in Figure 5.19.

Summarizing, all energy cuts we apply are the following

- **BEGe energy cut** $352\,\mathrm{keV} < E_{\mathrm{BEGe}} < 388\,\mathrm{keV}$
- **Coax energy cut** $E_{\mathrm{Coax}} > 272\,\mathrm{keV}$
- **Sum energy cut** $662\,\mathrm{keV} - 3\sigma < E_{\mathrm{Sum}} < 662\,\mathrm{keV} + 3\sigma$

Figure 6.15 shows a scatter plot of the BEGe and Coax1 energies for Run14; energy cuts are indicated in red.

Applying all energy cuts to simulation, we expect a reduction in the BEGe energy spectrum as is shown in Figure 6.16. The demonstrated energy spectra were obtained applying all energy cuts to the usual simulation with detector collimation of 10 mm, source collimation of 1.5 mm etc..

6.5 Comparing Monte Carlo simulations with measurements

To be able to compare MC simulations with measurements some general considerations have to be made. The MC simulations do not contain pile-up or random coincidences, and in order to save simulation time we do not simulate the full solid angle of incident photons from the ^{137}Cs source. In the next subsections we explain how the number of expected events is calculated from MC simulation.

6.5.1 Solid angle calculation

In order to save simulation time, only a part of the solid angle of incident photons from the ^{137}Cs source is simulated. The respective solid angle fraction can be

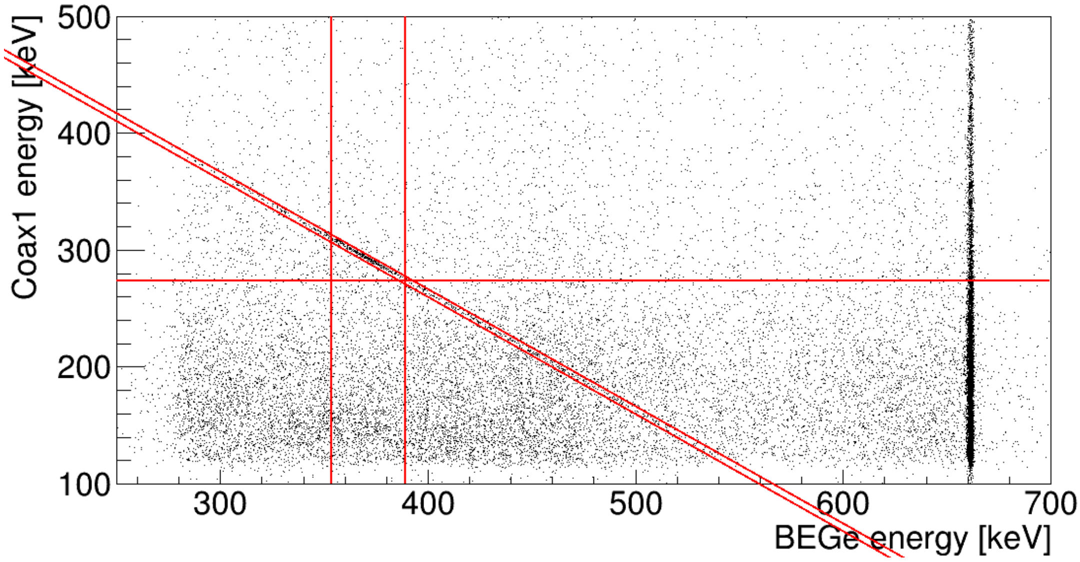

Figure 6.15: Scatter plot of the BEGe and Coax1 energy for Run14; all standard quality cuts are applied. The BEGe energy cut is indicated by two vertical lines, the Coax energy cut by one horizontal line and the sum energy cut by two diagonal lines.

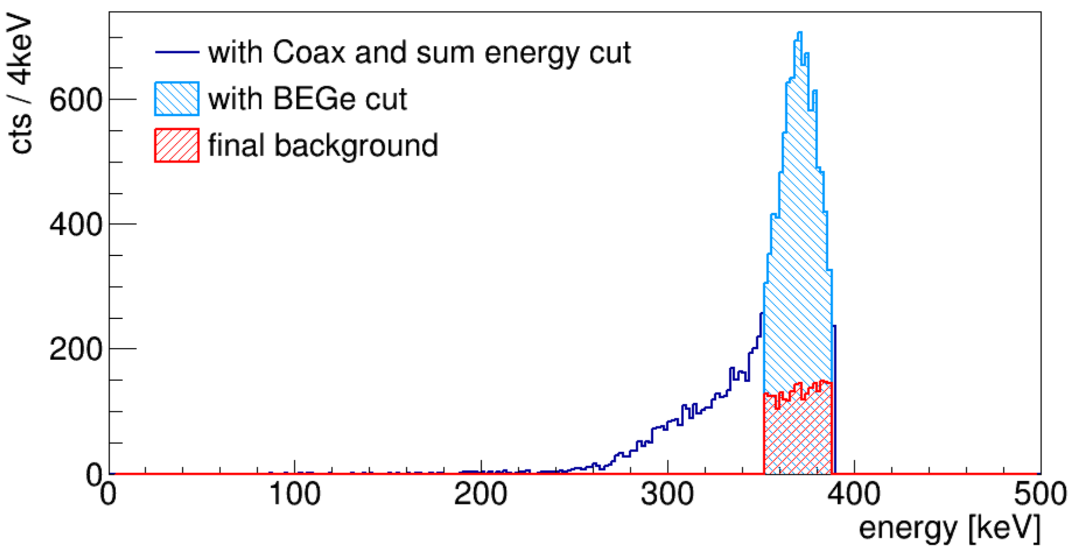

Figure 6.16: BEGe simulated energy spectrum; after Coax and sum energy cuts in dark blue and with the BEGe energy cut applied in light blue. The expected background contribution is indicated in red.

calculated, dividing the surface of the corresponding spherical sector

$$S_{\mathrm{C}} = 2\pi r^2(1 - \cos\alpha) \tag{6.4}$$

by the surface of the whole sphere

$$S_{\mathrm{S}} = 4\pi r^2 \tag{6.5}$$

In this manner the solid angle fraction

$$\Omega_{\mathrm{f}}(\alpha) = \frac{S_{\mathrm{C}}}{S_{\mathrm{S}}} = \frac{1 - \cos\alpha}{2} \tag{6.6}$$

is obtained. The opening angle α is measured from the vertical position as is shown in Figure 6.17.

We find $\Omega_{\mathrm{f}}(5^\circ) \approx 1.9 \cdot 10^{-3}$ and $\Omega_{\mathrm{f}}(1^\circ) \approx 7.6 \cdot 10^{-5}$.

6.5.2 Rate calculation

The expected singleCE rate depends upon the scanning position and collimation. For a specific configuration it can be calculated from MC simulation as follows:

$$R = \frac{N_{\mathrm{coinc}} \cdot \Omega_{\mathrm{f}} \cdot R_{\mathrm{b}}}{R_{\mathrm{sim}}} \tag{6.7}$$

with the solid angle fraction Ω_{f}, the branching ratio $R_{\mathrm{b}} = 0.8499 \pm 0.0020$ [67] of the 662 keV γ-line and the observed number of events, N_{coinc}. The simulated rate $R_{\mathrm{sim}} \cong A_{\mathrm{sim}} \cdot \Delta t_{\mathrm{sim}}$ corresponds to a combination of source activity A_{sim} and measurement time Δt_{sim} and has the unit [Bq s].

For the simulation discussed before — with a source collimation of 1.5 mm, a detector collimation of 10 mm, an observation angle of 90° and a scanning height of 1 cm — we expect an event rate of

$$R = \frac{9411\,\mathrm{cts} \cdot 1.9 \cdot 10^{-3} \cdot 0.85}{10^{10}\,\mathrm{Bq\,s}} \approx (5.26 \pm 0.05)\,\frac{\mathrm{cts}}{\mathrm{MBq\,day}}$$

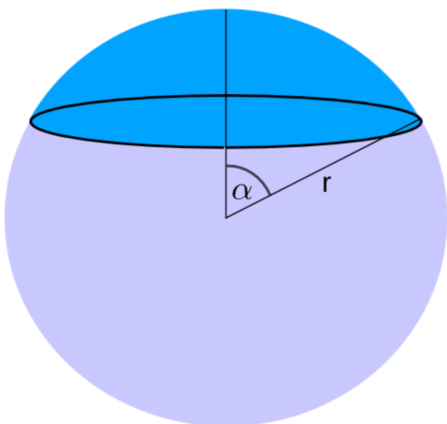

Figure 6.17: Opening angle in solid angle fraction calculation.

using four coincident detectors and a simulation opening angle of 5°. The expected signal to background ratio is $S/B = 7052/2359 \approx 3.0 \pm 0.1$. See also Figure 6.16 for the expected background contribution.

6.5.3 Expected number of events

The number of expected coincidences N_{exp} is given by

$$N_{\mathrm{exp}} = R \cdot A \cdot T_{\mathrm{R}} \cdot f_{\mathrm{D}} \cdot \frac{N_{\mathrm{D}}}{4} \tag{6.8}$$

where R is the expected rate calculated using Equation 6.7, A is the source activity, T_{R} is the real time of the measurement and N_{D} is the number of Coax detectors in coincidence. f_{D} denotes the fraction of data which is discarded by quality cuts and is not accounted for in the simulation.

It shall be noted here that the cumulative fraction $f_{\mathrm{D}} \cdot N_{\mathrm{D}}/4$ only holds if the source position is central; for all detectors the fraction of events discarded by the quality cuts is different. In the case of a non central source position the expected number of events should be calculated using

$$N_{\mathrm{exp}} = A \cdot T_{\mathrm{R}} \cdot \sum_{i=1}^{N_{\mathrm{D}}} R_i f_{\mathrm{D},i}, \tag{6.9}$$

where $R_i = N_{\mathrm{coinc},i} \cdot \Omega_f \cdot R_b / N_{\mathrm{sim}}$ and $f_{\mathrm{D},i}$ is the part of events, $N_{\mathrm{coinc},i}$, in coincidence with detector i and discarded by the quality cuts listed above.

In general, $f_{\mathrm{D},i}$ is difficult to obtain and is not constant in energy. Therefore, we take $f_{\mathrm{D},i} = 1$ in the following and keep in mind that the obtained expected number of events N_{exp} is only qualitative. The important information obtained from simulation is the energy and spatial distribution of events.

A comparison of the measured and expected rate, R, and number of coincidences, N_{exp}, for all central measurements of the data taking campaign presented in Section 5.5 can be found in the next chapter in Table 7.1. In the next Section 6.5.4 a comparison of simulation and measurement is demonstrated, using data of Run14.

6.5.4 Exemplary comparison of measurement and simulation

For each measurement of the data taking campaign a proper MC simulation was run. Combining Equation 6.7 and Equation 6.8 a normalization factor can be calculated in order to scale the MC spectra to match respective measured ones

$$\frac{N_{\mathrm{exp}}}{N_{\mathrm{coinc}}} = \frac{\Omega_f \cdot R_b}{R_{\mathrm{sim}}} \cdot A \cdot T_{\mathrm{R}} \cdot \frac{N_D}{4} \tag{6.10}$$

For Run14 a simulation with an opening angle $\alpha = 1°$ and $R_{\mathrm{sim}} = 10^{10}\,\mathrm{Bq\,s}$ — primary γ particles with an energy of 662 keV — was performed. The measurement real time of Run14 is $T_R = 73833\,\mathrm{s} \approx 20.5\,\mathrm{h}$ and the source activity is $A \approx 780\,\mathrm{MBq}$. A normalization factor of $N_{\mathrm{exp}}/N_{\mathrm{coinc}} \approx 0.28$ for three Coax detectors in coincidence is calculated.

The energy spectrum of the BEGe, after all quality cuts, and the respective spectrum, extracted from the normalized MC simulation, are shown in Figure 6.18. A peak is observed which is due to singleCE.

The measured peak is a little broadened and between 420 keV and 520 keV the measured background is slightly elevated with respect to the simulation. Considering that the energy resolution is not included in the MC, the simulation provides a good description of the measurement. The BEGe energy cuts could be slightly loosened to take the finite energy resolution into account. In the following, however, all energy cuts are kept as defined in Section 6.4. Thus, a small part of singleCE events is most probably lost.

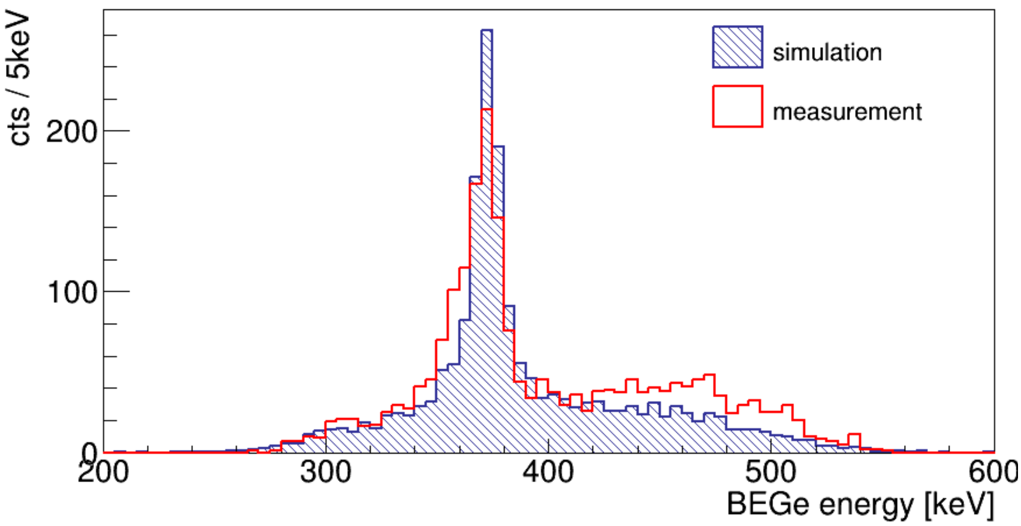

Figure 6.18: Measured and simulated BEGe energy spectra in the Run14 configuration. All quality cuts are applied to the measurement and the MC spectrum is normalized using Equation 6.10. All events with a sum energy of $662 \pm 20\,\mathrm{keV}$ are plotted.

Chapter 7

Compton coincidences: Analysis

The data taking is described in Section 5.5. Measurements were taken with different detector collimation windows, at different scanning heights, with different source positions and with different HV applied on the BEGe detector. In the following chapter the analysis flow of these measurements is briefly described. Important parameters, which describe the shape of pulses, are introduced and for each measurement an average pulse is constructed and compared. Finally, a comparison to another method of collecting SSE samples, using uncollimated ^{228}Th measurements, is made.

7.1 Analysis flow

The aim is to purify the data collected in the measurement campaign as much as possible to obtain clean SSE event samples from localized regions inside the BEGe detector. The following procedure is applied for all runs separately

- The standard quality cuts are applied; see Section 5.6.
- The energy calibration is carried out; as was explained in Section 4.5.
- If possible, energy cuts are applied. In some measurements there are not enough coincidence events to define an energy cut on the sum energy of the BEGe and Coax detectors. In Run3 and Run7 to Run11, no peak in the sum energies is observed. These measurements are not further processed and excluded in the following.
- An A/E cut is applied, which is introduced in the next Section 7.2.
- An average pulse is built from the final event sample of BEGe traces. This procedure will be explained in Section 7.5.

Figure 7.1 shows the remaining runs of the measurement campaign after having excluded Run3 and Run7 to Run11.

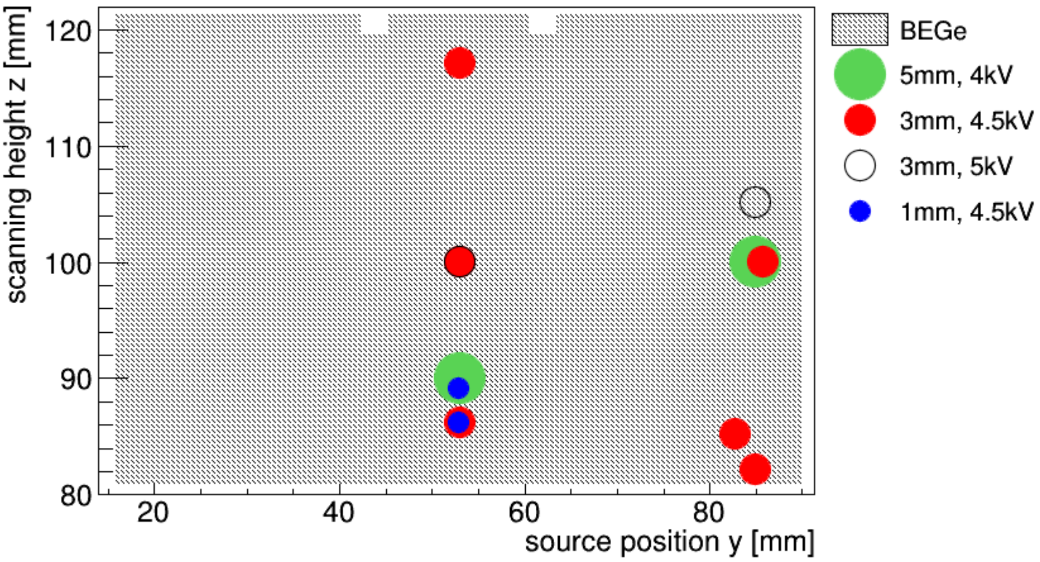

Figure 7.1: Remaining runs of the measurement campaign after measurements with too little statistics, Run3 and Run7 to Run11, were discarded.

Table 7.1: Summary table of data reduction by quality and energy cuts. The run index is given in the same color as in Figure 7.1 and [$\boldsymbol{y}$,$\boldsymbol{z}$] are the source position and table height in [mm,mm]. For each run the total number of events collected N_{tot}, the fraction of events discarded by the quality cuts f_{Q} and events surviving the energy cut N_{EC} are listed. The expected rate R and expected number of events, N_{exp}, for central scanning positions are calculated from simulations (see Section 6.5.2f).

Run	[$\boldsymbol{y}$,$\boldsymbol{z}$]	N_{tot}	f_{Q}	N_{EC}	R [cts/(MBq d)]	N_{exp}
1^a	[53,90]	135751	0.42	767	5.03 ± 0.05	734 ± 8
1^b	[53,90]	202978	0.43	1205	5.03 ± 0.05	1099 ± 12
2^a	[85,100]	222000	0.44	5013		
2^b	[85,100]	40370	0.45	381		
2^c	[85,100]	294039	0.46	2575		
4	[53,100]	500000	0.22	508	1.41 ± 0.03	451 ± 9
5	[53,100]	500000	0.20	611	1.41 ± 0.03	477 ± 10
6	[85,105]	500000	0.22	1340		
12	[53,89]	500000	0.28	156	0.19 ± 0.01	98 ± 5
13	[53,86]	500000	0.28	130	0.21 ± 0.01	108 ± 6
14	[53,86]	495033	0.26	889	1.84 ± 0.03	921 ± 16
15	[53,117]	500000	0.32	246	1.02 ± 0.02	531 ± 12
16	[86,100]	453801	0.25	1803		
17	[85,82]	500000	0.24	1934		
18	[83,85]	500000	0.26	2697		

A summary of the data reduction by quality and energy cuts is given in Table 7.1. Furthermore, the expected event rate and expected number of singleCE events from simulation for central source positions are listed. The MC simulation predicts a number of events N_{exp} which is on the same order of magnitude as the measured numbers. However, in some cases a difference in expected and measured number of events larger than 50% is observed; e.g. for Run15 and Run12. This can have various reasons: The BEGe geometry was implemented without the slight cone shape and loss of events due to surface layer effects has been neglected in the MC simulations. The MC spectra do not include effects of broadening due to the finite energy resolution of the detectors. Event loss due to noisy data and corrections for offsets in the energy calibration were not considered.

7.2 Improvement of single site event selection with A/E - cut

The event samples selected by quality and energy cuts can be purified further. To discard remaining Multiple Compton Events (multiCE) and improve the selection of SSE events we define an additional cut on the A/E parameter which is defined as

- A/E parameter: The amplitude of the current pulse divided by the energy of an event. Spatially well separated hits are seen as separated peaks of current pulses whereas the energy is reconstructed for the whole event. Hence, for a multiple site event (MSE) the amplitude of the current pulse is lower than for a single site event (SSE) at the same energy. A/E is expected to be constant for SSE events in particular as we select a narrow window in energy. Hence, we expect a well defined peak in the A/E distribution for SSE events.

The A/E distribution of each run, after having applied quality and energy cuts, is fitted using the Gaussian plus erfc fit function (Equation 4.3). The fitted distribution of Run14 can be seen in Figure 7.2. The cut is defined as

$$\mu - 3\sigma < A/E < \mu + 3\sigma \tag{7.1}$$

Only events inside the central peak region are kept.

7.2.1 Single site event to background ratio

The side bands in Figure 7.2 are marked in gray. We can estimate the number of SSE events N_{SSE} in the sample by subtracting the background (BKG) estimated from these side bands

$$N_{\mathrm{BKG}} = \frac{1}{2} \cdot \left(\sum_{i=\mathrm{bin}(\mu-6\sigma)}^{\mathrm{bin}(\mu-3\sigma)} b_i + \sum_{j=\mathrm{bin}(\mu+3\sigma)}^{\mathrm{bin}(\mu+6\sigma)} b_j \right) \tag{7.2}$$

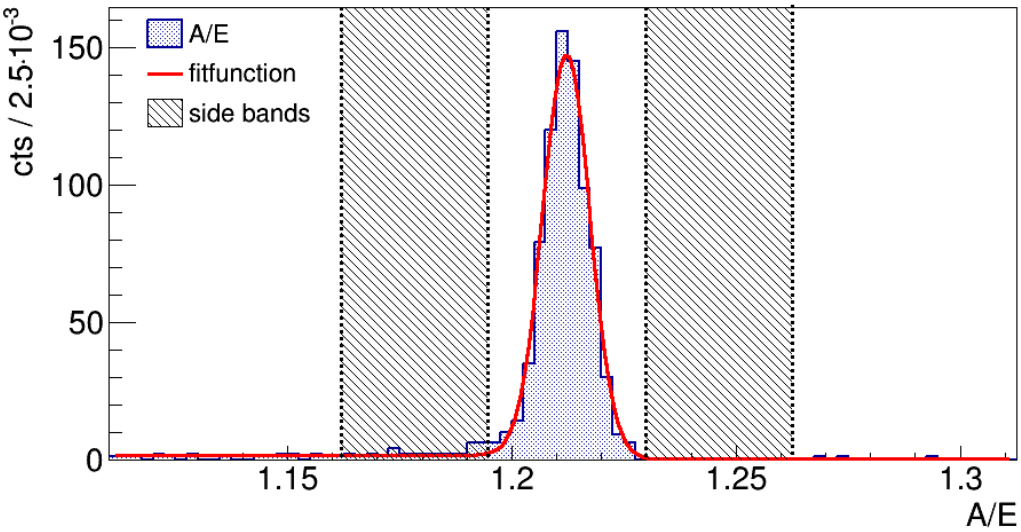

Figure 7.2: Fit of A/E distribution after quality and energy cuts. The marked regions are the side bands we use to estimate the number of background events in the central SSE region.

Table 7.2: Summary table of SSE and BKG content after the A/E-cut is applied. The scanning height H_S is given with respect to the BEGe top surface at $z = 81$ mm. For each run "pos" indicates: c for central, and b for source positions close to the BEGe border. For all measurements the SSE to BKG ratio improves with the cuts: $R^{a}_{SSE} > R^{b}_{SSE}$.

			after cuts			before cuts
Run	H_S [mm]	pos	N_{SSE}	N_{BKG}	R^{a}_{SSE}	R^{b}_{SSE}
1^a	9	c	498	32	15.6 ± 3.0	2.10 ± 0.04
1^b	9	c	785	48	16.4 ± 2.6	1.97 ± 0.03
2^a	19	b	4465	78	57.2 ± 6.7	2.65 ± 0.03
2^b	19	b	349.5	4.5	77.7 ± 37.3	2.95 ± 0.08
2^c	19	b	2284.5	46.5	49.1 ± 7.4	2.45 ± 0.03
4	19	c	316	30	10.5 ± 2.2	3.52 ± 0.03
5	19	c	405.5	33.5	12.1 ± 2.3	3.10 ± 0.03
6	24	b	1146	27	42.4 ± 8.5	5.22 ± 0.04
12	8	c	94	5	18.8 ± 9.1	3.12 ± 0.03
13	5	c	102.5	2.5	41.0 ± 26.9	3.14 ± 0.03
14	5	c	766	20	38.3 ± 8.9	3.16 ± 0.03
15	36	c	52	10	5.2 ± 2.1	3.09 ± 0.03
16	19	b	1590	33	48.2 ± 8.6	4.31 ± 0.03
17	1	b	1821	15	121.4 ± 31.7	4.19 ± 0.03
18	4	b	2513.5	33.5	75.0 ± 13.2	3.88 ± 0.03

from the counts inside the peak region

$$N_{\mathrm{SSE}} = \sum_{i\,=\,\mathrm{bin}(\mu-3\sigma)}^{\mathrm{bin}(\mu+3\sigma)} b_i - N_{\mathrm{BKG}} \tag{7.3}$$

with the bin number $\mathrm{bin}(x)$ at energy x and the bin content $b_{i/j}$ of bin i/j.

The SSE to BKG ratio

$$R_{\mathrm{SSE}} = \frac{N_{\mathrm{SSE}}}{N_{\mathrm{BKG}}} \pm \frac{(N_{\mathrm{SSE}} + N_{\mathrm{BKG}})}{N_{\mathrm{BKG}}} \sqrt{\frac{1}{(N_{\mathrm{SSE}} + N_{\mathrm{BKG}})} + \frac{1}{N_{\mathrm{BKG}}}} \tag{7.4}$$

gives an estimate of the purity of SSE event samples ultimately selected by all data cuts including the A/E - cut.

A summary of R_{SSE} estimated before, $R^{\mathrm{b}}_{\mathrm{SSE}}$, and after cuts, $R^{\mathrm{a}}_{\mathrm{SSE}}$, for all remaining runs can be found in Table 7.2. The same side band regions were used for background estimation before as well as after cuts. For all runs we find $R^{\mathrm{a}}_{\mathrm{SSE}} > R^{\mathrm{b}}_{\mathrm{SSE}}$ which means the applied cuts improve the purity of all event samples.

7.2.2 Systematic behavior

The ratio $R^{\mathrm{a}}_{\mathrm{SSE}}$ after cuts is plotted in Figure 7.3 for two sets of measurements taken with 3 mm detector collimation. Runs with a central source position $Set_1 = \{4, 5, 14, 15\}$ are shown in red whereas measurements close to the BEGe border $Set_2 = \{6, 16, 17, 18\}$ are shown in blue. $R^{\mathrm{a}}_{\mathrm{SSE}}$ decreases exponentially with increase of scanning height for both data sets. $R^{\mathrm{a}}_{\mathrm{SSE}}$ is systematically lower for central source positions from Set_1 than for those close to the BEGe border in Set_2.

We find the same behavior in the simulations comparing the ratio of singleCE events to multiCE events (see Figure 7.4).

Both the decrease of $R^{\mathrm{a}}_{\mathrm{SSE}}$ with the increase of the scanning height as well as the lower $R^{\mathrm{a}}_{\mathrm{SSE}}$ for central source positions with respect to positions close to the border of the BEGe can be explained by the behavior of singleCE with respect to multiCE. With increasing scanning height more singleCE are attenuated whereas the number of multiCE stays the same as can be seen in Figure 7.5. The figure shows the z-projection of the energy deposited inside the BEGe detector. Both the distribution of singleCE and multiCE are shown for the three MC simulations corresponding to experimental settings of Run6, Run16 and Run18. Supposing that each event deposits roughly the same amount of energy in the BEGe — which is ensured by the applied energy cuts — the energy deposition is directly proportional to the number of events. In the same manner a decrease of singleCE can be observed for central source positions whereas the number of multiCE events remains stable (see Figure 7.6).

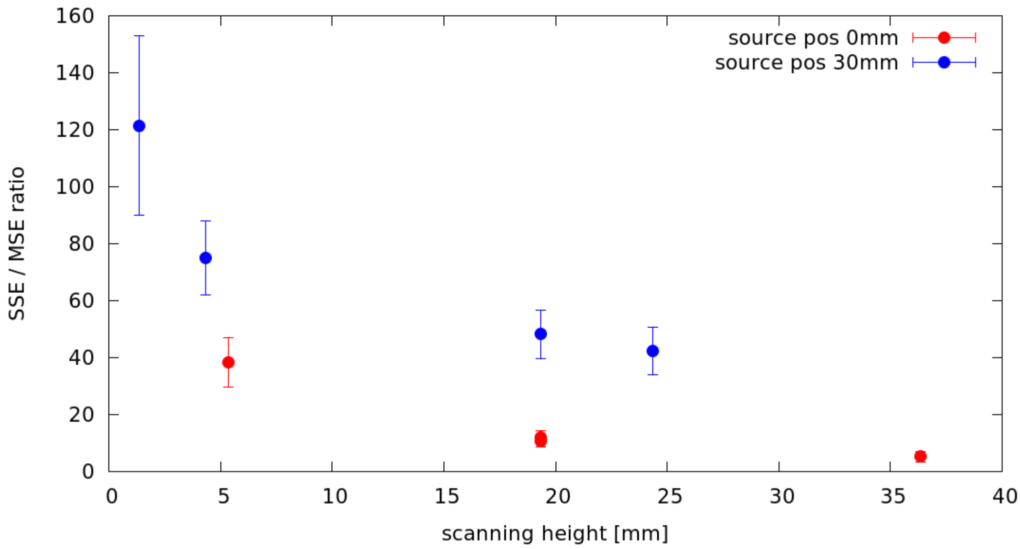

Figure 7.3: R^{a}_{SSE} for runs with a detector collimation of 3 mm in two samples as a function of the scanning height, measured from the BEGe top at z = 81 mm. The red points show runs with a central source position (Run4, 5, 14, 15), whereas blue points show runs with a source position close to the BEGe border (Run6, 16, 17, 18).

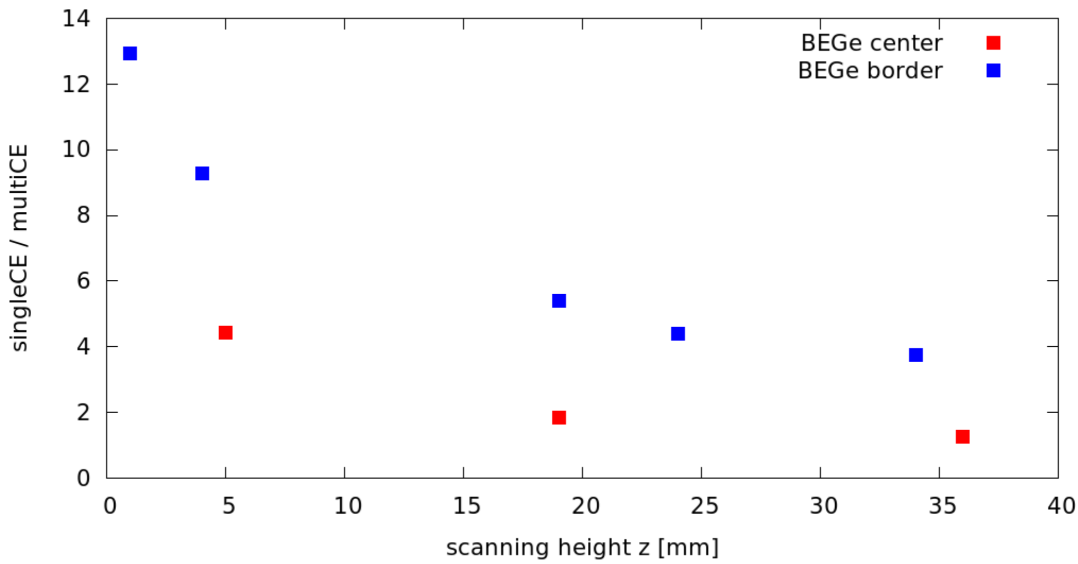

Figure 7.4: SingleCE to multiCE ratio from MC simulation as a function of the scanning height measured from the BEGe top at z = 81 mm. Central source positions are shown in red and source positions close to the BEGe border are drawn in blue.

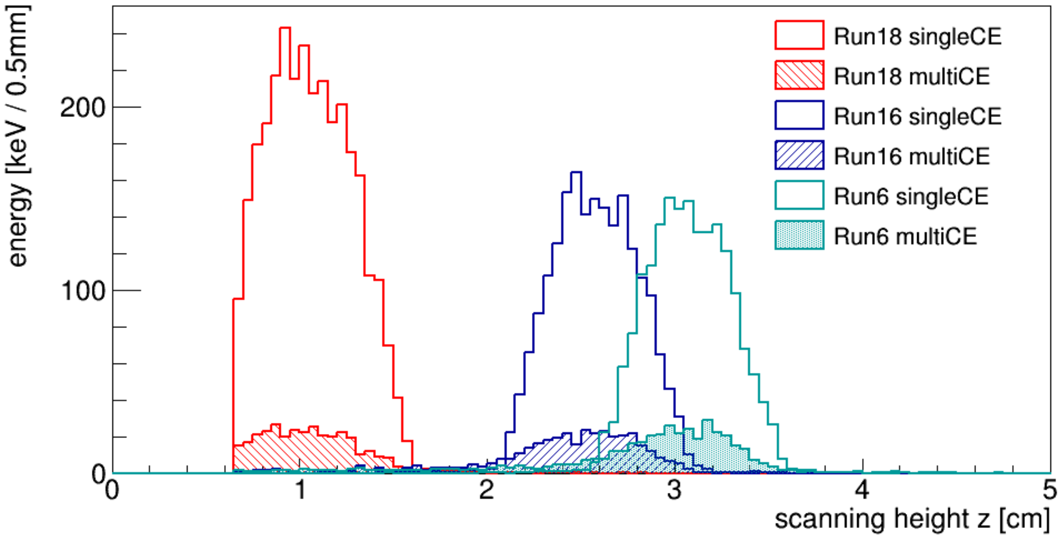

Figure 7.5: Z-projection of the energy deposited inside the BEGe detector. Distributions of singleCE and multiCE are shown for the three MC simulations corresponding to experimental settings of Run6, Run16 and Run18.

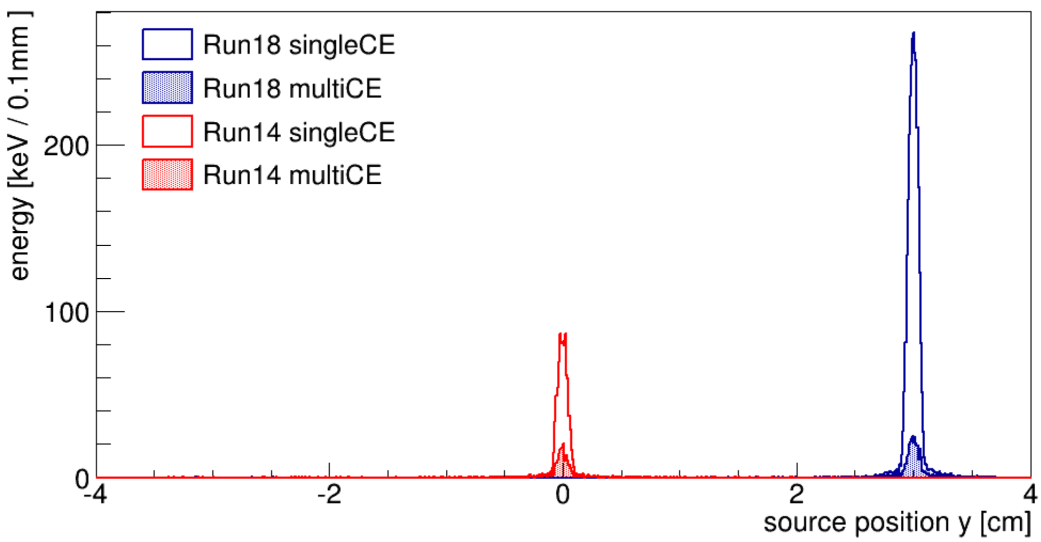

Figure 7.6: X-projection of the energy deposition inside the BEGe detector of singleCE and multiCE for two MC simulations which correspond to the experimental settings of Run14 and Run18.

The exponential drop of the SSE to BKG ratio $R^{\mathrm{a}}_{\mathrm{SSE}}$ implies an upper limit on the scanning height for any scanned HPGe detector depending on the desired SSE to BKG ratio. This limit depends also on the detector diameter.

The SSE to BKG ratio from measurement is about ten times higher than the singleCE to multiCE ratio calculated from simulation. This ratio depends strongly on the spatial resolution of the BEGe detector and on the spatial distance of the multiCE.

7.3 Selection confinement

From Figure 7.5 and Figure 7.6 the localization of the selected events can be estimated. For a source collimation of 1 mm a localization of roughly 2 mm in x (and equally in y) is achieved. This coincides with the previously estimated factor of two for source collimation and localization of events. The localization in z is roughly 10 mm for a detector collimation of 3 mm. This is slightly worse than the previously estimated factor of two because the detector collimators are placed at about 8 cm distance from the BEGe cryostat; this distance was previously set to zero.

7.4 Pulse shape discrimination parameters

To evaluate the goodness of selection of the quality and energy cuts and the A/E - cut we compare two other parameters which depend on the pulse shape:

- Rise time: The time in which pulses rise from 10% to 90% of their full height. We expect a peak for SSE events as their rise time should be constant within one measurement.
- Asymmetry: Defining the integral on the left side of the global maximum in the current pulse as A_{L} and respectively on the right side A_{R}. We define the asymmetry as $(A_{\mathrm{L}} - A_{\mathrm{R}})/(A_{\mathrm{L}} + A_{\mathrm{R}})$. Again, we expect a peak for SSE events as their asymmetry should be very similar within one measurement.

Comparing the rise time and asymmetry distributions of Run14 before and after cuts (Figure 7.7 and Figure 7.8) we note that the distribution after all cuts are applied is very narrow. The cuts eliminate all events in the side bands where background events are expected.

7.5 Average pulse construction

All BEGe events surviving the quality, the energy and finally also the A/E - cut are used to create an average pulse. The baseline of each event is fitted with an exponential to correct eventual pile-up and baseline offset. The properly corrected baselines are flat and have an average value of 0 ch. Trigger time offsets are corrected and all traces of one run are summed to build the average pulse. In this manner we create a representative trace for each measurement. To compare average pulses of different measurements, the height of all average pulses is normalized and time shifts are corrected. This ensures that all average pulses have the same height and that all of them are aligned in time at half their full height. Pulse height corrections are small, as the pulse height scales with energy and the BEGe energy cuts are narrow. Time shifts depend on DAQ settings for pre-trigger fraction and trace length. All average pulses presented in the following were corrected in this manner.

We define a slow rise and a fast rise part of traces as can be see in Figure 7.9. This is useful when comparing the shape of average pulses for different experimental settings.

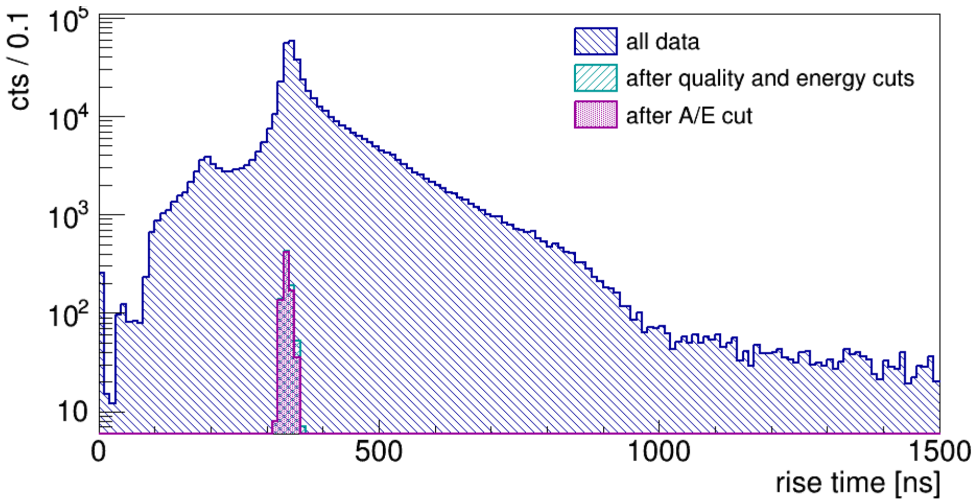

Figure 7.7: Rise time distribution before and after quality and energy cuts, and after the A/E-cut, of Run14. The distribution becomes narrower and zero events are observed in the side bands.

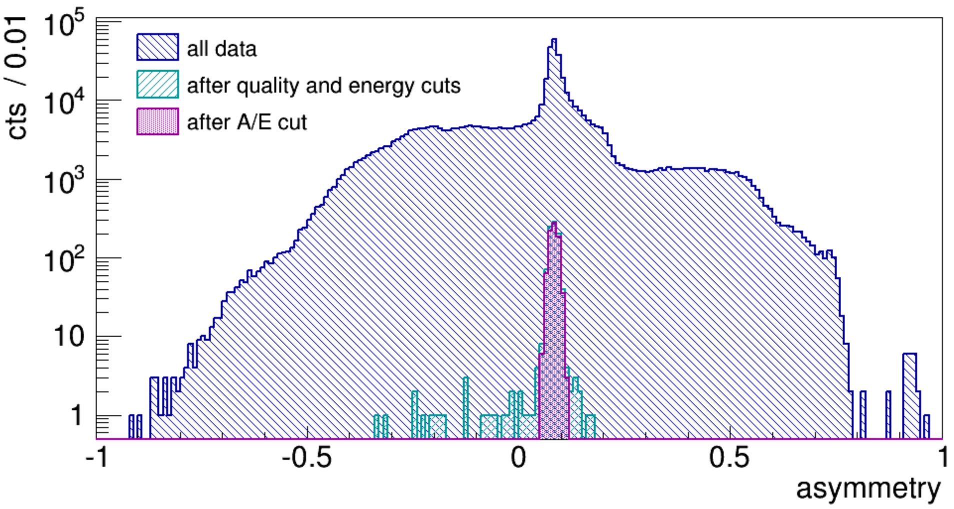

Figure 7.8: Asymmetry distribution before and after quality and energy cuts, and after the A/E-cut, of Run14. After the application of all cuts a narrower asymmetry distribution is observed, and zero events in the side bands remain.

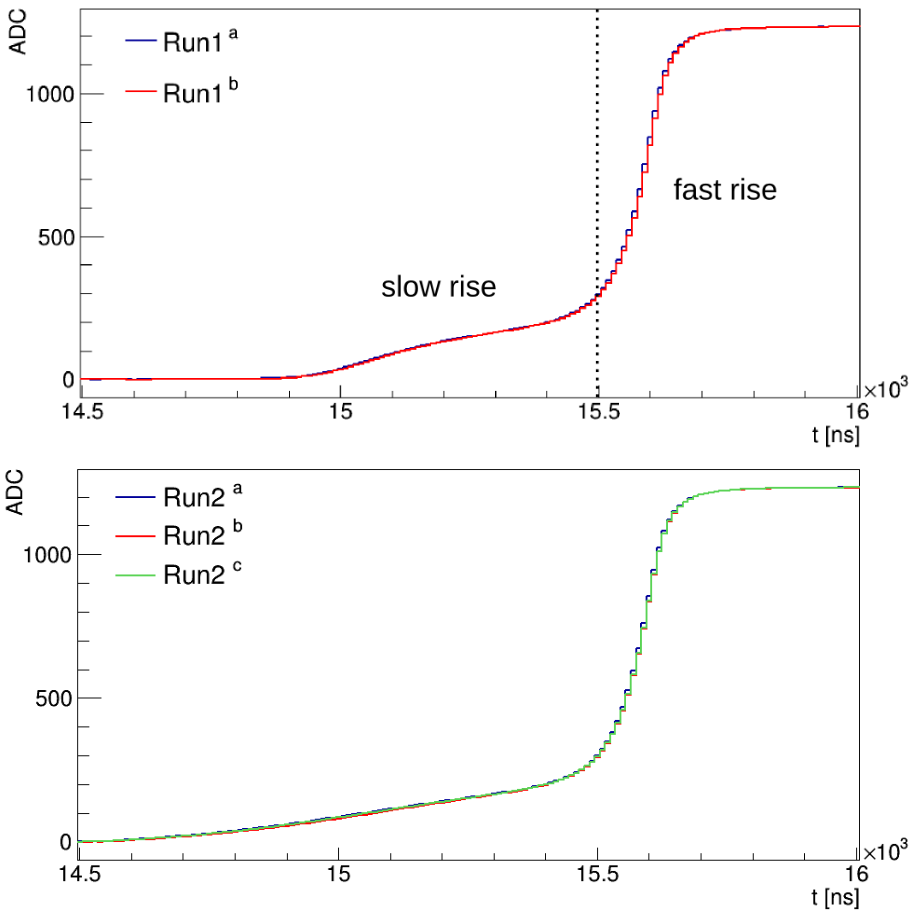

Figure 7.9: Comparison of average pulses from sub measurements in Run1 (top) and Run2 (bottom).

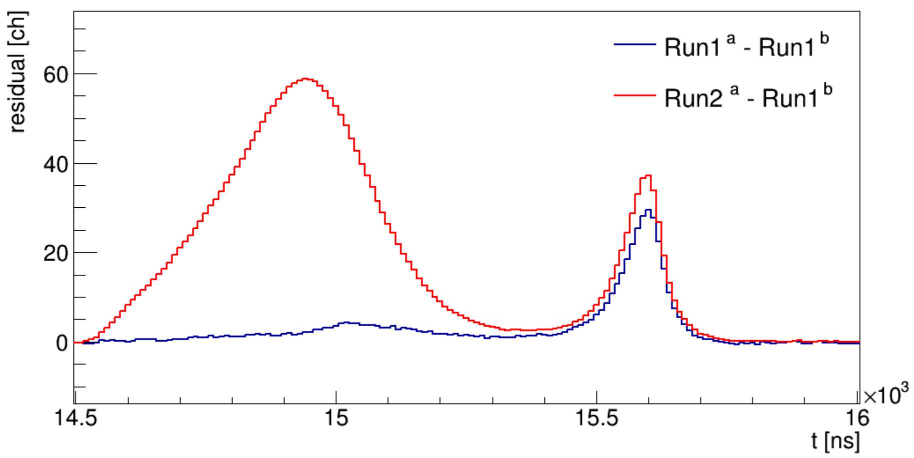

Figure 7.10: Comparison of average pulse residuals in Run1 and Run2. In blue residuals of two sub measurements of Run1 in red of sub measurements of Run1 and Run2. In the slow rise part of traces residuals are negligible for equal measurement setups, whereas measurements with different configuration show significant differences in the slow rise.

7.6 Reproducibility

To test the reproducibility of average pulses the sub measurements of Run1 and Run2 are compared to each other (see Figure 7.9).

The differences in each bin (residuals) of the two sub measurements of Run1 are shown in blue in Figure 7.10. In the fast rise residuals up to 30 ch are observed whereas in the slow rise part the difference is 5 ch at maximum.
The same Figure 7.10 shows the residuals between the two sub measurements Run1^{a} and Run2^{b} (histogram in red). Much higher residuals — up to 60 ch — can be observed at the beginning of the slow rise. The residuals of the fast rise part are comparable to the residuals of Run1.

We conclude: The average pulses remain stable for measurements with the same experimental settings. The residuals in the fast rise are due to the finite sampling frequency of the FADC, which results in slight misalignments of the traces. The position information is contained in the slow rise. As events are chosen from within a narrow energy window, the form of the average pulse depends only on the electric field configuration which the charge carriers traverse, on their trajectory through the detector (see Section 3.3.1). The fast rise is being measured when the charges pass the region close to the read out electrode, where the weighting field is high. Independently of the point of energy deposition, charges pass that region just before being collected on the read out contact. The slow rise instead depends on the detector location where energy was deposited.

7.7 Pulse shape comparison

The average pulse shape changes depending on the scanned interaction region and the inverse bias HV on the BEGe detector. In Figure 7.11 differences of the average pulse shape depending on the interaction region at 4.5 kV as well as at 5.0 kV BEGe HV are clearly observed.

Changing the BEGe HV also affects the pulse shape as can be seen in Figure 7.12.

We observe a faster rise for pulses with higher bias HV on the BEGe detector. The rise time for Run2^{a} with HV = 4 kV is on average more than 200 ns longer than for Run6 with HV = 5 kV as can be seen in Figure 7.13. A rise in drift velocity of charge carriers with augmented HV is a well known phenomenon (see Chapter 11 in Reference [44]), which is observed here by shorter pulse rise times.

In the central region of the BEGe we find a number of pulses which have higher asymmetry with respect to other locations (see Figure 7.14). This is seen both at HV = 4 kV as well as at HV = 5 kV.

A possible explanation is a contribution induced by the electrons to the current signal of the read out electrode. Moving charges induce mirror charges on the electrodes and are therefore visible in the current signal; the induced charge is proportional to the strength of the weighting field and their drift velocity (Equation 3.9). In the BEGe center the weighting field is higher than in outer regions. The electrons are not instantly collected on the n^+ contact and can thus contribute to the current signal.

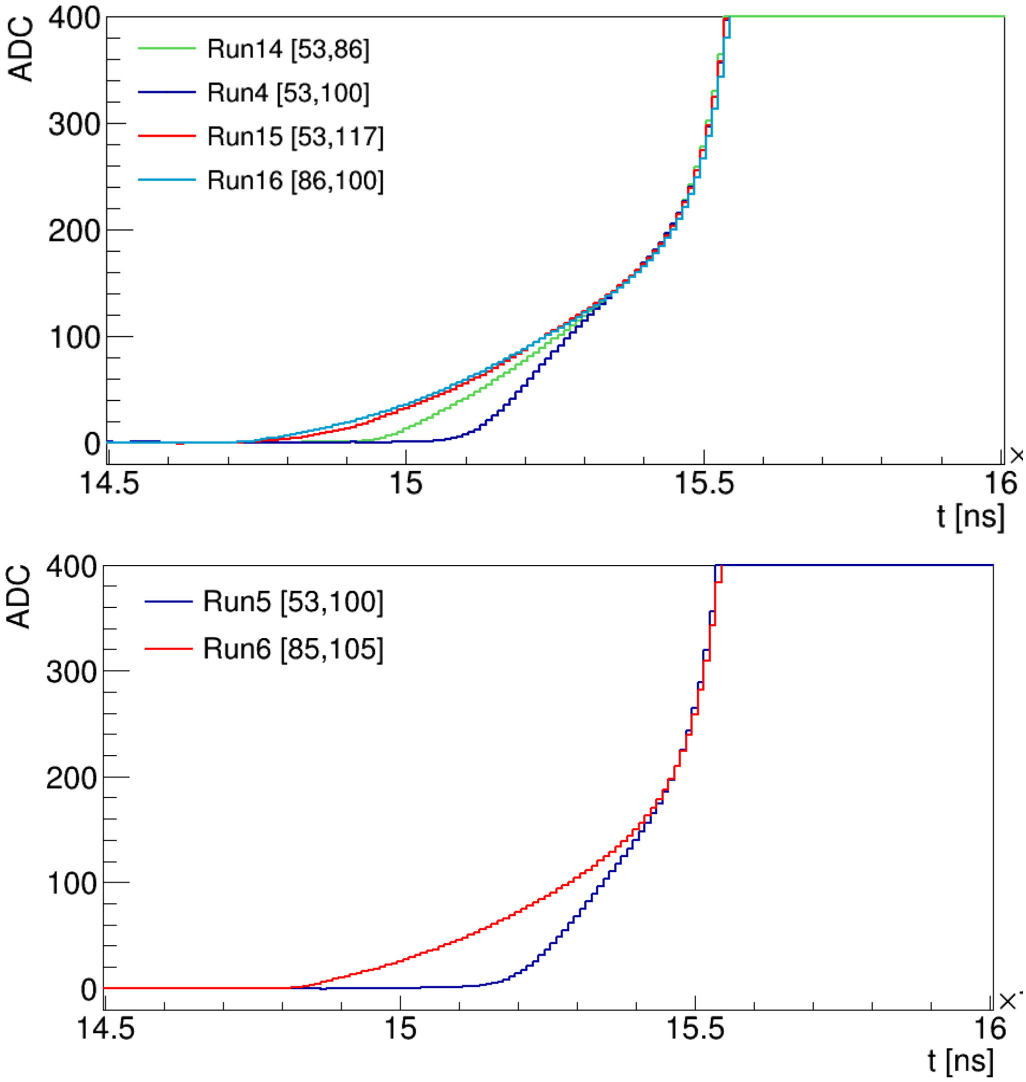

Figure 7.11: Average pulse comparison for different detector regions and the same $HV = 4.5\,\text{kV}$ (top), $HV = 5\,\text{kV}$ (bottom). The detector collimation is 3 mm for all measurements which are shown.

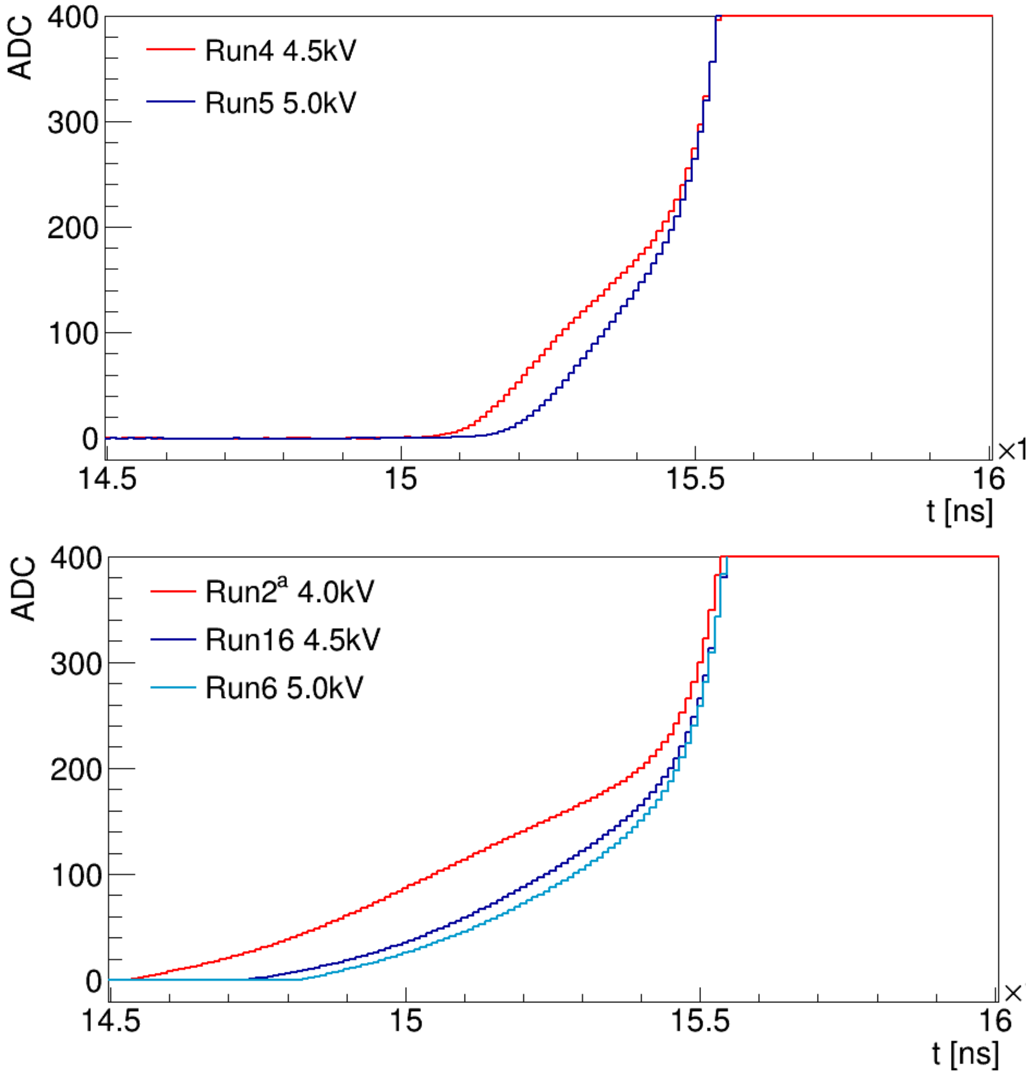

Figure 7.12: Average pulse comparison for different BEGe HV in central source positions (top) and source positions close to the BEGe border (bottom).

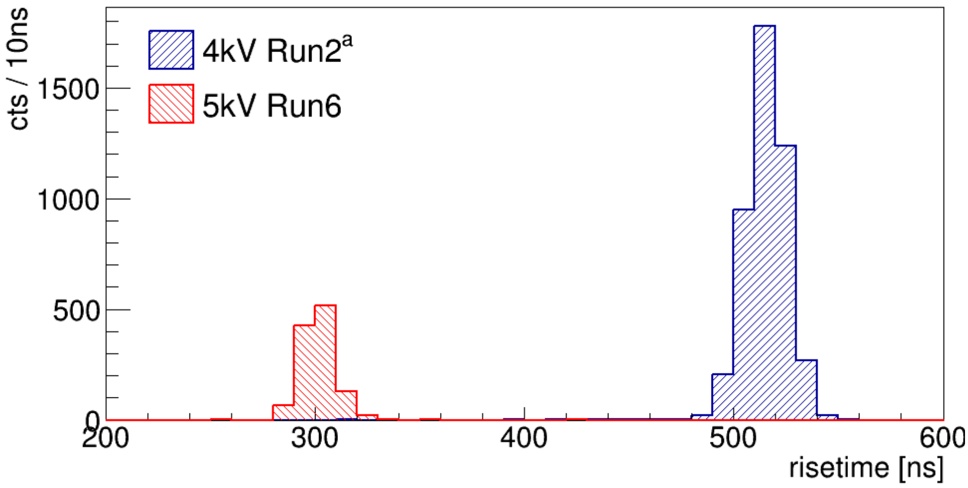

Figure 7.13: Rise time distribution for 4 kV and 5 kV BEGe detector HV. The rise time for Run2[a] with $HV = 4\,\mathrm{kV}$ is on average more than 200 ns longer than for Run6 with $HV = 5\,\mathrm{kV}$.

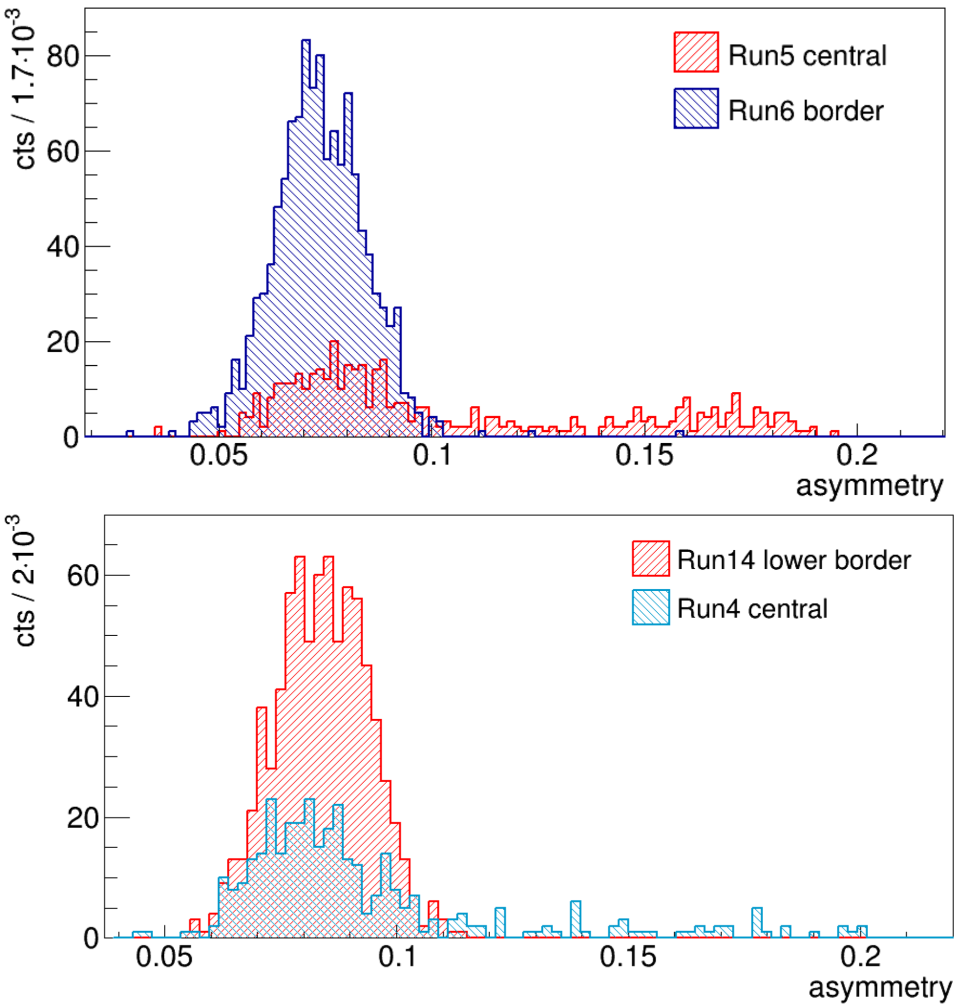

Figure 7.14: Asymmetry distribution for different detector regions at 5 kV (top) and 4 kV (bottom) BEGe HV. In the BEGe center a number of pulses with higher asymmetry are observed in comparison to other detector regions.

7.8 Signal to background ratio in ^{228}Th measurement

Samples of SSE events can be also collected using uncollimated ^{228}Th measurements. In the decay chain of ^{228}Th we find ^{208}Tl which emits the most energetic γ-line that can be found in nature with 2614.5 keV. At this energy pair production is the dominant process of photon interaction with matter. The positron which is created in this process thermalizes and subsequently annihilates with an electron, emitting two photons back-to-back with an energy of 511 keV each. Either photon can escape the detector and the respective energy is missing. Three characteristic lines can be see in ^{228}Th spectra. The Full Energy Peak (FEP) of the ^{208}Tl line at 2614.5 keV, the Single Escape Peak (SEP) at 2103.5 keV and the Double Escape Peak (DEP) at 1592.5 keV.

If both photons escape the detector the remaining energy is released in a very small volume thus events in the DEP are SSE events. The probability of both photons escaping the detector is highest on the detector surface and especially high in its corners. Hence, the spatial distribution of DEP events is very inhomogeneous.

A ^{228}Th measurement was conducted with the BEGe detector at $HV = 5$kV with a measurement real time of about 3 h. The distribution of A/E versus the calibrated energy can be seen in Figure 7.15. The SSE events emerge as a horizontal band. To estimate the background contribution in the DEP line we fit the A/E distribution of (1592 ± 5) keV (see Figure 7.16) with a Gaussian fit function and allow for a low energy tail (Equation 4.4). As for the ^{137}Cs coincidence measurements, the contribution is estimated from the two side bands left and right of the Gaussian; we find a SSE to background ratio of $(11759 - 747)/747 = 14.7 \pm 0.6$.

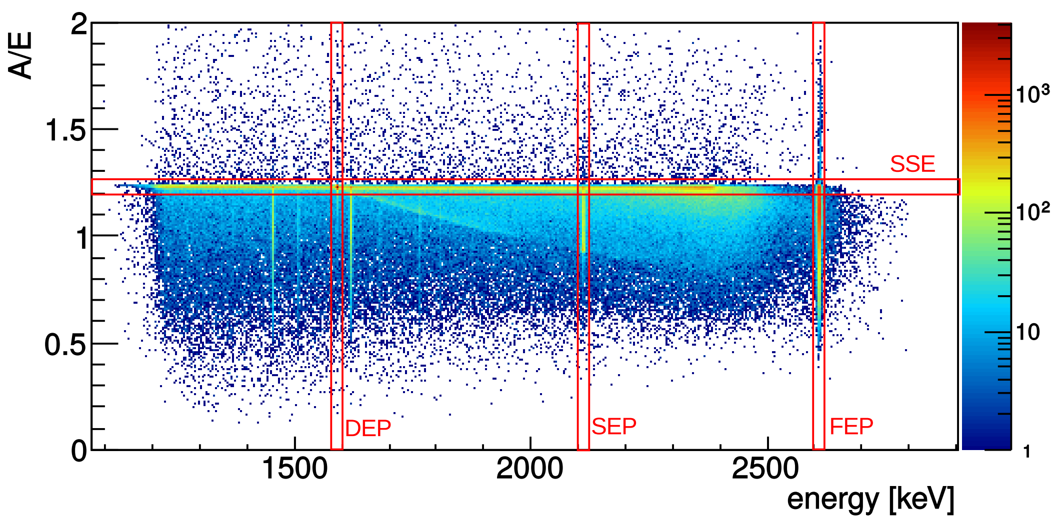

Figure 7.15: A/E versus calibrated energy of a ^{228}Th measurement recorded with the BEGe detector. The SSE events are visible as a horizontal band and the DEP with the highest SSE contribution at an energy of 1592 keV.

A low energy tail was not observed in the A/E distribution of the ^{137}Cs measurement, shown in Figure 7.2 and the SSE to background ratio achieved with the ^{137}Cs measurements is always higher except for Run4, Run5 and Run15 (see Table 7.2). Note that these measurements were central scans and the contribution of SSE events from the detector center in a ^{228}Th measurement is negligible. The best SSE to background ratio estimated is 121.4 ± 31.7 in Run17.

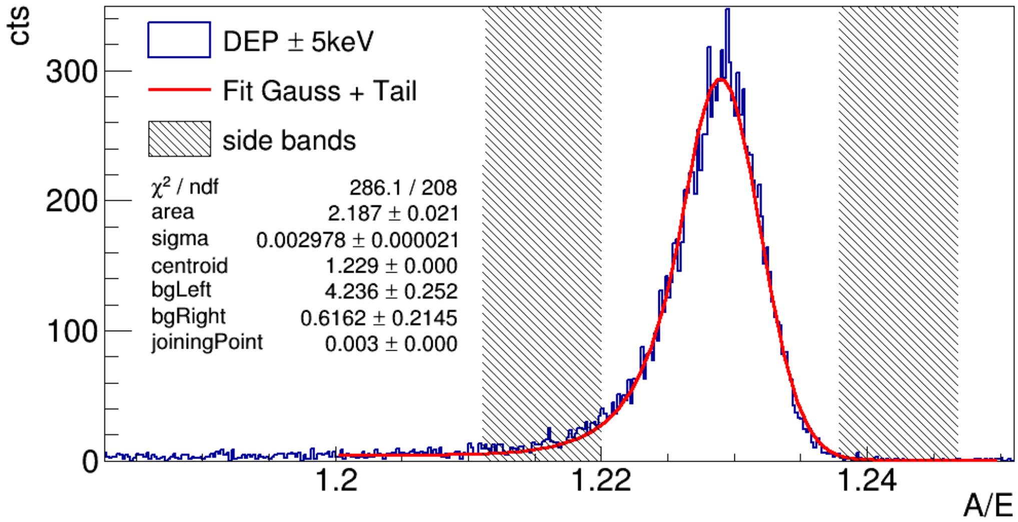

Figure 7.16: ^{228}Th A/E distribution of the DEP line. A Gaussian plus low energy tail fit is shown in red. The two side bands used to estimate the SSE to background ratio are shown as gray bands.

Chapter 8

Analysis of the background component ^{42}Ar in GERDA

As already mentioned in Chapter 2 background control is essential for low background experiments. All contributions have to be understood in order to minimize and estimate them. One important background component in GERDA is the β continuum of ^{42}K, daughter of ^{42}Ar which is naturally present in the cryo LAr of the GERDA setup.

The specific activity of ^{42}Ar in the GERDA LAr was estimated in a Bayesian binned maximum likelihood approach. The analysis and result is presented in the following.

8.1 Production mechanism of ^{42}Ar

The abundance of ^{42}Ar in natural LAr depends on the production of ^{42}Ar.

As pointed out in [68] ^{42}Ar can be produced via double neutron capture by ^{40}Ar

$$^{40}\mathrm{Ar} + n \longrightarrow {}^{41}\mathrm{Ar} + n \longrightarrow {}^{42}\mathrm{Ar} \tag{8.1}$$

They estimate the natural ^{42}Ar abundance from both naturally occurring neutrons and neutrons which are produced in nuclear explosions and come to an estimate of $^{42}\mathrm{Ar}/^{40}\mathrm{Ar} = 7.4 \cdot 10^{-22}$ corresponding to $A(^{42}\mathrm{Ar}) \approx 7.4\,\mu\mathrm{Bq/kg}$ (see Appendix F) for the latter as dominant mechanism.

However, they do not consider the cosmic-ray production of ^{42}Ar in the upper atmosphere via the reaction

$$^{40}\mathrm{Ar} + \alpha \longrightarrow {}^{42}\mathrm{Ar} + 2\,p \tag{8.2}$$

which could be about three orders of magnitude higher and therefore the main production mechanism for ^{42}Ar [69]. The authors estimate the ratio $^{42}\mathrm{Ar}/^{40}\mathrm{Ar}$ to be roughly 10^{-20} in the atmosphere. This would correspond to an activity of $A(^{42}\mathrm{Ar}) \approx 100\,\mu\mathrm{Bq/kg}$. The assumptions made in both references are more of qualitative nature and the calculated values can only be rough estimates.

8.2 Previous measurements

Before the $0\nu\beta\beta$ decay experiment GERDA was built, a proposal [70] was made. It states an upper limit of the ^{42}Ar specific activity in LAr of 43 μBq/kg [71] (see also Appendix F). This value would suggest a lower cross section for cosmic-ray production of ^{42}Ar as assumed by [69]. Now that GERDA has concluded Phase I data taking, this value can be checked. In fact first tests revealed that the background from ^{42}Ar is a lot higher than expected [72] from the proposal.

8.3 Methodology

^{42}Ar decays via β^- decay to ^{42}K which further decays to ^{42}Ca via another β^- decay with an endpoint of 3525.45 keV (see Figure 8.1 and Figure 8.2).

As the energy spectrum of electrons from a beta decay is continuous, this decay contributes also at lower energies to the background in GERDA, especially in the region of interest around $Q_{\beta\beta}^{0\nu} \approx 2039$ keV. All other unstable isotopes of Argon apart from ^{42}Ar can be neglected as source of background around $Q_{\beta\beta}^{0\nu}$ because either their lifetime is short and they have already decayed, e.g. ^{41}Ar has a lifetime of ca. 110 min, or the endpoint energy of the decay, $Q_{\beta\beta}$, is lower than $Q_{\beta\beta}^{0\nu}$, e.g. ^{39}Ar has an endpoint energy of $Q_{\beta\beta} = 565$ keV [73].

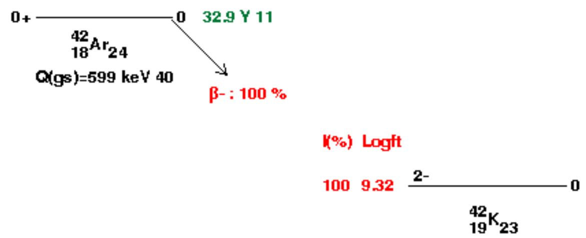

Figure 8.1: Decay scheme of ^{42}Ar taken from [74].

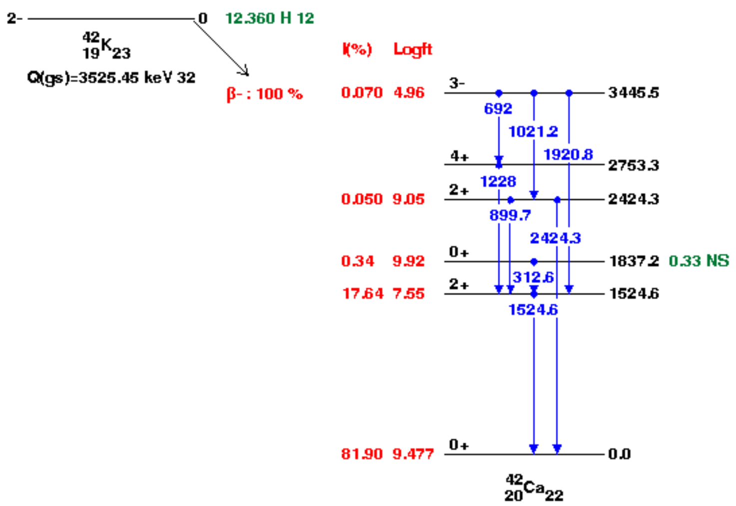

Figure 8.2: Decay scheme of ^{42}K taken from [74].

The Gerda LAr has been underground since November 2007. With the lifetime of ^{42}Ar being (32.9 ± 1.1) y (measured in 1965) [75] and the lifetime of ^{42}K being (12.360 ± 0.01) h, they are in secular equilibrium. This means the specific activity of ^{42}Ar and ^{42}K are the same.

In the following, the specific activity of ^{42}Ar is calculated by estimating the activity of ^{42}K using a selection of Gerda Phase I data. We use a γ-line of the ^{42}K spectrum which has an energy of (1524.65 ± 0.03) keV and perform a binned maximum likelihood fit using the Bayesian Analysis Toolkit (BAT) [76]. Finally the calculated specific activity is corrected for the half-life of ^{42}Ar in order to be comparable to other measurements and theoretical values and limits.

8.4 Distribution of ^{42}K

To estimate the specific activity of ^{42}K in the Gerda LAr we have to make assumptions about its distribution inside the LAr and here it starts to become tricky: As ^{42}K is born in a β^- decay it is born as a positive ion namely as ^{42}K$^+$. The detectors are operated at HV, typically with 4 kV inverse bias, which creates strong electric fields and under the influence of electric fields ions are drifted. Without further measures the distribution of ^{42}K would surely be inhomogeneous.

A lot of effort was put in making most of the LAr volume as field-free as possible by deploying small, electrically grounded copper cylinders around the detectors and by shielding the HV cables. These so called Mini-Shroud (MS) additionally form a physical barrier for ^{42}K$^+$ ions.

8.5 Efficiencies

The detection efficiency is a very crucial ingredient in the activity determination as it is fully anti correlated to the specific activity itself. It is determined with a MC Simulation assuming a specific distribution of ^{42}Ar in LAr inside Gerda. The simulation program we use is called MaGe; it is Geant4 based and is developed by the Gerda and Majorana experiments in a collaborative effort [66, 77].

8.5.1 Simulation

The Gerda setup (see Section 2) is available as MaGe [66] geometry for MC simulations. A cylinder of ^{42}K decays was simulated centered on the respective detector string. It is large enough in order not to miss important contributions to the efficiency of the detectors. A height of 2.10 m and a radius of 1 m were chosen according to a previous study [78]. In the following we call the incident simulated particles *primaries* and their starting position the *primary vertex*.

In Figure 8.3 all primaries are plotted that deposit energy in at least one of the detectors. The simulation contains only the one string arm in the configuration starting from Run34 (see Appendix G). Decays outside the simulated volume are considered as a systematic uncertainty (see Section 8.11).

The simulated volume is split in four parts as can be seen in Figure 8.4. The volume inside the MS, and the volume outside the MS which is split in top, bottom and tube volumes. The distribution of ^{42}K decays outside the MS is assumed to be homogeneous and the distribution of decays inside the MS can be varied in order to study systematic effects on the efficiency. Finally, the simulations from inside the MS and those from outside the MS can be combined without re-simulating the latter.

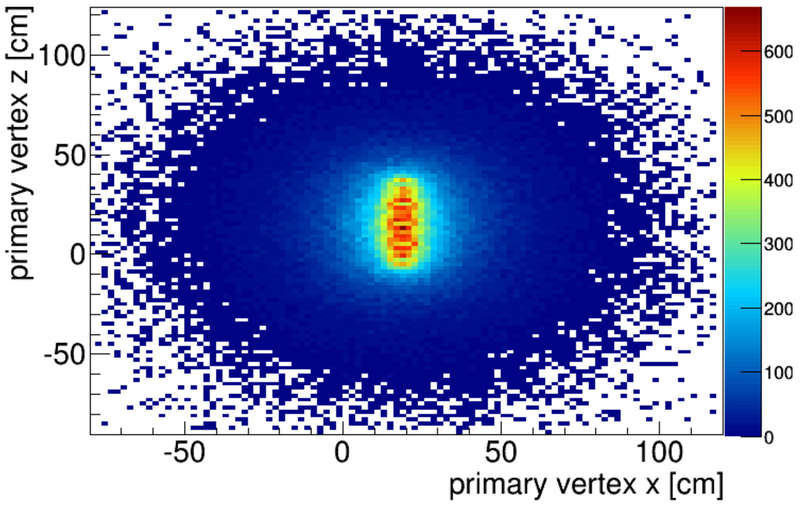

Figure 8.3: Vertex positions of primaries which deposit energy in at least one of the BEGe detectors.

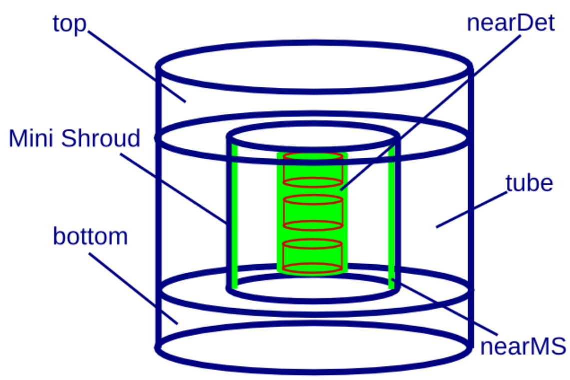

Figure 8.4: LAr cylinder in which ^{42}K decays are simulated. The cylinder is split in four separate volumes in order to be able to simulate different distributions inside the Mini-Shroud (MS) and combine them later.

In each of the above said volumes a total number of 10^9 decays were simulated using Decay0 [79] to create the primary vertices in order to account for correlations in γ cascade emissions. The spectrum of primary particles is plotted in Figure 8.5.

As a crosscheck of the Monte Carlo simulation a rough estimate of the branching ratio $R_\mathrm{B}(1525\,\mathrm{keV})$ of the 1525 keV γ-line was performed. From 1500 keV to 1550 keV the spectrum is binned in 51 bins. Dividing in three regions of equal size we estimate the background using side bands and subtract it from the central region which contains the γ-line.

$$\begin{aligned} R_\mathrm{B}(1525\,\mathrm{keV}) &= \frac{\sum_{i=18}^{34} n_i - \left(\sum_{i=1}^{17} n_i + \sum_{i=35}^{51} n_i\right)}{N_\mathrm{tot}} \\ &= (18.071 \pm 0.001) \cdot 10^{-2} \end{aligned} \tag{8.3}$$

The number of entries in bin i is denoted as n_i and N_tot is the total number of simulated decays. The calculated value is in accordance with the literature value of $R_\mathrm{B}^\mathrm{lit}(1525\,\mathrm{keV}) = (18.08 \pm 0.09) \cdot 10^{-2}$ [74].

8.5.2 Efficiency calculation

We calculate the efficiency of the GERDA detectors, to detect 1525 keV γs from ^{42}K decays, by estimating the signal counts in the same manner as we estimated the branching ration R_B. The detection efficiency is then given as as the number of signal counts divided by the total number of simulated decays. Last, the efficiencies are normalized with the simulated LAr volume and expressed as the rate per day, seen for a specific activity of 1 µBq/kg.

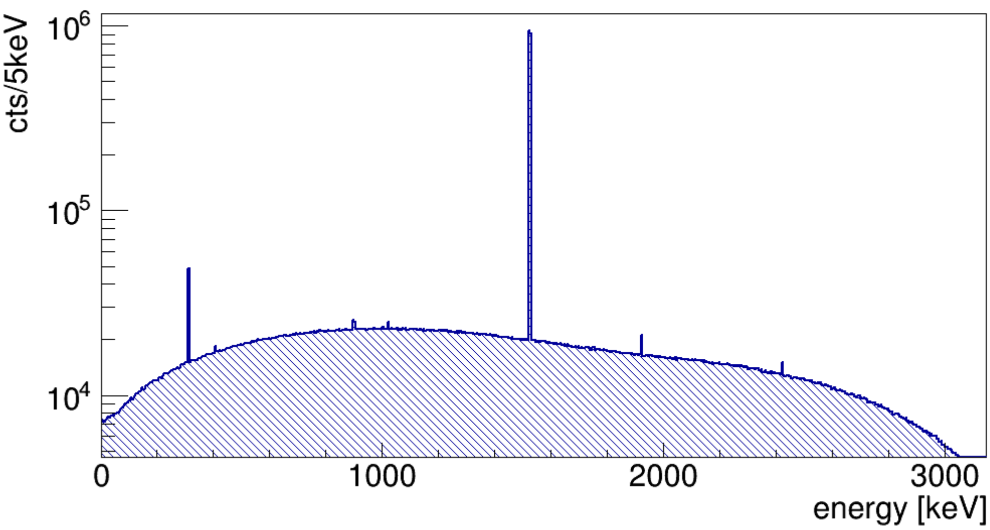

Figure 8.5: Primary spectrum of the efficiency simulations containing 10^7 primary decays.

To extract the signal counts, the energy window [1499 keV,1550 keV] of the simulation output spectra is subdivided in three regions of same size. B_1 and B_2 are the sidebands and M denotes the middle region which contains the ^{42}K γ-line at $\approx$ 1525 keV which we use to estimate the specific activity of ^{42}Ar. Using the two side bands we estimate the background contribution in region M and calculate the signal counts S as follows

$$S = M - \frac{B_1 + B_2}{2} \tag{8.4}$$

We calculate the efficiency ε by dividing S by the number of simulated decays N_{sim}

$$\varepsilon = \frac{S}{N_{\mathrm{sim}}} \tag{8.5}$$

Effectively we are not calculating the efficiency on the full decay but on the 1525 keV line which we will denote as ε_{15}

$$\varepsilon_{15} = \frac{S}{N_{\mathrm{sim}} \cdot R_{\mathrm{B}}} \tag{8.6}$$

To estimate the uncertainty on the efficiency we have to take the branching ratio R_{B} of the 1525 keV line into account. The uncertainty, which is calculated using binomial statistics, is then

$$\Delta\varepsilon_{15} = \sqrt{\frac{\varepsilon_{15}\,(1-\varepsilon_{15})}{N_{\mathrm{sim}} \cdot R_{\mathrm{B}}}} \tag{8.7}$$

The uncertainty on the total efficiency ε is therefore

$$\Delta\varepsilon = \sqrt{\left(\frac{\partial\varepsilon}{\partial\varepsilon_{15}} \cdot \Delta\varepsilon_{15}\right)^2 + \left(\frac{\partial\varepsilon}{\partial R_{\mathrm{B}}} \cdot \Delta R_{\mathrm{B}}\right)^2} \tag{8.8}$$

$$\frac{\Delta\varepsilon}{\varepsilon} = \sqrt{\left(\frac{\Delta\varepsilon_{15}}{\varepsilon_{15}}\right)^2 + \left(\frac{\Delta R_{\mathrm{B}}}{R_{\mathrm{B}}}\right)^2} \tag{8.9}$$

If we neglect the uncertainty on the branching ratio ΔR_{B} for $N_{\mathrm{sim}} \to \infty$ this tends to

$$\frac{\Delta\varepsilon}{\varepsilon} \approx \frac{\Delta\varepsilon_{15}}{\varepsilon_{15}} = \sqrt{\frac{\varepsilon_{15}\,(1-\varepsilon_{15})}{N_{\mathrm{sim}} \cdot R_{\mathrm{B}} \cdot \varepsilon_{15}^2}} = \sqrt{\frac{(1-\varepsilon_{15})}{S}} \xrightarrow{N_{sim}\to\infty} \frac{1}{\sqrt{S}} \tag{8.10}$$

With $R_{\mathrm{B}} = 0.1808 \pm 0.009$ [74] and $\Delta\varepsilon/\varepsilon \approx 10^{-2}$ though, the uncertainty on the branching ratio can not simply be neglected but contributes with approximately 10 % to the total uncertainty. In the following $\Delta\varepsilon$ contains this contribution. In the final analysis the efficiency enters as the rate per day which is seen by the respective detector for an ^{42}Ar activity of 1 µBq/kg. Therefore, we define the normalized efficiency ε_{n} as

$$\varepsilon_{\mathrm{n}} = \varepsilon \cdot m_{\mathrm{LAr}} \cdot f_{\mathrm{n}} \tag{8.11}$$

With the LAr mass m_{LAr}, which is given by the density of LAr $\rho_{\mathrm{LAr}} = 1.39\,\mathrm{g/cm^3}$ multiplied by its volume V_{LAr}

$$m_{\mathrm{LAr}} = \rho_{\mathrm{LAr}} \cdot V_{\mathrm{LAr}} \tag{8.12}$$

and the normalization factor

$$f_\mathrm{n} = 1\,\frac{\mu\mathrm{Bq}}{\mathrm{kg}} \cdot 8.64 \cdot 10^4\,\frac{\mathrm{s}}{\mathrm{d}} = 8.64 \cdot 10^{-2}\,\frac{\mathrm{decays}}{\mathrm{kg\,d}} \tag{8.13}$$

efficiencies of complementary simulations i can be combined by simply summing them up

$$E_\mathrm{n} = \Sigma_i \varepsilon_{\mathrm{n},i} \tag{8.14}$$

provided there is no overlap of the simulated LAr volume and if the single values are normalized. Supposing that complementary simulations are uncorrelated we add up the uncertainties on the single efficiencies in quadrature to obtain the combined uncertainty

$$\Xi_\mathrm{n} = \sqrt{\Sigma_i \Delta\varepsilon^2_{\mathrm{n},i}} \tag{8.15}$$

All simulations with their normalization factors are listed in Table 8.1. In order to ensure that the volume splitting, which was described in Section 8.5.1, leads to a reasonable result for the efficiencies, for detector string 3 (S3) a simulation without volume splitting as well as with volume splitting was done. S3 contains three detectors; their efficiencies for the split simulation and the full volume simulation are compared in Table 8.2.

Table 8.1: List of simulations and normalization factors. The normalization factor for inhomogeneous distributions inside the MS is the same as for the homogeneous distribution because a priori we do not know the real distribution and assume a homogeneous one.

#	string	position	V [cm^3]	m [kg]	$m\,f_\mathrm{n}$
1	S1	top	2543330	3535	305.444
2	S1	bottom	2544630	3537	305.600
3	S1	tube	1500070	2085	180.152
4	S1	hom	3285.45	4.57	0.395
5	S1	near BEGe	-	-	hom
6	S1	near MS	-	-	hom
7	S2	all	6591250	9162	791.583
8	S3	all	6591360	9162	791.596
9	S3	top	2543320	3535	305.443
10	S3	bottom	2544630	3537	305.600
11	S3	tube	1500600	2086	180.216
12	S3	hom	2746.51	3.82	0.330
13	S3	near BEGe	-	-	hom
14	S3	near MS	-	-	hom
15	S4	all	6591280	9162	791.586
16	S1	AC	6591070	9162	791.561

Table 8.2: Comparison of complete (all) and split efficiency simulations (hom). The split simulation has four different volume parts which are added like described in Equation 8.14. The difference $\Delta = (\varepsilon_\mathrm{n}(\mathrm{hom}) - \varepsilon_\mathrm{n}(\mathrm{all}))/\varepsilon_\mathrm{n}(\mathrm{hom})$ is well within the uncertainty bounds.

name	hom ε_n [10^{-3}/d]	all ε_n [10^{-3}/d]	Δ[%]
RGI	3.75 ± 0.03	3.75 ± 0.06	-0.08
ANG4	4.27 ± 0.03	4.20 ± 0.06	1.64
RGII	3.90 ± 0.03	3.86 ± 0.06	1.01

Table 8.3: Efficiencies of all Phase I detectors with the list of simulations which were combined to calculate them. The values indicated with *hom* are used as central value and the *nearDet* and *nearMS* values are used to estimate a systematic uncertainty due to the inhomogeneity of ^{42}K decays (see Section 8.11).

name	hom ε_n [10^{-3}/d]	nearDet ε_n [10^{-3}/d]	nearMS ε_n [10^{-3}/d]	sim list
GD32B	1.03 ± 0.01	1.01 ± 0.01	0.94 ± 0.01	1-6
GD32C	1.10 ± 0.01	1.22 ± 0.01	1.02 ± 0.01	1-6
GD32D	1.07 ± 0.01	1.19 ± 0.01	0.98 ± 0.01	1-6
GD35B	1.20 ± 0.01	1.32 ± 0.01	1.12 ± 0.01	1-6
GD35C	0.87 ± 0.01	0.87 ± 0.01	0.80 ± 0.01	1-6
ANG3	4.23 ± 0.06	-	-	15
ANG5	5.24 ± 0.07	-	-	15
RGIII	4.08 ± 0.06	-	-	15
RGI	3.75 ± 0.03	3.57 ± 0.03	3.59 ± 0.03	9-14
ANG4	4.27 ± 0.03	4.81 ± 0.03	4.10 ± 0.03	9-14
RGII	3.90 ± 0.03	3.97 ± 0.03	3.77 ± 0.03	9-14
GTF112	6.15 ± 0.08	-	-	7
ANG2	5.43 ± 0.07	-	-	7
ANG1	1.44 ± 0.03	-	-	7
GTF45	5.02 ± 0.07	-	-	16
GTF32	4.83 ± 0.07	-	-	16

8.5.3 Systematic uncertainty of efficiencies

To account for the systematic uncertainty due to the unknown distribution of the ^{42}K inside the MS, this distribution was varied as can be seen in Figure 8.4. Three different configurations were simulated: A homogeneous distribution to calculate the central value of the efficiencies, a distribution very close to the detectors (*nearDet*) and one with decays only in a thin tube close to the walls of the MS (*nearMS*). The last two give an upper and a lower bound on the efficiencies. The values are listed in Table 8.3.

8.6 Energy resolution

From calibration data between 2012-07-08 and 2013-03-20 the full width at half maximum (FWHM) at 1525 keV was extracted for each calibration run and BEGe detector. Similar for the two AC coupled detectors GTF45 and GTF32 the resolution was determined from calibration data between 2011-11-09 and 2012-05-22. The median and 68% interval are tabulated on the left side of Table 8.4. Detailed plots can be found in Appendix H. The energy resolution of the ANG, RG and GTF112 detectors are given on the right side of Table 8.4. They were taken from an internal Gerda publication [80].

Table 8.4: Left side: Median FWHM at 1525 keV from calibration data plotted in Figure H.1 and Figure H.2. The uncertainty is given as the smallest interval containing 68% of values around the median value and σ is simply FWHM divided by 2.35. Right side: Previously evaluated energy resolutions of ANG, RG and GTF112 detectors (see Table 9 in [80]). ANG1 and RG3 are not considered in this analysis.

detector	FWHM [keV]	σ [keV]	detector	FWHM [keV]	σ [keV]
GD32B	2.42 ± 0.03	1.03 ± 0.01	GTF112	3.64	1.55
GD32C	2.41 ± 0.04	1.02 ± 0.02	ANG2	3.93 ± 0.03	1.67 ± 0.01
GD32D	2.51 ± 0.04	1.07 ± 0.02	ANG3	4.37 ± 0.14	1.86 ± 0.06
GD35B	3.24 ± 0.11	1.38 ± 0.05	ANG4	4.00 ± 0.08	1.70 ± 0.03
GD35C	2.64 ± 0.06	1.12 ± 0.03	ANG5	3.95 ± 0.12	1.68 ± 0.05
GTF45	7.17 ± 1.47	3.05 ± 0.62	RG1	4.23 ± 0.25	1.80 ± 0.11
GTF32	7.46 ± 1.20	3.18 ± 0.51	RG2	4.67 ± 0.24	1.99 ± 0.10

8.7 Bayesian analysis

We use Bayes' theory to perform a binned maximum likelihood fit to the spectral shape of the ^{42}K γ-line and to estimate the ^{42}Ar specific activity in the Gerda LAr.

Poisson statistics expresses the probability of a discrete random variable k with an average rate λ

$$P(k|\lambda) = \frac{\lambda^k e^{-\lambda}}{k!} \tag{8.16}$$

The likelihood to observe n_i events in the i^{th} bin of a histogram for λ_i events expected is given by

$$P(\vec{n}\,|\lambda) = \prod_i \frac{\lambda_i^{n_i} e^{-\lambda_i}}{n_i!} \tag{8.17}$$

In the case of multiple detectors with index j the combined likelihood has the following form

$$P(\vec{n}\,|\lambda) = \prod_j \prod_i \frac{\lambda_{ij}^{n_{ij}} e^{-\lambda_{ij}}}{n_{ij}!} \tag{8.18}$$

The global posterior probability density function (pdf)

$$P(\lambda|\,\vec{n}) = \frac{P(\vec{n}\,|\lambda) \cdot P(\lambda)}{P(\vec{n})} \tag{8.19}$$

has to be marginalized over all nuisance parameters p_m in order to obtain the posterior pdf for the parameter of interest A

$$P(\lambda(A)|\,\vec{n}) = \int P(\lambda(A, p_m)|\,\vec{n})\;\mathrm{d}p_m \tag{8.20}$$

where $m = 1, 2 \ldots M$ and M is the total number of nuisance parameters. Note that here λ depends on the nuisance parameters p_m and the parameter of interest A so $\lambda = \lambda(A, p_m)$.

Using the law of total probability we can express

$$P(\vec{n}) = \int P(\vec{n}\,|\lambda) P(\lambda)\,\mathrm{d}\lambda \tag{8.21}$$

And as all parameters are assumed to be independent we can rewrite the prior probability

$$P(\lambda) = P(\lambda(A, p_m)) = P(A) \prod_m P(p_m) \tag{8.22}$$

The prior probability $P(\lambda)$ contains all our knowledge about the parameters. As it factorizes completely we can choose the prior conditions of each parameter separately. The last thing we have to do is define the model λ.

8.7.1 Choice of prior distributions

The prior distribution should reflect our degree of belief in a free fit parameter. If a fit tells us that we have a negative number of background counts we would not believe this result because it is not physical. Thus, in the prior distribution of the background index we exclude values below zero. A prior distribution should be normalizable otherwise it is called an improper prior. A common distribution we chose is a gaussian distribution of a parameter giving preference to the central value with some uncertainty. Having no value of preference is reflected in a so called non informative prior. A flat prior in a large enough closed range is quasi non informative and is also normalizable. The range should be large enough to cover all the posterior distribution without cutting it.

8.7.2 Building the likelihood

We want to approximate the ^{42}K γ-line with a Gaussian on a flat background. In this model the number of expected events in the i^{th} bin are expressed by

$$\lambda_{ij} = A\,\varepsilon_j\,T_j \int_{\Delta E_i} \frac{1}{\sqrt{2\pi}\,\sigma_j} \exp\left(-\frac{(E-(\mu+\Delta\mu_j))^2}{2\sigma_j^2}\right) \mathrm{d}E' + T_j \int_{\Delta E_i} B_j\,\mathrm{d}E' \quad (8.23)$$

The specific activity A is common to all detectors and is the parameter of interest. The fit parameters for each detector j are the efficiency ϵ_j, the resolution σ_j at 1525 keV, the γ-line shift $\Delta\mu_j$ and the background index B_j. They are all nuisance parameters, which means they are free parameters of the fit but we are not interested in their posterior pdf. The lifetimes T_j and the common γ-line energy $\mu = 1524.65$ keV are fixed. All parameters and their type of prior pdf are listed in Table 8.6. In the following we refer to this model as *flat background model.*

As each detector has four free fit parameters in this model, fitting the spectra of 13 detectors the number of nuisance parameters is $M = 13 \cdot 4 = 52$. All input values of Gaussian and fixed parameters are listed in Table 8.5. For the γ-line shift $\Delta\mu_j$ we use a Gaussian prior pdf with the same parameters for all detectors: As most probable value we choose no shift $\Delta\mu_j = 0$ and a reasonable assumption for the width of the prior pdf is the energy resolution of the detectors $\Delta\Delta\mu_j = \sigma_j$.

8.7.3 Building the refined likelihood

The statistics of the Phase I data is good enough to see a difference between the background level at the right and the left side of the γ-line. A refined model accounts for this difference modeling the background with an inverse error function. This adds another parameter to the model and we have now a flat background and the step size as additional parameter for the fit. In order to be more controllable we express the step size by the difference between the left and the right background level. Like this, it is easier to prohibit for example a negative background level.

With $\mu' = \mu + \Delta\mu_j$ we get

$$\begin{aligned}\lambda_{ij} = A\,\varepsilon_j\,T_j \int_{\Delta E_i} \frac{1}{\sqrt{2\pi}\,\sigma_j} \exp\left(-\frac{(E-\mu')^2}{2\sigma_j^2}\right) \mathrm{d}E' \\ + T_j \int_{\Delta E_i} B_j^{\text{left}} + \frac{B_j^{\text{right}} - B_j^{\text{left}}}{2} \cdot \operatorname{erfc}\left(\frac{\mu' - E}{\sqrt{2}\cdot\sigma_j}\right) \mathrm{d}E'\end{aligned} \tag{8.24}$$

An example of such a function can be seen in Figure 8.6. In the following we refer to this model as *erfc background model* or *refined background model*. Also for this model the fit parameters, their types and fit ranges can be found in Table 8.6.

Table 8.5: Input values used for the likelihood fit. Although ANG1, RG3 and GD35C are not considered in this analysis, the values are listed for completeness.

channel	Detector	T_j [d]	σ_j [keV]	$\Delta\sigma_j$ [keV]	ϵ_j [10^{-3}/d]	$\Delta\epsilon_j$ [10^{-5}/d]
0	ANG1	0	-	-	1.4379	3.37
1	ANG2	458.495	1.90594	0.05	5.4314	6.56
2	ANG3	458.495	1.83291	0.05	4.2342	5.79
3	ANG4	458.495	1.79515	0.05	4.2688	2.60
4	ANG5	458.495	1.67741	0.05	5.2356	6.44
5	RG1	458.495	1.79385	0.05	3.7485	2.52
6	RG2	384.789	1.98221	0.05	3.8950	2.67
7	RG3	0	-	-	4.0775	5.69
8	GTF112	458.495	1.55	0.05	6.1542	6.99
9	GD32B	260.923	1.03018	0.05	1.0272	1.33
10	GD32C	284.385	1.02454	0.05	1.1040	1.29
11	GD32D	264.900	1.06700	0.05	1.0669	1.26
12	GD35B	284.385	1.38013	0.05	1.2045	1.37
13	GD35C	0	1.12414	0.05	0.8689	1.27
9	GTF45	174.110	3.05259	0.05	5.0229	6.31
10	GTF32	174.110	3.17652	0.05	4.8317	6.19

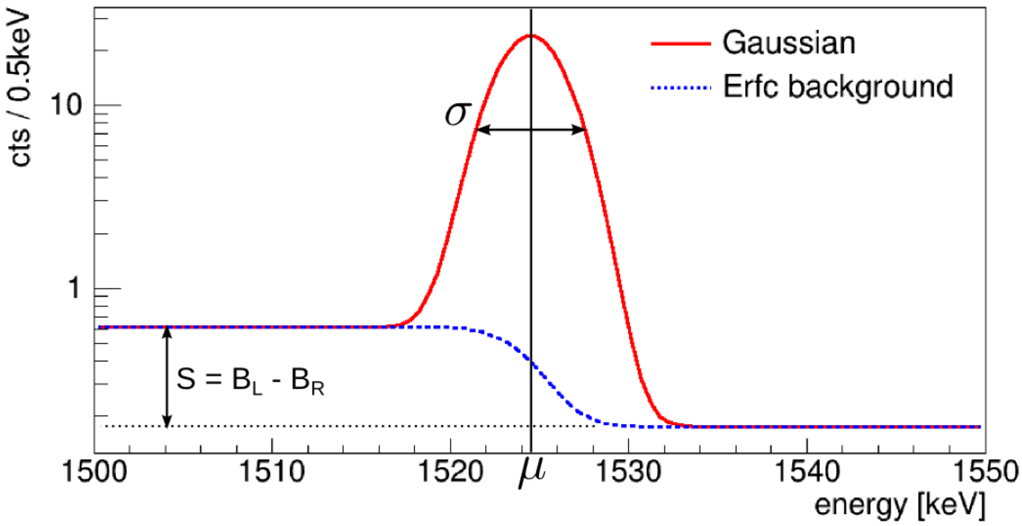

Figure 8.6: Gaussian function with inverse error function as background model. The whole function is plotted in red while the background is plotted again in blue dashed to illustrate the background below the γ-peak.

Table 8.6: List of priors and their types. If the symbol is indexed with a j each detector has its own fit parameter, if not the parameter is common to all detectors. A fixed parameter is in that sense not a fit parameter but has a fixed value.

model	parameter	symbol	prior pdf type	range
flat/erfc	specific activity	A	flat	$[0 : 200]$ µBq/kg
	efficiency	ε_j	Gaussian	$[0.09 : 1]\, 10^{-2}\, \mathrm{d}^{-1}$
	lifetime	T_j	fixed	-
	peak shift	$\Delta\mu_j$	Gaussian	$[-2 : 2]$ keV
	resolution	σ_j	Gaussian	$[0 : 4]$ keV
flat	background index	B_j	flat	$[0 : 0.01]\, \mathrm{keV}^{-1}\mathrm{d}^{-1}$
erfc	background left	B_j^{left}	flat	$[0 : 0.01]\, \mathrm{keV}^{-1}\mathrm{d}^{-1}$
	background right	B_j^{right}	flat	$[0 : 0.01]\, \mathrm{keV}^{-1}\mathrm{d}^{-1}$

8.7.4 The Bayesian Toolkit - BAT

The likelihood fits are done using the Bayesian Analysis Toolkit (BAT) version 0.9.4.1 [76]. It is based on a marginalization using the Metropolis Markov Chain Monte Carlo (MCMC) algorithm. Four predefined levels of fit precision can be chosen *kLow* (1 chain with 10^4 iterations), *kMedium* (5 chains with 10^5 iterations each), *kHigh* (10 chains with 10^6 iterations each) and *kVeryHigh* (10 chains with 10^7 iterations each). The number of chains and iterations per chain can also be chosen manually using *MCMCSetNChains* and *MCMCSetNIterationsRun* which are methods of the *BCEngineMCMC* class of BAT.

Both models, the flat and the erfc background model, are implemented inside one C++ class which inherits from the *BCModel* class of BAT. Two methods have to be implemented in a BCModel: *LogAPrioriProbability* which serves to calculate the natural logarithm (ln) of the prior probability $P(\lambda)$ and *LogLikelihood* to calculated the ln of $P(\vec{n}\,|\lambda)$. To estimate $P(\vec{n}\,|\lambda)$ the respective model is integrated over each bin. The integral of the Gaussian part can be done using the error function which is defined as

$$\operatorname{erf}(y) = \frac{2}{\sqrt{\pi}} \int_0^y e^{-t^2} \mathrm{d}t \tag{8.25}$$

Here $y = (E - \mu)/(\sqrt{2} \cdot \sigma)$.

Integrating the flat background model is trivial but the integration of the erfc background model has to be done numerically. We use the following approach

$$\int_{E_1}^{E_2} \operatorname{erfc}(z) dz \approx \frac{E_2 - E_1}{n} \left[\frac{\operatorname{erfc}(E_1) + \operatorname{erfc}(E_2)}{2} + \sum_{k=1}^{n-1} \operatorname{erfc}\left[E_1 + \frac{k \cdot (E_2 - E_1)}{n} \right] \right] \tag{8.26}$$

Where $z = (\mu - E)/(\sqrt{2} \cdot \sigma)$ and n which reflects the precision of the numerical integration was chosen as 1000.

8.7.5 P-value estimation

To calculated the p-value usually $P(\vec{n}) = \int P(\vec{n}\,|\lambda) P(\lambda)\, d\lambda$ has to be calculated for normalization. Apparently no algorithm is able to do this integration in our case but there is an elegant and fast method to estimate p-values which is described in the appendix of [81]. Here, the p-value is estimated using the Metropolis-Hastings algorithm. This algorithm is based on MCMC and is a method to obtain random samples of probability distributions for which direct sampling is difficult. As the counts in the fitted histograms are $\in \mathbb{N}_0$, a proposal distribution is chosen by the integer values just below $\lambda_{\text{best fit}}$ which is denoted by $\lfloor \lambda_{\text{best fit}} \rfloor$. In each sampling iteration each bin in each histogram is attempted to be randomly increased or decreased. The new value is randomly accepted or rejected and the probability is updated; values closer to $\lambda_{\text{best fit}}$ are more probable to be accepted. The likelihood of the new distribution, obtained with this methods, is compared to the likelihood of $\lambda_{\text{best fit}}$. Dividing the number of sampled distributions with a lower likelihood than $\lambda_{\text{best fit}}$ by the number of iterations gives the approximate p-value.

8.7.6 Global and marginalized mode

The global mode is the most probable fit parameter that is found by the MCMC algorithm while marginalizing over the nuisance parameters. BAT is not optimized to find the global mode and is "neither effective nor accurate" in doing so [76]. Nevertheless we mostly give that value to have a reference as it turns out to be quite stable. The marginalized mode is the most probable value for a parameter after marginalizing over all nuisance parameters. We use the root version of Minuit *TMinuit* to find all modes and call the most probable of them the *marginalized mode*. If the fit precision is high enough we obtain only one local mode in all posterior pdfs in this analysis. Hence, this local mode and the marginalized mode coincide. The uncertainty given is the smallest interval containing at least 68% of the posterior pdf and the marginalized mode.

8.8 Data selection and run configurations

A sketch and a table of the GERDA Phase I runs and their setup can be found in Appendix G. The Phase I GERDA setup consists of two so called arms. The first arm contains one string of detectors and the second arm consists of three detector strings. The configuration of the three string arm stays the same in all the Phase I run period. Run33, Run34 and Run35 were not included in the fits. Run33 is very unstable and in Run33 and Run34 the detector configuration was changed which leads to a higher background index for about 20 days. Run34 plus Run35 are about 32 days long which should be sufficient for the background index to decay to a normal level. Some of the detectors were unstable and had to be switched off after a while, which is why they were excluded in some later runs. The HV configurations of each run can be found in detail in Table G.4. All exclusions from this analysis are indicated.

8.8.1 Data cuts

Test pulser events and cosmic muon induced events are cut from the data; events with a detector multiplicity larger than 1 on the other hand are kept. The cut efficiency and therefore the detection efficiency would depend on which detector was included in the analysis. As the configuration of detectors suitable for analysis changes within the data sample, efficiencies would change for every run period. By including events with a detector multiplicity lager than 1 we keep one efficiency per detector. The respective data flags are listed in Table 8.7.

Table 8.7: Event flags which can be used for data cuts.

flag	description	kept/cut
isVetoed	muon induced event	cut
isTP	test pulser event	cut
multiplicity	number of det fired	kept

8.9 Final fit result

The final fit is done for all 13 detectors and Run25 to Run46 with the exception of Run33 to Run35. In Figure 8.7 the posterior pdf of the specific Activity A is plotted in the flat background model with fit precision *kHigh* and the sum fit function can be seen in Figure 8.8. Global and marginalized modes of fits with different precision for both background models are listed in Table 8.8. The number of local modes found in the posterior distribution gives a measure of how smooth the distribution is and how meaningful the statistical uncertainty is. The uncertainty is only meaningful if just one local mode is found. In general, the erfc background model has a higher p-value and thus seems to describe the data better. However, within uncertainties all values are very well compatible. Thus, as final fit value we take the value obtained with the flat background model and with precision kHigh

$$A = 91.5^{+2.3}_{-2.7}\ \mu\mathrm{Bq/kg} \tag{8.27}$$

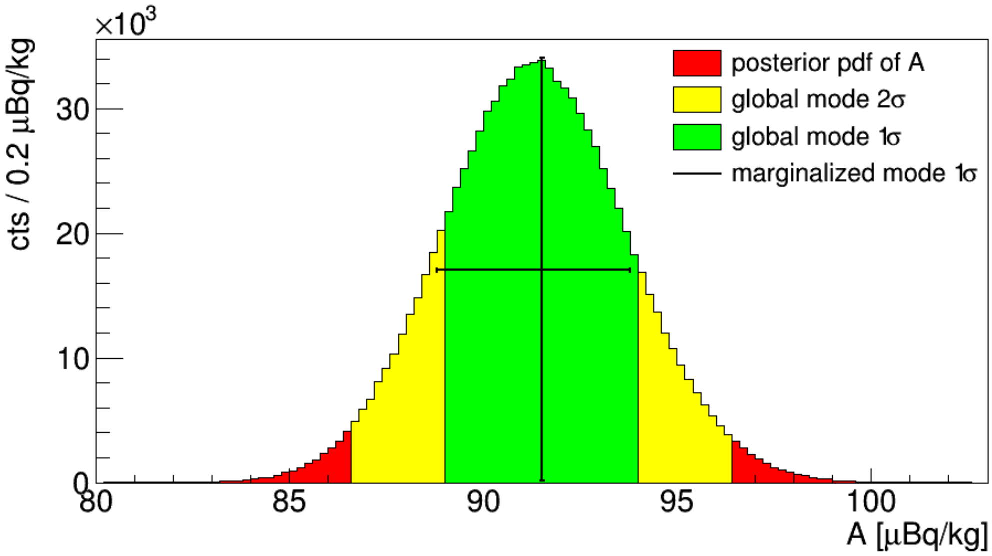

Figure 8.7: Posterior pdf of the specific activity A in the flat background model with fit precision *kHigh*.

Table 8.8: Final fit values of A [µBq/kg] in both background models and different fit precisions. The marginalized mode A (marg) is the highest local mode of all *modes* found. The uncertainties given are only meaningful if the number of local modes found is one.

model	fit precision	A (marg)	modes	A (glob)	p-value
flat	*kLow*	$89.9^{+0.3}_{-0.3}$	11	91.5 ± 2.4	0.39
flat	*kMedium*	$91.1^{+2.7}_{-2.3}$	1	91.5 ± 2.4	0.39
flat	*kHigh*	$91.5^{+2.3}_{-2.7}$	1	91.5 ± 2.4	0.39
erfc	*kLow*	$92.5^{+1.5}_{-4.5}$	1	91.5 ± 2.4	0.45

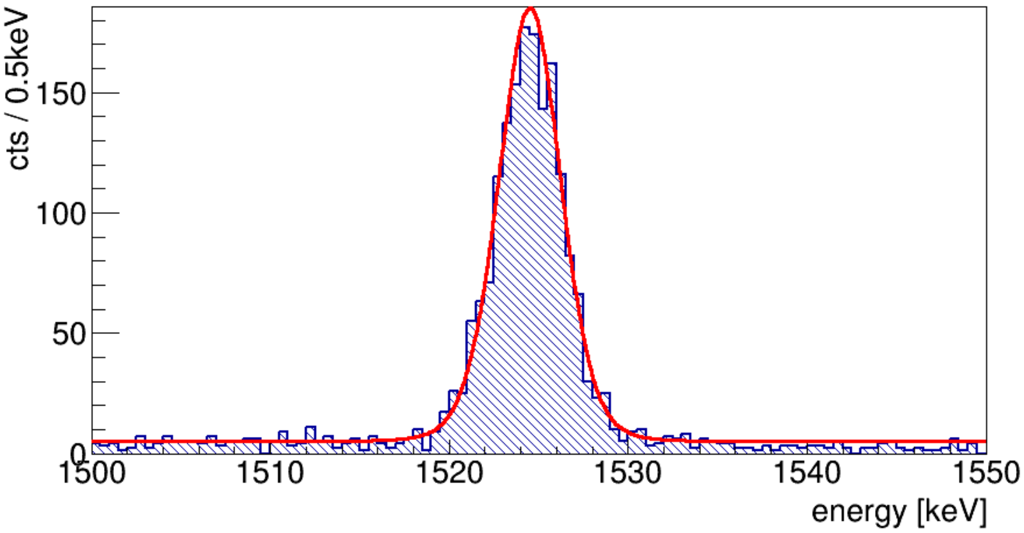

Figure 8.8: Sum histogram and combined fit function of all 13 detectors in the flat background model.

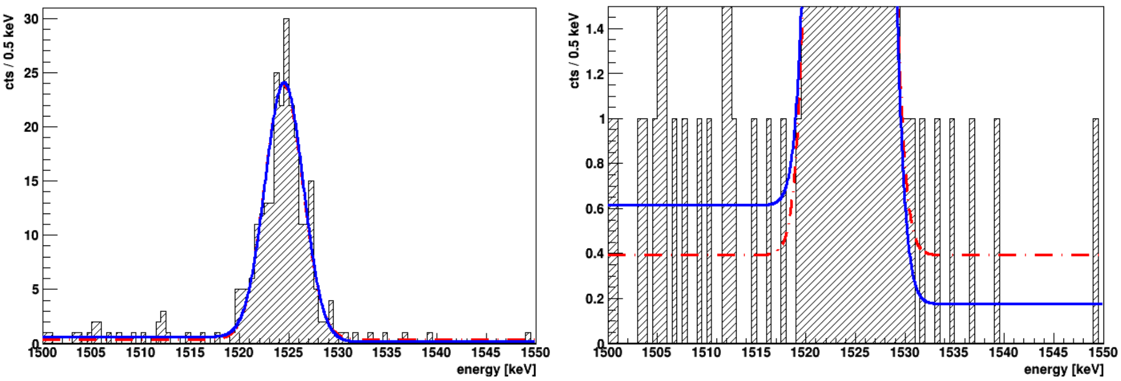

Figure 8.9: Comparison of background models for ANG2 with fit precision *kHigh*. Left) Full range; Right) Zoom on the background region. The flat background model is plotted in red dashed while the error function model is drawn in blue.

Table 8.9: Comparison of marginalized and global modes of fit parameter $A\,[\mu\text{Bq/kg}]$ in both background models with different fit precisions for detector ANG2.

model	precision	A (marg)	modes	A (glob)	p-value
flat	*kLow*	$93.5^{+3.7}_{-5.3}$	7	92.6 ± 6.4	0.50
flat	*kMedium*	$92.7^{+6.3}_{-6.3}$	3	92.6 ± 6.4	0.50
flat	*kHigh*	$93.5^{+5.7}_{-7.3}$	1	92.7 ± 6.4	0.50
flat	*kVeryHigh*	$92.5^{+7.5}_{-6.5}$	1	92.6 ± 6.4	0.50
erfc	*kLow*	$95.3^{+1.3}_{-0.1}$	13	92.7 ± 6.4	0.54
erfc	*kMedium*	$92.7^{+7.3}_{-5.5}$	2	92.7 ± 6.4	0.54
erfc	*kHigh*	$91.7^{+7.5}_{-5.5}$	1	92.7 ± 6.4	0.54

8.10 Crosschecks

In this section we want to compare fit precisions and the two different background models introduced in Section 8.7.2 and Section 8.7.3. In addition, we fit different parts of the data to check for the stability of the final result.

8.10.1 Comparison of fit precisions

In Table 8.9 the fitted specific activities for different fit precisions in both background models are listed for ANG2. All parameters are sampled with 1000 bins. Their ranges (see Table 8.6) are chosen such that no posterior distribution is cut. Note that the p-value is slightly higher for the refined background model and within uncertainties all values are well compatible. Also, already fit precision *kHigh* is sufficiently smooth in order to obtain just one local mode and the marginalized mode is in very good agreement with the value for precision *kVeryHigh*.

8.10.2 Comparison of flat and erfc background model

In Table 8.10 we compare the specific activity for all detectors in the two background models with fit precision *kHigh*. Both models are compatible and well within uncertainties. Note that the p-value is systematically higher or equal for the erfc background model.

Table 8.10: Comparison of fit parameter A [μBq/kg] of single detector fits in both background models and fit precision *kHigh*.

	flat background			erfc background		
detector	A (marg)	A (glob)	p-value	A (marg)	A (glob)	p-value
RG1	$73.1^{+6.7}_{-7.1}$	72.9 ± 6.7	0.30	$72.1^{+7.7}_{-6.1}$	72.9 ± 6.7	0.33
RG2	$101.9^{+9.3}_{-8.1}$	102.3 ± 8.6	0.88	$102.1^{+8.9}_{-8.5}$	102.3 ± 8.6	0.88
ANG2	$93.5^{+5.7}_{-7.3}$	92.7 ± 6.4	0.50	$91.7^{+7.5}_{-5.5}$	92.7 ± 6.4	0.54
ANG3	$91.3^{+7.5}_{-6.9}$	91.4 ± 7.2	0.58	$91.3^{+7.5}_{-7.1}$	91.4 ± 7.2	0.59
ANG4	$74.3^{+7.7}_{-5.3}$	75.4 ± 6.4	0.39	$74.5^{+7.5}_{-5.7}$	75.4 ± 6.4	0.40
ANG5	$100.1^{+8.5}_{-5.3}$	101.6 ± 6.8	0.38	$100.9^{+7.5}_{-6.3}$	101.6 ± 6.8	0.39
GTF112	$94.1^{+6.9}_{-5.3}$	94.7 ± 6.0	0.52	$94.3^{+6.5}_{-5.7}$	94.6 ± 6.0	0.58
GTF45	$107.1^{+14.1}_{-10.3}$	109.0 ± 12.2	0.25	$106.5^{+13.1}_{-11.1}$	108.4 ± 12.1	0.27
GTF32	$98.1^{+12.5}_{-11.3}$	98.9 ± 11.8	0.69	$96.5^{+13.1}_{-10.3}$	98.7 ± 11.8	0.70
GD32B	$119.9^{+21.9}_{-20.9}$	120.1 ± 21.3	0.45	$120.1^{+21.1}_{-21.3}$	120.1 ± 21.3	0.45
GD32C	$51.9^{+13.9}_{-12.7}$	51.9 ± 13.1	0.50	$52.3^{+13.3}_{-13.5}$	52.0 ± 13.1	0.50
GD32D	$89.7^{+18.9}_{-18.1}$	89.8 ± 18.6	0.44	$86.3^{+20.9}_{-15.7}$	89.9 ± 18.6	0.44
GD35B	$86.3^{+21.1}_{-13.1}$	89.7 ± 17.1	0.58	$88.5^{+17.5}_{-16.5}$	89.3 ± 17.0	0.59

Another issue we have to consider is computing time. The flat model is much less expensive than the refined model. It takes a full day fitting just one detector with precision *kMedium* with the erfc model which takes just hours with precision *kHigh* in the flat model. A combined fit with all 13 detectors has respectively 13 parameters more in the erfc model than in the flat model and is accordingly more expensive in computing time.

As fit parameters are compatible within uncertainties, the erfc model is preferable only for cosmetic reasons. Statistics is already good enough to see the different background levels on the right and on the left side of the γ-line by eye. Hence, the erfc model seems to represent the data better (see Figure 8.9) although the difference is marginal in the calculated specific activity.

8.10.3 Consistency checks

The fit result should be stable analyzing only parts of the data. We compare different run periods, detectors and detector strings. To save computing time, all comparisons are made using the flat background model with fit precision *kHigh*.

To compare different run periods we split the data in parts which are large enough for the fit to converge. In Figure 8.10 the following run periods are compared to each other: Run25-32 (174 d), Run36-39 (90 d), Run40-42 (88 d) and Run43-46 (98 d). They all agree very well within $1\,\sigma$.

A comparison of the single detectors can be found inFigure 8.11. If we suppose that all posterior pdfs are Gaussian six are compatible within $1\,\sigma$ with the final fit value, ten are compatible within $2\,\sigma$ and all are compatible within $3\,\sigma$.

The detector strings are all compatible well within $2\,\sigma$ (see Figure 8.12).

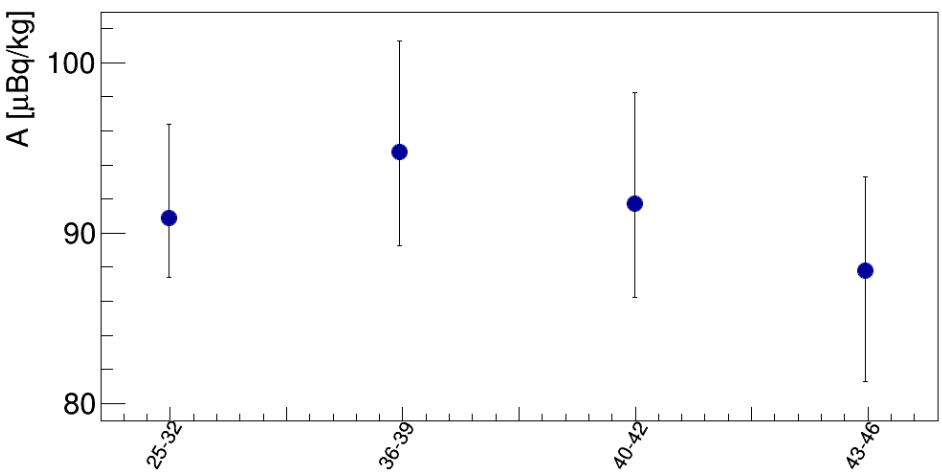

Figure 8.10: Stability of A fitting data from different run periods in the flat background model.

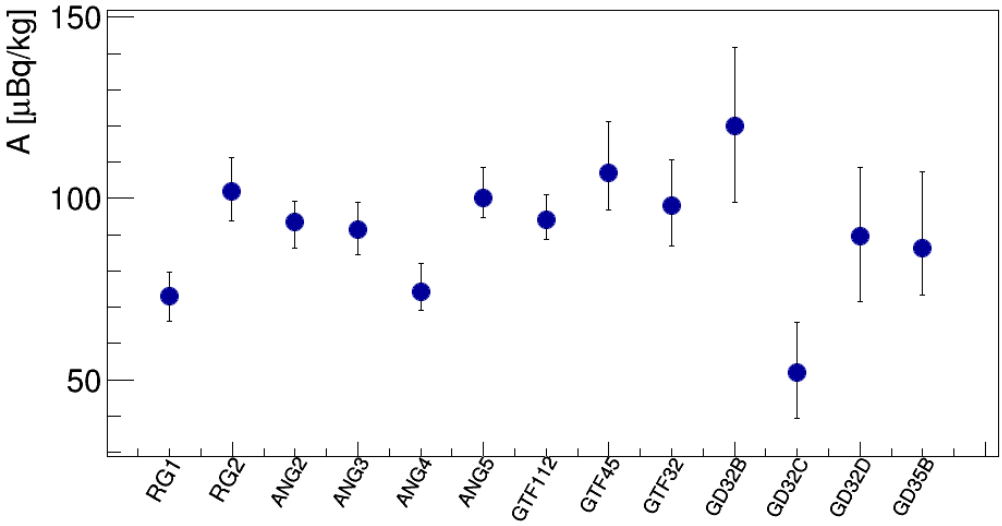

Figure 8.11: Stability of A fitting single detector data in the flat background model.

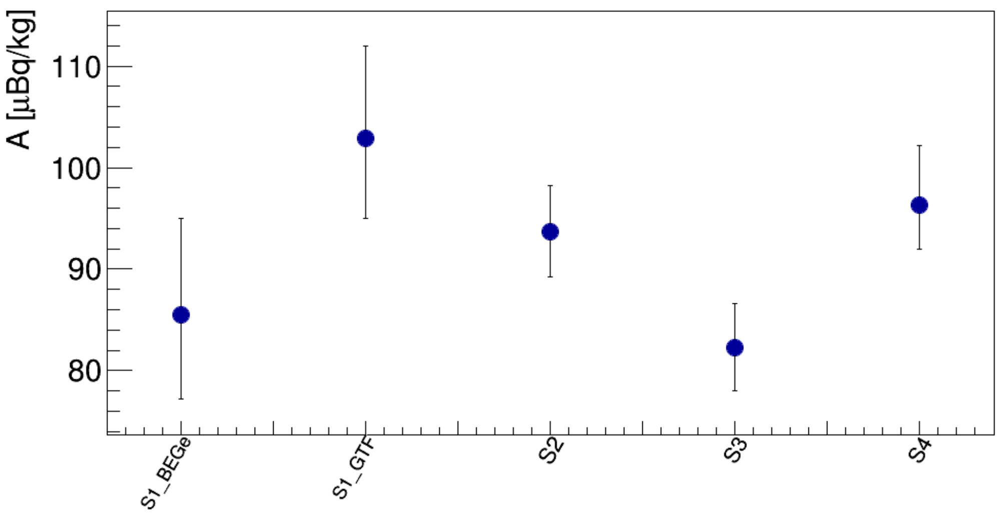

Figure 8.12: Stability of A fitting data from single detector strings in the flat background model. String 1 is plot in the GTF configuration (S1_GTF; Run25 – Run32) and in the BEGe configuration (S1_BEGe; Run36 – Run46)

8.11 Systematic uncertainties

The systematic uncertainties considered are

- **Active mass** As all Germanium detectors in the GERDA experiment are p-type they suffer non negligible efficiency loss due to the fact that the outer layer, which is Lithium diffused, is partly in-active. The thickness of this layer is only known with limited accuracy [82].
- **Dimensions in MaGe** Size of geometry details can influence the detection efficiency.
- **LAr density** Also an uncertainty on the LAr density affects the detection efficiency calculated using Monte Carlo simulation
- **Geometry details** Some details are only approximated and not implemented in full detail e.g. rounded corners of the detectors.
- **Decays outside sampling volume** As only a part of the LAr volume is simulated we consider a systematic error for decays out side the simulated volume
- **Non-uniformity** Inside the Mini-Shroud the distribution of ^{42}K decays is unknown. We consider two extreme cases to get a lower and an upper bound on the detection efficiency.
- **Geant4 physics** Deviations of cross-sections in the Monte Carlo simulation lead to an overall systematic uncertainty [83] which has to be taken into consideration for the detection efficiency.

The uncertainty on the non uniformity of ^{42}K decays inside the Mini-Shrouds is estimated by simulation of two extreme cases of the distribution. A sketch of these cases can be found in Figure 8.4. Outside the MS we assume the decays to be distributed homogeneously, inside the MS decays are simulated

1) Homogeneous to obtain a central value (*hom*)
2) Very close to the MS for a lower bound (*nearMS*)
3) Very close to the detectors for an upper bound (*nearDet*)

The detection efficiencies of all considered cases were evaluated and can be found in Table 8.3.

An average variation of efficiencies was calculated and the BAT fit was repeated using the lower and the upper bound of values assuming the uncertainty to be correlated. The variation in A from those fits was $\pm 4.4\,\%$. This value and all other systematic uncertainties considered can be found in Table 8.11. To obtain the final systematic uncertainty all values are summed in quadrature and the total uncertainty is multiplied by the final fit value.

8.12 Correction for ^{42}Ar lifetime

The value for the specific activity calculated as described above is averaged over the whole data taking phase. In reality A is exponentially decaying with the lifetime of ^{42}Ar: $T_{1/2} = (32.9 \pm 1.1)\,\mathrm{y}$ [74].

We suppose to be calculating an average value of A_a in the considered data taking period

$$A_\mathrm{a} = \frac{A_0}{t_2 - t_1} \cdot \int_{t_1}^{t_2} \exp\left(-\frac{\ln(2)}{T_{1/2}} \cdot t\right) \mathrm{d}t \tag{8.28}$$

Where t_1 is the start of Run25 and t_2 the end of Run46 after the LAr was put under ground. We want to know A_0, the equilibrium specific activity of ^{42}Ar in LAr above ground.

$$A_0 = A_\mathrm{a} \cdot \frac{t_2 - t_1}{\int_{t_1}^{t_2} \exp\left(-\frac{\ln(2)}{T_{1/2}} \cdot t\right) \mathrm{d}t} \tag{8.29}$$

The LAr was put under ground the 9th November 2007, exactly four years before Run25 started the 9th November 2011. With $t_1 = 4\,\mathrm{y}$, $t_2 - t_1 = 1.375\,\mathrm{y}$ and the final fit value A_a from Equation 8.27 we obtain

$$A_0 \approx (1.104 \pm 0.004) \cdot A_\mathrm{a} \tag{8.30}$$

The uncertainty is due to the uncertainty in the ^{42}Ar lifetime. The specific activity calculated with the BAT fit is about 10 % lower than it was when the Gerda LAr was brought underground. The uncertainty on this lifetime correction is with $\approx$ 0.4 % much lower than all other systematic uncertainties we consider in Section 8.11 and is therefore neglected in the following.

Table 8.11: Considered systematic uncertainties of the specific activity. The correlation is considered with respect to the other detectors.

systematic	correlation	value [%]
Active mass	no	2.9
Dimensions in MaGe	no	0.8
LAr density	yes	0.9
Geometry details	yes	2.8
Decays outside sampling volume	yes	0.9
Non-uniformity	yes	4.4
Geant4 physics	yes	4.0
	total	7.3

8.12.1 Equilibrium specific activity of ^{42}Ar above ground

The final fit value (see Equation 8.27) for the decay of ^{42}Ar is corrected using Equation 8.30. Finally, the systematic error is calculated with the values from Table 8.11. The final result for the equilibrium specific activity of ^{42}Ar in LAr is

$$A_0(^{42}\mathrm{Ar}) = 101.0^{+2.5}_{-3.0}(\mathrm{stat}) \pm 7.4(\mathrm{syst})\ \mu\mathrm{Bq/kg} \tag{8.31}$$

8.13 LArGe measurement

Data from the Gerda test facility Liquid Argon Germanium Experiment (LArGe) has also been used to determine the ^{42}Ar specific activity. A sample of LAr enriched in the isotope ^{42}Ar with known concentration was flushed into the LArGe cryostat. One Germanium detector (GTF44) was used for the analysis, encapsulated in a copper shroud. The count rates in the 1525 keV ^{42}K line were compared before and after flushing with the enriched LAr for different HV applied on the copper encapsulation. The final result was obtained by combining all values with a weighted average. The final result, uncorrected for the ^{42}Ar decay time, is

$$A_{\mathrm{LArGe}}(^{42}\mathrm{Ar}) = 65.6 \pm 3.7(\mathrm{stat}) \pm 13.5(\mathrm{syst})\ \mu\mathrm{Bq/kg} \tag{8.32}$$

If we suppose that the LAr inside LArGe has been underground for about 3 years and 8 months, which is roughly the middle of their data taking period, we have to correct this value by about 8% to be comparable with the final result of this analysis from Section 8.12.1. As corrected value we obtain

$$A^{\mathrm{corr}}_{\mathrm{LArGe}}(^{42}\mathrm{Ar}) = 70.8 \pm 4.0(\mathrm{stat}) \pm 14.6(\mathrm{syst})\ \mu\mathrm{Bq/kg} \tag{8.33}$$

8.14 Discussion

The ^{42}Ar specific activity obtained in this analysis is in very good agreement with the theoretical value quoted in [69]. However, the theoretical value is a qualitative guess. It results incompatible with the result of a previous measurement introduced in Section 8.2, which found an upper limit of 43 µBq/kg.

The final result is only compatible within 1.8 σ with the value obtained using LArGe data. There is some tension between the two analysis. It could well be that the HV cables which are connected to the detectors in the Gerda setup are not as well shielded as is assumed and residual electrical fields attract ^{42}K to the surface of the Mini-Shroud. But, no evidence has been found for a higher count rate of detectors closer to the top of the Mini-Shroud where the cables are located. By convection ^{42}K could be transported to the vicinity of the Mini-Shrouds and stay there due to an unknown mechanism.

Evaluating the count rate of the ^{42}K line right after applying HV on the detectors could give evidence for attraction of ^{42}K ions. Run33 and Run34 are taken with a new detector configuration and are the sole candidates for such a study in the

Gerda Phase I configuration. However, the count rate is so low that this study remains inconclusive. In the LArGe setup with augmented ^{42}Ar concentration a measurement like that would be possible but has never been performed. A Gerda like detector string should be deployed into LArGe and after a stabilization period the detectors switched on. The number of counts in the 1525 keV line of ^{42}K over time should give information about whether ^{42}K gets attracted towards the detectors and about how well the MS actually works as barrier and in closing the field lines of the electric field around the detectors in the Phase I setup.

In Gerda Phase II the analysis, presented in this chapter, can be refined with more statistics. It will substantially differ from this work as the MS in Phase II is transparent and a new veto system is installed using LAr scintillation light.

Chapter 9

Conclusions and Outlook

Finding Neutrinoless Double-Beta Decay ($0\nu\beta\beta$) decay is one of the holy grails of experimental neutrino physics. Its existence would clarify some of the problems regarding neutrino particles that are still unsolved. All experiments searching for $0\nu\beta\beta$ decay are low background experiments looking for an extremely rare — if existing — phenomenon. Their sensitivity depends strongly on the expected background: events which can mimic $0\nu\beta\beta$ decay. Hence, the reduction of background is essential to all of them. Background can be suppressed in various ways: by selecting radio-pure construction material, passive shielding against external γ and neutron radiation, by tagging cosmic muons using instrumented veto systems and by analyzing the form of pulses generated by signal events with respect to the background.

In the GERDA experiment $0\nu\beta\beta$ decay is searched for in the $0\nu\beta\beta$ candidate isotope ^{76}Ge. High Purity Germanium (HPGe) detectors, enriched in this isotope, serve as source and detector simultaneously. Recently, new detectors, of Broad Energy Germanium (BEGe) type, were produced to be hosted in the second experimental phase. They have excellent properties for pulse shape analysis, which will be one of the key features of the GERDA Phase II background reduction.

To create algorithms which effectively reduce background, based on the pulse shapes, signal-like events are extensively studied. The main property of $0\nu\beta\beta$ events is given by their localized energy deposition inside the detector crystals. An energy deposition in a volume smaller than the spatial resolution of the detector is commonly referred to as single site event (SSE). Hence, for studies of signal-like events pure samples of SSEs are prepared and analyzed. Furthermore, the study of SSEs permits to draw conclusions about the internal electric field properties of HPGe detectors. Pulse shape simulations rely on a precise description of these electric fields and comparison to real data is necessary in order to validate and improve them.

The standard procedure in GERDA to obtain SSE samples is the selection of events from a Double Escape Peak (DEP). They are observed in pair production processes if both created annihilation photons escape the detector volume. In that case the energy deposition is localized and in fact DEPs are dominated by SSEs. However, a part of hereby collected events is still due to background and the distribution of the selected events in the detector volume is extremely inhomogeneous. The probability for both annihilation photons to escape is largest on the detector surface and especially high in its corners.

For this work an experimental setup was built and optimized which is able to select pure samples of SSEs from distinct locations inside a HPGe detector: A test detector of BEGe type was implemented in the setup. The event selection of this system is based on Single Compton Events (singleCE) interactions, which meet the signal-like event condition, depositing energy in localized positions in the detector. In Compton scattering interactions, kinematics are defined by the scattering angle and the incident photon energy. singleCE interactions can, thus, be selected by tagging of the scattered photons and selection of the energies matching the scattering angle. A collimated photon beam, emitted by a ^{137}Cs source, is used to irradiate the BEGe detector. Additional HPGe detectors, with a semi-coaxial (Coax) geometry, are used to tag the photons which are Compton scattered inside the BEGe with a scattering angle of 90° with respect to the incident photon beam. Their angular acceptance is restricted by collimation in order to select a specific region inside the BEGe detector. The source can be moved, the BEGe can be rotated and the height at which the Coax detectors are placed with respect to the BEGe can be varied. In this manner, three-dimensional scans of the full volume of the BEGe detector can be made.

The dewar vessels of all detectors are connected to an automatized filling system and a safety High Voltage (HV) shut down prevents detector damage, in case a detector starts to warm up with its HV supply switched on. A data acquisition system (DAQ) system was assembled and tested which records the full event traces on disk. In order to record only true coincidences of the BEGe and one of the Coax detectors, a dedicated external trigger logic was designed and implemented. A calibration and optimization method for the external trigger was established and was successfully carried out. In order to augment the event rate a new collimator was designed and installed which can hold a ^{137}Cs source with an activity of about 780 MBq. The collimator is very easy to handle and effectively shields radiation in order to reduce personal risk.

This work contains a detailed description of the experimental setup, its way of operation and the results of the testing campaign undertaken.

An extensive characterization of the detectors used in the setup was carried out. This was necessary in order to optimize the energy reconstruction algorithm, determine the detector depletion and operational voltages and the energy resolutions. Furthermore, it was important to test the stability of the detector baselines in order to operate the system under stable conditions over a long time period. The internal geometry of the BEGe detector was studied in detail using a dedicated setup. Automatized fine grain surface scans give insight on the detector crystal geometry, the holder positioning and dimension, and on inhomogeneities of the outer contact layer. A comparison to a similar HPGe detector of P-type Point Contact (PPC) type was carried out. The fine grain surface scan can give valuable input to study the Compton coincidences in simulations.

A detailed description of the Compton coincidence setup was implemented in a Monte Carlo (MC) simulation framework. The simulations conducted allowed for an intense study of the energetic and spatial distribution of singleCE events with respect to Multiple Compton Events (multiCE) interactions. The energy selection of the BEGe as well as the Coax detectors were optimized in order to select confined singleCE events.

In a measurement campaign several locations of the BEGe detector were scanned at different HV values. The signal to background of the event samples was further improved using a descriptive parameter of the pulse shape. The selection of SSE samples with high purity was accomplished and the sample size of each location was large enough to compute average pulses for each scanned location. These average traces were found to be of high reproducibility. This enables a comparison of average pulses of BEGe detector regions and different HV values. Differences in the shape of the average pulse are observed when changing the scanned detector location or the HV on the BEGe detector. In particular it was found that the first part of the average pulse is most sensitive. The purity of the collected samples in function of the scanned location was analyzed and compared to the MC simulations. Conclusions can be drawn on the limitations of Compton coincidence measurements conducted with this experimental setup.

Finally, the purity of SSE samples was compared to the standard method used in the Gerda experiment. An uncollimated ^{228}Th spectrum was recorded and the SSE to background ratio of the DEP from the 2.6 MeV ^{208}Tl γ-line was analyzed. The purity of SSE samples from the Compton coincidence measurements proved to be superior in the surface regions of the BEGe detector where events from the DEP are located. Moreover, the Compton setup permits to collect SSEs from interior regions of the BEGe to which the DEP shows negligible sensitivity.

Future improvements of the Compton setup can be made by measuring at different scanning angles. The differential cross section for Compton scattering is larger for smaller scattering angles. This could augment the event rate and further improve the SSE to background ratio of the collected event samples.

The results from a first comparison of average pulse shapes is promising. A prospective key point is a more detailed scanning measurement of a BEGe detector and subsequent comparison to pulse shape simulations. The profile of the impurity concentration in a BEGe could be fine-tuned based on such measurements and improve the reliability of pulse shape simulations. Other detector geometries can be studied with the setup in order to compare their Pulse Shape Discrimination (PSD) power to the Gerda Phase II BEGe detectors and possibly more adapt geometries could be found.

Returning to $0\nu\beta\beta$ experiments in general and the GERDA experiment in particular, another important aspect in rare event searches is the full decomposition and analysis of background contributions. One major background component in GERDA Phase I is the isotope ^{42}Ar, which decays via β^- decay in ^{42}K. ^{42}K further decays via a $\beta-$ decay with an endpoint energy above the endpoint of the Two Neutrino Double-Beta Decay ($2\nu\beta\beta$) spectrum of ^{76}Ge. Thus, the continuous energy spectrum of the electrons can deposit energy in the region of $Q_{\beta\beta}$ contributing to the expected background of the GERDA experiment.

The specific activity of ^{42}Ar in the GERDA liquid Argon (LAr) was analyzed using a Bayesian approach. The unique, highly radiopure environment of GERDA permits this type of study. Two fit models were implemented in a Bayesian Analysis Framework to fit a γ-line of ^{42}K which is in secular equilibrium with ^{42}Ar. A binned maximum likelihood fit with four (five for the second fit model) nuisance parameters per detector and a common parameter for the activity was performed and the result was analyzed for its stability. The detection efficiencies, which introduce a major systematic uncertainty to the result, were calculated by means of MC simulations of part of the GERDA experimental setup. This permitted to study systematic effects introduced by inhomogeneities of the ^{42}K distribution in the LAr and provided a conservative estimate of the uncertainty on the efficiencies, which were then propagated to the activity.

This analysis is not only providing an estimate of the specific activity of ^{42}Ar in the GERDA LAr. Correcting the found value for the time the LAr was kept under ground it can be compared to other experimental results, and furthermore, to theoretical calculations regarding production mechanisms of ^{42}Ar in the atmosphere. This has been done as a last step of the analysis conducted in this work and the value is found compatible within $1.8\,\sigma$ with result found by the GERDA test facility LArGe and in very good agreement with a theoretical calculation based on a major production mechanisms of ^{42}Ar. However, the theoretical value is only an educated guess. More precise calculations are needed to fully comprehend the implications of the experimental value calculated in this thesis.

Appendix A

Multi-tier data structure and decoder implementation

The GERDA analysis program transforms data in a multi-tier structure approach. Raw data is called the *tier0* level data. A decoder step transforms tier0 level data in a compressed and rootified structure containing exactly the same information contained on tier0 level but compatible with all other GERDA analysis software. We call this the *tier1* level. In the next step transforms are applied to the traces and parameters like energy, current pulse amplitude and rise time are extracted. This information is contained on the *tier2* level of data analysis. Every higher analysis step is a higher level in the tier structure. E.g. the calibrated energy can be contained on a tier3 level.

In order to transform tier0 data into the tier1 rootified format an FADC specific decoder has to be implemented which reads the data from tier0 files and stores the event traces in a root tree. Also for data taken with the FADCs in this setup a dedicated decoder was implemented. The program Raw2MGDO has to be called with the option *-c LEGO* for the 100 MHz 4 channel FADC. A version for a 500 MHz 8 channel FADC has also been implemented and can be called via *-c LEGO_DIGI8*. The filename is handed with the option *-f*. FADC channels can be excluded from the transform with the *-e* option and the pre-trigger fraction f_{pre} of the trace can be handed calling the *-P* option. Per default all channels are processed with $f_{\mathrm{pre}} = 0.5$.

100 MHz digitizer	\$ Raw2MGDO	-c LEGO -f filename
500 MHz digitizer	\$ Raw2MGDO	-c LEGO_DIGI8 -f filename
Optional		-e FADC channel
		-P f_{pre}

Detectors with positive and negative voltage have to be analyzed separately as all data analysis works on positive pulses and negative traces get simply inverted. The polarity is expected to be the same in all channels for a tier0 → tier1 and tier1 → tier2 transformation.

Appendix B

Decay schemes of calibration sources

All decay schemes were taken from [73]. For some of them not all energy levels are shown, this is however indicated in the individual plots.

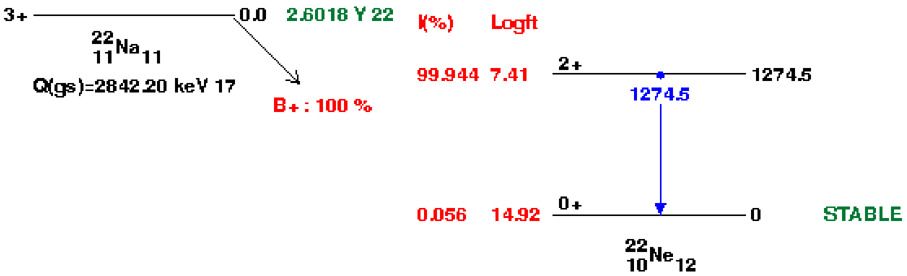

Figure B.1: Decay scheme of ^{22}Na.

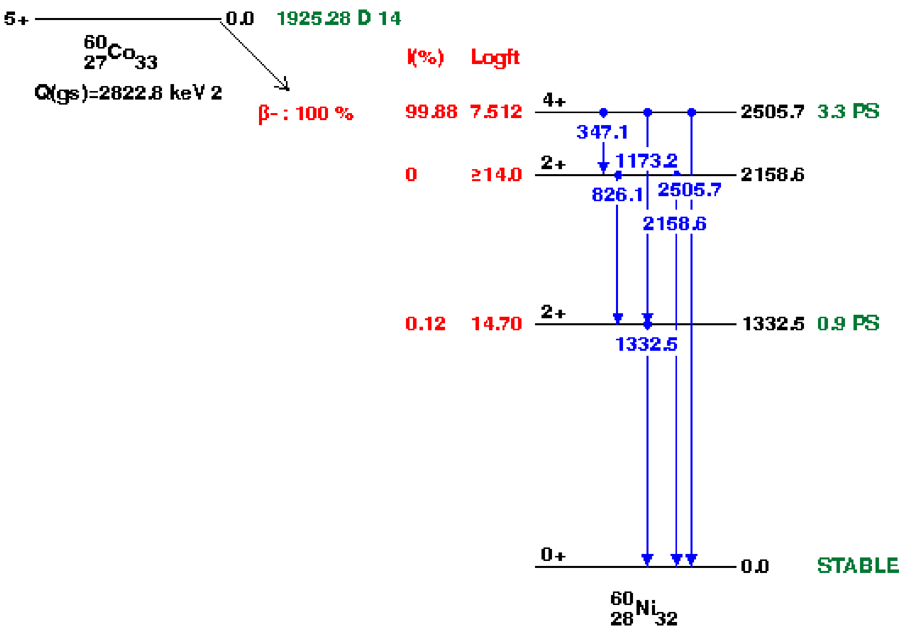

Figure B.2: Decay scheme of ^{60}Co.

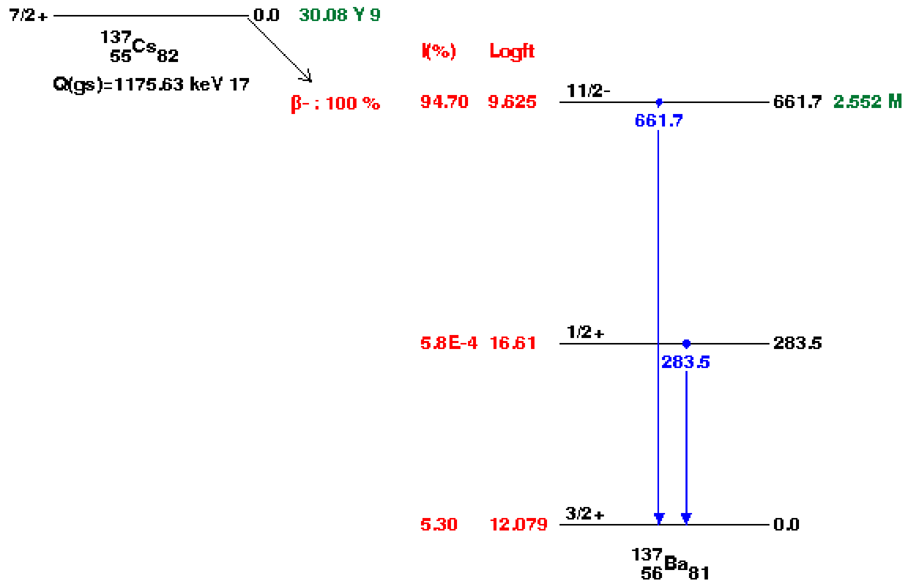

Figure B.3: Decay scheme of ^{137}Cs.

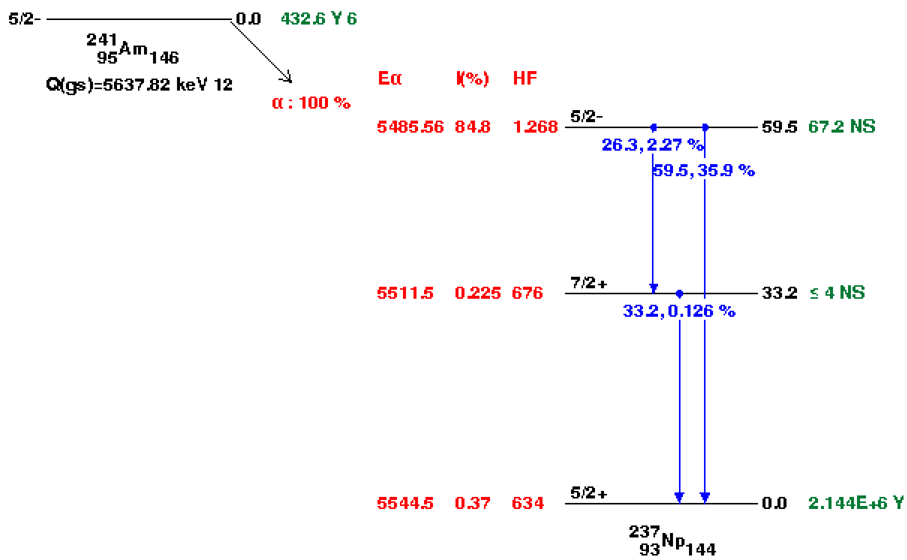

Figure B.4: Decay scheme of ^{241}Am for energy levels below 70 keV. Intensities of γ-lines indicated.

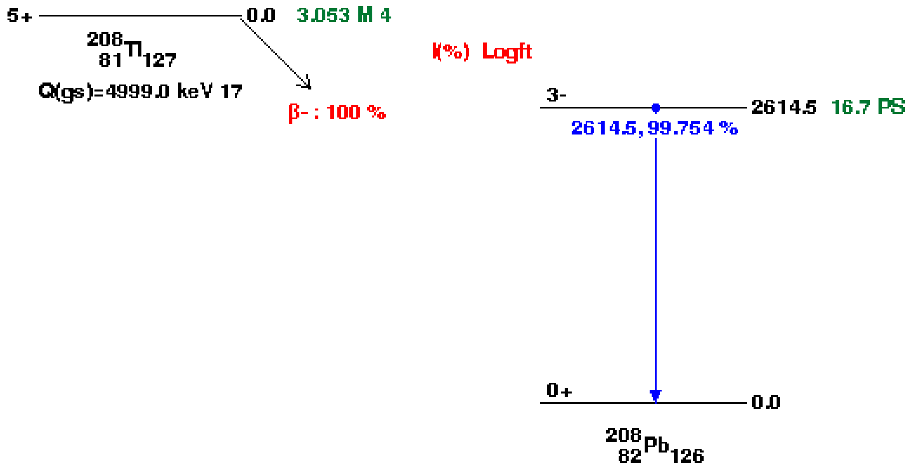

Figure B.5: Decay scheme of ^{208}Tl for energy levels below 3000 keV. Intensities of γ-lines indicated.

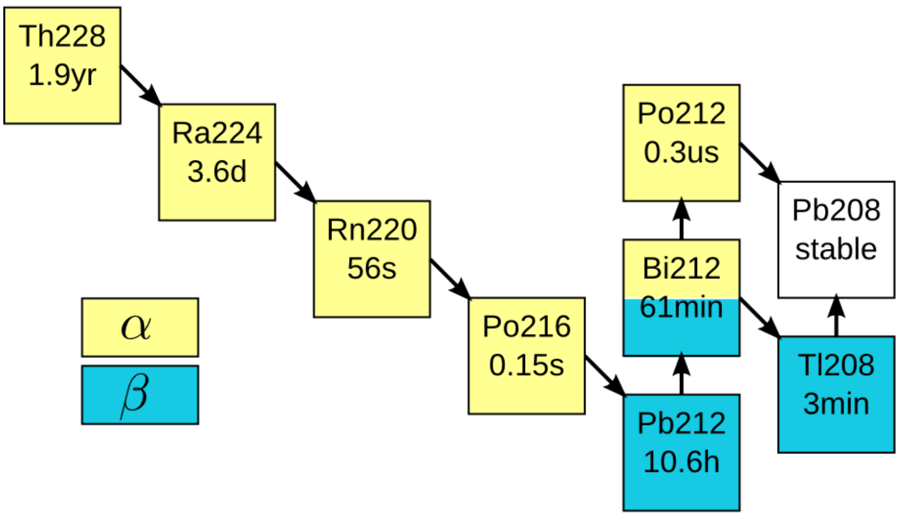

Figure B.6: Decay chain of ^{228}Th. Isotopes decaying via α in yellow, β decaying isotopes in blue, stable isotopes in white. The half-life of the decay is indicated below.

Appendix C

Full Width at f_w Maximum

To get the full width of a γ-line at some fraction f_w of the peak maximum (FWf_wM) the γ-line is fit using a Gaussian plus tail fit function (Equation 4.4). The corresponding x-value of the fit function is evaluated left and right of the peak centroid to satisfy $g(x) = f_w \cdot m_\mu$ and the difference is taken as the respective FWf_wM. m_μ is the maximum height of the Gaussian peak. The error is estimated as follows

$$\frac{\Delta \mathrm{FW}f_w\mathrm{M}}{\mathrm{FW}f_w\mathrm{M}} = \frac{\Delta\sigma}{\sigma} \tag{C.1}$$

Where σ and $\Delta\sigma$ are the standard deviation and its uncertainty from the Gaussian plus tail fit function. When calculating a fraction FWf_wM/FWHM the errors are assumed to be fully correlated and therefore

$$\begin{aligned}\frac{\Delta(\mathrm{FW}f_w\mathrm{M}/\mathrm{FWHM})}{(\mathrm{FW}f_w\mathrm{M}/\mathrm{FWHM})} &= \sqrt{\frac{\Delta \mathrm{FW}f_w\mathrm{M}}{\mathrm{FW}f_w\mathrm{M}}^2 + \frac{\Delta\mathrm{FWHM}}{\mathrm{FWHM}}^2 - 2\frac{\Delta \mathrm{FW}f_w\mathrm{M}}{\mathrm{FW}f_w\mathrm{M}}\frac{\Delta\mathrm{FWHM}}{\mathrm{FWHM}}} \\ &= 0\end{aligned} \tag{C.2}$$

Appendix D

Dual Timer Unit gate calibration

In Figure D.1 individual dual timer unit (DTU) gate calibration plots can be found. Without cuts and with standard quality and an energy cut on ^{22}Na annihilation γs of (511 ± 5) keV in red. With standard cuts we intend that all events satisfy the following criteria: 1) No over- or under-flow from the dynamic range of the Flash Analog to Digital Converter (FADC). 2) No error in event processing. 3) Number of found triggers is one. All coincident detectors behave very similar and a DTU gate size of 2 µs is fine for all of them.

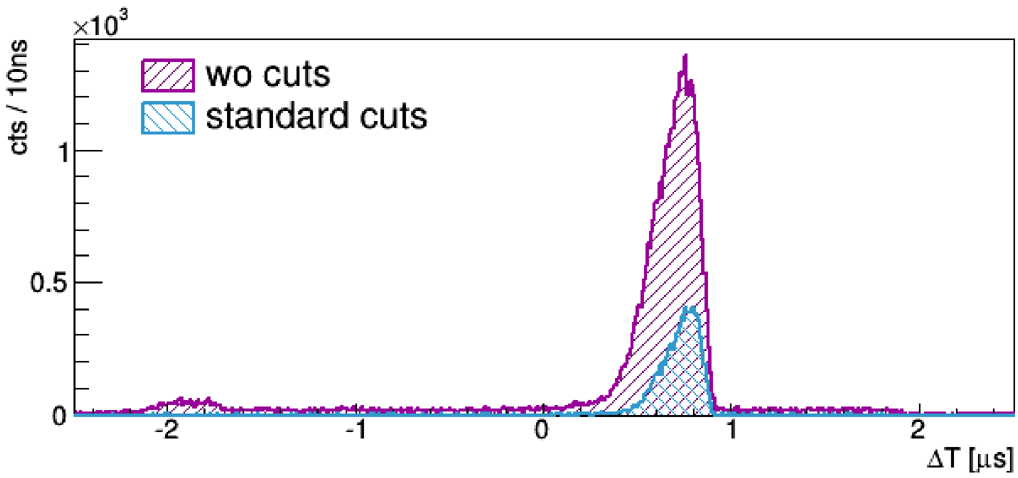

Figure D.1: DTU gate size calibration plot. Trigger time difference $\Delta T = T(\mathrm{BEGe}) - T(\mathrm{Coax})$ for BEGe and Coax1 of ^{22}Na coincidence measurements without data cuts and with standard quality and an energy cut (511 ± 5)keV. The small bump at -2µs appears because all event triggers before the start of trigger search are accumulated there.

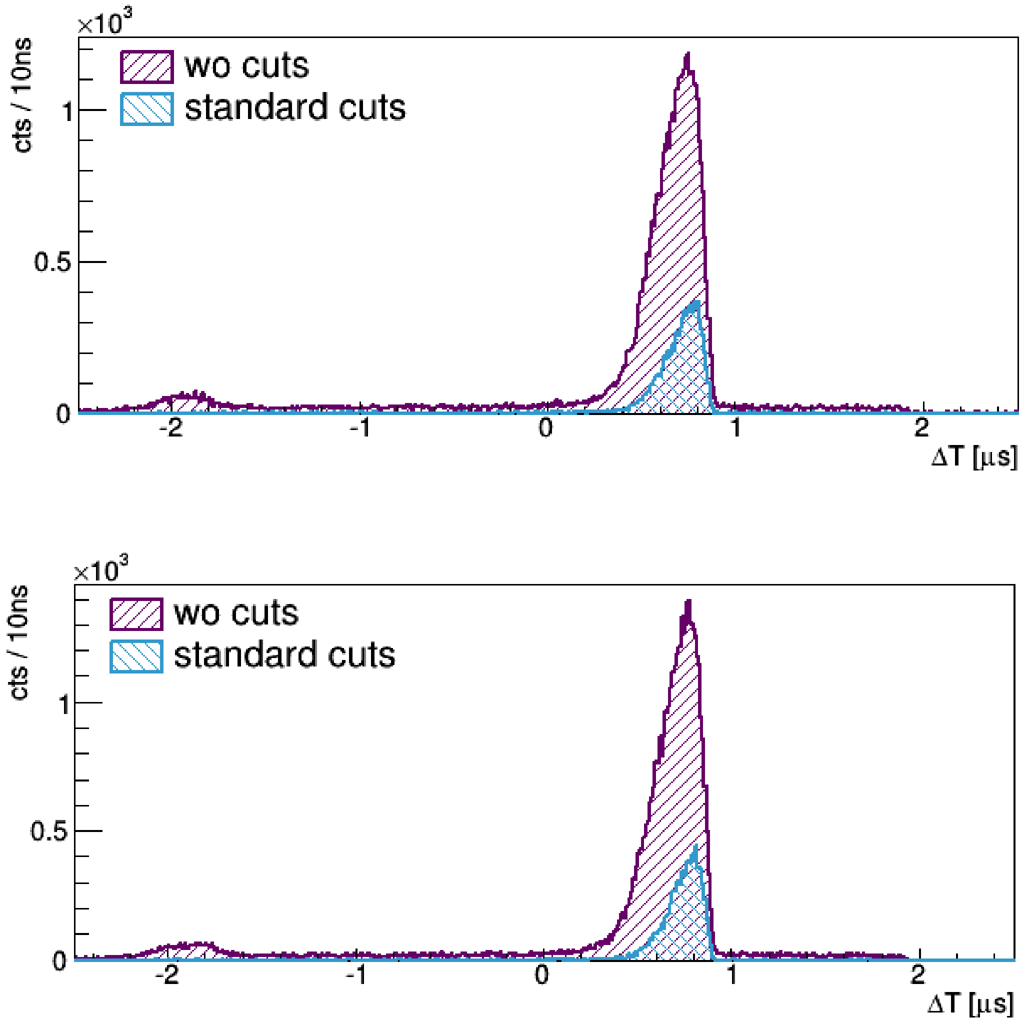

Figure D.1 continued for BEGe and Coax3 (top) BEGe and Coax3 (bottom).

Appendix E

Coincidence Monte Carlo simulation options

Some geometry details are implemented variable in size. The options that can be chosen and a short description can be found here

BEGe cryostat dimensions

/MG/geometry/LEGOTable/CryostatWindowThickness
Sets cryostat window thickness, which is the front part [mm]

/MG/geometry/LEGOTable/CryostatWallThickness
Sets cryostat wall thickness, which is the side part [mm]

/MG/geometry/LEGOTable/CryostatDiameter
Sets cryostat diameter [mm]

/MG/geometry/LEGOTable/CryostatHeight
Sets cryostat height [mm]

BEGe Xtal dimensions

/MG/geometry/LEGOTable/XtalDiameter
Sets crystal diameter (incl. DL) [mm]

/MG/geometry/LEGOTable/XtalHeight
Sets crystal height (incl. DL) [mm]

/MG/geometry/LEGOTable/XtalDistanceToWindow
Sets distance of crystal top to cryostat window [mm]

/MG/geometry/LEGOTable/XtalDitchInnerRadius
Sets inner radius of groove [mm]

/MG/geometry/LEGOTable/XtalDitchOuterRadius
Sets outer radius of groove [mm]

/MG/geometry/LEGOTable/XtalDitchDepth
Sets depth of groove [mm]

/MG/geometry/LEGOTable/XtalDitchOnBottom
Sets the ditch to a side of the detector (default: bottom side)

/MG/geometry/LEGOTable/XtalCornerDiameter
Sets diameter of top/bottom side with edge [mm]

/MG/geometry/LEGOTable/XtalCornerHeight
Sets height from top/bottom side to the end of the edge [mm]

/MG/geometry/LEGOTable/XtalCornerOnBottom
Sets the edge to a side of the detector (default: top side)

/MG/geometry/LEGOTable/XtalMaterial
Sets the detector material type. Available candidates are: (EnrichedGe DepletedGe NaturalGe)

Source collimator properties

/MG/geometry/LEGOTable/SourceCollimated
Use collimator for source or no. Default is true.

/MG/geometry/LEGOTable/SourceCollimatorCryoDistance
Sets distance of the source collimator to the BEGe cryostat

/MG/geometry/LEGOTable/SetCollimatorPosition
Sets the position of the collimator and the source in x direction [mm] 0 position is the middle of the detector

/MG/geometry/LEGOTable/SourceCollimatorLength
Sets the length of the collimator for the source. [mm]

/MG/geometry/LEGOTable/SourceBeamWidth
Sets the width of the beam in the source collimator [mm]

Source configuration

/MG/geometry/LEGOTable/SourceType
Sets the source type. Available candidates are: ("Cs137 Pointlike Tueb HS7 HS7like") Cs137 is the realistic source geometry of the string source

Scanning height and angle

/MG/geometry/LEGOTable/ScanningHeight
Sets distance of table and endcap of cryostat [mm]

/MG/geometry/LEGOTable/ScanningAngle
Set scanning angle starting from horizontal scanning and tilting the coaxial detectors towards the vertical 0deg here are 90deg Compton angle, 30deg here are 60deg Compton angle, 45deg here are 45deg Compton angle

BEGe holder configuration

/MG/geometry/LEGOTable/ActivateDepBEGeCryostatHolders
Activates the holder, cup and base for a depleted BEGe

Coincident Coax detectors

/MG/geometry/LEGOTable/CoincidentDetConfiguration
Sets the configuration of the coincident coaxial detectors. The numbering is clockwise starting with the x>0 and y>0 quadrant. Add 8 for the first 4 for the second 2 for the third and 1 for the fourth coax. Example: 8+4+2+1=15 all coax are active. Values between 0 (no coax) and 15 (all coax).

Coincident Coax collimators

/MG/geometry/LEGOTable/CollimatorMaterial
Sets material of source and coaxial collimators for studies only. Options are: lead, gold, copper and lcHybrid which is a hybrid of lead and half copper.

/MG/geometry/LEGOTable/CollimatorOpening
Sets the opening of the collimators. [mm]

/MG/geometry/LEGOTable/CollimatorLength
Sets the coaxial collimator length.[mm]
/MG/geometry/LEGOTable/CollimatorBEGeCryoDistance
Sets the distance from the BEGe cryo to the coaxial collimators. [mm]

/MG/geometry/LEGOTable/CollimatorCoaxCryoDistance
Sets distance from coaxial collimators to coaxial cryostat [mm]

Appendix F

Specific activity of ^{42}Ar from relative abundance

The specific activity of ^{42}Ar in LAr can be calculated from the relative abundance:

$$A(^{42}\mathrm{Ar}) = \frac{N_A}{m_a(^{40}\mathrm{Ar})} \cdot \frac{^{42}\mathrm{Ar}}{^{40}\mathrm{Ar}} \cdot \left(1 - \exp\left(-\frac{\ln(2)}{T_{1/2}} \cdot 1\,\mathrm{s}\right)\right) \approx \frac{^{42}\mathrm{Ar}}{^{40}\mathrm{Ar}} \frac{\mu\mathrm{Bq/kg}}{10^{-22}} \tag{F.1}$$

with

- Avogadro's number $N_A \approx 6 \cdot 10^{23}\,\mathrm{mol}^{-1}$,
- the molar mass of ^{40}Ar $m_a(^{40}\mathrm{Ar}) \approx 4 \cdot 10^{-2}\,\mathrm{kg/mol}$,
- and the half-life of ^{42}Ar $T_{1/2} = 32.9\,\mathrm{y} \approx 1.038 \cdot 10^{9}\,\mathrm{s}$

Hence, for a relative abundance of $^{42}\mathrm{Ar}/^{40}\mathrm{Ar} = 7.4 \cdot 10^{-22}$ we find the corresponding specific activity $A(^{42}\mathrm{Ar}) \approx 7.4\,\mu\mathrm{Bq/kg}$.

Appendix G

GERDA run setup

Figure G.1: Positioning of GERDA Phase I strings.

Table G.1: String setup of the Phase I runs. The strings are numbered S1 - S4 where S1 is the string in the one-string arm and S2 - S4 belong to the three-string arm as can be seen in figure G.1.

run	S1	S2	S3	S4
	GTF45	GTF112	RG1	ANG3
25-32	GTF32	ANG2	ANG4	ANG5
	-	ANG1	RG2	RG3
		GTF112	RG1	ANG3
33	-	ANG2	ANG4	ANG5
	-	ANG1	RG2	RG3
	GD32B	GTF112	RG1	ANG3
	GD32C	ANG2	ANG4	ANG5
34-46	GD32D	ANG1	RG2	RG3
	GD35B	-	-	
	GD35C	-	-	

Table G.2: Livetimes of the Phase I runs.

Run	livetime [d]	Run	livetime [d]	Run	livetime [d]
Run25	20.5105	Run35	17.7713	Run44a	1.42237
Run26	39.2802	Run36	37.745	Run44	22.8399
Run27	5.18356	Run37	23.4621	Run45	33.1296
Run28	9.57194	Run38	13.8776	Run46a	12.1286
Run29	20.4123	Run39a	15.277	Run46b	5.6078
Run30	30.9436	Run39b	9.46787		
Run31	21.6045	Run40	34.534		
Run32	26.6037	Run41	21.4982		
Run33	11.2161	Run42	32.0353		
Run34	14.8195	Run43	22.7819		

Table G.3: Detector total masses [82, 84].

detector	total mass [g]	detector	total mass [g]
ANG1	969	GTF112	2957
ANG2	2878	GTF45	2312
ANG3	2447	GTF32	2321
ANG4	2401	GD32B	716
ANG5	2782	GD32C	743
RG1	2152	GD32D	720
RG2	2194	GD35B	810
RG3	2121	GD35C	634

Table G.4: Detector High Voltage settings in the Gerda Phase I runs. Runs or detectors which are listed in red are completely excluded from ^{42}Ar analysis. If no voltage is given | means the detector is present in the setup and hasn't changed voltage. An empty space means the detector is not present in the setup. If the voltage value is given in red, the detector in the respective run is excluded from ^{42}Ar analysis.

	ANG			GD					RG			GTF	
run	1	2/3/4	5	32B	32C	32D	35B	35C	1	2	3	112	32/45
25	4.0	3.5	2.5						4.5	4.0	3.2	3.0	-3.0
26	|	|	|						|	|	2.5	|	|
27	|	|	|						|	|	|	|	|
28	|	|	|						|	|	2.3	|	|
29	|	|	|						|	|	2.0	|	|
30	2.0	|	|						|	|	1.0	|	|
31	|	|	|						|	|	0.0	|	|
32	1.5	|	|						|	|	|	|	|
33	0.0	|	|						|	|	|	|	
34	|	|	|						|	|	|	|	
35	|	|	|	3.5	3.5	3.5	3.5	3.5	|	|	|	|	
36	|	|	|	|	|	|	|	|	|	|	|	|	
37	|	|	|	3.5	|	|	|	|	|	|	|	|	
38	|	|	|	|	|	3.5	|	|	|	|	|	|	
39a	|	|	|	|	|	|	|	|	|	|	|	|	
39b	|	|	|	|	|	|	|	|	|	|	|	|	
40	|	|	|	|	|	|	|	|	|	3.5	|	|	
41	|	|	|	|	|	|	|	|	|	|	|	|	
42	|	|	|	|	|	|	|	|	|	|	|	|	
43	|	|	|	|	|	|	|	|	|	|	|	|	
44	|	|	|	|	|	|	|	|	|	2.0	|	|	
45	|	|	|	|	|	|	|	|	|	2.0	|	|	
46a	|	|	|	|	|	|	|	|	|	2.0	|	|	
46b	|	|	|	|	|	3.5	|	|	|	2.0	|	|	

Appendix H

Energy resolution plots

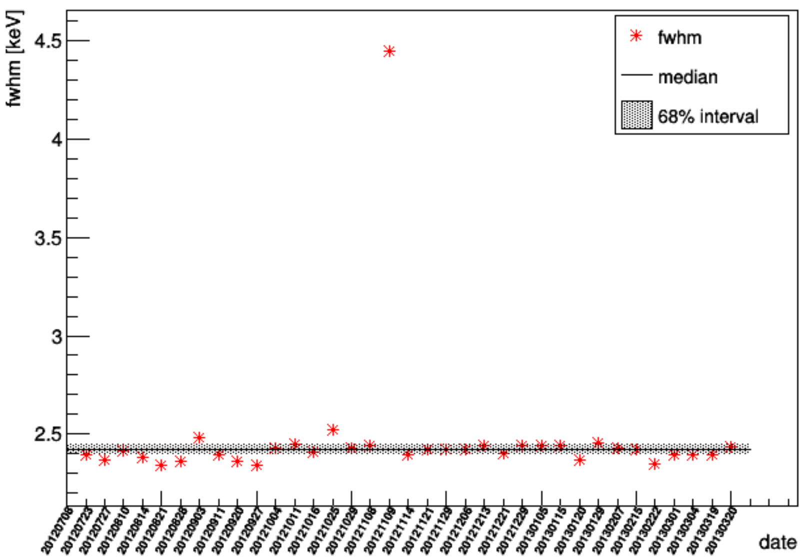

Figure H.1: FWHM from calibration data between 2012-07-08 and 2013-03-20 of GD32B. The black line indicates the median and the smallest 68% interval is indicated with a dotted area.

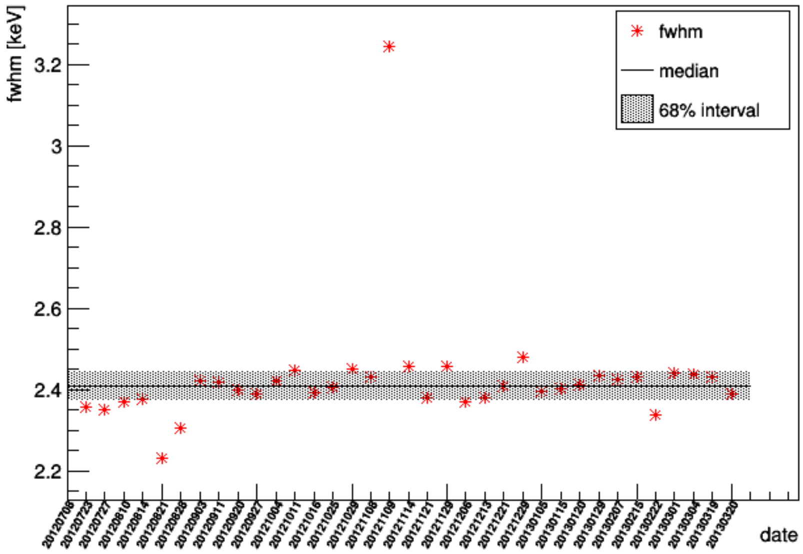

Figure H.1 (cont.): GD32C

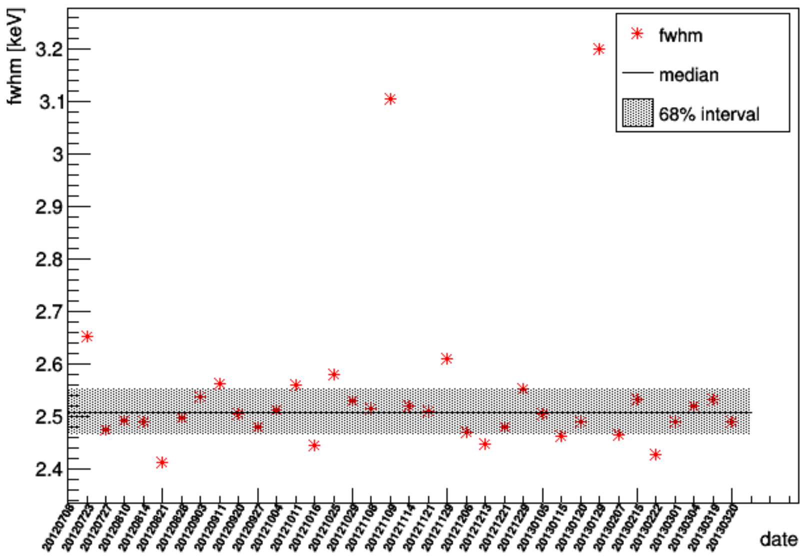

Figure H.1 (cont.): GD32D

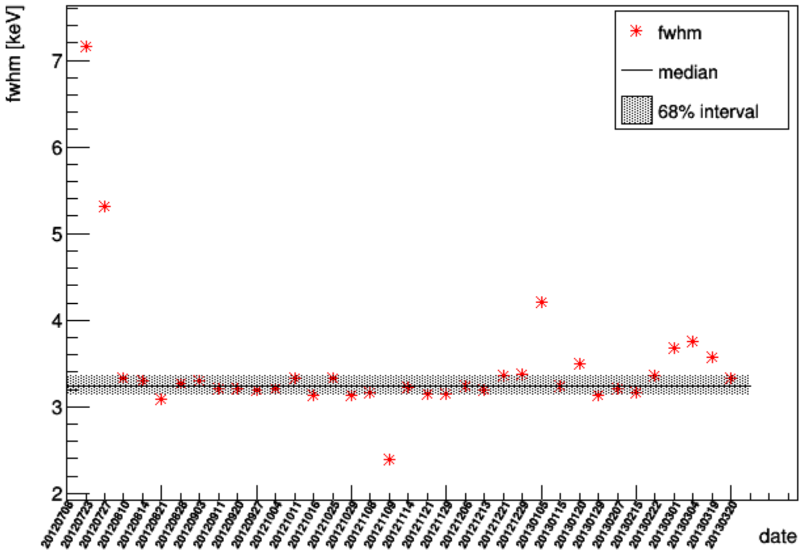

Figure H.1 (cont.): GD35B

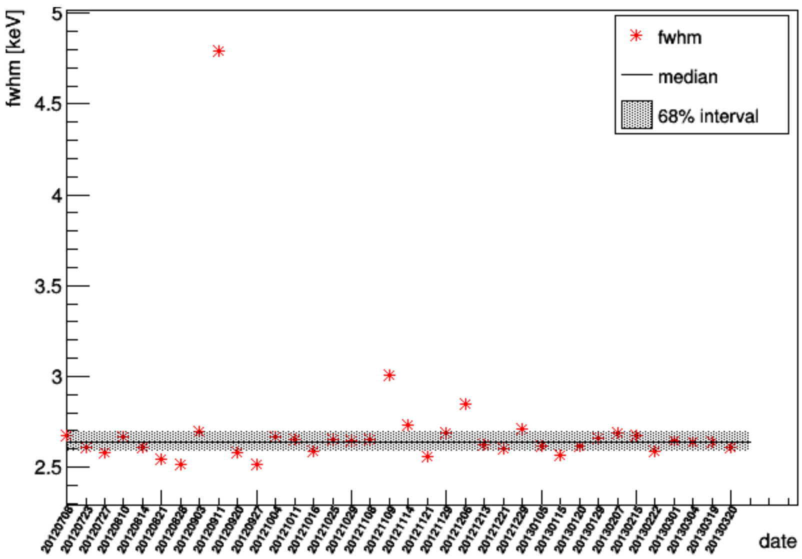

Figure H.1 (cont.): GD35C

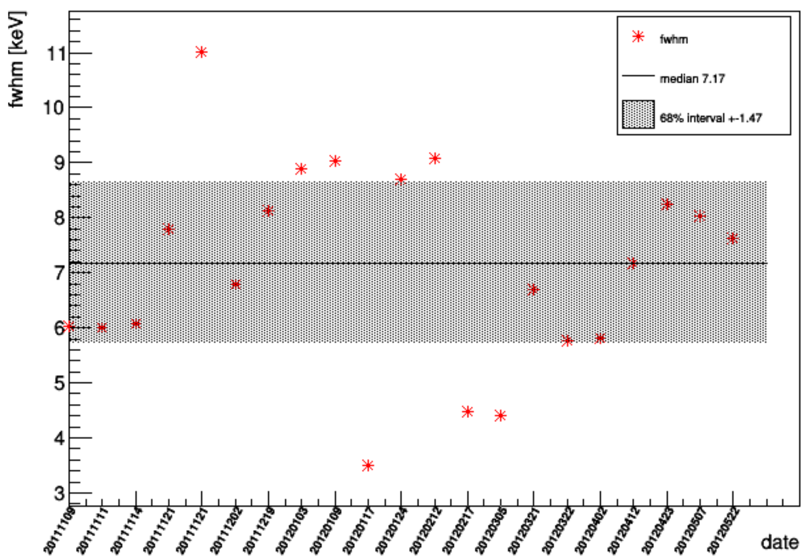

Figure H.2: FWHM from calibration data between 2011-11-09 and 2012-05-22 of GTF45. The black line indicates the median and the smallest 68% interval is indicated with a dotted area.

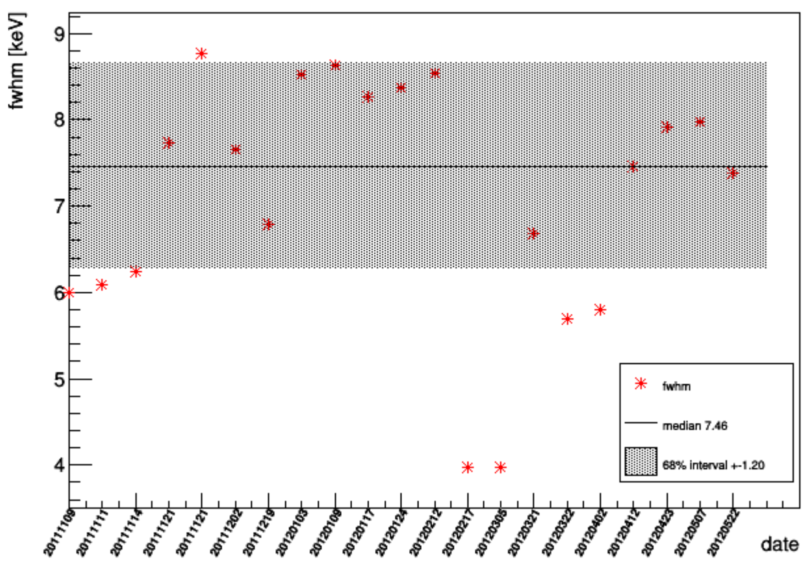

Figure H.2 (cont.): GTF32

List of Figures

List of Tables

List of Acronyms

$\beta\beta$	Double-Beta Decay
$0\nu\beta\beta$	Neutrinoless Double-Beta Decay
$2\nu\beta\beta$	Ordinary Double-Beta Decay
BAO	Baryon Acoustic Oscillations
BAT	Bayesian Analysis Toolkit
BEGe	Broad Energy Germanium
BI	background index
BKG	background
BL	baseline
CMB	Cosmic Microwave Background
Coax	semi-coaxial detector
CP	Charge Parity
CSDA	continuous-slowing-down approximation
DAQ	data acquisition system
DEP	Double Escape Peak
DTU	dual timer unit
erfc	inverse error function

FADC Flash ADC

FEP Full Energy Peak

FWHM Full Width at Half Maximum

FWTM Full Width at one Tenth Maximum

FWFM Full Width at one Fiftieth Maximum

GUI Graphical User Interface

GERDA Germanium Detector Array experiment

HDM Heidelberg-Moscow experiment

HPGe High Purity Germanium

HV High Voltage

IGEX International Germanium Experiment

IH inverted hierarchy

INFN Istituto Nazionale di Fisica Nucleare

LAr liquid Argon

LArGe Liquid Argon Germanium Experiment

LN_2 liquid Nitrogen

LNGS Laboratori Nazionali del Gran Sasso

LNV Lepton Number Violating

LV Low Voltage

MC Monte Carlo

MCA multichannel analyzer

MCMC Markov Chain Monte Carlo

multiCE Multiple Compton Events

MPIK Max-Planck-Institute for Nuclear Physics

MS Mini-Shroud

MSE multiple site event

MWA moving window average

NH	normal hierarchy
NME	Nuclear Matrix Element
pdf	probability density function
PMNS	Pontecorvo-Maki-Nakagawa-Sakata
PPC	P-type Point Contact
PSA	Pulse Shape Analysis
PSD	Pulse Shape Discrimination
PreAmp	Preamplifier
QD	quasi-degeneracy
ROI	Region of Interest
singleCE	Single Compton Events
SEP	Single Escape Peak
SM	Standard Model
SpecAmp	Spectroscopy Amplifier
SSE	single site event

Bibliography

[1] Bettini, A. *Introduction to elementary particle physics.* Cambridge University Press, 2014.

[2] Lesgourgues, J. and Pastor, S. *Massive neutrinos and cosmology.* Physics Reports, volume 429(6):pp. 307, 2006. doi:10.1016/j.physrep.2006.04.001.

[3] Cleveland, B. T., et al. *Measurement of the Solar Electron Neutrino Flux with the Homestake Chlorine Detector.* The Astrophysical Journal, volume 496(1):p. 505, 1998. doi:10.1086/305343.

[4] Fukuda, S. et al. *Tau Neutrinos Favored over Sterile Neutrinos in Atmospheric Muon Neutrino Oscillations.* Phys.Rev.Lett., volume 85(19):pp. 3999, Nov 2000. doi:10.1103/PhysRevLett.85.3999.

[5] Ahmad, Q. R. et al. *Measurement of the Rate of $\nu_e + d \to p + p + e^-$ Interactions Produced by ^8B Solar Neutrinos at the Sudbury Neutrino Observatory.* Phys.Rev.Lett., volume 87(7):p. 071301, Jul 2001. doi:10.1103/PhysRevLett.87.071301.

[6] Wolfenstein, L. *CP properties of Majorana neutrinos and double beta decay.* Physics Letters B, volume 107(1):pp. 77, 1981. doi:10.1016/0370-2693(81)91151-5.

[7] Kayser, B. *CPT, CP, and C phases, and their effects, in Majorana-particle processes.* Physical Review D, volume 30(5):p. 1023, 1984. doi:10.1103/PhysRevD.30.1023.

[8] Majorana, E. *Teoria simmetrica dell'elettrone e del positrone.* Il Nuovo Cimento (1924-1942), volume 14(4):pp. 171, 1937. doi:10.1007/BF02961314.

[9] Rodejohann, W. *Neutrino-less double beta decay and particle physics.* International Journal of Modern Physics E, volume 20(09):pp. 1833, 2011. doi:10.1142/S0218301311020186.

[10] Nakamura, K. and Petcov, S. T. *Neutrino mass, mixing, and oscillations.* RPP2014, 2014.

[11] Cremonesi, O. and Pavan, M. *Challenges in Double Beta Decay.* Advances in High Energy Physics, volume 2014, 2014. doi:10.1155/2014/951432.

[12] Auger, M., et al. *Search for Neutrinoless Double-Beta Decay in* ^{136}Xe *with EXO-200*. Phys.Rev.Lett., volume 109(3):p. 032505, Jul 2012. doi:10.1103/PhysRevLett.109.032505.

[13] The KamLAND-Zen Collaboration. *Limit on Neutrinoless Decay of Xe-136 from the First Phase of KamLAND-Zen and Comparison with the Positive Claim in Ge-76*. Physical Review Letters, 2014. doi:10.1103/PhysRevLett.110.062502.

[14] Ackermann, K.-H., et al. *The* GERDA *experiment for the search of* $0\nu\beta\beta$ *decay in* ^{76}*Ge*. The European Physical Journal C, volume 73(3), 2013. doi:10.1140/epjc/s10052-013-2330-0.

[15] Artusa, D. R., et al. *Searching for neutrinoless double-beta decay of* ^{130}*Te with CUORE*. Advances in High Energy Physics, volume 2015, 2015. doi:10.1155/2015/879871.

[16] Abgrall, N., et al. *The* MAJORANA DEMONSTRATOR *Neutrinoless Double-Beta Decay Experiment*. Advances in High Energy Physics, volume 2014, 2014. doi:10.1155/2014/365432.

[17] Ebert, J., et al. *Current status and future perspectives of the COBRA experiment*. Advances in High Energy Physics, volume 2013, 2013. doi:10.1155/2013/703572.

[18] Agostini, M., et al. *Characterization of a broad energy germanium detector and application to neutrinoless double beta decay search in* ^{76}*Ge*. Journal of Instrumentation, volume 6(04):p. P04005, 2011. doi:10.1088/1748-0221/6/04/P04005.

[19] Barabash, A. S. *Precise half-life values for two-neutrino double-*β *decay*. Phys.Rev.C, volume 81(3):p. 035501, Mar 2010. doi:10.1103/PhysRevC.81.035501.

[20] Tetyak, V. I. and Zdesenko, Y. G. *Tables of Double Beta Decay data — an update*. Atomic Data and Nuclear Data Tables, volume 80(1):pp. 83, 1 2002. doi:10.1006/adnd.2001.0873.

[21] The GERDA Collaboration. *Measurement of the half-life of the two-neutrino double beta decay of* ^{76}*Ge with the* GERDA *experiment*. Journal of Physics G: Nuclear and Particle Physics, volume 40(3):p. 035110, 2013. doi:10.1088/0954-3899/40/3/035110.

[22] The KATRIN Collaboration. *KATRIN: A next generation tritium beta decay experiment with sub-eV sensitivity for the electron neutrino mass*. 2001. arXiv:hep-ex/0109033.

[23] The KATRIN Collaboration. *KATRIN - direct measurement of a sub-eV neutrino mass*. Nuclear Physics B - Proceedings Supplements, volume 145:pp. 263, 8 2005. doi:10.1016/j.nuclphysbps.2005.04.019.

[24] The Planck Collaboration. *Planck 2013 results. XVI. Cosmological parameters.* A&A, volume 571:p. A16, 2014. doi:10.1051/0004-6361/201321591.

[25] Mohapatra, R. N. and Goran, S. *Neutrino Mass and Spontaneous Parity Nonconservation.* Phys.Rev.Lett., volume 44(14):pp. 912, Apr 1980. doi:10.1103/PhysRevLett.44.912.

[26] Schechter, J. and Valle, J. W. F. *Neutrinoless double β decay in SU(2)$\times$U(1) theories.* Phys.Rev.D, volume 25(11):pp. 2951, Jun 1982. doi:10.1103/PhysRevD.25.2951.

[27] Kotila, J. and Iachello, F. *Phase-space factors for double-β decay.* Phys.Rev.C, volume 85(3):p. 034316, Mar 2012. doi:10.1103/PhysRevC.85.034316.

[28] Mirea, M., et al. *Phase Space Factors for Double Beta Decay: an up-date.* 2014. ArXiv:1411.5506.

[29] Mount, B. J., et al. *Double-β-decay Q values of* ^{74}Se *and* ^{76}Ge. Phys.Rev.C, volume 81(3):p. 032501, Mar 2010. doi:10.1103/PhysRevC.81.032501.

[30] Capozzi, F., et al. *Status of three-neutrino oscillation parameters, circa 2013.* Phys.Rev.D, volume 89(9):p. 093018, May 2014. doi:10.1103/PhysRevD.89.093018.

[31] Pontecorvo, B. *Mesonium and antimesonium.* Zhur.Eksptl'.i Teoret.Fiz., volume 33, 1957.

[32] Pontecorvo, B. *Inverse β processes and non-conservation of lepton charge.* Zhur.Eksptl'.i Teoret.Fiz., volume 34, 1958.

[33] Maki, Z., et al. *Remarks on the unified model of elementary particles.* Progress of Theoretical Physics, volume 28(5):pp. 870, 1962. doi:10.1143/PTP.28.870.

[34] Barea, J., et al. *Nuclear matrix elements for double-β decay.* Phys.Rev.C, volume 87(1):p. 014315, Jan 2013. doi:10.1103/PhysRevC.87.014315.

[35] Dell'Oro, S., et al. *New expectations and uncertainties on neutrinoless double beta decay.* Physical Review D, volume 90(3):p. 033005, 2014. doi:10.1103/PhysRevD.90.033005.

[36] Päs, H. and Rodejohann, W. *Neutrinoless double beta decay.* New Journal of Physics, volume 17(11):p. 115010, 2015. doi:10.1088/1367-2630/17/11/115010.

[37] Forero, D. V., et al. *Neutrino oscillations refitted.* Physical Review D, volume 90(9):p. 093006, 2014. doi:10.1103/PhysRevD.90.093006.

[38] Avignone, F. T., et al. *Next generation double-beta decay experiments: metrics for their evaluation.* New Journal of Physics, volume 7(1):p. 6, 2005. doi:10.1088/1367-2630/7/1/006.

[39] Agostini, M., et al. *Results on Neutrinoless Double-β Decay of* ^{76}Ge *from Phase I of the* GERDA *Experiment*. Phys.Rev.Lett., volume 111(12):p. 122503, Sep 2013. doi:10.1103/PhysRevLett.111.122503.

[40] Klapdor-Kleingrothaus, H. V., et al. *Latest results from the HEIDELBERG-MOSCOW double beta decay experiment*. The European Physical Journal A-Hadrons and Nuclei, volume 12(2):pp. 147, 2001. doi:10.1007/s100500170022.

[41] Aalseth, C. E., et al. *IGEX* ^{76}*Ge neutrinoless double-beta decay experiment: prospects for next generation experiments*. Physical Review D, volume 65(9):p. 092007, 2002. doi:10.1103/PhysRevD.65.092007.

[42] Klapdor-Kleingrothaus, H. V., et al. *Search for neutrinoless double beta decay with enriched 76Ge in Gran Sasso 1990–2003*. Physics Letters B, volume 586(3–4):pp. 198, 4/29 2004. doi:10.1016/j.physletb.2004.02.025.

[43] The GERDA Collaboration. *Upgrade of the* GERDA *Experiment*. Proceedings of Science, p. Pos(TIPP2014)109, 2014.

[44] Knoll, G. F. *Radiation detection and measurement,* 4th *Edition*. John Wiley & sons, Hoboken, 2010.

[45] Ibach, H. and Lüth, H. *Festkörperphysik: Einführung in die Grundlagen*. Springer-Verlag, 2009.

[46] Haller, E. E., et al. *Physics of ultra-pure germanium*. Advances in Physics, volume 30(1):pp. 93, 02/01 1981. doi:10.1080/00018738100101357.

[47] He, Z. *Review of the Shockley–Ramo theorem and its application in semiconductor gamma-ray detectors*. Nuclear Instruments and Methods in Physics Research Section A: Accelerators, Spectrometers, Detectors and Associated Equipment, volume 463(1):pp. 250, 2001. doi:10.1016/S0168-9002(01)00223-6.

[48] Bruyneel, B., et al. *Characterization of large volume HPGe detectors. Part I: Electron and hole mobility parameterization*. Nuclear Instruments and Methods in Physics Research Section A: Accelerators, Spectrometers, Detectors and Associated Equipment, volume 569(3):pp. 764, 2006. doi:10.1016/j.nima.2006.08.130.

[49] Bruyneel, B., et al. *Characterization of large volume HPGe detectors. Part II: Experimental results*. Nuclear Instruments and Methods in Physics Research Section A: Accelerators, Spectrometers, Detectors and Associated Equipment, volume 569(3):pp. 774, 2006. doi:10.1016/j.nima.2006.08.129.

[50] Leo, W. R. *Techniques for nuclear and particle physics experiments: a how-to approach*. Springer Science & Business Media, 2012.

[51] Papp, T., et al. *A new approach to the determination of the Fano factor for semiconductor detectors*. X-Ray Spectrometry, volume 34(2):pp. 106, 2005. doi:10.1002/xrs.754.

[52] Andreotti, E., et al. *HEROICA: an underground facility for the fast screening of germanium detectors.* Journal of Instrumentation, volume 8(06):p. P06012, 2013. doi:10.1088/1748-0221/8/06/P06012.

[53] Brun, R. and Rademakers, F. *ROOT — An object oriented data analysis framework.* Nuclear Instruments and Methods in Physics Research Section A: Accelerators, Spectrometers, Detectors and Associated Equipment, volume 389(1–2):pp. 81, 4/11 1997. doi:10.1016/S0168-9002(97)00048-X.

[54] Agostini, M., et al. *GELATIO: a general framework for modular digital analysis of high-purity Ge detector signals.* Journal of Instrumentation, volume 6(08):p. P08013, 2011. doi:10.1088/1748-0221/6/08/P08013.

[55] Agostini, M., et al. *Off-line data processing and analysis for the* GERDA *experiment.* Journal of Physics: Conference Series, volume 368(1):p. 012047, 2012. doi:10.1088/1742-6596/368/1/012047.

[56] Agostini, M., et al. *Improvement of the energy resolution via an optimized digital signal processing in* GERDA *Phase I.* The European Physical Journal C, volume 75(6), 2015. doi:10.1140/epjc/s10052-015-3409-6.

[57] Petry, F., et al. *Background recognition in Ge detectors by pulse shape analysis.* Nuclear Instruments and Methods in Physics Research Section A: Accelerators, Spectrometers, Detectors and Associated Equipment, volume 332(1):pp. 107, 15 July 1993 1993. doi:10.1016/0168-9002(93)90746-5. ID: 271580271580.

[58] Abt, I., et al. *Test of pulse shape analysis using single Compton scattering events.* The European Physical Journal C, volume 54(3):pp. 425, 2008. doi:10.1140/epjc/s10052-008-0555-0.

[59] Vetter, K., et al. *Three-dimensional position sensitivity in two-dimensionally segmented HP-Ge detectors.* Nuclear Instruments and Methods in Physics Research Section A: Accelerators, Spectrometers, Detectors and Associated Equipment, volume 452(1–2):pp. 223, 9/21 2000. doi:10.1016/S0168-9002(00)00430-7.

[60] Nelson, L., et al. *Characterisation of an AGATA symmetric prototype detector.* Nuclear Instruments and Methods in Physics Research Section A: Accelerators, Spectrometers, Detectors and Associated Equipment, volume 573(1–2):pp. 153, 4/1 2007. doi:10.1016/j.nima.2006.11.042.

[61] Boston, A. J., et al. *Gamma-ray tracking: Characterisation of the AGATA symmetric prototype detectors.* Nuclear Instruments and Methods in Physics Research Section B: Beam Interactions with Materials and Atoms, volume 261(1–2):pp. 1098, 8 2007. doi:10.1016/j.nimb.2007.04.305.

[62] Berger, M. J., et al. *ESTAR, PSTAR, and ASTAR: Computer Programs for Calculating Stopping-Power and Range Tables for Electrons, Protons, and Helium Ions (version 1.23).* National Institute of Standards and Technology, Gaithersburg, MD., 2005. http://physics.nist.gov/Star [Wednesday, 09-Dec-2015].

[63] Budjáš, D., et al. *Pulse shape discrimination studies with a Broad-Energy Germanium detector for signal identification and background suppression in the* GERDA *double beta decay experiment.* Journal of Instrumentation, volume 4(10):p. P10007, 2009. doi:10.1088/1748-0221/4/10/P10007.

[64] Berger, M. J., et al. *XCOM: Photon Cross Section Database (version 1.5).* National Institute of Standards and Technology, Gaithersburg, MD., 2010. http://www.nist.gov/pml/data/xcom/ [Wednesday, 09-Dec-2015].

[65] Agostinelli, S., et al. *Geant4 — a simulation toolkit.* Nuclear Instruments and Methods in Physics Research Section A: Accelerators, Spectrometers, Detectors and Associated Equipment, volume 506(3):pp. 250, 7/1 2003. doi:10.1016/S0168-9002(03)01368-8.

[66] Boswell, M., et al. *MaGe - a Geant4-Based Monte Carlo Application Framework for Low-Background Germanium Experiments.* Nuclear Science, IEEE Transactions on, volume 58(3):pp. 1212, June 2011. doi:10.1109/TNS.2011.2144619.

[67] Bé, M. M., et al. *Table of Radionuclides (Vol. 3 — A = 3 to 244).* Bureau International des Poids et Mesures, Sèvres, France, 2006.

[68] Cennini, P., et al. *On atmospheric ^{39}Ar and ^{42}Ar abundance.* Nuclear Instruments and Methods in Physics Research Section A: Accelerators, Spectrometers, Detectors and Associated Equipment, volume 356(2–3):pp. 526, 3/15 1995. doi:10.1016/0168-9002(94)01234-2.

[69] Peurrung, A. J., et al. *Expected atmospheric concentration of ^{42}Ar.* Nuclear Instruments and Methods in Physics Research Section A: Accelerators, Spectrometers, Detectors and Associated Equipment, volume 396(3):pp. 425, 9/11 1997. doi:10.1016/S0168-9002(97)00819-X.

[70] Simgen, H. GERDA*: A new ^{76}Ge Double Beta Decay Experiment at Gran Sasso.* Nuclear Physics B - Proceedings Supplements, volume 143:p. 567, 6 2005. doi:10.1016/j.nuclphysbps.2005.01.232.

[71] Ashitkov, V. D., et al. *Liquid argon ionization detector for double beta decay studies.* 2003. ArXiv:nucl-ex/0309001.

[72] Agostini, M., et al. *The background in the $0\nu\beta\beta$ experiment* GERDA. The European Physical Journal C, volume 74(4):pp. 1, 2014. doi:10.1140/epjc/s10052-014-2764-z.

[73] Kinsey, R. R., et al. *The NUDAT/PCNUDAT program for nuclear data.* Springer, Hungary, 1997. http://www.nndc.bnl.gov/nudat2/ [Wednesday, 09-Dec-2015].

[74] Singh, B. and Cameron, J. A. *Nuclear Data Sheets for A = 42.* Nuclear Data Sheets, volume 92(1):pp. 1, 2001. doi:10.1006/ndsh.2001.0001.

[75] G. Audi, F.G. Kondev, M. Wang. *The* NUBASE*2012 evaluation of nuclear properties*. Chinese Physics C, volume 36(12), 2012. doi:10.1088/1674-1137/36/12/001.

[76] Caldwell, A., et al. *BAT – The Bayesian analysis toolkit*. Computer Physics Communications, volume 180(11):pp. 2197, 11 2009. doi:10.1016/j.cpc.2009.06.026.

[77] Bauer, M., et al. *MaGe: a Monte Carlo framework for the* GERDA *and* MAJORANA *double beta decay experiments*. Journal of Physics: Conference Series, volume 39(1):p. 362, 2006. doi:10.1088/1742-6596/39/1/097.

[78] Lehnert, B. *Analysis of Double Beta Decays in Germanium, Palladium and Argon*. Master's thesis, Technische Universität Dresden, Germany, Fakultät Mathematik und Naturwissenschaften Fachrichtung Physik 01062 Dresden, Germany, 2011. Diploma Thesis.

[79] Ponkratenko, O. A., et al. *Event generator DECAY4 for simulating double-beta processes and decays of radioactive nuclei*. Physics of Atomic Nuclei, volume 63(7):pp. 1282, 2000. doi:10.1134/1.855784.

[80] Benato, G. *FWHM at $Q_{\beta\beta}$ and Energy Reconstruction Uncertainty for the 3* GERDA *Phase I Data*. Gerda Scientific Technical Report, 03 2013.

[81] Beaujean, F., et al. *p-values for model evaluation*. Phys.Rev.D, volume 83(1):p. 012004, Jan 2011. doi:10.1103/PhysRevD.83.012004.

[82] Agostini, M., et al. *Production, characterization and operation of ^{76}Ge enriched BEGe detectors in* GERDA. The European Physical Journal C, volume 75(2), 2015. doi:10.1140/epjc/s10052-014-3253-0.

[83] Cirrone, G. A. P., et al. *Validation of the Geant4 electromagnetic photon cross-sections for elements and compounds*. Nuclear Instruments and Methods in Physics Research Section A: Accelerators, Spectrometers, Detectors and Associated Equipment, volume 618(1–3):pp. 315, 6/1–21 2010. doi:10.1016/j.nima.2010.02.112.

[84] Heider, M. B. *Performance and stability tests of bare high purity germanium detectors in liquid argon for the* GERDA *experiment*. Ph.D. thesis, Ruperto-Carola University Heidelberg, Germany. PhD Thesis.

[85] Watterson, B. *Calvin and Hobbes*. http://www.gocomics.com/calvinandhobbes/.

The End...

Having reached the end of this thesis I look back at three years of ups and downs, of frustration and success, and many precious experiences I wouldn't want to have missed for gold. Coming to Padova and leaving everything behind in Tübingen was one of the best choices I have ever made and has been a small personal adventure. The support I found, here in Padova, has been tremendous and at this point I want to thank some important people, for whose advice, backing, encouragement and existence I am endlessly grateful:

Thank you, Alberto Garfagnini, my supervisor, for your trust in my work and for the freedom to tackle problems on my own. Your advice and critics helped me a great deal to become a better physicist and to be proud of the things I have accomplished. Thank you for the involvement and stimulation in working with students, in schools and conferences, in letting me share and increase my knowledge and by getting to know a lot of other fascinating people. I am equally thankful to Riccardo Brugnera, your kind support and commitment were a fundamental basis in the creation of this thesis. You always gave importance to my work and made the impossible possible.

I want to thank Ivano Lippi, Luciano Modenese, Davide Rosso and Matteo Turcato and the guys from the mechanical workshop; your work and availability have been a vital ingredient in the creation of the experimental setup built in the "cage" at Legnaro. Ivano, you are a formidable physicist, a miracle worker in programing and one of the most tranquil, forward and humorous people I know. Thank you, Luciano, for your kindness and availability, without your skill in electronics this work would have not been possible. Davide, your knowledge, encouragement and supply with the semi-coaxial detectors of the former GASP experiment were a necessary ingredient in the creation of this thesis, thank you so much. Matteo and the guys from the mechanical workshop, thank for your time and sweat; without you there would be no Compton table, no source collimator and no thesis.

My thanks go to all the people in the GERDA collaboration for valuable input and discussions; especially to you, Luciano Pandola and Sabine Hemmer, for the basis of the ^{42}Ar analysis. I had so much fun with all of you at the legendary GERDA collaboration meetings, thank you for a little craziness and a great time. Getting stuck in the snow at three o'clock in the night (on purpose) is only fun with the right Panda and people.

I thank you, Marco Roda and Eduardo Medinaceli, for noisy office hours, open ears and hearts whenever necessary, and fruitful discussions and your support which meant a great deal to me. Marco, you are a kind and loud (but never off-key) soul, thanks for all the laughter and your legendary Risotto alla pilota and the Tigelle. Thank you, Edu, although you had a rough time in the last years, you did your very best to be there, help me understand what I was doing, and taking some workload off my shoulders when I needed it the most.

Max and the Torelle Sudate, you are one of the best things that happened to me in the last three years. Thank you for a great time, making me discover a passion in Rugby and the possibility to affront and surpass my fears and anxieties. Without you I wouldn't be the person I am today, I wouldn't know the "arts of the bestemmia" and I would have missed that happiness of mud and sweat and exhaustion. The team spirit I experience with you is an incredible gift to my life.

Mauro, Sandra, Davide, Rino and Dik, thank you for a second home and open arms and paws. Mauro, your friendship means a lot to me and your kind heart is a light that shines at every hour of the day.

Thank you, Ivonne, I always look forward to your visits in Padova, you are a splendid person and a very precious and very German friend.

I thank you all, my friends and colleagues in Padova and Tübingen and in all the world, for the PhD seminars, "Romolo il grande", Cena Cinema, Dark Heresy, Live Egea and the Isole senza Mare, the great times at the Mythodea Conquest and the Summer Breeze, and a lot of other things. Three years seem to have passed within the blink of an eye with all the enjoyable moments you gave me.

Finally, a very special thanks goes to Peter, Michaela, Max und Moritz, Theresa, Ferdinand and Ursula, Helga, and the rest of my family. You all have a special place in my heart, your support is my very essence and I feel blessed for heaving each and every one of you in my life. Peter, your fatherly love knows no boundaries and you are the backbone to this family, thank you. Michaela, thank you for being there, for being an incredible mother with a great heart and for always putting your children first. And, Elisabeth, thank you for supporting the "woman power" in our family, your encouragement endures the boundaries of time.

Ignacio Miguel, you are the one person that makes me shine, thank you for lifting me up and never letting me down, for enduring my moods, for being with me and the gift of your love ♡